PhD-FSTM-2025-090
Faculty of Science, Technology and Medicine

Faculty of Physics, Institute of Theoretical Physics

DISSERTATION

Defence held on 20 August 2025 in Luxembourg to obtain the

degree of

DOCTEUR DE L'UNIVERSITÉ DU LUXEMBOURG EN SCIENCES EXACTES ET NATURELLES

AND

DOCTEUR DE L'UNIVERSITÉ Technische Universität Dresden

EN Doctor rerum naturalium

by

Chen XU
Born on 31 August 1994 in Chongqing (China)

Semi-classical dynamics and quantum geometry

Dissertation defence committee

Prof. Dr Thomas SCHMIDT, Supervisor
Full professor in Physics, UNIVERSITÉ DU LUXEMBOURG / Esch-sur-Alzette / Luxembourg

Dr Tobias MENG, Co-Supervisor
Emmy-Noether Fellow, TECHNISCHE UNIVERSITÄT DRESDEN / Dresden / Germany

Prof. Dr Alex REDINGER, Chair
Full professor in Physics, UNIVERSITÉ DU LUXEMBOURG / Esch-sur-Alzette / Luxembourg

Prof. Dr Matthias VOJTA, Member
Professor, TECHNISCHE UNIVERSITÄT DRESDEN

Prof. Dr Alessandro BRAGGIO, Member
Professor, SCUOLA NORMALE SUPERIORE, PISA

Prof. Dr Peter ORTH, Member
Professor, UNIVERSITÄT DES SAARLAND

Affidavit

I hereby confirm that the PhD thesis entitled "Semi-classical dynamics and quantum geometry" has been written independently and without any other sources than cited.

Luxembourg, **27.06.2025** Name **Chen Xu**

Contents

Acknowledgment 2

Publications 3

1 Introduction 4

Part I 9

2 Basics of geometry of quantum states 10
- 2.1 Geometry of quantum states 10
  - 2.1.1 Geometry of quantum states 10
  - 2.1.2 Adiabatic evolution 12
  - 2.1.3 Quantum geometric tensor 15
- 2.2 Geometry of Bloch bands 20
  - 2.2.1 Bloch's theorem and band theory 20
  - 2.2.2 Quantum geometry of Bloch states 21
  - 2.2.3 Symmetry behavior 24

3 Operator approach to dynamics 27
- 3.1 Quantum geometry and projected moments 28
- 3.2 Introduction 28
  - 3.2.1 Band Projection 29
  - 3.2.2 Band-projected operators 30
- 3.3 Local expressions of the geometric operators 36
  - 3.3.1 Local projection operators and moment generating function 36
  - 3.3.2 Position and velocity operator 38
  - 3.3.3 Geometric quantities 40
- 3.4 Canonical momentum 42
  - 3.4.1 Canonical momentum and and real space Berry connections 42
  - 3.4.2 Mixed geometrical quantities 43
- 3.5 Semi-classical equation of motion 45
  - 3.5.1 Bloch electron in external fields 45
  - 3.5.2 Projected dynamics 47

3.5.3 Inhomogeneous electric field and geometry 51
3.5.4 Magnetic field 53
3.5.5 Wave-packet dynamics 56
3.6 Summary 60

Appendix for Part I **61**
A.1 Poisson summation formula 62
A.2 Dirac calculus 64
A.3 Moment generating operators 66
A.4 Moments of position 67
A.4.1 Average position distribution 67
A.4.2 Second moment distribution 68
A.5 Real space Berry connection 69
A.6 Center of mass operator 70
A.7 Perturbation theory via projection operator 71

Part II **73**

4 Analogue gravitational lensing **74**
4.1 Introduction 74
4.2 Tilted Weyl semi-metals 75
4.2.1 Weyl Semi-metals 75
4.2.2 Tilted Weyl systems 76
4.2.3 Gravitational analogue 78
4.3 Cylindrical tilt and lensing 80
4.3.1 Trajectory analysis 81
4.3.2 Lensing and deflection angle 86
4.3.3 Capture and Separatrix 87
4.4 Lattice simulations 90
4.4.1 Effective lattice model 90
4.4.2 The microscopic setup 95
4.4.3 Numerical results 97
4.5 Berry curvature and transverse shift 100
4.5.1 Spin precession 102
4.6 Summary 107

Appendix for Part II **108**
B.1 Geodesic equation 109
B.2 Deflection angle 114
B.3 Transverse shift 117

5 Conclusion **119**

References **121**

Acknowledgment

First of all, I would like to express my gratitude to both of my supervisors Tobias and Thomas, from whom I have received not just a PhD position, but also four years of continuous kindness, patience, and support. You provided guidance and help when I was confused, making mistakes and lost, without which I would not have been able to get here.

Special thanks also go to Suraj and Andreas, who have been the academic older brothers of mine in Dresden and in Luxembourg respectively. The physicists' discussions in front of the blackboard have been a special, fond memory that I will always keep.

To all my colleagues and peers, back in Dresden and here in Luxembourg, I thank you all for making the four years full of fun and joyful moments, and even during the downs, we have made it through together. I had the special luck of having two groups of office mates, and that means I have double the amount of scientific discussions, non-scientific talks, gossips, and good laughs.

Krinio and Anouar, how time flies! It is still a surprise to me that it has been six years since we came from different corners of the world and began our journey in physics in Utrecht, while it felt like yesterday.

Finally, Mom and Dad, throughout all these years of me drifting far from your side, you have given me unconditional support in every form. As the old Chinese saying goes, "When the child travels a thousand miles, the parent is concerned". I know you have carried that worry quietly, and only let it slip out when checking if I put on weight or not. This journey has been long but your support was with me every step of the way.

List of Publications

- *Quantum geometry in the dynamics of band-projected operators,*
  C. Xu, A. Haller, S. Hegde, T. Meng, and T.L.Schmidt,
  arXiv:2503.11425 [cond-mat.mes-hall]

- *Black hole mirages: Electron lensing and Berry curvature effects in inhomogeneously tilted Weyl semimetals,*
  A. Haller, S. Hegde, C. Xu, C. De Beule, T. L. Schmidt,and T. Meng,
  SciPost Physics **14**, 119 (2023).

- *The anomalous photo-Nernst effect of massive Dirac fermions in $HfTe_5$,*
  M. P. Singh, J. Kiemle, C. Xu, W. Schmunk, Q. Dong, G. Chen, T. Meng, and C. Kastl,
  Advanced Physics Research **3**, 2300099 (2024).

- *Topological phases of the interacting Su-Schrieffer-Heeger model: An analytical study,*
  E. Di Salvo, A. Moustaj, C. Xu, L. Fritz, A. K. Mitchell, C. Morais Smith, and D. Schuricht,
  Physics Review B **110**, 165145 (2024).

This thesis is based on the first two works listed above.

Chapter 1

Introduction

Ever since the beginning of the field in 1920s, band theory has been a cornerstone that lies at the very core of solid state physics, underpinning both theoretical developments and material science applications. Indeed, as far as single particle picture, or more fundamentally Landau Fermi liquid theory, applies, almost all of the properties of the electronic degrees of freedom in solid state systems have been studied within the framework of band theory. Band theory elegantly exploits symmetry to account for the quantum effects of a crystalline lattice via energy band formation. One of the most spectacular successes of band theory is its elegant and unified explanation of the categorization of insulators, semiconductors, and metals among a large portion of solid-state materials. Band theory and the foundational Bloch's theorem has been a part of every solid state physics curriculum [11, 81, 136]. For a long time the physics of the energy bands have been thought to be mature and well-understood until the emergence of topological phases of matter in recent decades. The discovery of the remarkable integer and fractional quantum Hall effects in the 1980s brought about a revolution in condensed matter physics, introducing the profound idea of topological order, which has sparked the investigation of a large variety of exotic quantum phases of matter: topological insulators, topological superconductors, and topological semi-metals just to name a few. Somewhat philosophically, one might say that one fundamental conceptual shift that the notion of topological order has brought forward is the realization of the physical significance of electronic wavefunctions, rather than the energy spectrum alone, as previously thought. Indeed, in the case of quantum Hall effect, the quantization of Hall conductance has been explained in terms of a topological invariant—the first Chern number—associated with the filled bands. Such a topological invariant characterizes the global property of the wavefunctions, as demonstrated by the seminal TKNN formula [149].

More recently it has been realized that not only the global topology but also the local

geometric property of quantum states plays a role in the study of various aspects of electrons in crystalline solids. In fact, from a more general perspective, the Berry curvature which has traditionally been related to the topology of the band structure, such as the first Chern number mentioned above, can itself be viewed as a local geometric quantity, even in the topologically trivial case. Closely related is the so-called quantum metric tensor, also known as the Fubini-Study metric, which has recently attracted much attention. Around the same time as the seminal work by Berry [20], who identified an intrinsic phase factor accompanying the adiabatic evolution of parameterized quantum states, namely the Berry phase, the quantum metric tensor emerged in the work by Provost and Vallee from the study of quantum information theory [121]. They realized that the Hilbert space of a family of parameterized quantum states can be endowed with a Riemannian geometry, where roughly speaking, a notion of distance between states is given by the degree of orthogonality, and quantified by the quantum metric tensor. Moreover, both the quantum metric tensor and the Berry curvature can be unified as the real and imaginary parts, respectively, of a quantity known as the quantum geometric tensor. Ever since its discovery, the quantum geometry of states has been exploited and applied in quantum information theory [17], and quantum phase transitions [31, 39]. Propelled by the intense study of exotic topological phases of matter, its significance in the solid state systems has also been noticed, and a variety of phenomena such as transport, optical and many-body effects to name a few, have been studied using quantum geometry [151].

Indeed, in crystalline solids, the Bloch states which constitute a basis of the Hilbert space of electrons moving in a background lattice periodic potential, provide a natural example of such parameterized states. The parameter is simply the crystal momentum, which is a good quantum number that is associated with the lattice symmetry and label the eigenstates, as dictated by Bloch's theorem. The manifold of crystal momentum, the Brillouin zone, forms a torus and geometric quantities such as the Berry curvature and quantum metric tensor encode information about how electronic wavefunctions twist, overlap, and connect across this manifold. Thus, the geometry of Bloch states may significantly influence physical observables, and dictate electronic, optical, and transport properties.

The central focus of this thesis is the exploration of such geometric effects on the semi-classical dynamics of lattice electron wave-packets. Semi-classical equations of motion provide a low-energy effective approach to study the various quantum mechanical effects due to the geometry of quantum states, which manifest as modifications to the classical equations of motion. For instance, this approach has been applied to study phenomena such as the

anomalous Hall effect [58] induced by Berry curvature, the chiral magnetic effect [47] and the anomalous magneto-resistance in topological semi-metals [95].

This thesis is structured into two parts, each exploring one aspect of the connection of quantum geometry of Bloch states with semi-classical equations of motion in solid state systems.

In Part I some more foundational and generic aspects of the way quantum geometry manifests itself in the dynamics of Bloch electrons. We start out by providing some basic background materials concerning the geometry of Hilbert space of parameterized states. We identify from a mathematical point of view how the projective Hilbert spaces, namely the space of physical states modulo the phase gauge redundancy, may be recognized as what is known as complex projective space, and its connection to fiber bundle theory. For later development, we also discuss the adiabatic evolution and the emergent geometric phase in great details, with the purpose of highlighting the often neglected significance of projection onto a subspace in bringing forward the non-trivial geometrical effects. Then we introduce the quantum geometric tensor for general parameterized quantum states, following the derivation of the original reference [121], via enforcing gauge invariance. In particular, we shall identify the imaginary and real part of the quantum geometric tensor is the precisely the Berry curvature and quantum metric tensor respectively. Furthermore, we point out that the quantum metric tensor provides a gauge invariant measure of distance between quantum states. Then we specialize to crystalline solids, where by Bloch's theorem, the Bloch states that emerge from the periodic potential of crystal lattices is an important, physical example of such parameterized quantum states. To complete the basic introduction, we mention how the time reversal and spatial inversion symmetry impose constraints on geometric quantities.

A core contribution of this part is the systematic development of an operator-based formalism for the study of quantum geometric contributions to lattice electron dynamics. The central observation is that the semi-classical dynamics is fundamentally a low energy effective description, and requires access to only a subset of all energy bands that are available. Formally such restriction to a low-energy sector is done by a projection to a certain set of bands, and the projected operators have substantially modified commutation relations, which is the origin of the various geometric contributions to the equations of motion. By analyzing commutation relations of band-projected operators, and identifying the operator form of geometric quantities, we reveal a hierarchy of geometric corrections, from familiar Berry curvature effects to higher-order geometric terms such as quantum geometric connections

when an inhomogeneous external field is applied.

In Part II, we shift our focus from Bloch momentum space geometry to real space geometric effects. We study the electron dynamics in tilted Weyl semi-metals—a class of topological materials characterized by linear band crossings known as Weyl nodes. Around the Weyl nodes, the quasi-particle may be described in terms of the Weyl Hamiltonian, and a remarkable parallel to the motion of massless particle around a black hole is given by a spatially varying tilt term added to the Weyl Hamiltonian. Specifically, we shall demonstrate an analogy between the semi-classical dynamics in tilted Weyl semi-metals and gravitational lensing phenomena in general relativity. Indeed, the effective Hamiltonian of tilted Weyl systems gives rise to an effective curved spacetime metric, known as the Painlevé-Gullstrand metric, and the electron wave-packet motion around the Weyl node may be mapped to that of a massless particle moving under the influence of the gravitational field of a black hole. We study analytically various aspects of such electron motion, including deflection angles, trapping, and critical separatrices between bound and unbound electron states. Moreover, the Berry curvature related anomalous shift is also investigated, which may be viewed as an analogue gravitational Magnus effect, inducing a transverse shift that is not present in the classical theory of particle motion under gravity. In fact, this transverse shift may be viewed as the spin dynamics of a Weyl fermion, which has an intrinsic spinor structure, and arises in a solid state system due to the topological property of the Weyl nodes. To confirm and better understand the analytics in the effective continuum picture, we also provide lattice-based simulations using a tight-binding model, which provides further insights concerning the lattice effects that may hint at microscopic details of electron dynamics under realistic conditions.

Part I

Chapter 2

Basics of geometry of quantum states

2.1 Geometry of quantum states

In this part of the thesis we will explore the geometry of the Bloch structure and its implications for semi-classical dynamics and transport in solid state materials. To set the stage, we shall briefly describe the meaning of "geometry" in the context of quantum states, and in particular Bloch states.

We first discuss the geometrization of Hilbert spaces in a rather general setting. More specifically, we describe how the space of parameterized states may be given the structure of a fiber bundle. Then we give an introduction to concepts such as quantum geometric tensor and its real and imaginary components: quantum metric tensor and Berry curvature, which characterize the geometry of Hilbert space. Finally we go to the specific situation where such parameterized Hilbert space arises as the Bloch states of a particle moving in a crystal lattice. Throughout the thesis we use units in which $\hbar = 1$, unless otherwise states

2.1.1 Geometry of quantum states

Hilbert space as a fiber bundle

We consider the following situation: we have a Hamiltonian $\hat{H}$ of some quantum mechanical system whose eigenstates are smoothly parameterized by, say N variables $\boldsymbol{\lambda} = (\lambda_1, \lambda_2, ...\lambda_N)$, normally some good quantum numbers associated with symmetry, such as the crystal momentum of Bloch states in a N-dimensional lattice. Another example of such parametrized states, which is actually the one considered in the original reference [121], is the generalized coherent states[17, 66]. We assume the Hilbert space $\mathcal{H}_{\boldsymbol{\lambda}}$ of all states with a given $\boldsymbol{\lambda}$ has dimension N, such as the number of energy bands in a solid. We may then always take $\mathcal{H}_{\boldsymbol{\lambda}}$

to be spanned by the eigenstates $|\psi_n(\boldsymbol{\lambda})\rangle$. Mathematically, therefore, the Hilbert space at each $\boldsymbol{\lambda}$ is $\mathbb{C}^N$, while the total Hilbert space $\mathcal{H}$ is the direct sum of all local Hilbert spaces $\mathcal{H}_{\boldsymbol{\lambda}}$:

$$\mathcal{H} = \bigoplus_{\boldsymbol{\lambda}} \mathcal{H}_{\boldsymbol{\lambda}}. \tag{2.1.1}$$

Equivalently put, since the eigenstates form a complete basis, we have a resolution of identity being $\mathbb{1} = \sum_n \sum_{\boldsymbol{\lambda}} |\psi_n(\boldsymbol{\lambda})\rangle \langle\psi_n(\boldsymbol{\lambda})|$ (of course, the "sum" over $\boldsymbol{\lambda}$ is actually an integral with an appropriately chosen measure). Take $\mathcal{H}'_{\boldsymbol{\lambda}} \subset \mathcal{H}_{\boldsymbol{\lambda}}$ to be the subspace consisting of all states that are all normalized, namely $\langle\psi|\psi\rangle = 1$, and then $\mathcal{H}'_{\boldsymbol{\lambda}}$ is just a hyper-sphere S^{2N-1}. Indeed, for an arbitrary state in $\mathcal{H}'_{\boldsymbol{\lambda}}$, let $|\psi(\boldsymbol{\lambda})\rangle = \sum_n c_n |\psi_n(\boldsymbol{\lambda})\rangle$ be its expansion in the eigenstate basis, then the map $|\psi(\boldsymbol{\lambda})\rangle \to (c_1, c_2, ...c_N)$ clearly takes a state in $\mathcal{H}'_{\boldsymbol{\lambda}}$ to the sphere, since $\sum_n |c_i|^2 = 1$ by normalization condition. A basic but crucial observation, which has profound implications in topological band theory[62, 122] is that there is a certain gauge freedom in this description: in quantum mechanics two states which differ by a phase are physically equivalent. Then the physically distinct states are obtained by identifying all states that are identical up to a phase, and the space of normalized, physical states with a given $\boldsymbol{\lambda}$ is actually the ray/projective Hilbert space $P\mathcal{H}_{\boldsymbol{\lambda}} = \mathcal{H}'_{\boldsymbol{\lambda}}/U(1)$, which mathematically is the same as the $(N-1)$-dimensional complex projective space $P\mathcal{H}_{\boldsymbol{\lambda}} = \mathbb{C}P^{N-1}$[83, 106]. Such a decomposition of the Hilbert space $\mathcal{H}$ into a smoothly parameterized sum enables us to view the collection of quantum states as a fiber bundle over the parameter manifold $\mathcal{M}$, such that at each point $\boldsymbol{\lambda}$ it is attached with a fiber $\mathcal{H}'_{\boldsymbol{\lambda}} = S^{2N-1}$, or $P\mathcal{H}_{\boldsymbol{\lambda}} = \mathbb{C}P^{N-1}$[17]. A family of states $|\psi(\boldsymbol{\lambda})\rangle$ with smoothly varying $\boldsymbol{\lambda}$ then defines a section over the fiber bundle.

Here we note that a physical state with a fixed phase is in one-to-one correspondence with the projection operator $\hat{P}_{\boldsymbol{\lambda}} = |\psi(\boldsymbol{\lambda})\rangle \langle\psi(\boldsymbol{\lambda})|$. Indeed, all states that differ from each other by a phase $e^{-i\theta(\boldsymbol{\lambda})}$ give the same $\hat{P}_{\boldsymbol{\lambda}}$. Put another way, a projection operator is naturally a gauge invariant object that uniquely defines a physical state, i.e. there is a state-operator correspondence. In our development later, we will heavily rely on the use of projection operators to study the semi-classical dynamics, and it is at times helpful to have the intuition that a local projection operator can be viewed as a state.

Sub-bundle

We note that in principle the fiber bundle constructed as above may in general be topologically trivial, namely the space of normalized states is just the product $\mathcal{M} \times S^{2N-1}$ or in terms of physical states $\mathcal{M} \times \mathbb{C}P^{N-1}$, which in mathematics jargon it is said to be a trivial bundle [83]. Does this mean no interesting or non-trivial topological and geometric phenomena arise? The

subtle but important point which will be discussed in detail in later chapters is that, often in physics we are working with not the entire Hilbert space given by the Hamiltonian, but a sub-bundle of it. Roughly speaking, an external probe, say a weak electric field, accesses only a subspace $\mathcal{H}_\mathcal{B} \subset \mathcal{H}$, and we may describe the effective physics using a low energy effective Hamiltonian $\hat{H}_\mathcal{B}$. When the eigenstates are parameterized as we described above, at each λ we need to consider only the $N_\mathcal{B}$-dimensional subspace, with $N_\mathcal{B} < N$. The resulting sub-bundle may then have highly non-trivial topological and geometric structures. Geometrically, one can think as an example how a sphere, regarded as embedding in the Euclidean space $\mathbb{R}^3$ has nontrivial topology and curved geometry where one can introduce covariant derivative, etc, while the $\mathbb{R}^3$ itself is rather trivial and flat, on which one differentiates using the usual partial derivative.

2.1.2 Adiabatic evolution

In the previous section, the Hilbert space as a geometric object was discussed in a rather abstract and formal way, and it is not clear how physically relevant such a picture is. Here we introduce the typical context where a projection as discussed above is invoked, and how such a geometric picture enters, namely the emergence of Berry phase in adiabatic evolution[20]. This is a widely discussed topic with a large amount of literature available; see, for example, [27]. But we would go into quite some details of the well known concept to put a perspective in things for later development. By this we mean that we would like to emphasize the role of projection in bringing out the geometric features.

We consider the following situation: a system with Hamiltonian $\hat{H}_0$, whose eigenstates take a smooth parameterization, is now perturbed by an external field that varies in time, so the system's Hamiltonian $\hat{H}(t)$ is now time dependent. Without loss of generality, we choose the interaction to be turned on at $t = 0$ so that the $|\psi_{n\boldsymbol{\lambda}}\rangle$'s are eigenstates of the unperturbed Hamiltonian $\hat{H}_0$. We assume that at any instant the eigenstates of $\hat{H}(t)$ can still be parameterized by the same parameters so that we may write $\hat{H}(t) = \sum_{n\boldsymbol{\lambda}} \epsilon_{n\boldsymbol{\lambda}}(t) \, |\psi^t_{n\boldsymbol{\lambda}}\rangle \langle\psi^t_{n\boldsymbol{\lambda}}|$, where $|\psi^t_{n\boldsymbol{\lambda}}\rangle$ are the instantaneous eigenstates of $\hat{H}(t)$. Due to the explicit time dependence, the spectrum $\epsilon_{n\boldsymbol{\lambda}}(t)$ in geneal differs from that of $\hat{H}_0$. In the case of Bloch states, the discrete label of energy levels n is called a band index.

Now we consider the evolution of a state $|\psi(t)\rangle$ which at time $t = 0$ is an eigenstate of the initial Hamiltonian, namely $|\psi(0)\rangle = \left|\psi^0_{n\boldsymbol{\lambda}_0}\right\rangle$ with some $\boldsymbol{\lambda}_0$, and $|\psi(t)\rangle = \left|\psi^0_{n\boldsymbol{\lambda}_0}(t)\right\rangle$. Note that due to the time dependence of the Hamiltonian, the state $\left|\psi^0_{n\boldsymbol{\lambda}_0}\right\rangle$ is no longer an eigenstate of the perturbed Hamiltonian except at $t = 0$, namely, that $\hat{U}(t, 0) \, |\psi^0_{n\boldsymbol{\lambda}}\rangle = |\psi^0_{n\boldsymbol{\lambda}}(t)\rangle \neq |\psi^t_{n\boldsymbol{\lambda}}\rangle$.

More importantly, the instantaneous eigenstates do not satisfy the Schrodinger equation, namely $i\partial_t |\psi^t_{n\boldsymbol{\lambda}}\rangle \neq \hat{H}(t) |\psi^t_{n\boldsymbol{\lambda}}\rangle = \epsilon_{n\boldsymbol{\lambda}}(t) |\psi^t_{n\boldsymbol{\lambda}}\rangle$. In fact $|\psi^t_{n\boldsymbol{\lambda}}\rangle$ should be thought to be fixed at some time say $t = 0$, and the evolving eigenstate which satisfies the Schrodinger equation, is $|\psi^t_{n\boldsymbol{\lambda}}(t')\rangle \equiv \hat{U}(t', 0) |\psi^t_{n\boldsymbol{\lambda}}\rangle$.

Without further assumptions such as symmetry, at a later time the evolved state $|\psi(t)\rangle$ is a superposition of all initial eigenstates:

$$|\psi(t)\rangle = \sum_{m\boldsymbol{\lambda}} c_{m\boldsymbol{\lambda}}(t) \left|\psi^0_{m\boldsymbol{\lambda}}\right\rangle, \tag{2.1.2}$$

where the coefficients are chosen to make $|\psi(t)\rangle$ normalized at all times, and $c_{m\boldsymbol{\lambda}}(0) = c_{n\boldsymbol{\lambda}}(0)\delta_{nm}\delta_{\boldsymbol{\lambda}\boldsymbol{\lambda}_0}$. Another way to put this is that the perturbed Hamiltonian is not diagonal in the basis of $|\psi^0_{m\boldsymbol{\lambda}}\rangle$, and in general allows for arbitrary transitions unless there are selections rules. Then the coefficients have to be solved by using, for instance, time-dependent perturbation theory, if the applied field is weak. However, if we assume the energy gap between $\epsilon^t_{n\boldsymbol{\lambda}}$ and all the other energy levels m is large enough throughout the duration that the external field acts (we exclude level crossings), or equivalently the external fields evolve slowly, then it can be shown that[28, 78] $|\psi(t)\rangle$ may be approximately taken as an instantaneous eigenstate, or $\hat{H}(t) |\psi(t)\rangle \approx \epsilon^t_{n\boldsymbol{\lambda}(t)} |\psi(t)\rangle$, for some $\boldsymbol{\lambda}(t)$. This is called adiabatic evolution. Note that adiabatic evolution only states that the initial eigenstate of $\hat{H}^0$ would remain an eigenstate of $\hat{H}(t)$ in the same band labeled n, but not necessarily with the same parameter $\boldsymbol{\lambda}_0$. By normalization this means $|\psi(t)\rangle$ can differ from $\left|\psi^t_{n\boldsymbol{\lambda}(t)}\right\rangle$ up to a phase, hence

$$|\psi(t)\rangle \approx e^{i\gamma_n(t)} \left|\psi^t_{n\boldsymbol{\lambda}(t)}\right\rangle = \hat{P}_{n\boldsymbol{\lambda}(t)} |\psi(t)\rangle \tag{2.1.3}$$

where $\hat{P}_{n\boldsymbol{\lambda}(t)} = \left|\psi^t_{n\boldsymbol{\lambda}(t)}\right\rangle \left\langle\psi^t_{n\boldsymbol{\lambda}(t)}\right|$ is the local projection operator that projects the state onto the eigenstates of $\hat{H}(t)$ with parameter $\boldsymbol{\lambda}(t)$. Thus under the assumption of adiabatic evolution, the transition amplitude is just the phase $\gamma_n(t)$. The Schrodinger equation now reads

$$i\frac{d}{dt} |\psi(t)\rangle \approx \hat{H}(t)\hat{P}_{n\boldsymbol{\lambda}(t)} |\psi(t)\rangle = \epsilon_{n\boldsymbol{\lambda}}(t) e^{i\gamma_n(t)} \left|\psi^t_{n\boldsymbol{\lambda}(t)}\right\rangle \tag{2.1.4}$$

On the other hand the left hand side may also be written out as

$$i\frac{d}{dt} |\psi(t)\rangle \approx i\frac{d}{dt}\left(e^{i\gamma_n(t)} \left|\psi^t_{n\boldsymbol{\lambda}(t)}\right\rangle\right) \tag{2.1.5}$$

$$= -\frac{d\gamma_n}{dt} e^{i\gamma_n(t)} \left|\psi^t_{n\boldsymbol{\lambda}(t)}\right\rangle + i e^{i\gamma_n(t)} \frac{d\boldsymbol{\lambda}}{dt} \partial_{\boldsymbol{\lambda}(t)} \left|\psi^t_{n\boldsymbol{\lambda}(t)}\right\rangle. \tag{2.1.6}$$

Equating these two expressions, we have

$$\mathrm{i}\frac{d\gamma_n}{dt} = -\mathrm{i}\epsilon_{n\boldsymbol{\lambda}}(t) + \frac{d\boldsymbol{\lambda}}{dt}\cdot\left\langle\psi^t_{n\boldsymbol{\lambda}(t)}\right|\partial_{\boldsymbol{\lambda}(t)}\left|\psi^t_{n\boldsymbol{\lambda}(t)}\right\rangle \tag{2.1.7}$$

$$= -\mathrm{i}\epsilon_{n\boldsymbol{\lambda}}(t) - \mathrm{i}\frac{d\boldsymbol{\lambda}}{dt}\cdot\boldsymbol{A}^t_n(\boldsymbol{\lambda}(t)), \tag{2.1.8}$$

where $\boldsymbol{A}^t_n(\boldsymbol{\lambda}) \equiv \mathrm{i}\left\langle\psi^t_{n\boldsymbol{\lambda}}\right|\partial_{\boldsymbol{\lambda}}\left|\psi^t_{n\boldsymbol{\lambda}}\right\rangle$ is the celebrated Berry connection in this case. Finally suppose the system goes back to the initial state after time T, we then have that by integration

$$\gamma_n(T) = -\int_0^T dt'\epsilon_{n\boldsymbol{\lambda}}(t') - \oint_{\mathcal{C}} d\boldsymbol{\lambda}\cdot\boldsymbol{A}^{t'}_n(\boldsymbol{\lambda}(t')), \tag{2.1.9}$$

where $\mathcal{C}$ is the path of the evolution of the parameter $\lambda(t)$. The emergence of a geometric phase in addition to the first, dynamical phase is the result of adiabatic evolution. Note in particular that adiabatic evolution amounts to effect a projection via the projector $\hat{P}_{n\boldsymbol{\lambda}}$. In fact the Berry connection be re-written as $\boldsymbol{A}^t_n(\boldsymbol{\lambda}) = \mathrm{i}\left\langle\psi^t_{n\boldsymbol{\lambda}}\right|\hat{P}_{n\boldsymbol{\lambda}}\left(\partial_{\boldsymbol{\lambda}}\hat{P}_{n\boldsymbol{\lambda}}\right)\left|\psi^t_{n\boldsymbol{\lambda}}\right\rangle$, which highlights the role of projection.

2.1.3 Quantum geometric tensor

Provost-Valle's derivation

Here we introduce the notions of quantum geometric tensor, quantum metric tensor and Berry curvature. To motivate the definitions, we give a derivation of these quantities following the original reference [121]. The problem is to define a notion of metric or distance for a family of parametrized states $|\psi(\boldsymbol{\lambda})\rangle$, i.e. a section over the bundle $\mathcal{M}\times\mathcal{H}'_{\boldsymbol{\lambda}}$, thereby defining a Riemannian geometry over the Hilbert space. All states are taken to be normalized, but not gauge fixed. The idea of Provost and Valle is to start from a tentative definition of distance between states, which turned out to be gauge dependent, and then, via introducing the notion of covariant derivative, deriving a gauge invariant metric tensor.

A naive measure of distance for such parameterized states is

$$d(\boldsymbol{\lambda}', \boldsymbol{\lambda}) = \| |\psi(\boldsymbol{\lambda}')\rangle - |\psi(\boldsymbol{\lambda})\rangle \|^2, \tag{2.1.10}$$

where $\| |\psi\rangle \| \equiv \langle\psi|\psi\rangle$ is the norm of the state. In particular the distance between a state with itself is 0. We want to define a metric tensor by considering an infinitesimal change of the parameters:

$$\| |\psi(\boldsymbol{\lambda}+\delta\boldsymbol{\lambda})\rangle - |\psi(\boldsymbol{\lambda})\rangle \|^2 = g_{ij}\delta\lambda^i\delta\lambda^j + O(\delta\boldsymbol{\lambda}^3), \tag{2.1.11}$$

or in terms of a line element

$$ds^2_{\boldsymbol{\lambda}} = g_{ij}(\boldsymbol{\lambda})d\lambda^i d\lambda^j, \tag{2.1.12}$$

where the real symmetric tensor $g_{ij}(\boldsymbol{\lambda})$, would then be the metric tensor corresponding to the notion of distance defined above, and thus potentially suitable for constructing a Riemannian geometry. Let us compute the metric tensor in terms of $|\psi(\boldsymbol{\lambda})\rangle$. We have

$$|\psi(\boldsymbol{\lambda}+d\boldsymbol{\lambda})\rangle - |\psi(\boldsymbol{\lambda})\rangle \approx |\partial_i\psi(\boldsymbol{\lambda})\rangle\, d\lambda_i, \tag{2.1.13}$$

where $|\partial_i\psi(\boldsymbol{\lambda})\rangle \equiv \frac{\partial}{\partial\lambda_i}|\psi(\boldsymbol{\lambda})\rangle$ and the summation convention is used. Thus

$$\begin{aligned}
\|\psi(\boldsymbol{\lambda}+\delta\boldsymbol{\lambda}) - \psi(\boldsymbol{\lambda})\|^2 &= \langle\partial_i\psi(\boldsymbol{\lambda})|\partial_j\psi(\boldsymbol{\lambda})\rangle\, d\lambda^i d\lambda^j && (2.1.14)\\
&= \frac{1}{2}\left(\langle\partial_i\psi(\boldsymbol{\lambda})|\partial_j\psi(\boldsymbol{\lambda})\rangle + \langle\partial_j\psi(\boldsymbol{\lambda})|\partial_i\psi(\boldsymbol{\lambda})\rangle\right) d\lambda^i d\lambda^j && (2.1.15)\\
&= \mathrm{Re}\,\langle\partial_i\psi(\boldsymbol{\lambda})|\partial_j\psi(\boldsymbol{\lambda})\rangle\, d\lambda^i d\lambda^j, && (2.1.16)
\end{aligned}$$

where in the second step we used the fact that i and j are just dummy variables that are summed over.

It seems like we have defined a metric tensor as $g_{ij} = \mathrm{Re}\,\langle\partial_i\psi(\boldsymbol{\lambda})|\partial_j\psi(\boldsymbol{\lambda})\rangle$, however there is a problem, namely that g_{ij} thus defined is not gauge invariant [121]. Indeed, under a gauge phase transformation, we have

$$|\psi'(\boldsymbol{\lambda})\rangle = e^{\mathrm{i}\alpha(\boldsymbol{\lambda})}\,|\psi(\boldsymbol{\lambda})\rangle \tag{2.1.17}$$

$$\partial_i\,|\psi'(\boldsymbol{\lambda})\rangle = e^{\mathrm{i}\alpha(\boldsymbol{\lambda})}\partial_i\,|\psi(\boldsymbol{\lambda})\rangle + \mathrm{i}(\partial_i\alpha)e^{\mathrm{i}\alpha(\boldsymbol{\lambda})}\,|\psi(\boldsymbol{\lambda})\rangle\,, \tag{2.1.18}$$

where the last term spoils the gauge invariance.

In fact, the naive metric tensor we have thus defined transforms as

$$\langle\partial_i\psi'(\boldsymbol{\lambda})|\partial_j\psi'(\boldsymbol{\lambda})\rangle = \langle\partial_i\psi(\boldsymbol{\lambda})|\partial_j\psi(\boldsymbol{\lambda})\rangle + \partial_i\alpha\partial_j\alpha - \partial_j\alpha\mathcal{A}_i - \partial_i\alpha\mathcal{A}_j, \tag{2.1.19}$$

where the quantity $\mathcal{A}_i = \mathrm{i}\,\langle\psi(\boldsymbol{\lambda})|\partial_i\psi(\boldsymbol{\lambda})\rangle$ is exactly the Berry connection [20]. Note that the Berry connection is gauge dependent itself, namely $\mathcal{A}_i \to \mathrm{i}\,\langle\psi'(\boldsymbol{\lambda})|\partial_i\psi'(\boldsymbol{\lambda})\rangle = \mathcal{A}_i - \mathrm{i}\partial_i\alpha$. Furthermore, due to normalization, we have

$$\partial_i\left(\langle\psi(\boldsymbol{\lambda})|\psi(\boldsymbol{\lambda})\rangle\right) = 0 = \langle\partial_i\psi(\boldsymbol{\lambda})|\psi(\boldsymbol{\lambda})\rangle + \langle\psi(\boldsymbol{\lambda})|\partial_i\psi(\boldsymbol{\lambda})\rangle\,, \tag{2.1.20}$$

and therefore the Berry connection is real: $\mathcal{A}_i = \mathcal{A}_i^*$.

Define a covariant derivative as $\nabla_i \equiv \partial_i - \mathrm{i}\mathcal{A}_i$, then under a gauge transformation, $\nabla_i\,|\psi(\boldsymbol{\lambda})\rangle \to e^{\mathrm{i}\alpha(\boldsymbol{\lambda})}\nabla_i\,|\psi(\boldsymbol{\lambda})\rangle$. Thus the quantity

$$Q_{ij} \equiv \langle\nabla_i\psi(\boldsymbol{\lambda})|\nabla_j\psi(\boldsymbol{\lambda})\rangle = \langle\partial_i\psi(\boldsymbol{\lambda})|\partial_j\psi(\boldsymbol{\lambda})\rangle - \mathcal{A}_i\mathcal{A}_j \tag{2.1.21}$$

is in fact gauge invariant. The quantity Q_{ij} is called quantum geometric tensor. Note that using the normalization condition Eq. (2.1.20) again, we can alternatively write

$$Q_{ij} = \langle\partial_i\psi(\boldsymbol{\lambda})|\left(1 - \hat{P}_{\boldsymbol{\lambda}}\right)|\partial_j\psi(\boldsymbol{\lambda})\rangle \tag{2.1.22}$$

where $\hat{P}_{\boldsymbol{\lambda}} = |\psi(\boldsymbol{\lambda})\rangle\,\langle\psi(\boldsymbol{\lambda})|$ is the projection operator onto the state $|\psi(\boldsymbol{\lambda})\rangle$. This form of the quantum geometric tensor will prove useful when we discuss the Bloch states later, which has a non-abelian gauge structure.

The quantum geometric tensor is gauge invariant but generally complex, and we may decompose it into its real and imaginary part

$$Q_{ij} = g_{ij} - \frac{\mathrm{i}}{2}\Omega_{ij}, \tag{2.1.23}$$

where $g_{ij} \equiv \mathrm{Re}Q_{ij}$ and $\Omega_{ij} = -2\mathrm{Im}Q_{ij}$. Note that by definition g_{ij} and Ω_{ij} are symmetric and anti-symmetric tensors respectively. The real part g_{ij} is called the quantum metric tensor[17, 121], which as we shall discuss below is indeed a measure of a certain distance. The imaginary part is the well known Berry curvature [20], which plays a fundamental role in topological materials [62, 122]. The more common definition of Berry curvature is $\Omega_{ij} = \partial_i\mathcal{A}_j - \partial_j\mathcal{A}_i$, but it is easy to show that this agrees with our definition. Indeed

$$\begin{aligned}\partial_i\mathcal{A}_j - \partial_j\mathcal{A}_i =& i\partial_i\langle\psi(\boldsymbol{\lambda})|\partial_j\psi(\boldsymbol{\lambda})\rangle - i\partial_j\langle\psi(\boldsymbol{\lambda})|\partial_i\psi(\boldsymbol{\lambda})\rangle &(2.1.24)\\ =& i(2i)\mathrm{Im}\langle\partial_i\psi(\boldsymbol{\lambda})|\partial_j\psi(\boldsymbol{\lambda})\rangle &(2.1.25)\\ =& -2\mathrm{Im}Q_{ij}. &(2.1.26)\end{aligned}$$

Quantum distance and quantum metric tensor

We started from a naive definition of a notion of distance between states given in Eq. (2.1.10), which we found to be gauge dependent, and now we have derived a gauge invariant, symmetric tensor, the quantum metric tensor g_{ij}. The question is then, what notion of distance does the metric g_{ij} actually describe. As it turned out, the quantum distance that the quantum metric tensor measures is the extent of orthogonality, or overlap between states. Namely it is the metric tensor corresponding to the distance

$$d(\boldsymbol{\lambda}', \boldsymbol{\lambda}) = 1 - |\langle\psi(\boldsymbol{\lambda}')|\psi(\boldsymbol{\lambda})\rangle|^2, \tag{2.1.27}$$

whose line element is $ds^2 = g_{ij}d\lambda^i d\lambda^j$. To prove this, we compute the overlap between states differing by infinitesimal parameters

$$\langle\psi(\boldsymbol{\lambda})|\psi(\boldsymbol{\lambda} + d\boldsymbol{\lambda})\rangle = 1 - i\mathcal{A}_i d\lambda^i + \frac{1}{2}\langle\psi(\boldsymbol{\lambda})|\partial_i\partial_j\psi(\boldsymbol{\lambda})\rangle\, d\lambda^i d\lambda^j, \tag{2.1.28}$$

so that up to second order in $d\lambda^i$

$$|\langle\psi(\boldsymbol{\lambda})|\psi(\boldsymbol{\lambda}+d\boldsymbol{\lambda})\rangle|^2 = \left(1 + i\mathcal{A}_i d\lambda^i + \frac{1}{2}\langle\partial_i\partial_j\psi(\boldsymbol{\lambda})|\psi(\boldsymbol{\lambda})\rangle d\lambda^i d\lambda^j\right) \tag{2.1.29}$$

$$\left(1 - i\mathcal{A}_m d\lambda^m + \frac{1}{2}\langle\psi(\boldsymbol{\lambda})|\partial_m\partial_n\psi(\boldsymbol{\lambda})\rangle d\lambda^m d\lambda^n\right) \tag{2.1.30}$$

$$= 1 + \mathcal{A}_i\mathcal{A}_j d\lambda^i d\lambda^j + \frac{1}{2}\left(\langle\partial_i\partial_j\psi(\boldsymbol{\lambda})|\psi(\boldsymbol{\lambda})\rangle + \langle\psi(\boldsymbol{\lambda})|\partial_i\partial_j\psi(\boldsymbol{\lambda})\rangle\right) d\lambda^i d\lambda^j \tag{2.1.31}$$

$$= 1 + \mathcal{A}_i\mathcal{A}_j d\lambda^i d\lambda^j + \mathrm{Re}\langle\psi(\boldsymbol{\lambda})|\partial_i\partial_j\psi(\boldsymbol{\lambda})\rangle d\lambda^i d\lambda^j. \tag{2.1.32}$$

But again normalization implies that $\mathrm{Re}\langle\psi(\boldsymbol{\lambda})|\partial_i\partial_j\psi(\boldsymbol{\lambda})\rangle = -\mathrm{Re}\langle\partial_i\psi(\boldsymbol{\lambda})|\partial_j\psi(\boldsymbol{\lambda})\rangle$, which can be shown by taking a second derivative

$$0 = \partial_i\partial_j\langle\psi(\boldsymbol{\lambda})|\psi(\boldsymbol{\lambda})\rangle \tag{2.1.33}$$

$$= 2\mathrm{Re}\langle\partial_i\psi(\boldsymbol{\lambda})|\partial_j\psi(\boldsymbol{\lambda})\rangle + 2\mathrm{Re}\langle\psi(\boldsymbol{\lambda})|\partial_i\partial_j\psi(\boldsymbol{\lambda})\rangle. \tag{2.1.34}$$

Using this we then have that indeed

$$ds^2 = 1 - |\langle\psi(\boldsymbol{\lambda})|\psi(\boldsymbol{\lambda}+d\boldsymbol{\lambda})\rangle|^2 \tag{2.1.35}$$

$$= -\mathcal{A}_i\mathcal{A}_j d\lambda^i d\lambda^j + \mathrm{Re}\langle\partial_i\psi(\boldsymbol{\lambda})|\partial_j\psi(\boldsymbol{\lambda})\rangle d\lambda^i d\lambda^j \tag{2.1.36}$$

$$= g_{ij} d\lambda^i d\lambda^j. \tag{2.1.37}$$

Example: Weyl Hamiltonian

Here we compute the quantum geometric tensor of a simple example, the Weyl Hamiltonian, which was originally devised to describe massless spin-$\frac{1}{2}$ particles in particle physics. The same Hamiltonian has also been used to describe the novel topological Weyl materials that have linear crossing around Weyl nodes, and we shall discuss its semi-classical dynamics in **Part II** of this thesis. The Hamiltonian reads

$$\hat{H} = \chi\boldsymbol{\sigma}\cdot\hat{\boldsymbol{p}}, \tag{2.1.38}$$

where $\hat{\boldsymbol{p}}$ is the momentum operator, and $\chi = \pm 1$ is called the chirality. In the following, we restrict to $\chi = 1$. Since $\hat{H}^2 = \boldsymbol{p}\cdot\boldsymbol{p}\mathbb{1}$, its eigenvalues are $\pm p$, with $p = |\boldsymbol{p}|$, and its eigenstates are then parametrized by the momentum eigenvalues, which we denote as $|\psi_{\pm\boldsymbol{p}}\rangle$, with eigenvalues $\pm\boldsymbol{p}$ respectively. Here we use $\pm$ to label the band/level in correspondence to n in previous sections, and $\boldsymbol{p}$ is the smooth parameter $\boldsymbol{\lambda}$ in this example. We can solve

them to be

$$|\psi_{\pm\boldsymbol{p}}\rangle = \frac{1}{\sqrt{2p(p \pm p_3)}} \begin{pmatrix} p_3 \pm p \\ p_1 - \mathrm{i}p_2 \end{pmatrix}. \tag{2.1.39}$$

For $|\psi_{+\boldsymbol{p}}\rangle$, the quantum geometric tensor can be computed to be

$$Q_{ij} = \begin{pmatrix} \frac{{p_2}^2+{p_3}^2}{4p^4} & -\frac{p_1p_2+\mathrm{i}pp_3}{4p^4} & \frac{-p_1p_3+\mathrm{i}pp_2}{4p^4} \\ -\frac{p_1p_2-\mathrm{i}pp_3}{4p^4} & \frac{{p_1}^2+{p_3}^2}{4p^4} & -\frac{p_2p_3+\mathrm{i}pp_1}{4p^4} \\ -\frac{p_1p_3+\mathrm{i}pp_2}{4p^4} & \frac{-p_2p_3+\mathrm{i}pp_1}{4p^4} & \frac{{p_1}^2+{p_2}^2}{4p^4} \end{pmatrix} \tag{2.1.40}$$

Specifically, the quantum metric tensor reads

$$g_{ij} = \begin{pmatrix} \frac{{p_2}^2+{p_3}^2}{4p^4} & -\frac{p_1p_2}{4p^4} & \frac{-p_1p_3}{4p^4} \\ -\frac{p_1p_2}{4p^4} & \frac{{p_1}^2+{p_3}^2}{4p^4} & -\frac{p_2p_3}{4p^4} \\ -\frac{p_1p_3}{4p^4} & \frac{-p_2p_3}{4p^4} & \frac{{p_1}^2+{p_2}^2}{4p^4} \end{pmatrix}, \tag{2.1.41}$$

while the Berry curvature tensor defines a vector as $(\boldsymbol{\Omega})_i = \epsilon_{ijk}\Omega_{jk}$, then $\boldsymbol{\Omega} = -\frac{1}{2}\frac{\boldsymbol{p}}{p^3}$. Note that the Berry curvature has the configuration in the parameter space ($\boldsymbol{p}$ in this case), identical to that of the electric field of a point charge distribution (or the magnetic field of a magnetic monopole): $\nabla \cdot \boldsymbol{\Omega} = -2\pi\delta^3(\boldsymbol{p})$, with charge 2π. More generally, we have $\boldsymbol{\Omega}_\chi = -\chi\frac{1}{2}\frac{\boldsymbol{p}}{p^3}$.

2.2 Geometry of Bloch bands

2.2.1 Bloch's theorem and band theory

The starting point of the study of solid state of matter is the idealization of solids as having a stable crystal lattice structure, formed by the periodic arrangement of ions through chemical bonding, and the remaining valance electrons move under the influence of the resulting periodic potential. Lying at the foundation of solid state physics is Bloch's theorem [25], which, despite the idealization of a perfect crystalline structure and neglection of electron-electron and electron-ion interaction, was able to predict a large number of physical properties of solid state [11].

Bloch's theorem in the most general form states that

Bloch's theorem
Suppose the Hamiltonian $\hat{H}$ of a system is invariant under lattice translations $\hat{T}(\boldsymbol{R}) = e^{i\boldsymbol{R}\cdot\hat{\boldsymbol{p}}}$, namely $[\hat{H}, \hat{T}(\boldsymbol{R})] = 0$, then the eigenstates of $\hat{H}$ can be chosen to be of the form of a modulated plane wave $|\psi_{\boldsymbol{k}}\rangle = e^{-i\boldsymbol{k}\cdot\hat{\boldsymbol{r}}} |u_{\boldsymbol{k}}\rangle$, where $|u_{\boldsymbol{k}}\rangle$ is invariant under lattice translations: $\hat{T}(\boldsymbol{R}) |u_{\boldsymbol{k}}\rangle = |u_{\boldsymbol{k}}\rangle$.

The relevance of Bloch's theorem in solid state physics is established by taking a single particle moving under the influence of a periodic lattice potential $V(\boldsymbol{r})$ such that $V(\boldsymbol{r}) = V(\boldsymbol{r} + \boldsymbol{R})$, to model the electron in a solid. Namely we consider the elementary Hamiltonian describing a non-relativistic particle moving in a periodic potential

$$\hat{H} = \frac{\hat{\boldsymbol{p}}^2}{2m} + V(\hat{\boldsymbol{r}}), \tag{2.2.1}$$

where in reduced zone scheme, the energy spectrum is organized into bands with eigenstates of the Bloch form: $\hat{H} |\psi_{n\boldsymbol{k}}\rangle = E_{n\boldsymbol{k}} |\psi_{n\boldsymbol{k}}\rangle$, with crystal momenta restricted to the first Brillouin zone $k_i \in [-\frac{\pi}{a_i}, \frac{\pi}{a_i}]$, $i = x, y, z$, where a_i is the lattice constant along the $i-$direction. This then implies that there is a resolution of identity

$$\mathbb{1} = \sum_{n\boldsymbol{k}} |\psi_{n\boldsymbol{k}}\rangle \langle\psi_{n\boldsymbol{k}}| . \tag{2.2.2}$$

In this basis the lattice Hamiltonian assumes a spectral decomposition as

$$\hat{H} = \sum_{n\boldsymbol{k}} E_{n\boldsymbol{k}} |\psi_{n\boldsymbol{k}}\rangle \langle\psi_{n\boldsymbol{k}}| . \tag{2.2.3}$$

In the limit where the number of lattice sites becomes infinite, the discrete sum over crystal momentum becomes an integral

$$\sum_{\boldsymbol{k}} \to \frac{N}{V_c} \int d\boldsymbol{k}, \tag{2.2.4}$$

where N the number of unit cells, V_c is the volume of a unit cell in the Brillouin zone, and we have the normalization $\langle \psi_{n\boldsymbol{k}} | \psi_{m\boldsymbol{k}'} \rangle = \delta_{nm} \delta(\boldsymbol{k} - \boldsymbol{k}')$.

Example: Mathieu-Floquet equation

As an illustration of Bloch's theorem, here we consider a classical problem in mathematical physics, which may be taken to model a one-dimensional periodic lattice. Consider the following Schrodinger equation which describes a particle in a cosine potential,

$$\left(\frac{\hbar^2}{2m} \frac{\partial^2}{\partial x^2} + V \cos 2\pi a x \right) \psi(x) = E \psi(x). \tag{2.2.5}$$

Setting $a = 1$, $e = \frac{2mE}{\hbar^2 \pi^2}$, $q = \frac{mV}{\hbar^2 \pi^2}$ and $z = \pi x$, then we may re-write it as

$$\left(\frac{\partial^2}{\partial z^2} + (\epsilon - 2q \cos 2z) \right) \psi(z) = 0, \tag{2.2.6}$$

which is known as Mathieu's equation [100], who first proposed it in the study of membrane vibrations. In fact it is from the study of Mathieu's equation and its generalization, the French mathematician Gaston Floquet[46] proved what is known as Bloch's theorem in the physics community and Floquet's theorem in the mathematics community. Indeed, it can be shown that [163] for a given value of q, there is a family of values of ϵ, known as Matheiu characteristics $\gamma_k(q)$ such that the solution may be written in Bloch form, namely

$$\psi(z) = e^{\mathrm{i}kz} u_k(z), \tag{2.2.7}$$

where $u_k(z) = u_k(z + \pi)$, and can be expressed explicitly in terms of the so-called Mathieu cosine and sine functions, and the corresponding eigenvalues $\epsilon_k = \gamma_k(q)$.

2.2.2 Quantum geometry of Bloch states

With Bloch's theorem, we know that the Bloch states of a particle moving in a periodic lattice are parametrized by the crystal momenta, and thus we may define the geometric quantities for the Bloch states as in Section 2.1.3. However, we have to also take into account the emergence of bands. The most natural generalization of the quantum geometric tensor might be $Q^n_{ij}(\boldsymbol{k}) \equiv \langle \partial_i \psi_{n\boldsymbol{k}} | \partial_j \psi_{n\boldsymbol{k}} \rangle - A^n_i A^n_j$, where $A^n_i = \mathrm{i} \langle \psi_{n\boldsymbol{k}} | \partial_i \psi_{n\boldsymbol{k}} \rangle$ is the Berry connection

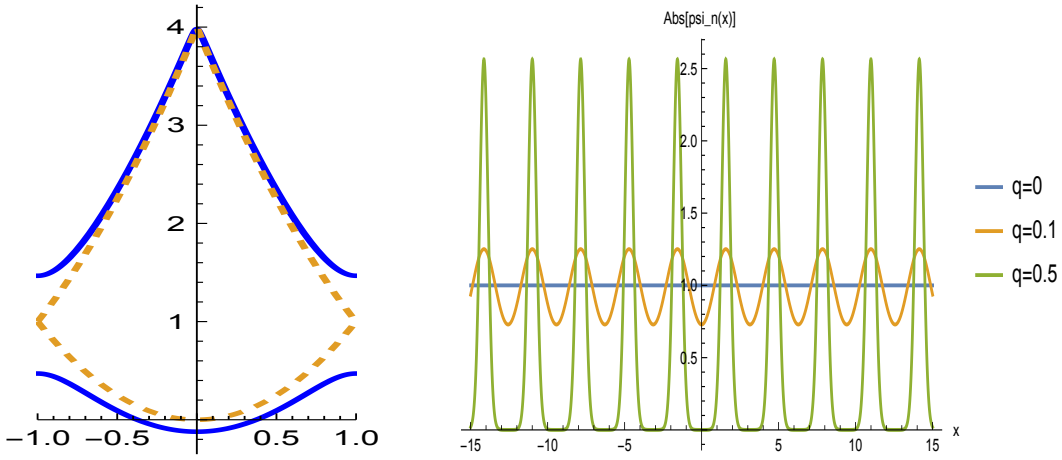

(a) Band structure (b) Wavefunction

Figure 2.1. In (a) we show the band structure of the cosine potential problem. The blue solid line is with $q = 0.3$, and dashed line is the parabolic dispersion for a free particle. In (b) the spatial profile for $|\psi_{nk}(x)|$ with $n = 1$ and $k = 0.3$ is plotted. Note when the potential is strong, the Bloch states become highly localized.

of the $n-$th band. This is indeed invariant under the gauge transformation of a Bloch state $|\psi_{n\boldsymbol{k}}\rangle \to e^{i\theta_n(\boldsymbol{k})} |\psi_{n\boldsymbol{k}}\rangle$. When degeneracy is present, the gauge transformation may in general generate a band rotation, such that $|\psi_{n\boldsymbol{k}}\rangle \to \sum_m U_{nm}(\boldsymbol{k}) |\psi_{m\boldsymbol{k}}\rangle$, where $U(\boldsymbol{k})$ is an $I \times I$ unitary matrix, with I being the degree of degeneracy. In this case the Berry curvature and quantum metric tensor will no longer be gauge invariant, whilst their traces will remain invariant [19]. In the following, we shall restrict to the non-degenerate case.

TKNN formula

The imaginary component of the quantum geometric tensor, the Berry curvature, has been found to be of fundamental significance in the study of topological phases of matter. To illustrate this, we gave a short proof of one of the most important results that makes use of Berry curvature, the TKNN formula of Hall conductance quantization, discovered by Thouless, Kohmoto, Nightingale, and den Nijs [149].

Consider a two dimensional system, where a uniform electric field, directed, say in the y-direction, is applied to , then the current response in the transverse direction, σ_{xy} can be derived using the Kubo formula [19] giving

$$\sigma_{xy} = ie^2 \sum_{n\in \text{occ}} \int_{\text{BZ}} \frac{d^2k}{(2\pi)^2} \sum_{m\neq n} \frac{\langle u_{n\boldsymbol{k}}| \partial_{k_x} \hat{H}(\boldsymbol{k}) |u_{m\boldsymbol{k}}\rangle \langle u_{m\boldsymbol{k}}| \partial_{k_y} \hat{H}(\boldsymbol{k}) |u_{n\boldsymbol{k}}\rangle - (x \leftrightarrow y)}{(\epsilon_n - \epsilon_m)^2}. \quad (2.2.8)$$

where the band summation is over all the occupied bands, $\hat{H}(\boldsymbol{k}) = e^{i\boldsymbol{k}\cdot\hat{r}}\hat{H}e^{-i\boldsymbol{k}\cdot\hat{r}}$, and the cell periodic part of Bloch states satisfies

$$H(\boldsymbol{k})\,|u_{n\boldsymbol{k}}\rangle = \epsilon_{n\boldsymbol{k}}\,|u_{nk}\rangle\,. \tag{2.2.9}$$

Differentiating the above eigenstate equation and projecting onto $|u_{m\boldsymbol{k}}\rangle$, we obtain

$$\langle u_{m\boldsymbol{k}}|\,\partial_{k_x}\,|u_{n\boldsymbol{k}}\rangle = \frac{\langle u_{m\boldsymbol{k}}|\,\partial_{k_x}\hat{H}(\boldsymbol{k})\,|u_{n\boldsymbol{k}}\rangle}{\epsilon_n - \epsilon_m}. \tag{2.2.10}$$

On the other hand, the $z-$component of Berry curvature for the n-th band may be rewritten as

$$\Omega_z^n(\boldsymbol{k}) = \partial_{k_x}A_y^n(\boldsymbol{k}) - \partial_{k_y}A_x^n(\boldsymbol{k}) \tag{2.2.11}$$

$$= i\left(\left\langle\partial_{k_x}u_{n\boldsymbol{k}}\middle|\partial_{k_y}u_{n\boldsymbol{k}}\right\rangle - \left\langle\partial_{k_y}u_{n\boldsymbol{k}}\middle|\partial_{k_x}u_{n\boldsymbol{k}}\right\rangle\right). \tag{2.2.12}$$

Locally at a given $\boldsymbol{k}$, a resolution of the identity is given by

$$\mathbb{I}_{\boldsymbol{k}} = \sum_n |u_{n\boldsymbol{k}}\rangle\,\langle u_{n\boldsymbol{k}}|\,. \tag{2.2.13}$$

Inserting this into the above equation we obtain

$$\Omega_z^n(\mathbf{k}) = i\sum_{m\neq n}\left(\langle\partial_{k_x}u_{n\boldsymbol{k}}|u_{m\boldsymbol{k}}\rangle\left\langle u_{m\boldsymbol{k}}\middle|\partial_{k_y}u_{n\boldsymbol{k}}\right\rangle - (x\leftrightarrow y)\right), \tag{2.2.14}$$

which after substituting Eq. (2.2.10) and its complex conjugate, we obtain yet another expression of Berry curvature as

$$\Omega_n(\mathbf{k}) = i\sum_{m\neq n}\left[\frac{\langle u_{n\boldsymbol{k}}|\,\partial_{k_x}\hat{H}(\boldsymbol{k})\,|u_{m\boldsymbol{k}}\rangle\,\langle u_{m\boldsymbol{k}}|\,\partial_{k_y}\hat{H}(\boldsymbol{k})\,|u_{n\boldsymbol{k}}\rangle}{(\epsilon_n-\epsilon_m)^2} - (x\leftrightarrow y)\right]. \tag{2.2.15}$$

We recognize that this is exactly the integrand in the Hall conductance formula Eq. (2.2.8), and therefore we have derived the TKNN formula:

$$\boxed{\sigma_{xy} = -2\pi e^2\sum_{n\in\text{occ}}C_n,} \tag{2.2.16}$$

where

$$C_n = \frac{1}{2\pi}\int_{\text{BZ}}d^2k\,\Omega_n^z(\boldsymbol{k}), \tag{2.2.17}$$

is known as the first Chern number [19, 106, 149]. This quantity is an integer valued topological invariant [106], and therefore the TKNN formula shows that the quantization of Hall conductance is a topological property of the electronic band structure.

2.2.3 Symmetry behavior

In this section we investigate the symmetry behaviors of the quantum metric tensor and Berry curvature. We confine ourselves to the single band case.

Symmetry transformations

We first briefly describe the time reversal and inversion transformation on Bloch states, from which the transformation properties of Berry curvature and quantum metric tensor would be deduced.

Time reversal

The time reversal transformation is implemented via an anti-unitary operator $\hat{\mathcal{T}}$ such that

$$\hat{\mathcal{T}}\hat{\boldsymbol{r}}\hat{\mathcal{T}}^{-1} = \hat{\boldsymbol{r}} \tag{2.2.18}$$

$$\hat{\mathcal{T}}\hat{\boldsymbol{p}}\hat{\mathcal{T}}^{-1} = -\hat{\boldsymbol{p}}. \tag{2.2.19}$$

Moreover, since $[\hat{r}_i, \hat{p}_j] = \mathrm{i}\delta_{ij}$, we have that

$$\hat{\mathcal{T}}\,(\mathrm{i})\,\hat{\mathcal{T}}^{-1}\delta_{ij} = \hat{\mathcal{T}}[\hat{r}_i, \hat{p}_j]\hat{\mathcal{T}}^{-1}\delta_{ij} = [\hat{r}_i, -\hat{p}_j]\delta_{ij} = -\mathrm{i}\delta_{ij}, \tag{2.2.20}$$

namely that the time reversal transformation does not commute with complex numbers, and effects complex conjugation

$$\hat{\mathcal{T}}\,(z)\,\hat{\mathcal{T}}^{-1} = z^*. \tag{2.2.21}$$

Such operators are known as anti-linear. It is clear that under the time-reversal transformation, the crystal momentum also transforms as $\hat{\mathcal{T}}\hat{\boldsymbol{k}}\hat{\mathcal{T}}^{-1} = -\hat{\boldsymbol{k}}$. From this we have

$$\hat{\boldsymbol{k}}\hat{\mathcal{T}}\,|\psi_{n\boldsymbol{k}}\rangle = \hat{\mathcal{T}}\hat{\mathcal{T}}^{-1}\hat{\boldsymbol{k}}\hat{\mathcal{T}}\,|\psi_{n\boldsymbol{k}}\rangle \tag{2.2.22}$$

$$= -\boldsymbol{k}\hat{\mathcal{T}}\,|\psi_{n\boldsymbol{k}}\rangle\,. \tag{2.2.23}$$

That is, the time reversed state $\hat{\mathcal{T}}\,|\psi_{n\boldsymbol{k}}\rangle$ is an eigenstate of the crystal momentum with eigenvalue $-\boldsymbol{k}$. In fact, we have

$$\hat{\mathcal{T}}\,|\psi_{n\boldsymbol{k}}\rangle = \hat{\mathcal{T}} e^{-\mathrm{i}\boldsymbol{k}\cdot\hat{\boldsymbol{r}}}\,|u_{n\boldsymbol{k}}\rangle = e^{+\mathrm{i}\boldsymbol{k}\cdot\hat{\boldsymbol{r}}}\hat{\mathcal{T}}\,|u_{n\boldsymbol{k}}\rangle \tag{2.2.24}$$

If the system has time reversal symmetry (i.e.$[\mathcal{T},\mathcal{H}]=0$), then $\hat{\mathcal{T}}\,|\psi_{n\boldsymbol{k}}\rangle$ must also be an eigenstate:

$$\hat{H}\mathcal{T}\,|\psi_{n\boldsymbol{k}}\rangle = \mathcal{T}\hat{H}\,|\psi_{n\boldsymbol{k}}\rangle = \epsilon_{n\boldsymbol{k}}\mathcal{T}\,|\psi_{n\boldsymbol{k}}\rangle\,. \tag{2.2.25}$$

However, as discussed above, the time reversed state has crystal momentum $-\boldsymbol{k}$. Assuming no degeneracy, this is consistent with the above results only if the spectrum is also time reversal invariant: $\epsilon_{n\boldsymbol{k}} = \epsilon_{n-\boldsymbol{k}}$, and the time reversed states differ up to a phase: $\mathcal{T}\,|\psi_{n\boldsymbol{k}}\rangle = e^{\mathrm{i}\alpha}\,|\psi_{n-\boldsymbol{k}}\rangle$. In the case where degeneracy is present, it is in the most general case a linear combination of the degenerate eigenstates.

Inversion

The spatial inversion transformation is a unitary operator defined by the action

$$\hat{\mathcal{I}}\hat{\boldsymbol{r}}\hat{\mathcal{I}}^{-1} = -\,\hat{\boldsymbol{r}} \tag{2.2.26}$$

$$\hat{\mathcal{I}}\hat{\boldsymbol{p}}\hat{\mathcal{I}}^{-1} = -\,\hat{\boldsymbol{p}}. \tag{2.2.27}$$

It follows immediately that $\hat{\mathcal{I}}\,|\boldsymbol{r}\rangle = |-\boldsymbol{r}\rangle$ for $\hat{\boldsymbol{r}}\hat{\mathcal{I}}\,|\boldsymbol{r}\rangle = \hat{\mathcal{I}}\hat{\mathcal{I}}^{-1}\hat{\boldsymbol{r}}\hat{\mathcal{I}}\,|\boldsymbol{r}\rangle = -\boldsymbol{r}\hat{\mathcal{I}}\,|\boldsymbol{r}\rangle$. Acting on a Bloch state we have that

$$(\mathcal{I}\psi_{n\boldsymbol{k}})\,(r) \equiv \langle\boldsymbol{r}|\,\hat{\mathcal{I}}\,|\psi_{n\boldsymbol{k}}\rangle = \langle-\boldsymbol{r}|\psi_{n\boldsymbol{k}}\rangle = \psi_{n\boldsymbol{k}}(-r). \tag{2.2.28}$$

Now suppose that the inversion transformation is a symmetry for the Bloch Hamiltonian, then $\hat{\mathcal{I}}\,|\psi_{\boldsymbol{k}}\rangle$ is also an eigenstate of the Bloch Hamiltonian, with momentum $-\boldsymbol{k}$. Assuming the state is non-degenerate, this then implies that $|\psi_{\boldsymbol{k}}\rangle$ and $|\psi_{-\boldsymbol{k}}\rangle$ differ up to a phase, namely

$$\mathcal{I}\psi_{\boldsymbol{k}}(-\boldsymbol{r}) = \psi_{\boldsymbol{k}}(-\boldsymbol{r}) = \mathrm{e}^{\mathrm{i}\alpha(\boldsymbol{k})}\psi_{-\boldsymbol{k}}(-\boldsymbol{r}) \tag{2.2.29}$$

Berry curvature and quantum metric tensor

In a system that is symmetric under time reversal symmetry, using the transformation properties of the Bloch states given above, it is straightforward to show the Berry curvature

satisfies $\Omega_i(\boldsymbol{k}) = -\Omega_i(-\boldsymbol{k})$, while for inversion invariant system $\Omega_i(\boldsymbol{k}) = \Omega_i(-\boldsymbol{k})$ [133] . Thus in a system with both time reversal and inversion symmetric system, the Berry curvature vanishes identically. For the quantum metric tensor on the other hand, when either $\mathcal{T}$ or $\mathcal{I}$ symmetry is present, $g_{ij}(\boldsymbol{k}) = g_{ij}(-\boldsymbol{k})$[90].

Chapter 3

Operator approach to dynamics

3.1 Quantum geometry and projected moments

3.2 Introduction

In this part of the thesis we shall discuss the quantum geometric contribution to the semi-classical dynamics in a rather general setting. In contrast to the conventional approach, we shall use an operator formalism to deal with the problem of Bloch electron dynamics under the influence of inhomogeneous perturbing field in a systematic manner. Historically, it had been realized already in the very early days that the local geometry of the Bloch states modified the equation of motion of crystal electrons, which includes a correction to the group velocity $\partial\mathcal{E}/\partial\boldsymbol{k}$ due to band dispersion. Indeed, such an observation was applied to explain the intrinsic anomalous Hall effect in ferromagnets [1, 26, 58, 77, 84, 97, 105, 109]. In fact, already in these works during the 1950s [1, 77], what is known today as the Berry connection [20] and the anomalous velocity related to the Berry curvature have been discovered [34, 147, 164]. A surge of renewed interest of such geometric effects in recent decades has been brought about due to the rapid development in the study of topological phases of matter, which has been applied in the study of various novel transport properties in topological materials [29, 60, 68, 92, 111, 118, 132, 137].

We have already discussed from a rather formal point of view that the projective Hilbert space admits a Riemannian structure, characterized by geometric quantities such as the Berry curvature and the quantum metric or Fubini-Study metric [12, 17, 121]. Such a connection is not just mathematical, however, and has been found to be relevant in a wide range of physical phenomena. As we already mentioned in the introduction part, these geometric concepts have been applied to quantum information theory and even quantum phase transitions. However, more recently it has also been known to be relevant in condensed matter physics, which included, for instance, fractional Chern insulators [37, 101, 112, 114, 116, 128], topological superfluidity and superconductivity in flat bands [72, 76, 94, 150], and nonlinear optical responses [3–5, 69]. In this work we shall focus on one aspect that is relevant in the study of transport properties of solid state system when an inhomogeneous field is applied. In fact, it has been discussed using a wave-packet approach that a metallic system subject to a spatially varying electric field may have non-trivial transport signature beyond that induced by the Berry curvature, where additional quantum geometric contributions due to the quantum metric tensor as well as the associated Christoffel symbols emerge [48, 86, 90].

Conventionally the semi-classical equations of Bloch electrons are derived using a wave-

packet approach. For example, under the influence of an applied field, a wave-packet is constructed using a superposition of instantaneous eigenstates of the effective Hamiltonian $\hat{H}(\boldsymbol{r}_c(t), \hat{\boldsymbol{k}})$, obtained from replacing $\boldsymbol{r}$ by the center of motion position $\boldsymbol{r}_c(t)$ [134, 147, 164], and corrections to the dynamics, such as the anomalous velocity term, emerge in a rather unexpected way. Naively this is rather surprising since it seems to contradict the Ehrenfest theorem [131], which states that the equations of motion in quantum mechanical systems shall formally parallel those of its classical counterpart, and in particular predicts no correction to the velocity when the external potential field is only position dependent. Another puzzle is that in this kind of derivations eigenstates that depend on the instantaneous center of mass position are used, and while it can be argued they do form a set of approximate eigenstates of the perturbed Hamiltonian, this seems like a particular mathematical trick to force out the geometric contributions. Furthermore, when one actually applies the semiclassical equations of motion in studying electron transport, the Berry curvature, for instance,is computed using the unperturbed lattice Hamiltonian. Thus, for the purposes of studying geometric effects in in-homogeneous field, and to clarify the physical origin of them, we shall develop an operator-based approach, which is capable of deriving the geometric contributions while avoiding reference to wave-packets. Such an operator based approach has been known to be very useful when studying quantum geometry in disordered systems, which require a real space formulation [96, 125]. We shall derive the operator forms of various quantum geometric quantities in terms of projected operators, and provide a systematic way to compute their matrix elements. Finally, in this approach we can demonstrate that such geometric contributions are fundamentally multi-band effects. Specifically, they emerge in the dynamics of electrons, where we project onto an effective low-energy subspace comprising of a restricted set of bands.

3.2.1 Band Projection

As we discussed above, in the reduced zone scheme, where we restrict the crystal momentum range to be within the first Brillouin zone, the eigenstates of the lattice Hamiltonian $\hat{H}_0$ organize into bands, so that we have a resolution of identity $\mathbb{1} = \sum_{\boldsymbol{k}n} |\psi_{n\boldsymbol{k}}\rangle \langle\psi_{n\boldsymbol{k}}|$, where the sum over $\boldsymbol{k}$ is restricted to the first Brillouin zone. When studying the low energy effective physics, we can impose a cutoff that restricts the relevant energy scale. In the reduced zone scheme of lattice systems, this translates to restriction to a specific subset of bands, limiting the matrix elements of observable in interest to a subspace of the entire Hilbert space. Formally, suppose the relevant subset of bands is $\mathcal{N}_{\mathcal{B}}$, then such restriction can be

effected by introducing the band projection operator

$$\hat{P}_{\mathcal{B}} = \sum_{\boldsymbol{k}} \sum_{n \in \mathcal{N}_{\mathcal{B}}} |\psi_{n\boldsymbol{k}}\rangle \langle \psi_{n\boldsymbol{k}}| \,. \tag{3.2.1}$$

Effective physics would then be described by states living in the restricted Hilbert space $\mathcal{H}_{\mathcal{B}} = \text{span}\{|\psi_{n\boldsymbol{k}}\rangle \,, n \in \mathcal{N}_{\mathcal{B}}\}$.

The complement operator is defined as $\hat{Q}_{\mathcal{B}} \equiv \mathbb{1} - \hat{P}_{\mathcal{B}} = \sum_{n \notin \mathcal{N}_{\mathcal{B}}} |\psi_{n\boldsymbol{k}}\rangle \langle \psi_{n\boldsymbol{k}}|$, which is orthogonal to the projection operator such that $\hat{P}_{\mathcal{B}}\hat{Q}_{\mathcal{B}} = 0$. Furthermore both operators are idempotent: $\hat{P}^2_{\mathcal{B}} = \hat{P}_{\mathcal{B}}$, and $\hat{Q}^2_{\mathcal{B}} = \hat{Q}_{\mathcal{B}}$. By definition, we also have that $[\hat{H}_0, \hat{P}_{\mathcal{B}}] = [\hat{H}_0, \hat{Q}_{\mathcal{B}}] = 0$. More generally, for an arbitrary operator $\hat{O}$, we have $[\hat{O}, \mathbb{1}] = 0 = [\hat{O}, \hat{P}_{\mathcal{B}}] + [\hat{O}, \hat{Q}_{\mathcal{B}}]$.

3.2.2 Band-projected operators

Band projection substantially modifies the commutation relation between position operators, as well as momentum operators. As we shall demonstrate later, such modified commutation relations are the origin of geometric contributions to the semi-classical dynamics. In this section, we would like to study the algebraic properties of band-projected products of position operator, and their decomposition into objects that we shall later identify as Bloch geometric quantities.

Quadruple moment: quantum geometric tensor

For later convenience, we shall denote the n-order moment as $\hat{r}^{(n)}_{i_1 i_2 \ldots i_n} = \hat{r}_{i_1}\hat{r}_{i_2}\ldots\hat{r}_{i_n}$. Let us first discuss the lowest order examples, the quadruple moment and quantum geometric tensor. In fact, the operator form of the quantum metric tensor has been reported previously; see for instance[22, 124]. This form has also been applied in the study of disorder systems [96, 125], where a real space formulation of the quantum metric tensor and Berry curvature is needed. We, however, will not only extend such operator correspondence to other geometric quantities but also point out how they appear from the modified commutation relations of band-projected operators. Inserting the identity $\mathbb{1} = \hat{P}_{\mathcal{B}} + \hat{Q}_{\mathcal{B}}$ between the position operators, we have

$$\left(\hat{r}^{(2)}_{ij}\right)_{\mathcal{B}} = (\hat{r}_i\hat{r}_j)_{\mathcal{B}} = \hat{P}_{\mathcal{B}}\hat{r}_i(\hat{P}_{\mathcal{B}} + \hat{Q}_{\mathcal{B}})\hat{r}_j\hat{P}_{\mathcal{B}} = \hat{r}_{i\mathcal{B}}\hat{r}_{j\mathcal{B}} + \left(\hat{r}_i\hat{Q}_{\mathcal{B}}\hat{r}_j\right)_{\mathcal{B}} \tag{3.2.2}$$

We may also re-write the last term as $\hat{\mathcal{Q}}^{(2)}_{ij} \equiv \left(\hat{r}_i\hat{Q}_{\mathcal{B}}\hat{r}_j\right)_{\mathcal{B}} = -\left(\left[\hat{r}_i, \hat{P}_{\mathcal{B}}\right]\hat{Q}_{\mathcal{B}}\left[\hat{r}_j, \hat{P}_{\mathcal{B}}\right]\right)_{\mathcal{B}}$. This is the first geometric operator we shall encounter, the quantum geometric tensor. Thus we may write more compactly that $\left(\hat{r}^{(2)}_{ij}\right)_{\mathcal{B}} = \hat{r}_{i\mathcal{B}}\hat{r}_{j\mathcal{B}} + \hat{\mathcal{Q}}^{(2)}_{ij}$. We note that the quantum geo-

metric tensor is also the projected cumulant $\hat{Q}^{(2)}_{ij} = \hat{P}_{\mathcal{B}}(\hat{r}_i - \hat{r}_{i\mathcal{B}})(\hat{r}_j - \hat{r}_{j\mathcal{B}})\hat{P}_{\mathcal{B}}$. Physically, this form shows the quantum geometric tensor quantifies the deviation of the position operator from the band projected one. It may seem that the complement space that is projected out is explicitly involved due to the appearance of $\hat{Q}_{\mathcal{B}}$. However, as we shall show in the next section where we compute the matrix elements of the geometric quantities, such explicit reference to the complement subspace actually disappears.

Following our discussion in the introduction section, let us decompose the quantum geometric tensor operator into the symmetric and anti-symmetric part as

$$\hat{\mathcal{Q}}^{(2)}_{ij} = \hat{\mathcal{G}}_{ij} - \frac{\mathrm{i}}{2}\hat{\Omega}_{ij}, \tag{3.2.3}$$

where $\hat{\mathcal{G}}_{ij} = \frac{1}{2}(\hat{\mathcal{Q}}^{(2)}_{ij} + \hat{\mathcal{Q}}^{(2)}_{ji})$ and $\hat{\Omega}_{ij} = \mathrm{i}\left(\hat{\mathcal{Q}}^{(2)}_{ij} - \hat{\mathcal{Q}}^{(2)}_{ji}\right)$ would be called the quantum metric and Berry curvature tensor operators, respectively. We shall show later that the definition is justified since their matrix elements in the Bloch basis are precisely the conventional form of the corresponding quantities.

Note that $\left(\hat{r}^{(2)}_{ij}\right)_{\mathcal{B}}$ is symmetric in ij indices, since the un-projected position operators commute with each other: $[\hat{r}_i, \hat{r}_j] = 0$. However, neither $\hat{r}_{i\mathcal{B}}\hat{r}_{j\mathcal{B}}$ nor $\hat{\mathcal{Q}}^{(2)}_{ij}$ is individually symmetric, since the projected position operators no longer commute with each other, except for the trivial case $\hat{P}_{\mathcal{B}} = \mathbb{1}$. In fact, it is easy to see neither of the operators is even Hermitian. To make the hermiticity and symmetry explicit, we symmetrize the previous expression as

$$\left(\hat{r}^{(2)}_{ij}\right)_{\mathcal{B}} = \hat{r}_{i\mathcal{B}}\hat{r}_{j\mathcal{B}} + \hat{\mathcal{Q}}^{(2)}_{ij} = \frac{1}{2}\{\hat{r}_{i\mathcal{B}}, \hat{r}_{j\mathcal{B}}\} + \frac{1}{2}\left(\hat{\mathcal{Q}}^{(2)}_{ij} + \hat{\mathcal{Q}}^{(2)}_{ji}\right) \tag{3.2.4}$$

$$= \frac{1}{2}\{\hat{r}_{i\mathcal{B}}, \hat{r}_{j\mathcal{B}}\} + \hat{\mathcal{G}}_{ij}. \tag{3.2.5}$$

For this to agree with the former expression, we need the anti-symmetric part of each term to cancel each other, which implies that

$$[\hat{r}_{i\mathcal{B}}, \hat{r}_{j\mathcal{B}}] = -\left(\hat{\mathcal{Q}}^{(2)}_{ij} - \hat{\mathcal{Q}}^{(2)}_{ji}\right) = \mathrm{i}\hat{\Omega}_{ij}. \tag{3.2.6}$$

We may also obtain this result by direct computation. Indeed, by definition of the curvature and geometric tensor operator, we have

$$-\mathrm{i}\hat{\Omega}_{ij} = \hat{\mathcal{Q}}^{(2)}_{ij} - \hat{\mathcal{Q}}^{(2)}_{ji} \tag{3.2.7}$$

$$= -\left([\hat{r}_i, \hat{P}_\mathcal{B}]\hat{Q}_\mathcal{B}[\hat{r}_j, \hat{P}_\mathcal{B}]\right)_\mathcal{B} \tag{3.2.8}$$

$$= \left(\left[\left[\hat{P}_\mathcal{B}, \hat{r}_i\right], \left[\hat{r}_j, \hat{P}_\mathcal{B}\right]\right]\right)_\mathcal{B} \tag{3.2.9}$$

$$= -\left[\hat{r}_{i\mathcal{B}}, \hat{r}_{j\mathcal{B}}\right]. \tag{3.2.10}$$

Here we see that rather remarkably, the band projected position operators no longer commute with each other, and the correction is exactly the Berry curvature. Of course, we shall still justify the definition of the operator form of the Berry curvature in the next section. Here we simply note that if we regard the projected position operator as a momentum space covariant derivative operator (see Section 3.3.2), which may be written as $\hat{r}_{i\mathcal{B}} = \mathrm{i}\hat{\nabla} = \mathrm{i}\left(\partial_{\hat{k}} - \mathrm{i}\hat{A}_i\right)_\mathcal{B}$, in terms of a gauge connection $\hat{A}_i$, then we may interpret the above result as

$$\hat{\Omega}_{ij} = -\mathrm{i}[\hat{r}_{i\mathcal{B}}, \hat{r}_{j\mathcal{B}}] \tag{3.2.11}$$

$$= \left[\partial_{\hat{k}_i\mathcal{B}} - \mathrm{i}\hat{\mathrm{A}}_{i\mathcal{B}}, \partial_{\hat{k}_j\mathcal{B}} - \mathrm{i}\hat{\mathrm{A}}_{j\mathcal{B}}\right] \tag{3.2.12}$$

$$= \left[\partial_{\hat{k}_i\mathcal{B}}, \hat{\mathrm{A}}_{j\mathcal{B}}\right] - \left[\partial_{\hat{k}_j\mathcal{B}}, \hat{\mathrm{A}}_{i\mathcal{B}}\right] + \mathrm{i}\left[\hat{\mathrm{A}}_{i\mathcal{B}}, \hat{\mathrm{A}}_{j\mathcal{B}}\right], \tag{3.2.13}$$

which is indeed very suggestive of the definition of a curvature tensor [106].

Octuple moment: quantum connection

As another example, we consider the octuple moment of the position operator, namely the product of three band-projected position operators. In the following, we will use interchangeably that $\hat{r}_{i\mathcal{B}} = \mathrm{i}\hat{\nabla}_i$. As previously, we insert $\mathbb{1} = \hat{P}_\mathcal{B} + \hat{Q}_\mathcal{B}$ between the position operators, and after some manipulation we have

$$\left(\hat{r}^{(3)}_{ijk}\right)_\mathcal{B} = (\hat{r}_i\hat{r}_j\hat{r}_k)_\mathcal{B} = \mathrm{i}^3\left(\hat{\nabla}_i\hat{\nabla}_j\hat{\nabla}_k - \left(\hat{\mathcal{Q}}^{(2)}_{ij}\hat{\nabla}_k + \hat{\mathcal{Q}}^{(2)}_{ik}\hat{\nabla}_j + \hat{\mathcal{Q}}^{(2)}_{jk}\hat{\nabla}_i + \left[\hat{\nabla}_i, \hat{\mathcal{Q}}^{(2)}_{jk}\right] + \hat{\mathcal{Q}}^{(3)}_{ijk}\right)\right), \tag{3.2.14}$$

which includes the quantum geometric tensor $\hat{\mathcal{Q}}^{(2)}_{ij}$ and a new geometric object $\hat{\mathcal{Q}}^{(3)}_{ijk}$. The latter is in fact the operator form of the quantum geometric connection introduced in Refs. [5, 12, 86]. To show this, as earlier, we symmetrize the above equation and after

some manipulations we may re-write it as:

$$\left(r^{(3)}_{ijk}\right)_{\mathcal{B}} = \frac{1}{6}\left(\hat{r}_{i\mathcal{B}}\hat{r}_{j\mathcal{B}}\hat{r}_{k\mathcal{B}} + \text{permutations of } ijk\right) + \frac{1}{2}\left(\{\hat{\mathcal{G}}_{ij}, \hat{r}_{k,\mathcal{B}}\} + \{\hat{\mathcal{G}}_{ik}, \hat{r}_{j,\mathcal{B}}\} + \{\hat{\mathcal{G}}_{jk}, \hat{r}_{i,\mathcal{B}}\}\right) \tag{3.2.15}$$

$$+ \mathrm{i}\left(Q^{(3)}_{ijk} + \frac{\mathrm{i}}{2}\left(\left[\hat{r}_{k,\mathcal{B}}, \hat{\mathcal{G}}_{ij}\right] + \left[\hat{r}_{j,\mathcal{B}}, \hat{\mathcal{G}}_{ik}\right] - \left[\hat{r}_{i,\mathcal{B}}, \hat{\mathcal{G}}_{jk}\right]\right) + \frac{1}{6}\left(\left[\hat{r}_{k,\mathcal{B}}, \hat{\Omega}_{ij}\right] + \left[\hat{r}_{j,\mathcal{B}}, \hat{\Omega}_{ik}\right]\right)\right). \tag{3.2.16}$$

To bring forward the symmetric tensor in $\hat{\mathcal{Q}}^{(3)}$, it is useful to define the following two operators, i.e.

$$\hat{\mathcal{Q}}^{(3)}_{ijk} = \hat{\Gamma}_{i,jk} - \frac{\mathrm{i}}{2}\hat{\tilde{\Gamma}}_{i,jk}, \tag{3.2.17}$$

$$\hat{\Gamma}_{i,jk} = \frac{1}{2}\left(\left[\hat{\nabla}_k, \hat{\mathcal{G}}_{ij}\right] + \left[\hat{\nabla}_j, \hat{\mathcal{G}}_{ik}\right] - \left[\hat{\nabla}_i, \hat{\mathcal{G}}_{jk}\right]\right), \ \hat{\tilde{\Gamma}}_{i,jk} = \frac{1}{3}\left(\left[\hat{\nabla}_k, \hat{\Omega}_{ij}\right] + \left[\hat{\nabla}_j, \hat{\Omega}_{ik}\right]\right) + 2\hat{\mathcal{T}}_{ijk}, \tag{3.2.18}$$

which reduces Eq. (3.2.16) to the symmetric tensor $\hat{\mathcal{T}}_{ijk}$. Note that the quantities $\hat{\Gamma}_{i,jk}$ thus defined can clearly be viewed as the Christoffel symbols associated with the metric tensor $\hat{\mathcal{G}}_{ij}$ [120, 160], and we show call it the quantum Christoffel symbols operator. Similarly, the imaginary part of $\hat{\mathcal{Q}}^{(3)}_{ijk}$, $\hat{\tilde{\Gamma}}_{i,jk}$ is known as the symplectic Christoffel symbols/connection of the first kind [106], whereas

$$\hat{\tilde{\Gamma}}^{i}_{jk} = \hat{\Omega}^{il}\hat{\tilde{\Gamma}}_{l,jk} \tag{3.2.19}$$

are the components of the symplectic connection $\hat{\tilde{\Gamma}}^{i}_{jk}$ of the second kind. Here $\hat{\Omega}^{ij}$ is the matrix inverse of $\hat{\Omega}_{ij}$ (with respect to ij indices). From Eq. (3.2.18), we can derive the following relation:

$$\left[\hat{\nabla}_i, \hat{\Omega}_{jk}\right] = \hat{\tilde{\Gamma}}_{j,ki} - \hat{\tilde{\Gamma}}_{k,ji}. \tag{3.2.20}$$

Using this, we may define a covariant derivative $\hat{\tilde{\nabla}}_i$ with respect to which the Berry curvature is "flat" [86, 106]: $\hat{\tilde{\nabla}}_i\hat{\Omega}_{jk} = [\hat{\nabla}_i, \hat{\Omega}_{jk}] + \hat{\Omega}_{jl}\hat{\tilde{\Gamma}}^{l}_{ki} + \hat{\Omega}_{lk}\hat{\tilde{\Gamma}}^{l}_{ji} = 0$.

General order

We would now consider such decomposition to arbitrary order. Following the same procedure as in the derivation of the quantum geometric tensor and quantum Christoffel symbols, for the n-th moment in the position operator, we insert a $\mathbb{1} = \hat{P}_{\mathcal{B}} + \hat{Q}_{\mathcal{B}}$ between each pair of

position operators, thus relating it to a lower order by , i.e.

$$\hat{P}_{\mathcal{B}}\hat{r}^{(n)}_{i_1\ldots i_n}\hat{P}_{\mathcal{B}} = \hat{P}_{\mathcal{B}}\hat{r}_{i_1}\left(\hat{P}_{\mathcal{B}}+\hat{Q}_{\mathcal{B}}\right)\hat{r}^{(n-1)}_{i_2\ldots i_n}\hat{P}_{\mathcal{B}} \tag{3.2.21}$$

$$= \hat{r}_{i_1\mathcal{B}}\hat{r}^{(n-1)}_{i_2\ldots i_n\mathcal{B}} + \hat{P}_{\mathcal{B}}\hat{r}_{i_1}\hat{Q}_{\mathcal{B}}\hat{r}^{(n-1)}_{i_2\ldots i_n}\hat{P}_{\mathcal{B}} \tag{3.2.22}$$

$$= \hat{r}_{i_1\mathcal{B}}\hat{r}^{(n-1)}_{i_2\ldots i_n\mathcal{B}} + \hat{\mathcal{Q}}^{(n)}_{i_1 i_2\ldots i_n}, \tag{3.2.23}$$

where we defined

$$\hat{\mathcal{Q}}^{(n)}_{i_1 i_2\ldots i_n} = \left(\hat{r}_{i_1}\hat{Q}_{\mathcal{B}}\hat{r}^{(n-1)}_{i_2\ldots i_n}\right)_{\mathcal{B}} = -\left(\left[\hat{r}_{i_1},\hat{P}_{\mathcal{B}}\right]\hat{Q}_{\mathcal{B}}\left[\hat{r}^{(n-1)}_{i_2\ldots i_n},\hat{P}_{\mathcal{B}}\right]\right)_{\mathcal{B}}. \tag{3.2.24}$$

Assuming that the $n-1$-th order is already understood, then any new geometric quantities that are associated with the Bloch structure shall emerge from the second term of Eq. (3.2.23). Let us zero in on Eq. (3.2.24). We may decompose it further by using the following identities:

$$\hat{P}_{\mathcal{B}}\prod_{n=1}^{2N-1}\left[\hat{O}_n,\hat{P}_{\mathcal{B}}\right]\hat{P}_{\mathcal{B}} = 0, \quad \hat{Q}_{\mathcal{B}}\prod_{n=1}^{2N}\left[\hat{O}_n,\hat{P}_{\mathcal{B}}\right]\hat{P}_{\mathcal{B}} = 0, \tag{3.2.25}$$

which are valid for an arbitrary set of operators $\{\hat{O}_n, N\in\mathbb{N}\}$, by exploiting the orthogonality and idempotence of $\hat{P}_{\mathcal{B}}$ and $\hat{Q}_{\mathcal{B}}$. We will prove them by induction. First of all, when $N=1$, it is easy to directly check that both identities hold. Now suppose the identity holds up to some $N\in\mathbb{N}$, then we have for $N+1$:

$$\hat{P}_{\mathcal{B}}\prod_{n=1}^{2N+1}\left[\hat{O}_n,\hat{P}_{\mathcal{B}}\right]\hat{P}_{\mathcal{B}} = \hat{P}_{\mathcal{B}}\prod_{n=1}^{2N-1}\left[\hat{O}_n,\hat{P}_{\mathcal{B}}\right]\left[\hat{O}_{2N},\hat{P}_{\mathcal{B}}\right]\left[\hat{O}_{2N+1},\hat{P}_{\mathcal{B}}\right]\hat{P}_{\mathcal{B}} \tag{3.2.26}$$

$$= \hat{P}_{\mathcal{B}}\prod_{n=1}^{2N-1}\left[\hat{O}_n,\hat{P}_{\mathcal{B}}\right]\left(\hat{P}_{\mathcal{B}}+\hat{Q}_{\mathcal{B}}\right)\left[\hat{O}_{2N},\hat{P}_{\mathcal{B}}\right]\left[\hat{O}_{2N+1},\hat{P}_{\mathcal{B}}\right]\hat{P}_{\mathcal{B}} \tag{3.2.27}$$

$$= 0 + \hat{P}_{\mathcal{B}}\prod_{n=1}^{2N-1}\left[\hat{O}_n,\hat{P}_{\mathcal{B}}\right]\hat{Q}_{\mathcal{B}}\left[\hat{O}_{2N},\hat{P}_{\mathcal{B}}\right]\left[\hat{O}_{2N+1},\hat{P}_{\mathcal{B}}\right]\hat{P}_{\mathcal{B}} \tag{3.2.28}$$

$$= 0 + \hat{P}_{\mathcal{B}}\prod_{n=1}^{2N-1}\left[\hat{O}_n,\hat{P}_{\mathcal{B}}\right]\times 0 \tag{3.2.29}$$

$$= 0, \tag{3.2.30}$$

where in the second step, we inserted $\mathbb{1} = \hat{P}_{\mathcal{B}}+\hat{Q}_{\mathcal{B}}$, and used the assumption that the first identity in Eq. (3.2.25) holds for $2N-1$. In going from the second to the last, we used that the second identity in Eq. (3.2.25) holds. A similar procedure also establishes the second identity.

Using Eq. (3.2.25), we may decompose $\hat{\mathcal{Q}}^{(n)}_{i_1 i_2 \ldots i_n}$ further. After some algebraic manipulations we obtain

$$\hat{Q}_{\mathcal{B}}\left[\hat{r}^{(n)}_{i_1\ldots i_n}, \hat{P}_{\mathcal{B}}\right]\hat{P}_{\mathcal{B}} = \hat{Q}_{\mathcal{B}}\left(\left[\hat{r}_{i_1}, \hat{Q}_{\mathcal{B}}\left[\hat{r}^{(n-1)}_{i_2\ldots i_n}, \hat{P}_{\mathcal{B}}\right]\hat{P}_{\mathcal{B}}\right] + \left[\hat{r}^{(n-1)}_{i_2\ldots i_n}, \hat{P}_{\mathcal{B}}\right]\hat{r}_{i_1,\mathcal{B}} + \left[\hat{r}_{i_1}, \hat{P}_{\mathcal{B}}\right]\hat{r}^{(n-1)}_{i_2\ldots i_n,\mathcal{B}}\right)\hat{P}_{\mathcal{B}}, \tag{3.2.31}$$

where in the first term of Eq. (3.2.31), we find that

$$\hat{Q}_{\mathcal{B}}\left[\hat{r}_{i_1}, \hat{Q}_{\mathcal{B}}\left[\hat{r}^{(n-1)}_{i_2\ldots i_n}, \hat{P}_{\mathcal{B}}\right]\hat{P}_{\mathcal{B}}\right]\hat{P}_{\mathcal{B}} = \hat{Q}_{\mathcal{B}}\left[\hat{r}_{i_1}, \left[\hat{r}^{(n-1)}_{i_2\ldots i_n}, \hat{P}_{\mathcal{B}}\right]\right]\hat{P}_{\mathcal{B}}. \tag{3.2.32}$$

This motivates the definition of the nth geometric quantity through a recursive commutator

$$\hat{\mathcal{G}}^{(n)}_{i_1 i_2\ldots i_n} = (-\mathrm{i})^n \hat{P}_{\mathcal{B}}\left[\hat{r}_{i_1}, \hat{P}_{\mathcal{B}}\right]\hat{Q}_{\mathcal{B}}\left[\hat{r}_{i_2}, \left[\ldots, \left[\hat{r}_{i_n}, \hat{P}_{\mathcal{B}}\right]\right]\right]\hat{P}_{\mathcal{B}}. \tag{3.2.33}$$

Note $\hat{\mathcal{G}}^{(2)}_{i_1 i_2}$ is precisely the quantum geometric tensor. It is convenient to introduce the moment generating function $\hat{M}(\boldsymbol{\lambda}) = \exp(\boldsymbol{\lambda}\cdot\hat{\boldsymbol{r}})$, using the projected version of which we have

$$\left(\hat{r}^{(n)}_{\boldsymbol{i}_n}\right)_{\mathcal{B}} = (\hat{r}_{i_1}\ldots\hat{r}_{i_n})_{\mathcal{B}} = \lim_{\boldsymbol{\lambda}\to\boldsymbol{0}} \partial_{\lambda_{\boldsymbol{i}_n}} \hat{M}_{\mathcal{B}}(\boldsymbol{\lambda}). \tag{3.2.34}$$

Previously in the case of quantum geometric tensor and quantum Christoffel symbols, we saw that the quantum geometric quantities appear in the symmetrized form of the decomposition of band-projected moments, and we expect that the same goes in any order, and we may write the moment generating function as

$$\hat{M}_{\mathcal{B}}(\boldsymbol{\lambda}) = \left(\mathrm{e}^{\boldsymbol{\lambda}\cdot\hat{\boldsymbol{r}}}\right)_{\mathcal{B}} = \exp\left(\lambda_i \hat{r}_{i,\mathcal{B}} + \sum_{n=2}^{\infty}\frac{1}{n!}\lambda_{\boldsymbol{i}_n}\hat{\mathcal{T}}^{(n)}_{\boldsymbol{i}_n}\right), \tag{3.2.35}$$

where we used the the multi-index $\boldsymbol{i}_n = i_1\ldots i_n$, and $\partial_{\lambda_{\boldsymbol{i}_n}} = \partial_{\lambda_{i_1}}\ldots\partial_{\lambda_{i_n}}$, $\lambda_{\boldsymbol{i}_n} = \lambda_{i_1}\ldots\lambda_{i_n}$. The quantities $\hat{\mathcal{T}}^{(n)}_{\boldsymbol{i}_n}$ are some rank-n tensor that are completely symmetric in all of its indices, and emerge from symmetrizing $\hat{\mathcal{Q}}^{(n)}_{\boldsymbol{i}_n}$. In fact, we can identify that $\hat{\mathcal{G}}_{ij} = \hat{\mathcal{T}}^{(2)}_{ij}$ and $\hat{\mathcal{T}}_{ijk} = \hat{\mathcal{T}}^{(3)}_{ijk}$. At the moment of writing the thesis, we could not find a general formula for $\hat{\mathcal{T}}^{(n)}_{\boldsymbol{i}_n}$ to arbitrary order. However, we conjecture that perhaps using the cumulant generating function $\log\hat{M}_{\mathcal{B}}(\boldsymbol{\lambda})$ a general formula of the geometric quantities might be obtained, and we leave it for future research.

3.3 Local expressions of the geometric operators

3.3.1 Local projection operators and moment generating function

In early parts of the thesis, we introduced the notion of quantum metric tensor and Berry curvature for generic parametrized quantum states. In contrast, in the previous section, we studied the algebraic properties of projected products of position operators, and the decompensation of a band projected product, namely the moments of position operators, in terms of geometric quantities in operator form. Apart from in the definition of projection operators, no explicit reference to states is invoked at all. To reconcile these two approaches and further understand our definition of the geometric operators, we compute the matrix elements of the geometric operators in the local Bloch basis, from which we may recover the more conventional expressions for the geometric quantities.

For including the case of multi-band case, it is convenient to introduce the local (in momentum space) projection and complement operators

$$\hat{P}_{\boldsymbol{q}} = \sum_n |u_{n\boldsymbol{q}}\rangle \langle u_{n\boldsymbol{q}}|, \quad \hat{P}_{\boldsymbol{q}\mathcal{B}} = \sum_{n\in\mathcal{N}_\mathcal{B}} |u_{n\boldsymbol{q}}\rangle \langle u_{n\boldsymbol{q}}|, \quad \hat{Q}_{\boldsymbol{q}\mathcal{B}} = \sum_{n\notin\mathcal{N}_\mathcal{B}} |u_{n\boldsymbol{q}}\rangle \langle u_{n\boldsymbol{q}}| = \hat{P}_{\boldsymbol{q}} - \hat{P}_{\boldsymbol{q}\mathcal{B}}. \tag{3.3.1}$$

Recall the orthogonality of the Bloch functions: $\langle u_{n\boldsymbol{k}}|u_{m\boldsymbol{k}}\rangle = \delta_{nm}$. Using this it is easy to show that, as the band projection and complement operators, the local $\hat{P}_{\boldsymbol{q}\mathcal{B}}$ and $\hat{Q}_{\boldsymbol{q}\mathcal{B}}$ are idempotent and orthogonal as well: $\hat{P}^2_{\boldsymbol{q}\mathcal{B}} = \hat{P}_{\boldsymbol{q}\mathcal{B}}$, $\hat{Q}^2_{\boldsymbol{q}\mathcal{B}} = \hat{Q}_{\boldsymbol{q}\mathcal{B}}$, $\hat{P}_{\boldsymbol{q}\mathcal{B}}\hat{Q}_{\boldsymbol{q}\mathcal{B}} = \hat{Q}_{\boldsymbol{q}\mathcal{B}}\hat{P}_{\boldsymbol{q}\mathcal{B}} = 0$. The band projection operators can be expressed as the sum over Bloch momenta of the local projection operators. More precisely we have that

$$\mathbb{1} = \sum_{\boldsymbol{q}} \mathrm{e}^{\mathrm{i}\boldsymbol{q}\cdot\hat{\boldsymbol{r}}}\hat{P}_{\boldsymbol{q}}\mathrm{e}^{-\mathrm{i}\boldsymbol{q}\cdot\hat{\boldsymbol{r}}}, \quad \hat{P}_{\mathcal{B}} = \sum_{\boldsymbol{q}} \mathrm{e}^{\mathrm{i}\boldsymbol{q}\cdot\hat{\boldsymbol{r}}}\hat{P}_{\boldsymbol{q}\mathcal{B}}\mathrm{e}^{-\mathrm{i}\boldsymbol{q}\cdot\hat{\boldsymbol{r}}}. \tag{3.3.2}$$

As already discussed previously in Section 3.2.2, a projected operator $O_\mathcal{B}(\hat{\boldsymbol{r}})$ that is a function of the position operators can be expressed in terms of the projected generating operator $\left(\mathrm{e}^{-\mathrm{i}\boldsymbol{a}\cdot\hat{\boldsymbol{r}}}\right)_\mathcal{B}$ via

$$O_\mathcal{B}(\hat{\boldsymbol{r}}) = \lim_{\boldsymbol{a}\to\boldsymbol{0}} O(\mathrm{i}\partial_{\boldsymbol{a}})\hat{P}_\mathcal{B}\,\mathrm{e}^{-\mathrm{i}\boldsymbol{a}\cdot\hat{\boldsymbol{r}}}\,\hat{P}_\mathcal{B}, \tag{3.3.3}$$

where for later convenience we now included a factor of i. Therefore, should we be able to compute the matrix elements of $\left(\mathrm{e}^{-\mathrm{i}\boldsymbol{a}\cdot\hat{\boldsymbol{r}}}\right)_\mathcal{B}$, we can then compute the corresponding local expressions of a projected product of position operators as well. Furthermore, in our discussion of the geometric operators, they are introduced via certain decomposition of band

projected moments of position operators, and we would like to compute their corresponding Bloch basis expressions as well.

The calculations will be done by using the following identities

$$\hat{P}_{\mathcal{B}}\, \mathrm{e}^{-\mathrm{i}\boldsymbol{a}\cdot\hat{\boldsymbol{r}}}\, \hat{P}_{\mathcal{B}} = \sum_{\boldsymbol{q}} \mathrm{e}^{\mathrm{i}\boldsymbol{q}\cdot\hat{\boldsymbol{r}}}\, \hat{P}_{\boldsymbol{q}\mathcal{B}}\, \mathrm{e}^{\boldsymbol{a}\cdot\partial_{\boldsymbol{q}}}\, \hat{P}_{\boldsymbol{q}\mathcal{B}}\, \mathrm{e}^{-\mathrm{i}\boldsymbol{q}\cdot\hat{\boldsymbol{r}}}, \tag{3.3.4}$$

$$\hat{Q}_{\mathcal{B}}\, \mathrm{e}^{-\mathrm{i}\boldsymbol{a}\cdot\hat{\boldsymbol{r}}}\, \hat{P}_{\mathcal{B}} = \sum_{\boldsymbol{q}} \mathrm{e}^{\mathrm{i}\boldsymbol{q}\cdot\hat{\boldsymbol{r}}}\, \hat{P}_{\boldsymbol{q}\mathcal{B}}\, \mathrm{e}^{\boldsymbol{a}\cdot\partial_{\boldsymbol{q}}}\, \hat{Q}_{\boldsymbol{q}\mathcal{B}}\, \mathrm{e}^{-\mathrm{i}\boldsymbol{q}\cdot\hat{\boldsymbol{r}}}, \tag{3.3.5}$$

where the exponential of derivatives acts on everything to the right.

We first note that unlike the band projection operator, the local projection and complement operator are not orthogonal since the Bloch functions are not simple plane waves in general, and have finite overlap, i.e. $\langle u_{n\boldsymbol{k}}|u_{m\boldsymbol{q}}\rangle \neq \delta_{nm}\delta(\boldsymbol{q}-\boldsymbol{k})$. Consequently, we do not have $\hat{P}_{\boldsymbol{q}}\hat{P}_{\boldsymbol{k}} \neq \delta(\boldsymbol{k}-\boldsymbol{q})$ as one might have guessed. However, we have that

$$\hat{P}_{\boldsymbol{q}}\mathrm{e}^{\mathrm{i}(\boldsymbol{k}-\boldsymbol{q})\cdot\hat{\boldsymbol{r}}}\hat{P}_{\boldsymbol{k}} = \delta(\boldsymbol{q}-\boldsymbol{k})\hat{P}_{\boldsymbol{q}}, \tag{3.3.6}$$

which follows trivially from the orthonormality of $\langle\psi_{n\boldsymbol{q}}|\psi_{m\boldsymbol{k}}\rangle = \delta_{nm}\delta(\boldsymbol{q}-\boldsymbol{k})$, and holds still when band projected, namely $\hat{P}_{\boldsymbol{q}} \to \hat{P}_{\boldsymbol{q}\mathcal{B}}$. The above central formulas, Eqs. (3.3.4) and (3.3.5) can be obtained from a generalization of the modified orthogonality formula, namely that

$$\hat{P}_{\boldsymbol{q}}\mathrm{e}^{\mathrm{i}(\boldsymbol{k}-\boldsymbol{q}-\boldsymbol{a})\cdot\hat{\boldsymbol{r}}}\hat{P}_{\boldsymbol{k}} = \mathrm{e}^{\boldsymbol{a}\cdot\partial_{\boldsymbol{q}}}\left(\delta(\boldsymbol{q}-\boldsymbol{k})\right)\hat{P}_{\boldsymbol{q}}\hat{P}_{\boldsymbol{k}} \tag{3.3.7}$$

$$= e^{-\boldsymbol{a}\cdot\partial_{\boldsymbol{k}}}\left(\delta(\boldsymbol{q}-\boldsymbol{k})\right)\hat{P}_{\boldsymbol{q}}\hat{P}_{\boldsymbol{k}}. \tag{3.3.8}$$

The detailed proof is given in the appendix. Basically, it is done by inserting an identify using the position basis $\mathbb{1} = \int d\boldsymbol{r}\,|\boldsymbol{r}\rangle\langle\boldsymbol{r}|$, and then apply the Poisson summation formula, hence transforming the exponential to a Dirac delta , so that we have

$$\hat{P}_{\boldsymbol{q}}\mathrm{e}^{\boldsymbol{a}\cdot\partial_{\boldsymbol{q}}}\left(\mathrm{e}^{+\mathrm{i}(\boldsymbol{k}-\boldsymbol{q})\cdot\hat{\boldsymbol{r}}}\right)\hat{P}_{\boldsymbol{k}} = \mathrm{e}^{\boldsymbol{a}\cdot\partial_{\boldsymbol{q}}}\left(\delta(\boldsymbol{q}-\boldsymbol{k})\right)\hat{P}_{\boldsymbol{q}}\hat{P}_{\boldsymbol{k}}, \tag{3.3.9}$$

from which the identity is established. Note that we intentionally do not transform the whole of $\mathrm{e}^{+\mathrm{i}(\boldsymbol{k}-\boldsymbol{q}-\boldsymbol{a})\cdot\hat{\boldsymbol{r}}}$ into a Dirac delta, because $\boldsymbol{q}-\boldsymbol{k}-\boldsymbol{a}$ is no longer confined within the first Brillouin zone. This might then cause a phase term due to crossing the Brillouin boundary since $|u_{n\boldsymbol{q}}\rangle = \mathrm{e}^{\mathrm{i}\theta}\,|u_{n\boldsymbol{q}+\boldsymbol{G}}\rangle$, where $\boldsymbol{G}$ is a reciprocal lattice vector. In fact when applying the Poisson summation formula, one obtains instead of $\delta(\boldsymbol{q}-\boldsymbol{k}-\boldsymbol{a})$, rather $\sum_{\boldsymbol{K}_i}\delta(\boldsymbol{q}-\boldsymbol{k}-\boldsymbol{a}-\boldsymbol{K}_i)$,

where the sum is over all reciprocal lattice vectors $\boldsymbol{K}_i$; see Appendix A.1.

Using Eq. (3.3.8), we immediately obtain that the moment generating function can be written as

$$\mathrm{e}^{-\mathrm{i}\boldsymbol{a}\cdot\hat{\boldsymbol{r}}} = \sum_{\boldsymbol{q}} \mathrm{e}^{\mathrm{i}\boldsymbol{q}\cdot\hat{\boldsymbol{r}}} \hat{P}_{\boldsymbol{q}} \mathrm{e}^{\boldsymbol{a}\cdot\partial_{\boldsymbol{q}}} \hat{P}_{\boldsymbol{q}} \mathrm{e}^{-\mathrm{i}\boldsymbol{q}\cdot\hat{\boldsymbol{r}}}, \tag{3.3.10}$$

where the derivative acts on everything to the right. By applying band projection operators accordingly we immediately obtain Equations (3.3.4) and (3.3.5). The matrix element of the generating operator in the Bloch basis can be easily obtained from the above as

$$\begin{aligned} &\langle \psi_{n\boldsymbol{q}} | \, \mathrm{e}^{-\mathrm{i}\boldsymbol{a}\cdot\hat{\boldsymbol{r}}} \, | \psi_{m\boldsymbol{k}} \rangle && (3.3.11) \\ &= \langle u_{n\boldsymbol{q}} | \, \mathrm{e}^{\mathrm{i}(\boldsymbol{k}-(\boldsymbol{a}+\boldsymbol{q}))\cdot\hat{\boldsymbol{r}}} \, | u_{m\boldsymbol{k}} \rangle \\ &= \langle u_{n\boldsymbol{q}} | u_{m\boldsymbol{k}} \rangle \, \mathrm{e}^{\boldsymbol{a}\cdot\partial_{\boldsymbol{q}}} \delta(\boldsymbol{q}-\boldsymbol{k}). && (3.3.12) \end{aligned}$$

If we keep in mind that $\boldsymbol{a}$ is a parameter that is taken to be zero in the end pf the calculations, then we may also summarize the above as $\langle \psi_{n\boldsymbol{q}} | \, \mathrm{e}^{-\mathrm{i}\boldsymbol{a}\cdot\hat{\boldsymbol{r}}} \, | \psi_{m\boldsymbol{k}} \rangle = \langle u_{n\boldsymbol{q}} | u_{m\boldsymbol{a}+\boldsymbol{q}-\boldsymbol{k}} \rangle \, \delta(\boldsymbol{a}+\boldsymbol{q}-\boldsymbol{k})$. Note that here and everywhere else in the thesis, the inner product between the cell-periodic part of the Bloch states, or their derivatives, are given as an integration over unit cells, with a normalization factor $(2\pi)^d/V_{uc}$ included, with U_{uc} the volume of a unit cell. This implies that (derivative on δ is w.r.t $\boldsymbol{q}$)

$$\langle \psi_{n\boldsymbol{q}} | \, \hat{\boldsymbol{r}}^n \, | \psi_{m\boldsymbol{k}} \rangle = (i)^n \delta^{(n)}(\boldsymbol{q}-\boldsymbol{k}) \, \langle u_{n\boldsymbol{q}} | u_{m\boldsymbol{k}} \rangle \tag{3.3.13}$$

Note $(-\mathrm{i})^n \delta^{(n)}(\boldsymbol{q}) = \mathrm{i}^n \delta^{(n)}(-\boldsymbol{q})$, where $\delta^{(n)}(\boldsymbol{q}) \equiv \partial_{\boldsymbol{q}}^n \delta(\boldsymbol{q})$. We see that the product of position operators encode information on the overlap between Bloch states, which characterize the band structure, and this explains the importance of the moment. Put another way, the physical significance of the quantum geometric quantities lies in the fact that they actually carry information about the momentum space profile of the Bloch states.

3.3.2 Position and velocity operator

We mentioned before that the position operator may be rather suggestively decomposed as

$$\hat{r}_i = i\partial_{\hat{k}_i} + \hat{\mathrm{A}}_i, \tag{3.3.14}$$

where

$$\partial_{\hat{k}_i} = \sum_n \sum_{\boldsymbol{k}} |\psi_{n\boldsymbol{k}}\rangle \, \partial_{k_i} \, \langle \psi_{n\boldsymbol{k}}| \, , \quad \hat{\mathrm{A}}_i = \sum_{nm} \sum_{\boldsymbol{k}} |\psi_{n\boldsymbol{k}}\rangle \, \mathrm{A}_{nm,i}(\boldsymbol{k}) \, \langle \psi_{m\boldsymbol{k}}| \, , \tag{3.3.15}$$

and $\boldsymbol{A}_{nm}(\boldsymbol{k}) = \mathrm{i} \langle u_{n\boldsymbol{k}}| \, \partial_{\boldsymbol{k}} \, |u_{m\boldsymbol{k}}\rangle$ is the non-abelian Berry connection. This motivated us to denote the projected position operator as a covariant derivative $\hat{r}_{i\mathcal{B}} = \mathrm{i}\hat{\nabla}_i$. Let us now show this by applying the results in the previous section. Using Eq. (3.3.10) we have, (derivatives act on everything to the right)

$$\hat{r}_i = \lim_{\boldsymbol{a}\to\boldsymbol{0}} \mathrm{i}\partial_{a_i} \mathrm{e}^{-\mathrm{i}\boldsymbol{a}\cdot\hat{\boldsymbol{r}}} = \mathrm{i} \sum_{\boldsymbol{k}} \mathrm{e}^{\mathrm{i}\boldsymbol{k}\cdot\hat{\boldsymbol{r}}} \hat{P}_{\boldsymbol{k}} \partial_{k_i} \hat{P}_{\boldsymbol{k}} \mathrm{e}^{-\mathrm{i}\boldsymbol{k}\cdot\hat{\boldsymbol{r}}} = \mathrm{i} \sum_{nm} \sum_{\boldsymbol{k}} |\psi_{n\boldsymbol{k}}\rangle \, \langle u_{n\boldsymbol{k}}| \, \partial_{k_i} \, |u_{m\boldsymbol{k}}\rangle \, \langle \psi_{m\boldsymbol{k}}| \tag{3.3.16}$$

$$= \sum_{nm} \sum_{\boldsymbol{k}} |\psi_{n\boldsymbol{k}}\rangle \, (\delta_{nm}\partial_{k_i} + A_{nm,i}(\boldsymbol{k})) \, \langle \psi_{m\boldsymbol{k}}| \, , \tag{3.3.17}$$

where ∂_{k_i} in Eq. (3.3.16) acts on $\hat{P}_{\boldsymbol{k}} \mathrm{e}^{-\mathrm{i}\boldsymbol{k}\cdot\hat{\boldsymbol{r}}} = \sum_m |u_{m\boldsymbol{k}}\rangle \, \langle \psi_{m\boldsymbol{k}}|$. It can be shown that the un-projected Berry connection operators satisfy $\mathrm{i}\left(\partial_{k_i}\hat{A}_j - \partial_{k_j}\hat{A}_i\right) = [\hat{A}_i, \hat{A}_j]$. This is simply the statement that the position operators commute, $[\hat{r}_i, \hat{r}_j] = 0$.

To further illustrate that the position operator can be viewed as a covariant derivative, let us study its action on operators. Consider a general Bloch diagonal operator, which is of the form $\hat{O} = \sum_n \sum_{\boldsymbol{k}} |\psi_{n\boldsymbol{k}}\rangle \, O_{nm}(\boldsymbol{k}) \, \langle \psi_{m\boldsymbol{k}}|$. We have

$$\frac{1}{i}[\hat{r}_i, \hat{O}] = \sum_{nm} \sum_{\boldsymbol{k}} |\psi_{n\boldsymbol{k}}\rangle \, (\partial_{k_i} O_{nm}(\boldsymbol{k}) - i[\mathrm{A}_i(\boldsymbol{k}), O(\boldsymbol{k})]_{nm}) \, \langle \psi_{m\boldsymbol{k}}| \tag{3.3.18}$$

$$= \sum_{nm} \sum_{\boldsymbol{k}} |\psi_{n\boldsymbol{k}}\rangle \, [\nabla_i(\boldsymbol{k}), O(\boldsymbol{k})]_{nm} \, \langle \psi_{m\boldsymbol{k}}| \, , \tag{3.3.19}$$

where the derivative acts on $O_{nm}(\boldsymbol{k})$ only, and $[\mathrm{A}_i(\boldsymbol{k}), O(\boldsymbol{k})]_{nm} = \sum_l \mathrm{A}_{i,nl}(\boldsymbol{k}) O_{lm}(\boldsymbol{k}) - O_{nl}(\boldsymbol{k})\mathrm{A}_{i,lm}(\boldsymbol{k})$. In the second line we also introduced the covariant derivative $\nabla_i = \partial_{k_i} - \mathrm{i}A_i(\boldsymbol{k})$. Note that the second term vanishes for an operator whose matrix elements are band-independent, such as the Bloch momentum operator $\hat{\boldsymbol{k}}$. When band projected, the above receives little modification:

$$\frac{1}{i}[\hat{r}_{i\mathcal{B}}, \hat{O}_{\mathcal{B}}] = [\hat{\nabla}_i, \hat{O}_{\mathcal{B}}] = \sum_{n,m\in\mathcal{N}_{\mathcal{B}}} \sum_{\boldsymbol{k}} |\psi_{n\boldsymbol{k}}\rangle \, (\partial_{k_i} O_{nm}(\boldsymbol{k}) - i[\mathrm{A}_{i\mathcal{B}}(\boldsymbol{k}), O_{\mathcal{B}}(\boldsymbol{k})]_{nm}) \, \langle \psi_{m\boldsymbol{k}}| \tag{3.3.20}$$

$$= \sum_{n,m\in\mathcal{N}_{\mathcal{B}}} \sum_{\boldsymbol{k}} |\psi_{n\boldsymbol{k}}\rangle \, [\nabla_i, O_{\mathcal{B}}(\boldsymbol{k})]_{nm} \, \langle \psi_{m\boldsymbol{k}}| \, , \tag{3.3.21}$$

where the band summation in the commutator is also restricted to the projected bands.

In particular, we have

$$[\hat{r}_i, \hat{k}_j] = \mathrm{i}[\partial_{\hat{k}_i}, \hat{k}_j] = \mathrm{i}\delta_{ij} \tag{3.3.22}$$

The velocity operator is defined as $\hat{\boldsymbol{v}} = \frac{1}{\mathrm{i}}[\hat{\boldsymbol{r}}, \hat{H}_0]$. In terms of the above decomposition, we have

$$\hat{\boldsymbol{v}} = \frac{1}{\mathrm{i}}[\hat{\boldsymbol{r}}, \hat{H}_0] = \sum_{nm\boldsymbol{k}} |\psi_{n\boldsymbol{k}}\rangle \langle\psi_{m\boldsymbol{k}}| \left(\delta_{nm}\partial_{\boldsymbol{k}}\mathcal{E}_{n\boldsymbol{k}} + \mathrm{i}\Delta_{nm}(\boldsymbol{k})\mathsf{A}_{nm}(\boldsymbol{k})\right), \tag{3.3.23}$$

where $\Delta_{nm}(\boldsymbol{k}) = \mathcal{E}_{n\boldsymbol{k}} - \mathcal{E}_{m\boldsymbol{k}}$ is the direct band gap. The first term is nothing but the familiar band dispersion related group velocity. The second term can be neglected only when all inter-band transitions is negligible, and in particular in a single-band approximation. Note that with the specific Hamiltonian $\hat{H}_0 = (\hat{\boldsymbol{p}}^2/2m) + V(\hat{\boldsymbol{r}})$, the velocity operator has a direct relation with the canonical momentum as $\hat{\boldsymbol{v}} = \frac{\hat{\boldsymbol{p}}}{m}$. This, however, is a special case, and no longer holds, for instance, for the Pauli Hamiltonian with a spin orbit coupling or a Dirac electron moving in periodic potential [26]. Later we shall discuss a more relevant form of the canonical momentum, as a sort of dual to the position operator as a covariant derivative in real sapce.

3.3.3 Geometric quantities

Previously we defined various operators, and identified them as the operator form of the quantum geometric quantities associated with the Bloch structure. We would now show that the forms of the geometric quantities conventionally seen in the literature are simply the matrix elements of these operators. We do this by using Eq. (3.3.10), which by applying derivatives gives

$$\left(\hat{r}_i\hat{Q}_{\mathcal{B}}\hat{r}^{(n)}_{i_n}\right)_{\mathcal{B}} = -\left([\hat{r}_i, \hat{P}_{\mathcal{B}}]\hat{Q}_{\mathcal{B}}[\hat{r}^{(n)}_{i_n}, \hat{P}_{\mathcal{B}}]\right)_{\mathcal{B}} \tag{3.3.24}$$

$$= \mathrm{i}^{n+1}\sum_{\boldsymbol{k}} e^{i\boldsymbol{k}\cdot\hat{\boldsymbol{r}}}\hat{P}_{\boldsymbol{k}\mathcal{B}}\left(\partial_{k_i}\hat{Q}_{\boldsymbol{k}\mathcal{B}}\right)\hat{Q}_{\boldsymbol{k}\mathcal{B}}\left(\partial_{k_{i_1}}\ldots\partial_{k_{i_n}}\hat{P}_{\boldsymbol{k}\mathcal{B}}e^{-i\boldsymbol{k}\cdot\hat{\boldsymbol{r}}}\right), \tag{3.3.25}$$

where as in the previous section $\hat{r}^{(n)}_{\boldsymbol{i}_n} = \hat{r}_{i_1}\hat{r}_{i_2}\ldots\hat{r}_{i_n}$. Of course, in principle, the results below can also be obtained by direct methods. We present two examples of such calculations in the appendix, both to confirm the results obtained here, as well as to demonstrate the efficiency of the methods that we introduce.

Quantum geometric tensor

Let us first consider the quantum geometric tensor $\hat{\mathcal{Q}}^{(2)}_{ij} = \mathrm{i}^2 \left(\left[\hat{r}_i, \hat{P}_{\mathcal{B}} \right] \hat{Q}_{\mathcal{B}} \left[\hat{r}_j, \hat{P}_{\mathcal{B}} \right] \right)_{\mathcal{B}}$. This corresponds to the $n = 1$ case of the above. In the Bloch basis we have

$$\hat{\mathcal{Q}}^{(2)}_{ij} = \sum_{n,m \in \mathcal{N}_{\mathcal{B}}} \mathcal{Q}_{ij,nm}(\boldsymbol{k}) \left| \psi_{n\boldsymbol{k}} \right\rangle \left\langle \psi_{m\boldsymbol{k}} \right| . \tag{3.3.26}$$

The matrix element can be computed by using Eq. (3.3.25), with $n = 1$, where we have

$$\begin{aligned}
\mathcal{Q}_{ij,nm}(\boldsymbol{k}) &= \left\langle \psi_{m\boldsymbol{k}} \right| \hat{\mathcal{Q}}^{(2)}_{ij} \left| \psi_{n\boldsymbol{k}} \right\rangle && (3.3.27)\\
&= \mathrm{i}^2 \left\langle u_{n\boldsymbol{k}} \right| \left(\partial_{k_i} \hat{Q}_{\boldsymbol{k}\mathcal{B}} \right) \hat{Q}_{\boldsymbol{k}\mathcal{B}} \left(\partial_{k_i} \hat{P}_{\mathcal{B}} \left| u_{m\boldsymbol{k}} \right\rangle \right) && (3.3.28)\\
&= \left\langle u_{n\boldsymbol{k}} \right| \left(\partial_{k_i} \hat{Q}_{\boldsymbol{k}\mathcal{B}} \right) \left(\partial_{k_i} \hat{Q}_{\boldsymbol{k}\mathcal{B}} \right) \hat{P}_{\mathcal{B}} \left| u_{m\boldsymbol{k}} \right\rangle && (3.3.29)\\
&= \left\langle u_{n\boldsymbol{k}} \right| \left(\partial_{k_i} \hat{P}_{\boldsymbol{k}\mathcal{B}} \right) \left(\partial_{k_j} \hat{P}_{\boldsymbol{k}\mathcal{B}} \right) \left| u_{m\boldsymbol{k}} \right\rangle , && (3.3.30)
\end{aligned}$$

with k-derivatives that act only on the closest local projection operators. In going from the second to the third line, we used that

$$0 = \partial_{\boldsymbol{k}}(\hat{P}_{\mathcal{B}}\hat{Q}_{\mathcal{B}}) = \partial_{\boldsymbol{k}}(\hat{P}_{\mathcal{B}})\hat{Q}_{\mathcal{B}} + \hat{P}_{\mathcal{B}}\partial_{\boldsymbol{k}}(\hat{Q}_{\mathcal{B}}). \tag{3.3.31}$$

The form of the matrix element $\mathcal{Q}_{ij,nm}(\boldsymbol{k})$ is precisely the multi-band version of quantum geometric tensor [86], which in the single band cases reduced to Eq. (2.1.22).

Christoffel symbols and symplectic connection

Now let us consider the $n = 2$ case. Applying the formula Eq. (3.3.25) we have

$$\begin{aligned}
&\hat{P}_{\mathcal{B}}[\hat{r}_i, \hat{P}_{\mathcal{B}}]\hat{Q}_{\mathcal{B}}[\hat{r}_j\hat{r}_k, \hat{P}_{\mathcal{B}}]\hat{P}_{\mathcal{B}} && (3.3.32)\\
=&i^3 \sum_{\boldsymbol{k}} e^{i\boldsymbol{k}\cdot\hat{\boldsymbol{r}}} \hat{P}_{\boldsymbol{k}\mathcal{B}} \left[\left(\partial_{k_j} \hat{P}_{\boldsymbol{k}\mathcal{B}} \right) \left(\partial_{k_k} \hat{P}_{\boldsymbol{k}\mathcal{B}} e^{-i\boldsymbol{k}\cdot\hat{\boldsymbol{r}}} \right) + \left(\partial_{k_k} \hat{P}_{\boldsymbol{k}\mathcal{B}} \right) \left(\partial_{k_j} \hat{P}_{\boldsymbol{k}\mathcal{B}} e^{-i\boldsymbol{k}\cdot\hat{\boldsymbol{r}}} \right) \right]\\
&+ e^{i\boldsymbol{k}\cdot\hat{\boldsymbol{r}}} \hat{P}_{\boldsymbol{k}\mathcal{B}} \left(\partial_{k_i} \hat{Q}_{\boldsymbol{k}\mathcal{B}} \right) \left(\partial_{k_j} \partial_{k_k} \hat{P}_{\boldsymbol{k}\mathcal{B}} \right) \hat{P}_{\boldsymbol{k}\mathcal{B}} e^{-i\boldsymbol{k}\cdot\hat{\boldsymbol{r}}} && (3.3.33)\\
=&\hat{Q}^{(2)}_{ij} \hat{r}_{k\mathcal{B}} + \hat{Q}^{(2)}_{ik} \hat{r}_{j\mathcal{B}} + \hat{Q}^{(3)}_{ijk}, && (3.3.34)
\end{aligned}$$

where we introduced the geometric quantity $\hat{Q}^{(3)}_{ijk} = \sum_{n\in\mathcal{B}} \sum_{\boldsymbol{k}} Q^{(3)}_{ijk,nm}(\boldsymbol{k}) \left| \psi_{n\boldsymbol{k}} \right\rangle \left\langle \psi_{m\boldsymbol{k}} \right|$, whose matrix elements are[86] $Q^{(3)}_{ijk,nm}(\boldsymbol{k}) = i \left\langle u_{n\boldsymbol{k}} \right| \left(\partial_{k_i} \hat{P}_{\boldsymbol{k}\mathcal{B}} \right) \left(\partial_{k_j} \partial_{k_k} \hat{P}_{\boldsymbol{k}\mathcal{B}} \right) \left| u_{m\boldsymbol{k}} \right\rangle$. Its relation to quantum Christoffel symbols are given by eq.(3.2.17).

3.4 Canonical momentum

So far we have considered the projected product of position operators. It is natural to wonder about the momentum. In fact, this is a crucial issue when it comes to consider the dynamics in a magnetic field, for we know that interaction between the field and particle is given by the minimal coupling $\boldsymbol{p} \to \boldsymbol{p} - q\boldsymbol{A}$. Thus the modified commutation relations of the projected momentum might also lead to modification of the dynamics. Hence in this section we shall study the projected canonical momentum.

3.4.1 Canonical momentum and and real space Berry connections

The canonical momentum is defined as the infinitesimal translation generator, such that

$$\langle \boldsymbol{r} | \, \hat{\boldsymbol{p}} \, | \psi \rangle = -i\partial_{\boldsymbol{r}} \psi(\boldsymbol{r}). \tag{3.4.1}$$

On the other hand, the crystal or Bloch momentum operator may be defined in the Bloch basis as $\hat{\boldsymbol{k}} = \sum_{n\boldsymbol{k}} \boldsymbol{k} \, |\psi_{n\boldsymbol{k}}\rangle \langle \psi_{n\boldsymbol{k}}|$. Even though both the canonical momentum and Bloch momentum satisfies the commutation relation $[\hat{\boldsymbol{r}}, \hat{\boldsymbol{p}}] = [\hat{\boldsymbol{r}}, \hat{\boldsymbol{k}}] = \mathrm{i}$, the crystal momentum generates lattice translation: $\mathrm{e}^{-\mathrm{i}\hat{\boldsymbol{k}}\cdot\boldsymbol{R}} \, |\boldsymbol{r}\rangle = |\boldsymbol{r} + \boldsymbol{R}\rangle$, where $\boldsymbol{R}$ is a lattice vector. In fact the canonical momentum as is related to the Bloch momentum as $\hat{\boldsymbol{p}} = \hat{\boldsymbol{k}} - \hat{\mathcal{A}}^{\boldsymbol{r}}$, with matrix elements

$$\langle \psi_{n\boldsymbol{q}} | \, \hat{\boldsymbol{p}} \, | \psi_{m\boldsymbol{k}} \rangle = (\boldsymbol{k}\delta_{nm} - \mathcal{A}^{\boldsymbol{r}}_{nm}(\boldsymbol{q}))\, \delta(\boldsymbol{q} - \boldsymbol{k}), \tag{3.4.2}$$

where the second term is a real space Berry connection

$$\mathcal{A}^{\boldsymbol{r}}_{nm}(\boldsymbol{q}) = i \, \langle u_{n\boldsymbol{q}} | \, \partial_{\boldsymbol{r}} \, | u_{m\boldsymbol{q}} \rangle \equiv i \frac{(2\pi)^d}{V_{uc}} \int_{cell} d\boldsymbol{r} \, u^*_{n\boldsymbol{q}}(\boldsymbol{r}) \partial_{\boldsymbol{r}} u_{m\boldsymbol{q}}(\boldsymbol{r}). \tag{3.4.3}$$

The detailed derivation is given in the appendix. Here we have abused the notation somewhat, since $\boldsymbol{r}$ is a dummy variable that is integrated over, and $\mathcal{A}^{\boldsymbol{r}}_{nm}(\boldsymbol{q})$ has no explicit dependence on $\boldsymbol{r}$. But given the lack of a better alternative, we stick with it. The same result has been obtained by Blount [26]. It may be shown in the Wannier basis that the Bloch momentum operator generates inter-cell translations, while the real space Berry connection generates intra-cell displacements.

Note that in the literature there is another notion of real-space Berry connection, which arises for band systems that have arise from band structure that have spatial in-homogeneity, such as systems in a magnetic texture; see for instance [134, 152, 164]. This is different

from our $\mathcal{A}^r_{nm}(\boldsymbol{q})$, as we can see from the matrix elements characterizes the spatial modulation of the Bloch states. Indeed, $\mathcal{A}^r_{nm}(\boldsymbol{q})$ vanishes in the plane-wave limit, where $u_{n\boldsymbol{k}}(\boldsymbol{r})$ is a constant. This occurs in the limiting case where the lattice potential is just a uniform background, the system essentially just describes a free particle and the crystal momentum reduces to the canonical momentum. Finally, we note that only the band diagonal part of the real-space Berry connection is gauge-invariant under a Bloch gauge transformation.

3.4.2 Mixed geometrical quantities

In the previous part we have extended the discussion on the geometric quantities related to the projected product of position operators. On the other hand, in the presence of magnetic field, the canonical momentum is coupled to the vector potential, and this might induce contributions that are expressed in terms of new geometric quantities, which depends on the spatial gradient of the cell-periodic part of Bloch states as well as the real space Berry connection.

Mixed quantum geometric tensor

Analogously to the quantum geometric tensor intoduced before $\hat{\mathcal{Q}}^{(2)}_{ij} \equiv -\hat{P}_{\mathcal{B}}[\hat{r}_i, \hat{Q}_{\mathcal{B}}][\hat{r}_j, \hat{Q}_{\mathcal{B}}]\hat{P}_{\mathcal{B}}$, we introduce a mixed quantum geometric tensor

$$\hat{\mathcal{L}}_{ij} \equiv -\hat{P}_{\mathcal{B}}[\hat{r}_i, \hat{Q}_{\mathcal{B}}][\hat{p}_j, \hat{Q}_{\mathcal{B}}]\hat{P}_{\mathcal{B}} = ((\hat{r}_i - \hat{r}_{i\mathcal{B}})\hat{p}_j)_{\mathcal{B}}. \tag{3.4.4}$$

We can see from the definition that $\hat{\mathcal{L}}_{ij}$ is odd under time reversal transformation and even under inversion. For a Bloch diagonal operator $\hat{O}$, i.e. operators which conserves the Bloch momentum $\langle\psi_{n\boldsymbol{q}}|\,\hat{O}\,\langle\psi_{m\boldsymbol{k}}| = \hat{O}_{nm}(\boldsymbol{q})\delta(\boldsymbol{q}-\boldsymbol{k})$, we may define a local (in momentum) operator

$$\hat{O}_{\boldsymbol{q}} \equiv e^{-i\boldsymbol{q}\cdot\hat{\boldsymbol{r}}}\hat{O}e^{i\boldsymbol{q}\cdot\hat{\boldsymbol{r}}}. \tag{3.4.5}$$

The local operator has the property that its matrix elements evaluated on Bloch functions (the cell-periodic part of Bloch states) are simply the matrix elements of $\hat{O}$ in Bloch states, namely

$$\langle u_{n\boldsymbol{q}}|\,\hat{O}_{\boldsymbol{q}}\,|u_{m\boldsymbol{q}}\rangle = O_{nm}(\boldsymbol{q}) = \langle\psi_{n\boldsymbol{q}}|\,\hat{O}\,|\psi_{m\boldsymbol{q}}\rangle\,. \tag{3.4.6}$$

Now we may compute its matrix elements using Eq. (3.3.5):

$$\hat{\mathcal{L}}_{ij} = \lim_{\boldsymbol{a}\to 0} \mathrm{i}\partial_{a_i}\hat{P}_N e^{-i\boldsymbol{a}\cdot\hat{\boldsymbol{r}}}\hat{Q}_N\hat{p}_j\hat{P}_N = \mathrm{i}e^{i\boldsymbol{q}\cdot\hat{\boldsymbol{r}}}\hat{P}_{\boldsymbol{q}\mathcal{B}}\left(\partial_{q_i}\hat{Q}_{\boldsymbol{q}\mathcal{B}}\right)\hat{Q}_{\boldsymbol{q}\mathcal{B}}\hat{A}^r_{j\boldsymbol{q}}\hat{P}_{\boldsymbol{q}\mathcal{B}}e^{-i\boldsymbol{q}\cdot\hat{\boldsymbol{r}}}, \tag{3.4.7}$$

or

$$\hat{\mathcal{L}}_{ij,nm}(\boldsymbol{q})\delta(\boldsymbol{q}-\boldsymbol{k}) = \langle\psi_{n\boldsymbol{q}}|\,\hat{\mathcal{L}}_{ij}\,|\psi_{m\boldsymbol{k}}\rangle = \mathrm{i}\,\langle u_{n\boldsymbol{q}}|\left(\partial_{q_i}\hat{Q}_{\boldsymbol{q}\mathcal{B}}\right)\hat{Q}_{\boldsymbol{q}\mathcal{B}}\hat{A}^r_{j\boldsymbol{q}}\,|u_{m\boldsymbol{q}}\rangle\,\delta(\boldsymbol{q}-\boldsymbol{k}). \tag{3.4.8}$$

This is a new geometric quantity that is local in momentum space. Note that unlike the geometric quantities such as the quantum metric tensor and Christoffel symbols, this quantity depends on the spatial gradient of the Bloch states as well, and thus encodes information about the spatial profile of the Bloch states.

Modified canonical commutation relation

We saw before that band projected operators have modified commutation relations, for instance the commutator between projected position operators is in fact the Berry curvature, whereas their un-projected counterparts commute with each other. Let us now discuss how the commutation relation between the projected position and canonical momentum is modified, where the un-projected position and canonical momentum satisfy the canonical commutation relation $[\hat{r}_i, \hat{p}_j] = \delta_{ij}$. Recall that we showed the canonical momentum may be written as $\hat{\boldsymbol{p}} = \hat{\boldsymbol{k}} - \mathcal{A}^r$, and thus we have

$$[\hat{r}_{i\mathcal{B}}, \hat{p}_{j\mathcal{B}}] = \mathrm{i}\mathbb{1}_{\mathcal{B}}\delta_{ij} - \mathrm{i}[\hat{\nabla}_i, \hat{\mathcal{A}}^r_{j\mathcal{B}}]. \tag{3.4.9}$$

This shows that the projected position and momentum no longer form a canonical pair. We may express this in terms of the mixed geometric quantity we introduced above. We have

$$[\hat{r}_{i\mathcal{B}}, \hat{p}_{j\mathcal{B}}] = [\hat{r}_i, \hat{p}_j]_{\mathcal{B}} - \left(\hat{r}_i\hat{Q}_N\hat{p}_j - \hat{p}_j\hat{Q}_N\hat{r}_i\right)_{\mathcal{B}} \tag{3.4.10}$$

$$= \mathrm{i}\hat{P}_{\mathcal{B}}\delta_{ij} - \left(\hat{\mathcal{L}}_{ij} - \hat{\mathcal{L}}^\dagger_{ij}\right), \tag{3.4.11}$$

from which we have that

$$[\hat{\nabla}_i, \hat{\mathcal{A}}^r_{j\mathcal{B}}] = \frac{1}{\mathrm{i}}\left(\hat{\mathcal{L}}_{ij} - \hat{\mathcal{L}}^\dagger_{ij}\right). \tag{3.4.12}$$

Note this is manifestly Hermitian.

Higher mixed geometric quantities

Consider now the quantity $\left(\hat{r}_i\hat{r}_j\hat{Q}_{\mathcal{B}}\hat{p}_k\right)_{\mathcal{B}}$. We have that

$$\left(\hat{r}_i\hat{r}_j\hat{Q}_{\mathcal{B}}\hat{p}_k\right)_{\mathcal{B}} = \hat{r}_{i\mathcal{B}}\left(\hat{r}_j\hat{Q}_{\mathcal{B}}\hat{p}_k\right)_{\mathcal{B}} + \left(\hat{r}_i\hat{Q}_{\mathcal{B}}\hat{r}_j\hat{Q}_{\mathcal{B}}\hat{p}_k\right)_{\mathcal{B}} \equiv \mathrm{i}\hat{\nabla}_i\hat{\mathcal{L}}_{jk} + \hat{\Lambda}_{ijk}, \tag{3.4.13}$$

where $\hat{\Lambda}_{ijk} \equiv \left(\hat{r}_i\hat{Q}_{\mathcal{B}}\hat{r}_j\hat{Q}_{\mathcal{B}}\hat{p}_k\right)_{\mathcal{B}} = \left([\hat{r}_i, \hat{Q}_{\mathcal{B}}]\hat{r}_j\hat{Q}_{\mathcal{B}}[\hat{p}_k, \hat{P}_{\mathcal{B}}]\right)_{\mathcal{B}}$, and we used $\hat{r}_{i\mathcal{B}} = \mathrm{i}\hat{\nabla}_i$. Note that by symmetry we have

$$\hat{\Lambda}_{ijk} - \hat{\Lambda}_{jik} = -\mathrm{i}\left(\hat{\nabla}_i\hat{\mathcal{L}}_{jk} - \hat{\nabla}_j\hat{\mathcal{L}}_{ik}\right). \tag{3.4.14}$$

In fact we have

$$\begin{aligned}
\hat{\Lambda}_{ijk} &= \left([\hat{r}_i, \hat{Q}_{\mathcal{B}}]\hat{r}_j\hat{Q}_{\mathcal{B}}[\hat{p}_k, \hat{P}_{\mathcal{B}}]\right)_{\mathcal{B}} && (3.4.15)\\
&= \left([[\hat{r}_i, \hat{Q}_{\mathcal{B}}], \hat{r}_j]\hat{Q}_{\mathcal{B}}[\hat{p}_k, \hat{P}_{\mathcal{B}}]\right)_{\mathcal{B}} + \left([\hat{r}_i, \hat{Q}_{\mathcal{B}}]\hat{Q}_{\mathcal{B}}\hat{r}_j\hat{Q}_{\mathcal{B}}[\hat{p}_k, \hat{P}_{\mathcal{B}}]\right)_{\mathcal{B}} && (3.4.16)\\
&= \left([\hat{r}_j, [\hat{r}_i, \hat{P}_{\mathcal{B}}]]\hat{Q}_{\mathcal{B}}[\hat{p}_k, \hat{P}_{\mathcal{B}}]\right)_{\mathcal{B}} - \left(\hat{r}_j\hat{P}_{\mathcal{B}}[\hat{r}_i, \hat{P}_{\mathcal{B}}]\hat{Q}_{\mathcal{B}}[\hat{p}_k, \hat{P}_{\mathcal{B}}]\right)_{\mathcal{B}} && (3.4.17)\\
&= \hat{\mathcal{L}}^{(2)}_{ijk} + i\hat{\nabla}_j\hat{\mathcal{L}}_{ik}, && (3.4.18)
\end{aligned}$$

where we introduced a geometric quantity $\hat{\mathcal{L}}^{(2)}_{ijk} \equiv \left([\hat{r}_j, [\hat{r}_i, \hat{P}_{\mathcal{B}}]]\hat{Q}_{\mathcal{B}}[\hat{p}_k, \hat{P}_{\mathcal{B}}]\right)_{\mathcal{B}}$, which is symmetric in ij and local in momentum space. Substituting this back in Eq. (3.4.13), we have

$$\left(\hat{r}_i\hat{r}_j\hat{Q}_{\mathcal{B}}\hat{p}_k\right)_{\mathcal{B}} = \hat{\mathcal{L}}^{(2)}_{ijk} + i\hat{\nabla}_i\hat{\mathcal{L}}_{jk} + i\hat{\nabla}_j\hat{\mathcal{L}}_{ik}, \tag{3.4.19}$$

which is manifestly ij symmetric as it should.

Name	Definition
Covariant derivative	$\hat{\nabla}_j \equiv -\mathrm{i}\hat{r}_{j\mathcal{B}}$
Quantum geometric tensor	$\hat{\mathcal{Q}}^{(2)}_{jk} = -([\hat{r}_j, \hat{P}_{\mathcal{B}}]\hat{Q}_{\mathcal{B}}[\hat{r}_k, \hat{P}_{\mathcal{B}}])_{\mathcal{B}}$
Mixed geometric tensor 1	$\hat{\mathcal{L}}_{jk} \equiv -([\hat{r}_j, \hat{P}_{\mathcal{B}}][\hat{p}_k, \hat{P}_{\mathcal{B}}])_{\mathcal{B}}$
Mixed geometric tensor 2	$\hat{\mathcal{L}}^{(2)}_{jkl} \equiv ([\hat{r}_k, [\hat{r}_j, \hat{P}_{\mathcal{B}}]]\hat{Q}_{\mathcal{B}}[\hat{p}_l, \hat{P}_{\mathcal{B}}])_{\mathcal{B}}$

Table 3.1. A table of the operator forms of geometric quantities.

3.5 Semi-classical equation of motion

3.5.1 Bloch electron in external fields

Having understood how the operator form of the geometric quantities appear from the projected product of position operators, we would now study how the geometric quantities modify the motion of a Bloch electron. Previous works [12, 86, 90] have shown that in the presence of in-homogeneous electric fields, there would be additional geometric contributions to the semi-classical equations of motion, besides the well known Berry curvature related

anomalous velocity. We shall now apply our operator formalism to study the effective electron dynamics, where not only we do not need to rely on any specific wave-packet construction, but we shall also consider the case of in-homogeneous magnetic fields.

For this, consider a particle with charge q and mass m moving in a lattice potential in the presence of an applied electromagnetic field. The free lattice Hamiltonian is simply $\hat{H}_0 = \hat{\boldsymbol{p}}^2/(2m) + V(\hat{\boldsymbol{r}})$, where $V(\hat{\boldsymbol{r}}) = V(\hat{\boldsymbol{r}} + \boldsymbol{R})$ is the background lattice potential invariant under lattice translation by a lattice vector $\boldsymbol{R}$. The eigenstates of the lattice are the Bloch states $|\psi_{n\boldsymbol{k}}\rangle$, which satisfy $\hat{H}_0 |\psi_{n\boldsymbol{k}}\rangle = \mathcal{E}_{n\boldsymbol{k}} |\psi_{n\boldsymbol{k}}\rangle$. They form a complete basis of the Hilbert space, so that we have the resolution of identity $\mathbb{1} = \sum_{n\boldsymbol{k}} |\psi_{n\boldsymbol{k}}\rangle \langle\psi_{n\boldsymbol{k}}|$ and $\hat{H}_0$ in this basis is decomposed as $\hat{H}_0 = \sum_{n\boldsymbol{k}} \mathcal{E}_{n\boldsymbol{k}} |\psi_{n\boldsymbol{k}}\rangle \langle\psi_{n\boldsymbol{k}}|$. We now apply an external electromagnetic field, which are assumed to be, but may otherwise have spatial inhomogeneity. The Bloch Hamiltonian coupled to this external field is of textbook type

$$\hat{H} = \frac{\hat{\boldsymbol{\pi}}^2}{2m} + q\phi(\hat{\boldsymbol{r}}) + V(\hat{\boldsymbol{r}}) = \hat{H}_0 + U(\hat{\boldsymbol{p}}, \hat{\boldsymbol{r}}). \tag{3.5.1}$$

The kinetic momentum $\hat{\boldsymbol{\pi}} = \hat{\boldsymbol{p}} - q\boldsymbol{A}(\hat{\boldsymbol{r}})$ is gauge invariant under a gauge transformation of the electromagnetic potentials: $\boldsymbol{A} \to \boldsymbol{A} - \nabla_r \chi, \phi \to \phi + \partial_t \chi$. We may divide the external perturbations into electric, diamagnetic and paramagnetic terms as

$$U(\hat{\boldsymbol{p}}, \hat{\boldsymbol{r}}) = U_\phi(\hat{\boldsymbol{r}}) + U_{\text{dia}}(\hat{\boldsymbol{r}}) + U_{\text{para}}(\hat{\boldsymbol{p}}, \hat{\boldsymbol{r}}). \tag{3.5.2}$$

The electric field is given by the static electrostatic potential $U_\phi(\hat{\boldsymbol{r}}) = q\phi(\hat{\boldsymbol{r}})$, and has been considered previously in [86, 90], and we shall see that our operator approach reproduces the results indeed. The vector potential gives rise to both the diamagnetic terms $U_{\text{dia}}(\hat{\boldsymbol{r}}) = q^2\boldsymbol{A}(\hat{\boldsymbol{r}})^2/(2m)$, and the paramagnetic contribution $U_{\text{para}}(\hat{\boldsymbol{p}}, \hat{\boldsymbol{r}}) = -q(\boldsymbol{A}(\hat{\boldsymbol{r}}) \cdot \hat{\boldsymbol{p}} + \hat{\boldsymbol{p}} \cdot \boldsymbol{A}(\hat{\boldsymbol{r}}))/(2m)$. Note that since $\hat{\boldsymbol{r}}$ does not commute with $\hat{\boldsymbol{p}}$, the order of the coupling between $\boldsymbol{A}(\hat{\boldsymbol{r}})$ and $\hat{\boldsymbol{p}}$ matters. Since the electromagnetic fields are static, we choose a gauge in which the potentials are time-independent, and thus external fields are given by

$$\boldsymbol{B}(\hat{\boldsymbol{r}}) = \partial_{\hat{\boldsymbol{r}}} \times \boldsymbol{A}(\hat{\boldsymbol{r}}), \quad \boldsymbol{E}(\hat{\boldsymbol{r}}) = -\partial_{\hat{\boldsymbol{r}}}\phi(\hat{\boldsymbol{r}}). \tag{3.5.3}$$

We consider applied electromagnetic fields that act as external probes to the low-energy physics of the lattice system, and thus the field strength is assumed to be weak, where $U(\hat{\boldsymbol{p}}, \hat{\boldsymbol{r}})$ can be taken as a perturbation to the Bloch electrons. More specifically, the field strength is assumed to be smaller than the relevant band gaps, and thus it is natural to neglect the matrix elements of the perturbing term between the high-lying bands. For exam-

ple, in the case of band metals under the influence of a weak driving field, where the Fermi intersects a set of partially filled bands, the conduction bands, we may only need to consider the contributions from the conduction bands. Similarly, in the case of insulators, where the band gap between the valence conduction band is much larger than the applied fields, so that few excitations into the valence band are driven by the perturbing field, the effective physics can be entirely phrased in terms of the fully occupied bands. This is actually the same line of reasoning as the lowest Landau level projection in the quantum Hall effect [44].

Such a restriction of observables onto a subspace might be formally effected by the projection operator, which, however, as we discussed in the previous section, has nontrivial effects. Indeed, we saw there that the band-projected operators, which represent the low energy effective observables, have modified commutation relations, and this leads to the quantum geometric quantities. For example, we showed that the projected position operators $\hat{r}_{j\mathcal{B}}$ ($j = x, y, z$) no longer commute with each other, and the correction is exactly the Berry curvature operator: $[\hat{r}_{j\mathcal{B}}, \hat{r}_{k\mathcal{B}}] = \mathrm{i}\hat{\Omega}_{jk}$. This is a key observation from which we shall show that such modified operator algebra gives rise to the geometric contributions to the electron dynamics in the presence of perturbing fields.

3.5.2 Projected dynamics

Here we recall the definition of projection operator and its complement:

$$\hat{P}_{\mathcal{B}} = \sum_{n\in\mathcal{N}_{\mathcal{B}}} \sum_{\boldsymbol{k}} |\psi_{n\boldsymbol{k}}\rangle \langle\psi_{n\boldsymbol{k}}| , \quad \hat{Q}_{\mathcal{B}} = \mathbb{1} - \hat{P}_{\mathcal{B}}, \tag{3.5.4}$$

where $\mathcal{N}_{\mathcal{B}}$ denotes a subset of bands that are relevant for low-energy physics, and a band-projected operator is denoted as $\hat{O}_{\mathcal{B}} = \hat{P}_{\mathcal{B}}\hat{O}\hat{P}_{\mathcal{B}}$. Note that the projection operator $\hat{P}_{\mathcal{B}}$ and its complement $\hat{Q}_{\mathcal{B}}$ are invariant under a band-dependent gauge transformation of the Bloch states $|\psi_{n\boldsymbol{k}}\rangle \to e^{\mathrm{i}\phi_n(\boldsymbol{k})} |\psi_{n\boldsymbol{k}}\rangle$.

Consider a general observable $\hat{O}$ in the Heisenberg picture, whose expectation value in an arbitrary state within the projected Hilbert space is $O_{\mathcal{B}}(t) = \langle\psi_{\mathcal{B}}| \hat{O}_{\mathcal{B}}(t) |\psi_{\mathcal{B}}\rangle$. Using Heisenberg's equation of motion, the dynamics of the observable is given by

$$\mathrm{i}\dot{O}_B(t) = \langle\psi_{\mathcal{B}}| [\hat{O}_{\mathcal{B}}(t), \hat{H}] |\psi_{\mathcal{B}}\rangle = \langle\psi_{\mathcal{B}}| [\hat{O}_{\mathcal{B}}(t), \hat{H}_{\mathcal{B}}] |\psi_{\mathcal{B}}\rangle , \tag{3.5.5}$$

where we assume that the observable $\hat{O}$ does not explicitly depend on time. Crucially, the effective dynamics requires not projecting the commutator only, and in particular we need

the projected Hamiltonian, whose matrix elements are restricted to be within the effective subspace. Physically, we may say that the effective dynamics of a projected operator is governed by an effective Hamiltonian $\hat{H}_{\mathcal{B}}$, which is a cutoff version of the full Hamiltonian. The same effective Heisenberg equations of motion can also be derived using the Feshbach formalism of perturbation theory [108, 109], truncated to first order in the perturbation. See also Appendix A.7. Since the state is completely arbitrary, we only need to consider the operator equation

$$\dot{\hat{O}}_{\mathcal{B}} = -\mathrm{i}[\hat{O}_{\mathcal{B}}, \hat{H}_{\mathcal{B}}] = \hat{P}_{\mathcal{B}}(\mathrm{d}\hat{O}_{\mathcal{B}}/\mathrm{d}t)\hat{P}_{\mathcal{B}}, , \tag{3.5.6}$$

where the second equality follows from $\mathrm{d}\hat{O}_{\mathcal{B}}/\mathrm{d}t = -\mathrm{i}[\hat{O}_{\mathcal{B}}, \hat{H}]$.

Momentum dynamics: force equation

We shall now study the dynamics of the projected position and momentum. From now on and throughout the text, we shall use the Einstein summation convention, where repeated indices are summed. Let us first discuss the "force" equation, the dynamics of the momentum. Note that any band-diagonal operator (i.e., operators that have the decomposition $\hat{O} = \sum_{n\boldsymbol{k}} O_{n\boldsymbol{k}} |\psi_{n\boldsymbol{k}}\rangle \langle\psi_{n\boldsymbol{k}}|$ in the Bloch basis) commutes with the projection operator. Trivially, this includes the Bloch momentum operator $\hat{\boldsymbol{k}}$ itself, defined as $\hat{\boldsymbol{k}} = \sum_{n\boldsymbol{k}} \boldsymbol{k} |\psi_{n\boldsymbol{k}}\rangle \langle\psi_{n\boldsymbol{k}}|$ and thus we have $\hat{P}_{\mathcal{B}}\hat{\boldsymbol{k}}\hat{P}_{\mathcal{B}} = \hat{P}_{\mathcal{B}}\hat{\boldsymbol{k}} = \hat{\boldsymbol{k}}\hat{P}_{\mathcal{B}}$. Therefore, the projected dynamics of the crystal momentum is simply

$$\mathrm{i}\left(\dot{\hat{k}}_{i\mathcal{B}}\right)_{\mathcal{B}} = [\hat{P}_{\mathcal{B}}\hat{k}_i\hat{P}_{\mathcal{B}}, \hat{P}_{\mathcal{B}}\hat{H}\hat{P}_{\mathcal{B}}] = \hat{P}_{\mathcal{B}}[\hat{k}_i, \hat{H}]\hat{P}_{\mathcal{B}}, \tag{3.5.7}$$

where $\hat{H} = \frac{\hat{\boldsymbol{\pi}}^2}{2m} + q\phi(\hat{\boldsymbol{r}}) + V(\hat{\boldsymbol{r}})$. It is easy to show on the Bloch basis that $[\hat{\boldsymbol{k}}, \hat{H}_0] = 0$, which is simply the statement that the Bloch momentum is conserved in the absence of an external field and feels no force due to the lattice potential alone. For simplicity let us use the Coulomb gauge, for now, where we have $\nabla_{\boldsymbol{r}} \cdot \boldsymbol{A}(\boldsymbol{r}) = 0$. It is easy to show that this implies the vector potential commutes with the canonical momentum $\hat{\boldsymbol{p}}$, and the equation

of motion of the crystal momentum read

$$\dot{\hat{k}}_{i\mathcal{B}} = \frac{1}{\mathrm{i}}\hat{P}_{\mathcal{B}}[\hat{k}_i, U(\hat{\boldsymbol{p}}, \hat{\boldsymbol{r}})]\hat{P}_{\mathcal{B}} \tag{3.5.8}$$

$$= \frac{1}{\mathrm{i}}\hat{P}_{\mathcal{B}}[\hat{k}_i, q\phi(\hat{\boldsymbol{r}}) - \frac{q\boldsymbol{A}(\hat{\boldsymbol{r}})\cdot\boldsymbol{p}}{m} + \frac{q^2\boldsymbol{A}^2(\hat{\boldsymbol{r}})}{2m}]\hat{P}_{\mathcal{B}} \tag{3.5.9}$$

$$= -q\left(\partial_{r_i}\phi(\hat{\boldsymbol{r}})\right)_{\mathcal{B}} + \frac{q}{m}\left((\partial_{r_i}\boldsymbol{A})\cdot(\hat{\boldsymbol{p}} - q\boldsymbol{A})\right)_{\mathcal{B}} \tag{3.5.10}$$

$$= qE_{i\mathcal{B}}(\hat{\boldsymbol{r}}) + \frac{q}{m}\left(\partial_{r_i}\boldsymbol{A}\cdot\hat{\boldsymbol{\pi}}\right)_{\mathcal{B}} \tag{3.5.11}$$

$$= qE_{i\mathcal{B}}(\hat{\boldsymbol{r}}) + \frac{q}{m}\left([\partial_{\hat{r}_i}, A_j(\hat{\boldsymbol{r}})]\,\hat{\pi}_j\right)_{\mathcal{B}}, \tag{3.5.12}$$

where we used $[\hat{k}_i, f(\hat{\boldsymbol{r}})] = -i\,[\partial_{\hat{r}_i}, f(\hat{\boldsymbol{r}})]$. Note that while the first term is clearly the Coulomb force due to the electric field, the Lorentz force does not really show up in the force equation. In fact, when a magnetic field is applied, the suitable quantity to consider is not the crystal momentum $\hat{\boldsymbol{k}}$. From classical mechanics, we know that the interaction between charged particles and the magnetic field is introduced via the minimal coupling between the canonical momentum $\boldsymbol{p}$ and the vector gauge potential $\boldsymbol{A}$. However, the canonical momentum $\boldsymbol{p}$ is a gauge-dependent quantity that is not invariant under a transformation of the electromagnetic potentials $\boldsymbol{A} \to \boldsymbol{A} - \nabla_{\boldsymbol{r}}\chi$, and is not an observable itself without gauge fixing. The gauge-invariant dynamical variable is the kinematic momentum $\boldsymbol{\pi} = \boldsymbol{p} - q\boldsymbol{A}(\boldsymbol{r})$. Similarly in the case of Bloch electrons, the crystal momentum is not gauge invariant either, and while the kinematic momentum $\hat{\boldsymbol{\pi}}$ is gauge-invariant, it feels a physically irrelevant lattice force due to the lattice potential, even in the absence of external perturbation. The existence of this lattice force simply means that the canonical momentum is not a conserved quantity due to the breaking of full translation invariance. A gauge-invariant observable more suited for studying the Bloch electron dynamics is the crystal kinematic momentum $\hat{\boldsymbol{\kappa}} \equiv \hat{\boldsymbol{k}} - q\boldsymbol{A}(\hat{\boldsymbol{r}})$. It is straightforward to show that $[\hat{\kappa}_i, \hat{\kappa}_j] = \mathrm{i}q\epsilon_{ijk}B_k(\hat{r})$, and thus the (un-projected) equation of motion of the crystal kinematic momentum is

$$\dot{\hat{\boldsymbol{\kappa}}} = \frac{q}{2}\left(\hat{\boldsymbol{\pi}}\times\boldsymbol{B}(\hat{r}) - \boldsymbol{B}\times\hat{\boldsymbol{\pi}}(\hat{r}) + 2\boldsymbol{E}\right). \tag{3.5.13}$$

The first and second terms are precisely the Lorentz force, and this operator equation is exact and gauge-independent. Note that the gauge-invariant $\boldsymbol{\pi}$ (and not $\dot{\hat{\boldsymbol{r}}}$) appears in the Lorentz force terms. This equation does not hold strictly for the projected dynamics of the gauge-invariant crystal momentum $\hat{\boldsymbol{\kappa}}$, but to the lowest order in the physical electromagnetic

field we can still take as approximation:

$$\dot{\hat{\boldsymbol{\kappa}}}_{\mathcal{B}} \approx q\boldsymbol{E}_{\mathcal{B}}(\hat{\boldsymbol{r}}) + \frac{q}{2m}\left(\hat{\boldsymbol{\pi}} \times \boldsymbol{B}(\hat{\boldsymbol{r}}) - \boldsymbol{B}(\hat{\boldsymbol{r}}) \times \hat{\boldsymbol{\pi}}\right)_{\mathcal{B}}. \tag{3.5.14}$$

Position dynamics

Let us now consider the projected dynamics of the position operator. Using the identity $\mathbb{1} = \hat{P}_{\mathcal{B}} + \hat{Q}_{\mathcal{B}}$, we have

$$\begin{aligned}
\dot{\hat{\boldsymbol{r}}}_{\mathcal{B}} &= -\mathrm{i}[\hat{\boldsymbol{r}}_{\mathcal{B}}, \hat{H}_{\mathcal{B}}] && (3.5.15)\\
&= -\mathrm{i}\left([\hat{\boldsymbol{r}}, (\mathbb{1} - \hat{Q}_{\mathcal{B}})\hat{H}]\right)_{\mathcal{B}} && (3.5.16)\\
&= \frac{\hat{\boldsymbol{\pi}}_{\mathcal{B}}}{m} + \mathrm{i}\left(\hat{\boldsymbol{r}}\hat{Q}_{\mathcal{B}}U(\hat{\boldsymbol{p}}, \hat{\boldsymbol{r}}) - U(\hat{\boldsymbol{p}}, \hat{\boldsymbol{r}})\hat{Q}_{\mathcal{B}}\hat{\boldsymbol{r}}\right)_{\mathcal{B}}, && (3.5.17)\\
& && (3.5.18)
\end{aligned}$$

where we used $-\mathrm{i}\,[\hat{\boldsymbol{r}}, \hat{H}] = \hat{\boldsymbol{\pi}}$, and $\hat{Q}_{\mathcal{B}}\hat{H}_0\hat{P}_{\mathcal{B}} = 0$. Here we see that the projected dynamics contains the term

$$\begin{aligned}
\dot{\hat{\boldsymbol{r}}}_{\perp} &\equiv \mathrm{i}\left(\hat{\boldsymbol{r}}\hat{Q}_{\mathcal{B}}U(\hat{\boldsymbol{p}}, \hat{\boldsymbol{r}}) - U(\hat{\boldsymbol{p}}, \hat{\boldsymbol{r}})\hat{Q}_{\mathcal{B}}\hat{\boldsymbol{r}}\right)_{\mathcal{B}} && (3.5.19)\\
&= \mathrm{i}\,[\hat{\boldsymbol{r}} - \hat{\boldsymbol{r}}_{\mathcal{B}}, U(\hat{\boldsymbol{p}}, \hat{\boldsymbol{r}})]_{\mathcal{B}}, && (3.5.20)
\end{aligned}$$

which involves matrix elements of the perturbation between the projected and un-projected bands, and thus we shall call it the inter-band velocity, while $\hat{\boldsymbol{\pi}}_{\mathcal{B}}$ the intra-band velocity. and in particular this correction vanishes without projection, namely $\dot{\hat{\boldsymbol{r}}}_{\perp} = 0$ if $\mathcal{B} = \mathcal{H}$. Physically, the inter-band velocity capture effects due to virtual scatterings between the set of low-energy bands $\mathcal{B}$ and the high-lying states, and thus this correction is a purely quantum mechanical effect. Often the inter-band velocity is neglected, and we see this is an approximation $\dot{\hat{\boldsymbol{r}}}_{\mathcal{B}} \approx \hat{\boldsymbol{\pi}}_{\mathcal{B}}/m$, justified when the transition amplitudes between the projected subspace and its complement are suppressed due to band baps. However, for example, in systems where the highest-occupied bands have point crossings to the empty valence band, such as the Weyl semi-metal, the inter-band velocity cannot be ignored, and this is the reason that the Berry curvature induced anomalous velocity must be taken into account in studying the Weyl systems. As we shall demonstrate below, more generally all the quantum geometric contributions to the equation of motion can be understood as such multi-band effects that are captured by the inter-band velocity term.

3.5.3 Inhomogeneous electric field and geometry

In the above, we derived the inter-band velocity in the projected dynamics that corrects the equations of motion, while in the previous section, we discussed how the geometric quantities appear from the projected product of position and momentum operators. We shall now demonstrate explicitly that this is exactly how the quantum geometric contributions to the equations of motion emerge.

Let us first consider the electric field case, where the external perturbation includes only the electrostatic potential: $U(\hat{\boldsymbol{p}}, \hat{\boldsymbol{r}}) = U_\phi(\hat{\boldsymbol{r}})$. Then the projected equation of motion reads

$$\dot{\hat{\boldsymbol{r}}}_{\mathcal{B}} = \frac{\hat{\boldsymbol{p}}_{\mathcal{B}}}{m} + \dot{\hat{\boldsymbol{r}}}_{\perp}, \tag{3.5.21}$$

where the intra-band contribution is simply the projected velocity operator $\hat{\boldsymbol{v}}_{\mathcal{B}}$, which reduces to the familiar group velocity in the single band case as we discussed in the previous section. The inter-band velocity reads

$$\dot{\hat{r}}_{j\perp} = -\frac{q}{\mathrm{i}}\left(\hat{r}_j\hat{Q}_{\mathcal{B}}\phi(\hat{\boldsymbol{r}}) - \phi(\hat{\boldsymbol{r}})\hat{Q}_{\mathcal{B}}\hat{r}_j\right)_{\mathcal{B}} = \frac{q}{\mathrm{i}}[\hat{r}_{j\mathcal{B}}, \phi_{\mathcal{B}}(\hat{\boldsymbol{r}})]. \tag{3.5.22}$$

We shall now show the fundamental result that the inter-band velocity may be expressed as the sum of quantum geometric contributions:

$$\dot{\hat{r}}_{j\perp} = -\frac{q}{2}\{\hat{\Omega}_{jk}, E_{k\mathcal{B}}(\hat{\boldsymbol{r}})\} + \hat{R}_{j\perp}, \tag{3.5.23}$$

where the first term involving the Berry curvature tensor $\hat{\Omega}_{ij}$ is exactly the operator form of the anomalous velocity. Recall the force equation Eq. (3.5.14), which in the electric field case is actually exact, and reads

$$\dot{\boldsymbol{k}}_{\mathcal{B}} = q\boldsymbol{E}_{\mathcal{B}}(\hat{\boldsymbol{r}}). \tag{3.5.24}$$

Then the anomalous velocity can be written as $-\dot{\boldsymbol{k}}_{\mathcal{B}} \times \hat{\boldsymbol{\Omega}}$, where $(\hat{\boldsymbol{\Omega}})_i \equiv \epsilon_{ijk}\hat{\Omega}_{jk}$. While the anomalous velocity is rather well known in the solid state community[34, 147, 164], we see that there is actually an additional term $\hat{R}^{\phi}_{i\perp}$, which includes the contributions due to geometric quantities other than the Berry curvature which arise because of the spatial in-homogeneity of the electric field. Note that $\phi_{\mathcal{B}}(\hat{\boldsymbol{r}}) \neq \phi(\hat{\boldsymbol{r}}_{\mathcal{B}})$ except for a uniform electric field, where only the anomalous velocity term would appear. For a non-uniform electric field, however, even if one makes the approximation $\phi_{\mathcal{B}}(\hat{\boldsymbol{r}}) \approx \tilde{\phi}(\hat{\boldsymbol{r}}_{\mathcal{B}})$, where $\tilde{\phi}(\hat{\boldsymbol{r}}_{\mathcal{B}})$ has the position operators symmetrized so as to remain hermitian, the other geometric contributions would

still appear in addition to the anomalous velocity.

Let us now calculate explicitly the geometric contributions. Assume that the field configuration is such that it is centered around a reference point $\boldsymbol{r}_0$, and varies slowly enough around it. In application, the physically more relevant choice of the reference point might be the center of mass of a wave-packet $\boldsymbol{r}_c(t) = \langle \hat{\boldsymbol{r}}(t) \rangle$, but for our purpose of demonstrating the origin of the geometric contributions, let us for simplicity take it to be the origin. In Appendix A.6, we shall show that the expansion around the center of mass position can be organized in terms of cumulants, instead of moments of position operators, which however, presents no further difficulties otherwise. Then in this case, we may take the gradient expansion

$$\phi(\hat{\boldsymbol{r}}) \approx -E_i^{(0)} \hat{r}_i - \frac{1}{2!} E_{ij}^{(1)} \hat{r}_i \hat{r}_j - \frac{1}{3!} E_{ijk}^{(2)} \hat{r}_i \hat{r}_j \hat{r}_k, \tag{3.5.25}$$

or in terms of the electric field

$$E_i(\hat{\boldsymbol{r}}) \approx E_i^{(0)} + \frac{1}{2!} E_{ij}^{(1)} \hat{r}_j + \frac{1}{3!} E_{ijk}^{(2)} \hat{r}_j \hat{r}_k, \tag{3.5.26}$$

Substituting the expansion into Eq. (3.5.22), we have to first order the inter-band velocity is $\dot{\hat{r}}_{i\perp} = \mathrm{i} q E_j^{(0)} [\hat{r}_{i\mathcal{B}}, \hat{r}_{j\mathcal{B}}] = -q E_j^{(0)} \hat{\Omega}_{ij}$, which we recognize as precisely the anomalous velocity given by a uniform electric field $\boldsymbol{E}(\hat{\boldsymbol{r}}) = \boldsymbol{E}^{(0)}$. However, for a spatially in-homogeneous field, additional geometric contributions emerge. Consider the second order expansion of the scalar potential $\phi(\hat{\boldsymbol{r}}) = -\frac{1}{2!} E_{ij}^{(1)} \hat{r}_i \hat{r}_j$, corresponding to the the electric field being $E_i(\hat{\boldsymbol{r}}) = E_{ij}^{(1)} \hat{r}_j$. We showed in the previous section that $(\hat{r}_i \hat{r}_j)_{\mathcal{B}} = \{\hat{r}_{i\mathcal{B}}, \hat{r}_{j\mathcal{B}}\} + \hat{\mathcal{G}}_{ij}$, where $\hat{\mathcal{G}}_{ij}$ is the quantum metric tensor. Using this we have that

$$\mathrm{i}\dot{\hat{r}}_{i\perp} = [\hat{r}_{i\mathcal{B}}, q\phi_{\mathcal{B}}(\hat{\boldsymbol{r}})] = -\frac{q}{2} E_{jk}^{(1)} [\hat{r}_{i\mathcal{B}}, (\hat{r}_j \hat{r}_k)_{\mathcal{B}}] \tag{3.5.27}$$

$$= -\frac{q}{2} E_{jk}^{(1)} \left(\frac{1}{2} \mathrm{i} \{\hat{\Omega}_{ij}, \hat{r}_{k\mathcal{B}}\} + \frac{1}{2} \mathrm{i} \{\hat{\Omega}_{ik}, \hat{r}_{j\mathcal{B}}\} + [\hat{r}_{i\mathcal{B}}, \hat{\mathcal{G}}_{jk}] \right) \tag{3.5.28}$$

$$= -\mathrm{i} \frac{q}{4} \left(\{\hat{\Omega}_{ij}, E_{j\mathcal{B}}(\hat{\boldsymbol{r}})\} + \{\hat{\Omega}_{ik}, E_{k\mathcal{B}}(\hat{\boldsymbol{r}})\} \right) - \frac{q}{2} E_{jk}^{(1)} [\hat{r}_{i\mathcal{B}}, \hat{\mathcal{G}}_{jk}] \tag{3.5.29}$$

$$= -\mathrm{i} \frac{q}{2} \{\hat{\Omega}_{ij}, E_{j\mathcal{B}}(\hat{\boldsymbol{r}})\} - \frac{q}{2} E_{jk}^{(1)} [\hat{r}_{i\mathcal{B}}, \hat{\mathcal{G}}_{jk}], \tag{3.5.30}$$

or in terms of the covariant derivative $\hat{\nabla}_j = \frac{1}{\mathrm{i}} \hat{r}_{j\mathcal{B}}$,

$$\dot{\hat{r}}_{i\perp} = -\frac{q}{2} \{\hat{\Omega}_{ij}, E_{j\mathcal{B}}(\hat{\boldsymbol{r}})\} - \frac{q}{2} E_{jk}^{(1)} [\hat{\nabla}_i, \hat{\mathcal{G}}_{jk}]. \tag{3.5.31}$$

We see that indeed there is a new geometric contribution in addition to the anomalous velocity that emerges, which depends on the quantum metric tensor $\hat{\mathcal{G}}_{jk}$, thus establishing our assertion above. The same terms have been obtained using a wave-packet approach in [90] and [86], whereas our operator equation not only reproduces their result, but also presents the generalization to the multi-band case. By using higher order expansion, it can be shown that such a decomposition of the inter-band velocity into the sum of a Berry curvature induced anomalous velocity and additional geometric terms would continue to hold, and our operator formalism is able to systematically study them in an arbitrary order.

3.5.4 Magnetic field

In the above we showed how the geometric quantities appear in the inter-band velocity using our operator formalism, for electric fields. We shall now apply the formalism to an inhomogeneous magnetic field. Except for assuming the gauge potentials to be static, we leave the gauge un-fixed otherwise. The Hamiltonian in a magnetic field is $\hat{H} = \hat{\boldsymbol{\pi}}^2/2m + V(\hat{\boldsymbol{r}}) = \hat{H}_0 + U(\hat{\boldsymbol{r}}, \hat{\boldsymbol{p}})$, where the perturbation is the sum of the diamagnetic and paramagnetic term $U(\hat{\boldsymbol{r}}, \hat{\boldsymbol{p}}) = U_{\text{dia}}(\hat{\boldsymbol{r}}) + U_{\text{para}}(\hat{\boldsymbol{p}}, \hat{\boldsymbol{r}})$, with

$$U_{\text{dia}}(\hat{\boldsymbol{r}}) = \frac{q^2}{2m}\boldsymbol{A}(\hat{\boldsymbol{r}})^2 \tag{3.5.32}$$

$$U_{\text{para}}(\hat{\boldsymbol{p}}, \hat{\boldsymbol{r}}) = -\frac{q}{2m}(\boldsymbol{A}(\hat{\boldsymbol{r}}) \cdot \hat{\boldsymbol{p}} + \hat{\boldsymbol{p}} \cdot \boldsymbol{A}(\hat{\boldsymbol{r}})). \tag{3.5.33}$$

The projected dynamics of the position operator then reads

$$\frac{\mathrm{d}}{\mathrm{d}t}\hat{\boldsymbol{r}}_{\mathcal{B}} = -\mathrm{i}\left[\hat{\boldsymbol{r}}_{\mathcal{B}}, \hat{H}_{\mathcal{B}}\right] \tag{3.5.34}$$

$$= \frac{\hat{\boldsymbol{\pi}}_{\mathcal{B}}}{m} + \mathrm{i}\left(\hat{\boldsymbol{r}}\hat{Q}_{\mathcal{B}}U(\hat{\boldsymbol{p}}, \hat{\boldsymbol{r}}) - U(\hat{\boldsymbol{p}}, \hat{\boldsymbol{r}})\hat{Q}_{\mathcal{B}}\hat{\boldsymbol{r}}\right)_{\mathcal{B}} \tag{3.5.35}$$

$$= \frac{\hat{\boldsymbol{\pi}}_{\mathcal{B}}}{m} + \dot{\hat{\boldsymbol{r}}}_{\perp}, \tag{3.5.36}$$

where again $\left(\hat{Q}_{\mathcal{B}}\hat{H}_0\right)_{\mathcal{B}} = 0$ is used to obtain the second equality. As we commented earlier, the first, intra-band term is the gauge-invariant kinematic momentum.

The diamagnetic contribution to the inter-band velocity can be dealt with in the similar way as the electric field case with the only modification being replacing the scalar potential

$\phi(\hat{\boldsymbol{r}})$ by $(\boldsymbol{A}(\hat{\boldsymbol{r}}))^2$, which explicitly reads

$$\mathrm{i}\dot{\hat{r}}^{\mathrm{dia}}_{j\perp} = \frac{q^2}{2m}[\hat{r}_{j\mathcal{B}}, (A_k(\hat{\boldsymbol{r}})A_k(\hat{\boldsymbol{r}}))_{\mathcal{B}}] \tag{3.5.37}$$

$$= \frac{q^2}{2m}\left(\{[\hat{r}_{j\mathcal{B}}, A_{k\mathcal{B}}(\hat{\boldsymbol{r}})], A_{k\mathcal{B}}(\hat{\boldsymbol{r}})\} + [\hat{r}_{j\mathcal{B}}, \left(A_k(\hat{\boldsymbol{r}})\hat{Q}_{\mathcal{B}}A_k(\hat{\boldsymbol{r}})\right)_{\mathcal{B}}]\right). \tag{3.5.38}$$

The paramagnetic contribution is more involved. Rather than directly considering the inter-band velocity, for the calculation it would prove helpful to include the paramagnetic contribution at first. Thus we consider projected dynamics

$$\mathrm{i}\dot{\hat{r}}^{\mathrm{para}}_{j} = [\hat{r}_{j\mathcal{B}}, U_{\mathrm{para}}(\hat{\boldsymbol{p}}, \hat{\boldsymbol{r}})] \tag{3.5.39}$$

$$= -\frac{q}{2m}[\hat{r}_{j\mathcal{B}}, (\{A_k(\hat{\boldsymbol{r}}), \hat{p}_k\})_{\mathcal{B}}] \tag{3.5.40}$$

$$= -\frac{q}{2m}\left([\hat{r}_{j\mathcal{B}}, \{A_{k\mathcal{B}}(\hat{\boldsymbol{r}}), \hat{p}_{k\mathcal{B}}\}] + [\hat{r}_{j\mathcal{B}}, \left(A_k(\hat{\boldsymbol{r}})\hat{Q}_{\mathcal{B}}\hat{p}_k + \hat{p}_k\hat{Q}_{\mathcal{B}}A_k(\hat{\boldsymbol{r}})\right)_{\mathcal{B}}]\right) \tag{3.5.41}$$

$$= -\frac{q}{2m}\left(\{[\hat{r}_{j\mathcal{B}}, \hat{p}_{k\mathcal{B}}], A_{k\mathcal{B}}(\hat{\boldsymbol{r}})\} + \{[\hat{r}_{j\mathcal{B}}, A_{k\mathcal{B}}(\hat{\boldsymbol{r}})], \hat{p}_{k\mathcal{B}}\} + [\hat{r}_{j\mathcal{B}}, \left(A_k(\hat{\boldsymbol{r}})\hat{Q}_{\mathcal{B}}\hat{p}_k + \hat{p}_k\hat{Q}_{\mathcal{B}}A_k(\hat{\boldsymbol{r}})\right)_{\mathcal{B}}]\right), \tag{3.5.42}$$

where in the third line we inserted the identity $\mathbb{1} = \hat{P}_{\mathcal{B}} + \hat{Q}_{\mathcal{B}}$. Note that in contrast to the electric field case previously considered, the projected dynamics due to a magnetic field is more complicated, where the projected canonical momentum and position operators no longer satisfy the canonical commutation relation, but rather Eq. (3.4.9) , $[\hat{r}_{i\mathcal{B}}, \hat{p}_{j\mathcal{B}}] = \mathrm{i}\mathbb{1}_{\mathcal{B}}\delta_{ij} - \mathrm{i}[\hat{\nabla}_i, \hat{\mathcal{A}}^r_{j\mathcal{B}}]$. Note the paramagnetic intra-band velocity is $-\mathrm{i}\frac{q}{m}A_{j\mathcal{B}}(\hat{\boldsymbol{r}})$, after subtracting it from the first term in the bracket, and using the modified commutation relation, we obtain the para-magnetic inter-band velocity

$$\mathrm{i}\dot{\hat{r}}^{\mathrm{para}}_{j\perp} = -\frac{q}{2m}\left(-\{[\hat{r}_{j\mathcal{B}}, \hat{\mathcal{A}}^r_{k\mathcal{B}}], A_{k\mathcal{B}}(\hat{\boldsymbol{r}})\} + \{[\hat{r}_{j\mathcal{B}}, A_{k\mathcal{B}}(\hat{\boldsymbol{r}})], \hat{p}_{k\mathcal{B}}\} + [\hat{r}_{j\mathcal{B}}, \left(A_k(\hat{\boldsymbol{r}})\hat{Q}_{\mathcal{B}}\hat{p}_k + \hat{p}_k\hat{Q}_{\mathcal{B}}A_k(\hat{\boldsymbol{r}})\right)_{\mathcal{B}}]\right) \tag{3.5.43}$$

Let us comment on the origin of these terms. The last two terms arise for the reason as the inter-velocity in the electric field case considered previously, due to the non-commutativity of the projected position operators. On the other hand, the first term involving the real space Berry connection emerges due to the modified canonical commutation, where by Eq. (3.4.9) receives a correction, and we expect it to give new contributions to the dynamics involving the mixed geometric quantities that we discussed in the previous section.

Gradient expansion

Combining the diamagnetic and paramagnetic contributions, we obtain that the inter-band velocity in a magnetic field reads

$$\mathrm{i}\dot{\hat{r}}_{j\perp} = -\frac{q}{2m}\left(-\{[\hat{r}_{j\mathcal{B}}, \hat{\mathcal{A}}^r_{k\mathcal{B}}], A_{k\mathcal{B}}(\hat{\boldsymbol{r}})\} + \{[\hat{r}_{j\mathcal{B}}, A_{k\mathcal{B}}(\hat{\boldsymbol{r}})], \hat{\pi}_{k\mathcal{B}}\} + [\hat{r}_{j\mathcal{B}}, \left(A_k(\hat{\boldsymbol{r}})\hat{Q}_{\mathcal{B}}p_k + p_k\hat{Q}_{\mathcal{B}}A_k(\hat{\boldsymbol{r}})\right)_{\mathcal{B}}]\right) \tag{3.5.44}$$

$$+\frac{q^2}{2m}\left([\hat{r}_{j\mathcal{B}}, \left(A_k(\hat{\boldsymbol{r}})\hat{Q}_{\mathcal{B}}A_k(\hat{\boldsymbol{r}})\right)_{\mathcal{B}}]\right). \tag{3.5.45}$$

To bring about the geometric contributions, we expand the magnetic vector potential as in the electric case, with $A_i(\hat{\boldsymbol{r}}) = A^{(1)}_{ij}\hat{r}_j + \frac{1}{2}A^{(2)}_{ijk}\hat{r}_j\hat{r}_k$, where the corresponding magnetic field is given by $\boldsymbol{B}(\boldsymbol{r}) = \nabla_{\boldsymbol{r}} \times \boldsymbol{A}(\boldsymbol{r})$.

Substituting in the first order gradient expansion, we obtain

$$\begin{aligned}\dot{\hat{r}}^{(1)}_{l\perp} &= \mathrm{i}A^{(1)}_{jk}\frac{q}{m}\left(\{\hat{\nabla}_k, [\hat{\nabla}_l, \hat{\mathcal{A}}^r_{j\mathcal{B}}]\} + \{\hat{\Omega}_{lk}, \hat{\pi}_{j\mathcal{B}}\} - [\hat{\nabla}_l, \hat{\mathcal{L}}_{jk}]\right) \\ &\quad + \frac{q^2}{2m}A^{(1)}_{ka}A^{(1)}_{kb}[\hat{\nabla}_l, \hat{\mathcal{Q}}^{(2)}_{ab}] \qquad (3.5.46)\\ &= \mathrm{i}A^{(1)}_{jk}\frac{q}{m}\left(\{\hat{\nabla}_k, [\hat{\nabla}_l, \hat{\mathcal{A}}^r_{j\mathcal{B}}]\} + \{\hat{\Omega}_{lk}, \hat{\pi}_{j\mathcal{B}}\} - [\hat{\nabla}_l, \hat{\mathcal{L}}_{jk}]\right) \\ &\quad + \frac{q^2}{2m}A^{(1)}_{ka}A^{(1)}_{kb}[\hat{\nabla}_l, \hat{\mathcal{G}}_{ab}], \qquad (3.5.47)\end{aligned}$$

where $\hat{\mathcal{Q}}^{(2)}_{ab}$ is the quantum geometric tensor, and in arriving at the second equality, we used that a and b are dummy variables to re-write the last term due to diamagnetic contribution in a manifestly Hermitian form. We may identify the second term in the parenthesis is precisely the anomalous velocity term, with the force equation of $\dot{\boldsymbol{k}}_{\mathcal{B}}$ evaluated to the same order. The other two terms are new geometric contributions, involving both the real space Berry connection $\hat{\mathcal{A}}^r_{j\mathcal{B}}$ as well as the mixed geometric tensor $\hat{\mathcal{L}}_{jk}$, where we recall the latter has matrix elements $\mathcal{L}_{jk,nm}(\boldsymbol{q}) = \mathrm{i}\langle u_{n\boldsymbol{q}}|\left(\partial_{q_j}\hat{Q}_{\boldsymbol{q}\mathcal{B}}\right)\hat{Q}_{\boldsymbol{q}\mathcal{B}}\hat{\mathcal{A}}^r_{k\boldsymbol{q}}|u_{m\boldsymbol{q}}\rangle$. This implies that in the magnetic field case, in contrast to the electric field case, the spatial variation of the Bloch states, i.e. the real space profile, also contributes to the projected dynamics.

Some calculations give, to second order in the gradient expansion,

$$\dot{\hat{r}}^{(2)}_{i\perp} = \frac{+q}{2m} A^{(2)}_{jkl}\{[\hat{\nabla}_i, \hat{\mathcal{A}}^r_{j\mathcal{B}}], (\hat{r}_k\hat{r}_l)_{\mathcal{B}}\} - \frac{q}{2m} A^{(2)}_{jkl}\{[\hat{\nabla}_{i\mathcal{B}}, (\hat{r}_k\hat{r}_l)_{\mathcal{B}}], p_{j\mathcal{B}}\}$$
$$- \frac{q}{2m} A^{(2)}_{jkl}\Big([\hat{\nabla}_i, \mathrm{i}(\hat{\mathcal{L}}_{lj} + \hat{\mathcal{L}}^\dagger_{lj})\hat{\nabla}_k + \mathrm{i}(\hat{\mathcal{L}}_{kj} + \hat{\mathcal{L}}^\dagger_{kj})\hat{\nabla}_l + i[\hat{\nabla}_k, \hat{\mathcal{L}}_{lj}] + i[\hat{\nabla}_l, \hat{\mathcal{L}}_{kj}]] + [\hat{\nabla}_i, \hat{\mathcal{L}}^{(2)}_{klj} + \hat{\mathcal{L}}^{(2)\dagger}_{klj}]\Big), \tag{3.5.48}$$

where in arriving at the second line we used

$$\mathrm{i}\hat{\nabla}_k\hat{\mathcal{L}}_{lj} + \mathrm{i}\hat{\mathcal{L}}^\dagger_{lj}\hat{\nabla}_k = i(\hat{\mathcal{L}}_{lj} + \hat{\mathcal{L}}^\dagger_{lj})\hat{\nabla}_k + i[\hat{\nabla}_k, \hat{\mathcal{L}}_{lj}]. \tag{3.5.49}$$

We may also identify the anomalous velocity from the second term using

$$(\hat{r}_k\hat{r}_l)_{\mathcal{B}} = \hat{r}^{(2)}_{kl,\mathcal{B}} = \mathrm{i}^2\left(\frac{1}{2}\{\hat{\nabla}_k, \hat{\nabla}_l\} - \hat{\mathcal{G}}_{kl}\right), \tag{3.5.50}$$

where $\hat{\mathcal{G}}_{kl}$ is the quantum metric tensor.

3.5.5 Wave-packet dynamics

In the above, we have identified the inter-band velocity that arises from using the projected dynamics as the source of the geometric contributions. The discussion has been done on the level operators, and no reference to specific states has been made, with the only assumption being that the projected dynamics provides an effective low-energy description of Bloch electrons in the presence of a weak perturbing field. To make contact with the standard semi-classical approach, as well as for applications to transport, in this section we shall apply the results to the semi-classical dynamics of wave-packets.

Consider a wave-packet that is initially prepared by a superposition of states in the projected subspace, but otherwise of arbitrary shape. In Schrodinger picture, we may than write $|W(0)\rangle = \sum_{n\in\mathcal{N}_\mathcal{B}} \int_{\mathrm{BZ}} d\boldsymbol{q}\, c_{n\boldsymbol{q}}(0)\,|\psi_{n\boldsymbol{q}}\rangle$. The evolution of the state is encoded in the coefficients $c_{n\boldsymbol{k}}(t)$, namely

$$|W(t)\rangle = \sum_n \int_{\mathrm{BZ}} d\boldsymbol{q}\; c_{n\boldsymbol{q}}(t)\,|\psi_{n\boldsymbol{q}}\rangle\,, \tag{3.5.51}$$

subject to the normalization condition

$$\langle W(t)|W(t)\rangle = \sum_n \int d\boldsymbol{q}|c_{n\boldsymbol{q}}(t)|^2 = 1. \tag{3.5.52}$$

Note that the band summation is not restricted, for as the wave-packet evolves, in the absence of special symmetry which leads to certain selection rules, the coefficients $c_{n\boldsymbol{k}}(t)$ for which $n \notin \mathcal{N}_\mathcal{B}$ may develop to be non-zero, even if we prepared the wave-packet initially in the projected subspace. However, as we argued in the beginning of Section 3.5.2, when the perturbing field is weak enough, those matrix elements are suppressed by the band baps, and we may then assume only $c_{n\boldsymbol{k}}(t)$ with $n \in \mathcal{N}_\mathcal{B}$ are non-vanishing, so that the wave-packet remains within the projected subspace: $\hat{P}_\mathcal{B} |W(t)\rangle = |W(t)\rangle$, and evolves with the effective Hamiltonian $\hat{H}_\mathcal{B}$. The solution of the state evolution, namely integrating the Schrodinger equation to determine $c_{n\boldsymbol{k}}(t)$ is a separate question, and we taken them to be given.

Previously, the dynamics was discussed in the Heisenberg picture, which was more suitable there since we were working with operators. Transforming to the Schrodinger picture, we note that the dynamics of an observable $O(t) \equiv \langle\psi| \hat{O}(t) |\psi\rangle$ in the Heisenberg picture can be equivalently written as $\mathrm{i}dO(t)/dt = \langle\psi(t)| [\hat{O}, \hat{H}] |\psi(t)\rangle$ [131], where the Heisenberg state $|W\rangle = |W(0)\rangle$ is obtained from the Schrodinger state using the evolution operator $|W(t)\rangle = \hat{U}(t,0) |W\rangle$, and $\hat{O}(t) = \hat{U}^\dagger(t,0)\hat{O}\hat{U}(t,0)$. It is easy to see that the same holds for the projected dynamics, where thus our earlier operator form of the equations of motion Eq. (3.5.5) is translated to

$$\dot{O}_\mathcal{B} = -\mathrm{i} \langle W(t)| [\hat{O}_\mathcal{B}, \hat{H}_\mathcal{B}] |W(t)\rangle .$$

In particular, applying this to the center of mass and the gauge-invariant crystal momentum, we have

$$\begin{aligned} \dot{\boldsymbol{R}} &= -\mathrm{i} \langle W(t)| [\hat{\boldsymbol{r}}_\mathcal{B}, \hat{H}_\mathcal{B}] |W(t)\rangle , \\ \dot{\boldsymbol{K}} &= -\mathrm{i} \langle W(t)| [\hat{\boldsymbol{\kappa}}_\mathcal{B}, \hat{H}_\mathcal{B}] |W(t)\rangle . \end{aligned} \tag{3.5.53}$$

The geometric contributions to the semi-classical wave-packet motion in the presence of an in-homogeneous electric field has been reported previously, see for instance [86, 90, 147], and we shall consider only the magnetic field here. As in the operator approach, we expand the magnetic vector potential around a reference point, taken for simplicity to be origin, so that $A_j(\hat{\boldsymbol{r}}) \approx A^{(1)}_{jk} \hat{r}_k + \frac{1}{2} A^{(2)}_{jkl} \hat{r}_k \hat{r}_l$, and the inter-band velocity are correspondingly expanded as $\dot{r}_{j\perp} = \dot{r}^{(1)}_{j\perp} + \dot{r}^{(2)}_{j\perp} + \ldots$, with each term given by the respective term in the expansion of A_j.

Concretely, let us consider a band metal, in which the Fermi level lies within a non-degenerate band, so that we may use the single band approximation. In this scenario, the projection

operator is simply $\hat{P}_{\mathcal{B}} = \sum_{\boldsymbol{k}} |\psi_{n\boldsymbol{k}}\rangle \langle\psi_{n\boldsymbol{k}}|$, with n denoting the conduction band that intersects the Fermi level. To leading order in magnetic field, the inter-band velocity reads

$$\dot{r}_{l\perp}^{(1)} = \mathrm{i}A_{jk}^{(1)} \frac{q}{m} \left\langle\!\!\left\langle R_k(\boldsymbol{q},t) \frac{\partial \mathcal{A}^r_{j\mathcal{B}}(\boldsymbol{q})}{\partial q_l} + \Omega_{lk}(\boldsymbol{q})\pi_j(\boldsymbol{q}) - \frac{\partial \mathcal{L}_{jk}(\boldsymbol{q})}{\partial q_l} \right\rangle\!\!\right\rangle, \tag{3.5.54}$$

where the double angle bracket is defined as the the weighted average $\langle\langle ... \rangle\rangle \equiv \int_{\mathrm{BZ}} d\boldsymbol{q} c^\dagger_{\boldsymbol{q}}(t) ... c_{\boldsymbol{q}}(t)$. Here $R_j(\boldsymbol{q},t)$ is the instantaneous center-of-mass position of the wave-packet, which as we show in the appendix explicitly reads

$$\langle W|\, \hat{r}_j(t)\, |W\rangle = \langle\langle R_j(\boldsymbol{q},t)\rangle\rangle = \int d\boldsymbol{q} R_j(\boldsymbol{q},t) |c_{\boldsymbol{q}}(t)|^2, \tag{3.5.55}$$

where $R_j(\boldsymbol{q},t) \equiv \mathrm{i}\partial_{q_j}\theta(\boldsymbol{q},t) + \mathcal{A}_j(\boldsymbol{q})$, and $\theta(\boldsymbol{q},t)$ is the phase of the expansion coefficient $c_{\boldsymbol{q}}(t) = |c_{\boldsymbol{q}}(t)| e^{-\mathrm{i}\theta(\boldsymbol{q},t)}$. The last term is of special interest, since as we shall demonstrate in the following, is a Fermi surface contribution, which gives rise to a magnetization current density.

Recall that in the Boltzmann theory of transport, the semi-classical equations of motion are used for calculating the density current[11], and we now discuss the possible transport signatures of the geometric contributions. In the Boltzmann theory, the current density is given by

$$\boldsymbol{J}(\boldsymbol{r}) = \int \frac{d\boldsymbol{k}}{(2\pi)^3} \dot{\boldsymbol{R}}(\boldsymbol{k}) f(\boldsymbol{k},\boldsymbol{r},t), \tag{3.5.56}$$

where $\boldsymbol{R}(\boldsymbol{k})$ is the center of motion of a state with momentum $\boldsymbol{k}$, and $f(\boldsymbol{k},\boldsymbol{r},t)$ the distribution function. In the ballistic regime, the mean free path l is much larger than the lattice spacing, and by the Heisenberg uncertainty principle, we may then take the momentum width of the typical wave-packets to be narrow, so that the wave-packet may be approximately taken to be sharply peaked at a single momentum. A net current may then arise when system is driven to a non-equilibrium state, where the distribution $f(\boldsymbol{k},\boldsymbol{r},t)$ differs from the equilibrium Fermi-Dirac distribution. There is a second scenario, where the semi-classical equations has additional corrections to the group velocity, and a net currents might appear even using the equilibrium distribution as approximation. One well known example of the second case is the Berry curvature induced anomalous velocity term, which has been extensively studied in a wide range of contexts, such as the intrinsic anomalous Hall effect [105]. See also the second part of the thesis, where we discuss this effect in the topological Weyl semimetal. To isolate the geometric effects, we would then assume that the external field is weak enough and an equilibrium distribution can be taken as approximation. Therefore, at zero

temperature, we take $f(\boldsymbol{K}, t) \approx \Theta[\epsilon_{FS} - \epsilon_n(\boldsymbol{K})]$, where ϵ_{FS} is the Fermi energy. In the sharp momentum approximation, we may take $|c_{\boldsymbol{q}}|^2 \approx \delta(\boldsymbol{q} - \boldsymbol{K})$, where $\boldsymbol{K}(t) = \langle W(t)| \hat{\boldsymbol{\kappa}} |W(t)\rangle$ is the mean gauge-invariant crystal momentum of the wave-packet. Consider the last term in semi-classical equation of motion Eq. (3.5.54). Substituting this in the Boltzmann equation, we see that the last term involving the mixed geometric tensor gives rise to a geometric contribution the current density, which reads

$$J_l = -\mathrm{i} A^{(1)}_{jk} \frac{q}{m} \oint_{\mathrm{FS}} \frac{dS}{|\nabla_{\boldsymbol{K}} \epsilon(\boldsymbol{K})|} \frac{\partial \epsilon(\boldsymbol{K})}{\partial K_l} \mathcal{L}_{jk}(\boldsymbol{K}), \tag{3.5.57}$$

where the integration is over the Fermi surface given by $\epsilon_{FS} = \epsilon_n(\boldsymbol{k})$. This shall be understood as a magnetization current: integrated over space it sums up to be zero, and thus inducing no net current. This is physically reasonable, for to this order of the gradient expansion, we have a uniform magnetic field.

3.6 Summary

In Part I of this thesis, we studied the quantum geometric contributions to the dynamics of electrons in crystalline solids. We began with a review of the geometry of quantum states in general, where we discussed the concept of quantum geometric tensor whose real and imaginary component are the quantum metric tensor and the Berry curvature respectively. We showed that these geometric quantities encode information about the electronic wavefunctions. Following the general review, we specialized to Bloch states as the background where such geometric quantities naturally arise from band theory.

A central contribution of this part is the development of an operator formalism of quantum geometric quantities, which was then applied to understand the geometric contributions to the semiclassical electron dynamics of Bloch electrons. We provided the operator forms of the quantum geometric quantities, and how they emerge from the decomposition of projected product of position and momentum operators. In this way, we also demonstrated that band projection onto a subset of energy bands significantly alters the commutation relations among position and momentum operators, and the resultant nontrivial commutation relations between projected operators is the source of the quantum geometric corrections to the semiclassical equations of motion. Using this formalism, we studied the effective dynamics of crystal electrons in the presence of inhomogeneous electromagnetic fields. Beside reproducing and extending previous results in operator form, we also studied the hitherto unexplored case of magnetic fields. We found that we also need to consider the projected canonical momentum, where a dual concept of Berry connection, which we call real space Berry connection also merges, and leads to further geometric quantities that depend on the spatial modulation of Bloch states as well.

Appendix for Part I

A.1 Poisson summation formula

One of the crucial step of the calculations in the Bloch basis is to exploit the lattice translation invariance of the Bloch states, and turn certain integrals over the entire volume into a sum of integrals over only one unit cell. This relies on the Poisson summation formula.

A:Lattice Poisson formula

We shall show that, in the thermodynamic limit where the number of lattice sites $N \to \infty$, we have

$$\frac{1}{N}\sum_{\boldsymbol{R}_i} e^{-i\boldsymbol{k}\cdot\boldsymbol{R}_i} = \sum_{\boldsymbol{G}_i} \delta_{\boldsymbol{k},\boldsymbol{G}_i} \tag{A.1.1}$$

where $\boldsymbol{R}_i$ and $\boldsymbol{G}_i$ are $d-$dimensional lattice and reciprocal lattice vectors respectively.

Proof:
We first convert the lattice vector sum into a geometric series by noting we can express the lattice vector and **k** vector as

$$\mathbf{R}_i = \sum n_a \mathbf{a}_a \tag{A.1.2}$$

$$\mathbf{k} = \sum k_a \mathbf{b}_a \tag{A.1.3}$$

where $\mathbf{a}_i$ and $\mathbf{b}_i$ are the basis vectors in the lattice and reciprocal lattice respectively, normal to each other as $\mathbf{a}_i \cdot \mathbf{b}_j = 2\pi\delta_{ij}$, so that $\mathbf{R}_i \cdot \mathbf{k} = \sum n_a k_a$. Since we will take the thermodynamic limit anyway, we may assume, without loss of generality that along a given direction, say the $a-$th, there are $2N_a + 1$ lattice sites (including the origin), then we have the total number number of sites is simply

$$N = (2N_1 + 1)(2N_2 + 1)...(2N_d + 1), \tag{A.1.4}$$

so that

$$\sum_{\boldsymbol{R}_i} = \sum_{n_1=-N_1}^{N_1} \sum_{n_2=-N_2}^{N_2} ... \sum_{n_d=-N_d}^{N_d} . \tag{A.1.5}$$

The left hand-side thus factorizes into a product of geometric series as

$$\frac{1}{N}\sum_{\boldsymbol{R}_i} e^{-i\boldsymbol{k}\cdot\boldsymbol{R}_i} = \frac{1}{(2N_1+1)...(2N_d+1)} \sum_{n_1=-N_1}^{N_1} ... \sum_{n_d=-N_d}^{N_d} e^{-i2\pi n_1 R_1} e^{-i2\pi n_2 R_2} ... e^{-i2\pi n_d R_d} \tag{A.1.6}$$

$$= \prod_{a=1}^{d} \left(\frac{1}{2N_a+1} \sum_{n_a=-N_a}^{N_a} e^{-i2\pi n_a R_a} \right) \tag{A.1.7}$$

$$= \prod_{a=1}^{d} \frac{\sin\left(\pi k_a (2N_a+1)\right)}{(2N_a+1)\sin \pi k_a}, \tag{A.1.8}$$

where in the last step we used the fact the term above is a geometric series.

Now elementary calculus gives

$$\lim_{x\to 0} \frac{\sin nx}{n \sin x} = 1 \tag{A.1.9}$$

$$\lim_{n\to\infty} \frac{\sin nx}{n \sin x} = 0 \qquad \sin x \neq 0 \tag{A.1.10}$$

thus

$$\lim_{N_a\to\infty} \frac{\sin\left(\pi k_a (2N_a+1)\right)}{(2N_a+1)\sin \pi k_a} = 1 \qquad k_a \in \mathbb{Z} \tag{A.1.11}$$

$$= 0 \qquad \text{otherwise} \tag{A.1.12}$$

But $k_a \in \mathbb{Z}$ is equivalent to $\mathbf{k} = \mathbf{G}_i$ for some reciprocal lattice vector $\mathbf{G}_i$, thus we have proved discrete Poisson summation formula.

B: Continuum

Now we pass on to the continuum approximation, where the discrete crystal momentum is now concinnous, and the Kronecker delta goes to a Dirac delta with a normalization factor $\frac{(2\pi)^d}{V}$, so that

$$\delta_{\mathrm{k},\mathrm{G}_i} \to \frac{(2\pi)^d}{V} \delta^d(\mathbf{k} - \mathbf{G}_i). \tag{A.1.13}$$

Specifically, this means understood as distributions, we have

$$\frac{1}{N}\sum_{\boldsymbol{R}_i} e^{-i\boldsymbol{k}\cdot\boldsymbol{R}_i} = \sum_{\boldsymbol{G}_i} \delta_{\boldsymbol{k},\boldsymbol{G}_i} = \frac{(2\pi)^d}{V}\sum_{\boldsymbol{G}_i} \delta(\boldsymbol{k}-\boldsymbol{G}_i), \tag{A.1.14}$$

where the last term is understood to be always inside an integral with measure $\int d^d k$ (not restricted to one Brillouin zone cell). Note that in the reduced zone scheme, where $\boldsymbol{k}$ is restricted to the first Brillouin zone, the identity reduces to

$$\sum_{\boldsymbol{R}_i} \mathrm{e}^{-\mathrm{i}\boldsymbol{k}\cdot\boldsymbol{R}_i} = \frac{N(2\pi)^d}{V}\delta(\boldsymbol{k}) = \frac{(2\pi)^d}{V_c}\delta(\boldsymbol{k}), \tag{A.1.15}$$

since the only reciprocal lattice vector in the first Brillouin zone is the center $\boldsymbol{G}_0$, chosen to be at the origin . Here $V_c = \frac{V}{N}$ is the volume of one unit cell in the real space.

A.2 Dirac calculus

In the following, we shall show how to compute the matrix elements of various operators in local Bloch basis, we would be dealing with distributions. In those calculations, the order of the placement of derivatives must be carefully taken into account, and here we recall some calculus rules to properly deal with the Dirac delta function.

Lemma

$$\int d\boldsymbol{k}\partial_{\boldsymbol{q}}\Big(\delta(\boldsymbol{q}-\boldsymbol{k})f(\boldsymbol{k})\Big)\partial_{\boldsymbol{k}}\Big(\delta(\boldsymbol{q}-\boldsymbol{k})h(\boldsymbol{p})\Big) \tag{A.2.1}$$

$$\neq \int d\boldsymbol{k}\delta(\boldsymbol{q}-\boldsymbol{k})f(\boldsymbol{k})\partial_{\boldsymbol{q}}\partial_{\boldsymbol{k}}\Big(\delta(\boldsymbol{k}-\boldsymbol{p})h(\boldsymbol{p})\Big) \tag{A.2.2}$$

unless $f(\boldsymbol{k})$ is a constant.

Proof:

To assert the properties of the distributions, we need to act on them a generic test function $g(\boldsymbol{q})$. On the one hand we have that

$$\int d\boldsymbol{q}d\boldsymbol{k}g(\boldsymbol{q})\partial_q\Big(\delta(\boldsymbol{q}-\boldsymbol{k})f(\boldsymbol{k})\Big)\partial_k\Big(\delta(\boldsymbol{k}-\boldsymbol{p})h(\boldsymbol{p})\Big) \tag{A.2.3}$$

$$= -\int d\boldsymbol{q}d\boldsymbol{k}\partial_q\Big(g(\boldsymbol{q})\Big)\delta(\boldsymbol{q}-\boldsymbol{k})f(\boldsymbol{k})\partial_k\Big(\delta(\boldsymbol{k}-\boldsymbol{p})h(\boldsymbol{p})\Big) \tag{A.2.4}$$

$$= -\int d\boldsymbol{k}\partial_k(g(\boldsymbol{k})f(\boldsymbol{k}))\partial_k\Big(\delta(\boldsymbol{k}-\boldsymbol{p})h(\boldsymbol{p})\Big) \tag{A.2.5}$$

$$= \int d\boldsymbol{k}\partial_k\Big(\partial_k(g(\boldsymbol{k}))f(\boldsymbol{k})\Big)\delta(\boldsymbol{k}-\boldsymbol{p})h(\boldsymbol{p}) \tag{A.2.6}$$

$$= \partial_p\Big(\partial_p(g(\boldsymbol{p}))f(\boldsymbol{p})\Big)h(\boldsymbol{p}). \tag{A.2.7}$$

Here the derivatives act on the bracket immediately next to it. On the other hand we have

$$\int d\boldsymbol{q}d\boldsymbol{k}g(\boldsymbol{q})\delta(\boldsymbol{q}-\boldsymbol{k})f(\boldsymbol{k})\partial_k\partial_k\Big(\delta(\boldsymbol{k}-\boldsymbol{p})h(\boldsymbol{p})\Big) \tag{A.2.8}$$

$$= \int d\boldsymbol{k}g(\boldsymbol{k})f(\boldsymbol{k})\partial_k\partial_k\Big(\delta(\boldsymbol{k}-\boldsymbol{p})h(\boldsymbol{p})\Big) \tag{A.2.9}$$

$$= \int d\boldsymbol{k}\partial_k\partial_k\Big(g(\boldsymbol{k})f(\boldsymbol{k})\Big)\delta(\boldsymbol{k}-\boldsymbol{p})h(\boldsymbol{p}) \tag{A.2.10}$$

$$= \partial_p\partial_p\Big(g(\boldsymbol{p})f(\boldsymbol{p})\Big)h(\boldsymbol{p}). \tag{A.2.11}$$

Indeed, we see when f is a constant the two equations equal, while otherwise they do not agree. We can also obtain as a corollary, via induction that

Corollary

$$\int d\boldsymbol{k}e^{\boldsymbol{a}\cdot\partial_q}\Big(\delta(\boldsymbol{q}-\boldsymbol{k})f(\boldsymbol{k})\Big)e^{\boldsymbol{b}\cdot\partial_k}\Big(\delta(\boldsymbol{k}-\boldsymbol{p})h(\boldsymbol{p})\Big) \tag{A.2.12}$$

$$\neq \int d\boldsymbol{k}\delta(\boldsymbol{q}-\boldsymbol{k})f(\boldsymbol{k})e^{(\boldsymbol{a}+\boldsymbol{b})\cdot\partial_k}\Big(\delta(\boldsymbol{k}-\boldsymbol{p})h(\boldsymbol{p})\Big) \tag{A.2.13}$$

unless f is a constant. Note the second form is symmetric in $\boldsymbol{a}$ and $\boldsymbol{b}$. In fact, this generalization is the reason why band projection leads to non-commutativity, and thus non-trivial dynamics.

A.3 Moment generating operators

Here we compute the matrix elements of the projected moment generating function $\left(\mathrm{e}^{-\mathrm{i}\boldsymbol{a}\cdot\hat{\boldsymbol{r}}}\right)_{\mathcal{B}}$ in the Bloch basis. Assuming $n, m \in \mathcal{B}$, we have, upon inserting $\mathbb{1} = \int d\boldsymbol{r}\, |\boldsymbol{r}\rangle \langle \boldsymbol{r}|$,

$$
\begin{aligned}
&\langle \psi_{n\boldsymbol{q}}|\, \mathrm{e}^{-\mathrm{i}\boldsymbol{a}\cdot\hat{\boldsymbol{r}}}\, |\psi_{m\boldsymbol{k}}\rangle \\
=&\int d\boldsymbol{r} \mathrm{e}^{\mathrm{i}(\boldsymbol{k}-\boldsymbol{q}-\boldsymbol{a})\cdot\hat{\boldsymbol{r}}} \langle u_{n\boldsymbol{q}}|\boldsymbol{r}\rangle \langle \boldsymbol{r}|u_{m\boldsymbol{k}}\rangle \\
=&\int d\boldsymbol{r} \mathrm{e}^{\boldsymbol{a}\cdot\boldsymbol{\partial}_{\boldsymbol{q}}} \left(\mathrm{e}^{\mathrm{i}(\boldsymbol{k}-\boldsymbol{q})\cdot\hat{\boldsymbol{r}}}\right) \langle u_{n\boldsymbol{q}}|\boldsymbol{r}\rangle \langle \boldsymbol{r}|u_{m\boldsymbol{k}}\rangle \\
=&\sum_{\boldsymbol{R}_j} \int_{cell} d\boldsymbol{r} \mathrm{e}^{\boldsymbol{a}\cdot\boldsymbol{\partial}_{\boldsymbol{q}}} \left(\mathrm{e}^{\mathrm{i}(\boldsymbol{k}-\boldsymbol{q})\cdot(\boldsymbol{r}+\boldsymbol{R}_j)}\right) \langle u_{n\boldsymbol{q}}|\boldsymbol{r}+\boldsymbol{R}_j\rangle \langle \boldsymbol{r}+\boldsymbol{R}_j|u_{m\boldsymbol{k}}\rangle \\
=&\sum_{\boldsymbol{R}_j} \int_{cell} d\boldsymbol{r} \mathrm{e}^{\boldsymbol{a}\cdot\boldsymbol{\partial}_{\boldsymbol{q}}} \left(\mathrm{e}^{\mathrm{i}(\boldsymbol{k}-\boldsymbol{q})\cdot(\boldsymbol{r}+\boldsymbol{R}_j)}\right) \langle u_{n\boldsymbol{q}}|\boldsymbol{r}\rangle \langle \boldsymbol{r}|u_{m\boldsymbol{k}}\rangle \\
=&\mathrm{e}^{\boldsymbol{a}\cdot\partial_{\boldsymbol{q}}} \left(\delta(\boldsymbol{k}-\boldsymbol{q})\right) \langle u_{n\boldsymbol{q}}|u_{m\boldsymbol{k}}\rangle \\
=&\langle u_{n\boldsymbol{q}}|\, e^{\boldsymbol{a}\cdot\boldsymbol{\partial}_{\boldsymbol{q}}} \left(\delta(\boldsymbol{k}-\boldsymbol{q})\hat{P}'_{\boldsymbol{k}}\right) e^{\boldsymbol{b}\cdot\boldsymbol{\partial}_{\boldsymbol{k}}} \left(\delta(\boldsymbol{p}-\boldsymbol{k})\, |u_{l\boldsymbol{p}}\rangle\right)
\end{aligned}
\tag{A.3.1}
$$

In the derivation we used the lattice invariance of the Bloch functions: $\langle \boldsymbol{r}+\boldsymbol{R}_j|u_{m\boldsymbol{k}}\rangle = \langle \boldsymbol{r}|u_{m\boldsymbol{k}}\rangle$, and the Poisson summation formula $\sum_{\boldsymbol{R}_j} \mathrm{e}^{\mathrm{i}(\boldsymbol{k}-\boldsymbol{q})\cdot\boldsymbol{R}_j} = \delta(\boldsymbol{k}-\boldsymbol{q})$, for $\boldsymbol{q}, \boldsymbol{k}$ in the first Brillouin zone. We also stress here that the bra-ket between two Bloch functions have the normalization factor $\frac{(2\pi)^d}{V_{uc}}$ included in the definition.

A.4 Moments of position

As shown in the main texts, using the moment generating function $e^{-i\boldsymbol{a}\cdot\hat{\boldsymbol{r}}}$ we may compute the matrix elements of operator quantities such as the moments, as well as the quantum metric tensor, Berry curvature, etc., in a systematic and efficient way, which agree with their more conventional definition of these quantities in the momentum space. We may confirm the results in yet another way, namely by direct calculation. Besides checking the results, we hope to demonstrate the advantage of our operator based approach.

A.4.1 Average position distribution

Let us start with the matrix elements of the position operator. Note that we have the identity in the position basis reads $\mathbb{1} = \int d\boldsymbol{r}\, |\boldsymbol{r}\rangle \langle \boldsymbol{r}|$, where $d\boldsymbol{r} \equiv d^d r$ and the integration range is over the entire volume V. Inserting this, we have

$$\langle \psi_{n\boldsymbol{q}}| \hat{r}_i |\psi_{m\boldsymbol{k}}\rangle \tag{A.4.1}$$
$$= \int d\boldsymbol{r}\, r_i e^{i\boldsymbol{r}\cdot(\boldsymbol{k}-\boldsymbol{q})} u^*_{n\boldsymbol{q}}(\boldsymbol{r}) u_{m\boldsymbol{k}}(\boldsymbol{r}) \tag{A.4.2}$$
$$= \int d\boldsymbol{r} \left(i\partial_{q_i} e^{i\boldsymbol{r}\cdot(\boldsymbol{k}-\boldsymbol{q})}\right) u_{n\boldsymbol{q}}(\boldsymbol{r}) u_{m\boldsymbol{k}}(\boldsymbol{r}) \tag{A.4.3}$$
$$= i\partial_{q_i} \int d\boldsymbol{r} \left(e^{i\boldsymbol{r}\cdot(\boldsymbol{k}-\boldsymbol{q})} u^*_{n\boldsymbol{q}}(\boldsymbol{r}) u_{m\boldsymbol{k}}(\boldsymbol{r})\right) - i \int d\boldsymbol{r} e^{i\boldsymbol{r}\cdot(\boldsymbol{k}-\boldsymbol{q})} \partial_{q_i} \left(u^*_{n\boldsymbol{q}}(\boldsymbol{r}) u_{m\boldsymbol{k}}(\boldsymbol{r})\right) \tag{A.4.4}$$
$$= i\partial_{q_i} \langle \psi_{n\boldsymbol{q}} | \psi_{n,\boldsymbol{k}}\rangle - i \sum_{\boldsymbol{R}} e^{i\boldsymbol{R}\cdot(\boldsymbol{k}-\boldsymbol{q})} \int_{cell} d\boldsymbol{r} e^{i\boldsymbol{r}\cdot(\boldsymbol{k}-\boldsymbol{q})} \partial_{q_i} \left(u^*_{n\boldsymbol{q}}(\boldsymbol{r}) u_{m\boldsymbol{k}}(\boldsymbol{r})\right) \tag{A.4.5}$$
$$= \delta_{nm} i\partial_{q_i} \delta(\boldsymbol{q}-\boldsymbol{k}) - \delta(\boldsymbol{q}-\boldsymbol{k}) i \frac{(2\pi)^d}{V_{uc}} \int d\boldsymbol{r}\, u_{m\boldsymbol{q}}(\boldsymbol{r}) \partial_{q_i} u^*_{n\boldsymbol{q}}(\boldsymbol{r}) \tag{A.4.6}$$
$$= \delta_{nm} i\partial_{q_i} \delta(\boldsymbol{q}-\boldsymbol{k}) + \delta(\boldsymbol{q}-\boldsymbol{k}) i \frac{(2\pi)^d}{V_{uc}} \int_{cell} d\boldsymbol{r}\, u^*_{n\boldsymbol{q}}(\boldsymbol{r}) \partial_{q_i} u_{m\boldsymbol{q}}(\boldsymbol{r}) \tag{A.4.7}$$
$$= \delta_{nm} i\partial_{q_i} \delta(\boldsymbol{q}-\boldsymbol{k}) + \delta(\boldsymbol{q}-\boldsymbol{k}) A^i_{nm}(\boldsymbol{q}), \tag{A.4.8}$$

where in going from Eq. (A.4.4) to Eq. (A.4.5) we transformed the integral over the whole volume to one over the unit cells, and the exponential is swapped to a Dirac delta using the Poisson summation formula. Also recall that the Berry connection is defined as

$$A^i_{nm}(\boldsymbol{q}) = i \frac{(2\pi)^d}{v} \int_{cell} d\boldsymbol{r}\, u^*_{n\boldsymbol{q}}(\boldsymbol{r}) \partial_{q_i} u_{m\boldsymbol{q}}(\boldsymbol{r}) = i \langle u_{n\boldsymbol{q}}| \partial_{q_i} |u_{m\boldsymbol{q}}\rangle . \tag{A.4.9}$$

A.4.2 Second moment distribution

We shall now calculate the matrix elements of the quadrupole moments. Exactly the same as in the position operator case, we insert an identity using the position basis, and we have:

$$\langle \psi_{n\boldsymbol{q}} | \, \hat{r}_i \hat{r}_j \, | \psi_{m\boldsymbol{k}} \rangle \tag{A.4.10}$$

$$= \int d\boldsymbol{r} \, r_i r_j \mathrm{e}^{\mathrm{i}\boldsymbol{r}\cdot(\boldsymbol{k}-\boldsymbol{q})} u_{n\boldsymbol{q}}(\boldsymbol{r}) u_{m\boldsymbol{k}}(\boldsymbol{r}) \tag{A.4.11}$$

$$= \int d\boldsymbol{r} \left(\mathrm{i}^2 \partial_{k_i} \partial_{k_j} \mathrm{e}^{\mathrm{i}\boldsymbol{r}\cdot(\boldsymbol{k}-\boldsymbol{q})} \right) u^*_{n\boldsymbol{q}}(\boldsymbol{r}) u_{m\boldsymbol{k}}(\boldsymbol{r}) \tag{A.4.12}$$

$$\begin{aligned} =& \mathrm{i}^2 \partial_{k_i} \partial_{k_j} \int d\boldsymbol{r} \left(\mathrm{e}^{\mathrm{i}\boldsymbol{r}\cdot(\boldsymbol{k}-\boldsymbol{q})} u^*_{n\boldsymbol{q}}(\boldsymbol{r}) u_{m\boldsymbol{k}}(\boldsymbol{r}) \right) - \mathrm{i}^2 \int d\boldsymbol{r} \mathrm{e}^{\mathrm{i}\boldsymbol{r}\cdot(\boldsymbol{k}-\boldsymbol{q})} u^*_{n\boldsymbol{q}}(\boldsymbol{r}) \partial_{k_i} \partial_{q_j} u_{m\boldsymbol{k}}(\boldsymbol{r}) \\ & - \mathrm{i}^2 \int d\boldsymbol{r} \partial_{k_i} \left(\mathrm{e}^{\mathrm{i}\boldsymbol{r}\cdot(\boldsymbol{k}-\boldsymbol{q})} u^*_{n\boldsymbol{q}}(\boldsymbol{r}) \right) \partial_{k_j} u_{m\boldsymbol{k}}(\boldsymbol{r}) - \mathrm{i}^2 \int d\boldsymbol{r} \partial_{k_j} \left(\mathrm{e}^{\mathrm{i}\boldsymbol{r}\cdot(\boldsymbol{k}-\boldsymbol{q})} u^*_{n\boldsymbol{q}}(\boldsymbol{r}) \right) \partial_{k_i} u_{m\boldsymbol{k}}(\boldsymbol{r}) \end{aligned} \tag{A.4.13}$$

$$\begin{aligned} =& \mathrm{i}^2 \partial_{k_i} \partial_{k_j} \int d\boldsymbol{r} \left(\mathrm{e}^{\mathrm{i}\boldsymbol{r}\cdot(\boldsymbol{k}-\boldsymbol{q})} u^*_{n,\boldsymbol{q}}(\boldsymbol{r}) u_{m\boldsymbol{k}}(\boldsymbol{r}) \right) - \mathrm{i}^2 \int d\boldsymbol{r} \mathrm{e}^{\mathrm{i}\boldsymbol{r}\cdot(\boldsymbol{k}-\boldsymbol{q})} u^*_{n,\boldsymbol{q}}(\boldsymbol{r}) \partial_{k_i} \partial_{k_j} u_{m\boldsymbol{k}}(\boldsymbol{r}) \\ & - \mathrm{i}^2 \partial_{k_i} \int d\boldsymbol{r} \mathrm{e}^{\mathrm{i}\boldsymbol{r}\cdot(\boldsymbol{k}-\boldsymbol{q})} u^*_{n\boldsymbol{q}}(\boldsymbol{r}) \partial_{k_j} u_{m\boldsymbol{k}}(\boldsymbol{r}) + \mathrm{i}^2 \int d\boldsymbol{r} \mathrm{e}^{\mathrm{i}\boldsymbol{r}\cdot(\boldsymbol{k}-\boldsymbol{q})} u^*_{n,\boldsymbol{q}}(\boldsymbol{r}) \partial_{k_i} \partial_{k_j} u_{m\boldsymbol{k}}(\boldsymbol{r}) \\ & - \mathrm{i}^2 \partial_{k_j} \int d\boldsymbol{r} \mathrm{e}^{\mathrm{i}\boldsymbol{r}\cdot(\boldsymbol{k}-\boldsymbol{q})} u^*_{n,\boldsymbol{q}}(\boldsymbol{r}) \partial_{k_i} u_{m\boldsymbol{k}}(\boldsymbol{r}) + \mathrm{i}^2 \int d\boldsymbol{r} \mathrm{e}^{\mathrm{i}\boldsymbol{r}\cdot(\boldsymbol{k}-\boldsymbol{q})} u^*_{n\boldsymbol{q}}(\boldsymbol{r}) \partial_{k_i} \partial_{k_j} u_{m\boldsymbol{q}}(\boldsymbol{r}) \end{aligned} \tag{A.4.14}$$

$$\begin{aligned} =& \mathrm{i}^2 \partial_{k_i} \partial_{k_j} \int d\boldsymbol{r} \left(\mathrm{e}^{\mathrm{i}\boldsymbol{r}\cdot(\boldsymbol{k}-\boldsymbol{q})} u^*_{n\boldsymbol{q}}(\boldsymbol{r}) u_{m\boldsymbol{k}}(\boldsymbol{r}) \right) + \mathrm{i}^2 \int d\boldsymbol{r} \mathrm{e}^{\mathrm{i}\boldsymbol{r}\cdot(\boldsymbol{q}-\boldsymbol{q})} u^*_{n\boldsymbol{q}}(\boldsymbol{r}) \partial_{k_i} \partial_{k_j} u_{m\boldsymbol{k}}(\boldsymbol{r}) \\ & - \mathrm{i}^2 \partial_{k_i} \int d\boldsymbol{r} \mathrm{e}^{\mathrm{i}\boldsymbol{r}\cdot(\boldsymbol{k}-\boldsymbol{q})} u^*_{n\boldsymbol{q}}(\boldsymbol{r}) \partial_{k_j} u_{m\boldsymbol{k}}(\boldsymbol{r}) - \mathrm{i}^2 \partial_{k_j} \int d\boldsymbol{r} \mathrm{e}^{\mathrm{i}\boldsymbol{r}\cdot(\boldsymbol{k}-\boldsymbol{q})} u^*_{n\boldsymbol{q}}(\boldsymbol{r}) \partial_{k_i} u_{m\boldsymbol{k}}(\boldsymbol{r}) \end{aligned} \tag{A.4.15}$$

$$\begin{aligned} =& - \partial_{k_i} \partial_{k_j} \int d\boldsymbol{r} \left(\mathrm{e}^{\mathrm{i}\boldsymbol{r}\cdot(\boldsymbol{k}-\boldsymbol{q})} u^*_{n\boldsymbol{q}}(\boldsymbol{r}) u_{m\boldsymbol{k}}(\boldsymbol{r}) \right) - \int d\boldsymbol{r} \mathrm{e}^{\mathrm{i}\boldsymbol{r}\cdot(\boldsymbol{k}-\boldsymbol{q})} u^*_{n\boldsymbol{q}}(\boldsymbol{r}) \partial_{k_i} \partial_{k_j} u_{m\boldsymbol{k}}(\boldsymbol{r}) \\ & - \mathrm{i} \partial_{k_i} \left(\delta(\boldsymbol{q}-\boldsymbol{k}) A^j_{nm}(\boldsymbol{q}) \right) - \mathrm{i} \partial_{k_j} \left(\delta(\boldsymbol{q}-\boldsymbol{k}) A^i_{nm}(\boldsymbol{q}) \right) \end{aligned} \tag{A.4.16}$$

$$= \left(\delta_{nm} \partial_{q_i} \partial_{q_j} - \langle u_{n\boldsymbol{q}} | \, \partial_{q_i} \partial_{q_j} \, | u_{m\boldsymbol{q}} \rangle \right) \delta(\boldsymbol{q}-\boldsymbol{q}) - \mathrm{i} A^j_{nm}(\boldsymbol{q}) \partial_{k_i} \delta(\boldsymbol{q}-\boldsymbol{k}) - \mathrm{i} A^i_{nm}(\boldsymbol{q}) \partial_{k_j} \delta(\boldsymbol{q}-\boldsymbol{k}) \tag{A.4.17}$$

$$= \left(\delta_{nm} \partial_{q_i} \partial_{k_j} - \langle u_{n\boldsymbol{q}} | \, \partial_{q_i} \partial_{q_j} \, | u_{m\boldsymbol{q}} \rangle \right) \delta(\boldsymbol{q}-\boldsymbol{k}) + \mathrm{i} A^j_{nm}(\boldsymbol{q}) \partial_{q_i} \delta(\boldsymbol{q}-\boldsymbol{k}) + \mathrm{i} A^i_{nm}(\boldsymbol{q}) \partial_{q_j} \delta(\boldsymbol{q}-\boldsymbol{k}) \tag{A.4.18}$$

A straightforward, but tedious calculation of $\langle \psi_{n\boldsymbol{q}} | \left(\{ \hat{r}_{i\mathcal{B}}, \hat{r}_{j\mathcal{B}} \} + \mathcal{G}_{ij} \right) | \psi_{n\boldsymbol{q}} \rangle$ will give identical results. Note that the same result will be obtained for any choice of the projected bands, except for when $\hat{P}_{\mathcal{B}} = \mathbb{1}$, which includes the special case of a single band projection: $\hat{P}_{\mathcal{B}} = \sum_{\boldsymbol{k}} |\psi_{n\boldsymbol{k}}\rangle \langle \psi_{n\boldsymbol{k}}|$.

It should be clear that the calculations become very tedious with increasing orders, and while they will give the same results, the method that we develop is much more efficient.

A.5 Real space Berry connection

To derive the real space Berry connection, we compute the matrix elements of canonical $\boldsymbol{p}$ in Bloch states. We have that upon inserting a resolution of identity in terms of the position states,

$$\langle \psi_{n\boldsymbol{q}} | \hat{\boldsymbol{p}} | \psi_{m\boldsymbol{k}} \rangle = -i \int d\boldsymbol{r} e^{-i\boldsymbol{q}\cdot\boldsymbol{r}} u^*_{n\boldsymbol{q}}(\boldsymbol{r}) \partial_{\boldsymbol{r}} \left(e^{i\boldsymbol{k}\cdot\boldsymbol{r}} u_{m\boldsymbol{k}}(\boldsymbol{r}) \right) \tag{A.5.1}$$

$$= \int d\boldsymbol{r} e^{-i(\boldsymbol{q}-\boldsymbol{k})\cdot\boldsymbol{r}} \left(u^*_{n\boldsymbol{q}}(\boldsymbol{r}) \boldsymbol{k} u_{m\boldsymbol{k}}(\boldsymbol{r}) - i u^*_{n\boldsymbol{q}}(\boldsymbol{r}) \partial_{\boldsymbol{r}} u_{m\boldsymbol{k}}(\boldsymbol{r}) i \right) \tag{A.5.2}$$

$$= \sum_{\boldsymbol{R}_i} e^{-i(\boldsymbol{q}-\boldsymbol{k})\cdot\boldsymbol{R}_i} \int_{cell} d\boldsymbol{r} e^{-i(\boldsymbol{q}-\boldsymbol{k})\cdot\boldsymbol{r}} \left(u^*_{n\boldsymbol{q}}(\boldsymbol{r}) \boldsymbol{k} u_{m\boldsymbol{k}}(\boldsymbol{r}) - i u^*_{n\boldsymbol{q}}(\boldsymbol{r}) \partial_{\boldsymbol{r}} u_{m\boldsymbol{k}}(\boldsymbol{r}) i \right) \tag{A.5.3}$$

$$= \frac{(2\pi)^d}{V_{uc}} \delta(\boldsymbol{q}-\boldsymbol{k}) \int_{cell} d\boldsymbol{r} e^{-i(\boldsymbol{q}-\boldsymbol{k})\cdot\boldsymbol{r}} \left(u^*_{n\boldsymbol{q}}(\boldsymbol{r}) \boldsymbol{k} u_{m\boldsymbol{k}}(\boldsymbol{r}) - i u^*_{n\boldsymbol{q}}(\boldsymbol{r}) \partial_{\boldsymbol{r}} u_{m\boldsymbol{k}}(\boldsymbol{r}) i \right) \tag{A.5.4}$$

$$= \frac{(2\pi)^d}{V_{uc}} \delta(\boldsymbol{q}-\boldsymbol{k}) \int_{cell} d\boldsymbol{r} \left(u^*_{n\boldsymbol{q}}(\boldsymbol{r}) \boldsymbol{q} u_{m\boldsymbol{q}}(\boldsymbol{r}) - i u^*_{n\boldsymbol{q}}(\boldsymbol{r}) \partial_{\boldsymbol{r}} u_{m\boldsymbol{q}}(\boldsymbol{r}) i \right) \tag{A.5.5}$$

$$= \boldsymbol{k} \delta(\boldsymbol{q}-\boldsymbol{k}) \delta_{nm} - i \langle u_{n\boldsymbol{q}} | \partial_{\boldsymbol{r}} | u_{m\boldsymbol{q}} \rangle \delta(\boldsymbol{q}-\boldsymbol{k}), \tag{A.5.6}$$

where we used the trick of translating the integral to a cell integral, thus getting a Poisson sum. Also recall that the normalization of $u_{n\boldsymbol{q}}$ over cells is

$$\langle u_{n\boldsymbol{q}} | u_{m\boldsymbol{q}} \rangle = \frac{(2\pi)^d}{V_{uc}} \int_{cell} d\boldsymbol{r} u^*_{n\boldsymbol{q}}(\boldsymbol{r}) \boldsymbol{q} u_{m\boldsymbol{q}}(\boldsymbol{r}) = \delta_{nm}. \tag{A.5.7}$$

We recognize that the second term in the matrix element is a real space Berry connection, which we may denote as

$$\mathcal{A}^r_{nm}(\boldsymbol{q}) = i \langle u_{n\boldsymbol{q}} | \partial_{\boldsymbol{r}} | u_{m\boldsymbol{q}} \rangle \tag{A.5.8}$$

$$\langle \psi_{n\boldsymbol{q}} | \hat{\boldsymbol{p}} | \psi_{m\boldsymbol{k}} \rangle = \boldsymbol{k} \delta(\boldsymbol{q}-\boldsymbol{k}) \delta_{nm} - \mathcal{A}^r_{nm}(\boldsymbol{q}) \delta(\boldsymbol{q}-\boldsymbol{k}) \tag{A.5.9}$$

Here we recall that

$$\langle \psi_{n\boldsymbol{q}} | \hat{\boldsymbol{r}} | \psi_{m\boldsymbol{k}} \rangle = i \partial_{\boldsymbol{k}} \delta(\boldsymbol{q}-\boldsymbol{k}) \delta_{nm} + A_{nm}(\boldsymbol{q}) \delta(\boldsymbol{q}-\boldsymbol{k}) \tag{A.5.10}$$

Despite of the apparent duality, one crucial difference is that the canonical momentum is diagonal in crystal momentum.

A.6 Center of mass operator

We may expand the inhomogeneous potential around the center of mass position using the cumulant generating function. Define the center of mass position operator $\hat{\boldsymbol{r}}_c$ as such that, when evaluated at an arbitrary state it satisfies

$$\langle \hat{\boldsymbol{r}}_c \hat{\boldsymbol{r}}_c ... \hat{\boldsymbol{r}}_c \rangle = \langle \hat{\boldsymbol{r}} \rangle \langle \hat{\boldsymbol{r}} \rangle ... \langle \hat{\boldsymbol{r}} \rangle , \tag{A.6.1}$$

where $\boldsymbol{r}_c = \langle \hat{\boldsymbol{r}} \rangle = \langle \hat{\boldsymbol{r}}_c \rangle$ is the center of mass position. In particular it has the property

$$\langle f(\hat{\boldsymbol{r}}_c) \rangle = f(\langle \hat{\boldsymbol{r}} \rangle). \tag{A.6.2}$$

We may then expand a generic position dependent operator as

$$\langle f(\hat{\boldsymbol{r}}) \rangle = \langle f(\hat{\boldsymbol{r}} - \hat{\boldsymbol{r}}_c + \hat{\boldsymbol{r}}_c) \rangle = \sum_{n=0}^{\infty} \frac{f^{(n)}(\langle \hat{\boldsymbol{r}} \rangle)}{n!} \langle (\hat{\boldsymbol{r}} - \hat{\boldsymbol{r}}_c)^n \rangle \tag{A.6.3}$$

$$= \sum_{n=0}^{\infty} \frac{f^{(n)}(\langle \hat{\boldsymbol{r}} \rangle)}{n!} \langle (\hat{\boldsymbol{r}} - \langle \hat{\boldsymbol{r}}_c \rangle)^n \rangle \tag{A.6.4}$$

$$= \sum_{n=0}^{\infty} \frac{f^{(n)}(\boldsymbol{r}_c)}{n!} \langle \hat{\boldsymbol{r}}^n \rangle_c \tag{A.6.5}$$

where $\langle \hat{\boldsymbol{r}}^n \rangle_c = \langle (\hat{\boldsymbol{r}} - \langle \hat{\boldsymbol{r}}_c \rangle)^n \rangle$ are the connected parts or cumulants, while $\langle \hat{\boldsymbol{r}}^n \rangle$ are the moments.

The cumulants can still be generated from the log of the momentum generating function

$$\langle \hat{\boldsymbol{r}}^n \rangle_c = (\mathrm{i})^n \partial_{\boldsymbol{a}} \partial_{\boldsymbol{a}} ... \partial_{\boldsymbol{a}} \log \left\langle e^{-i\boldsymbol{a}\cdot\hat{\boldsymbol{r}}} \right\rangle. \tag{A.6.6}$$

A.7 Perturbation theory via projection operator

In this appendix we show how perturbation theory may be phrased in terms of projection operators, also known as Feshbach formalism[45]. The aim is to show how the effective Hamiltonian may be understood from a perturbative point of view, which makes contact with the adiabatic evolution that is also phrased in terms of projection operators.

We consider a perturbed Hamiltonian $\hat{H} = \hat{H}_0 + \hat{V}$, where the unperturbed part $\hat{H}$ is assumed to be solved so that we know its spectrum ϵ_n^0 and the corresponding eigenstates $\hat{H}_0 |\epsilon_n^0\rangle = \epsilon_n^0 |\epsilon_n^0\rangle$. We split the Hilbert space into two parts using $\mathbb{1} = \hat{P} + \hat{Q}$, where the projection operator $\hat{P}$ and its complement $\hat{Q}$ are both idempotent: $\hat{P}^2 = \hat{P}$, $\hat{Q}^2 = \hat{Q}$, and orthogonal to each other $\hat{P}\hat{Q} = 0$. We take the projection operator to be formed by a subset of the unperturbed eigenstates, then we have that $[\hat{H}, \hat{P}] = [\hat{H}, \hat{Q}] = 0$.

An eigenstate of the full Hamiltonian satisfies

$$\hat{H} |\psi\rangle = E |\psi\rangle . \tag{A.7.1}$$

We would like to consider the system within the subspace given by $\hat{P}$, say within some energy range. Split the eigenstate as $|\psi\rangle = \hat{P} |\psi\rangle + \hat{Q} |\psi\rangle \equiv |\psi_P\rangle + |\psi_Q\rangle$. The aim is to construct an effective Hamiltonian such that $\hat{H}_{eff} |\psi_P\rangle = E |\psi_P\rangle$. To achieve this, we assume there is an operator $\hat{S}$ which can re-construct the full eigenstate from the projected state, namely $\hat{S} |\psi_P\rangle = |\psi\rangle$, then $\hat{H}_{eff} = \hat{P}\hat{H}\hat{S}\hat{P}$ is the sought-after effective Hamiltonian in the projected subspace. To determine $\hat{S}$, we note that from Eq. (A.7.1), we have

$$\left(E - \hat{H}_0\right) |\psi_Q\rangle = \hat{Q}\left(E - \hat{H}_0\right) |\psi\rangle = \hat{Q}\left(E - \hat{H} + \hat{V}\right) |\psi\rangle = \hat{Q}\hat{V} |\psi\rangle \tag{A.7.2}$$

hence the orthogonal part can be solved as

$$|\psi_Q\rangle = \frac{1}{E - \hat{H}_0}\hat{Q}\hat{V} |\psi\rangle \tag{A.7.3}$$

and

$$|\psi\rangle = \hat{S} |\psi_P\rangle = |\psi_P\rangle + |\psi_Q\rangle = |\psi_P\rangle + \frac{1}{E - \hat{H}_0}\hat{Q}\hat{V} |\psi\rangle \tag{A.7.4}$$

Although this is exact, the right-hand side still involves the full $|\psi\rangle$. We may iterate this equation, thus eliminating $|\psi_Q\rangle$ using Eq. (A.7.3), so that we have a series solution to $\hat{S}$ as

$$\hat{S} = \sum_{n=0}^{\infty} \left((E - \hat{H}_0)^{-1} \hat{Q} \hat{V} \right)^n . \tag{A.7.5}$$

Thus the effective Hamiltonian now reads

$$\hat{H}_{eff} = \sum_{n=0}^{\infty} \hat{P} \hat{H} \left((E - \hat{H}_0)^{-1} \hat{Q} \hat{V} \right)^n \hat{P}, \tag{A.7.6}$$

which to lowest order is simply the projected Hamiltonian $\hat{P}\hat{H}\hat{P}$.

Part II

Chapter 4
Analogue gravitational lensing

4.1 Introduction

In the **Part II** of the thesis we shall explore a surprising connection between the semi-classical dynamics of quasi-particles and the geodesics of particles moving around curved spacetimes, which represents an example of theintersection between solid state and relativistic physics. The key observation is that the low-energy states in a class of topological materials, the so-called Weyl semi-metals [10] can be described by the massless limit of the Dirac equation, the Weyl Hamiltonian, which was first applied in relativistic quantum mechanics. In fact, such a connection was already noticed in graphene [32]. Despite connecting two extremely different physical situations, such an analogy allows for the study of phenomena in high-energy physics using tabletop solid state systems. Indeed, such an observation underlie the Klein tunneling in graphene [79] and the chiral anomaly in Weyl semimetals [2, 6, 15, 16, 82, 107, 138], as well as a connection between various quantum anomalies and transport properties in solids [18, 52, 145, 158].

Fueled by such progress, it has been proposed that Weyl semimetals with a modified dispersion relation, namely those with a spatially varying nodal tilt gives rise to an effective curved spacetime metric around a black hole [21, 56, 63, 70, 71, 80, 85, 93, 130, 154–156, 161, 169]. More specifically, the linear dispersion relation of Weyl nodes may be taken to model a light-cone in relativistic physics, and the in-homogeneously tilted Weyl nodes forms a family of lightcones in curved spacetimes [93, 161]. Such a mapping allows us to take the wave-packet dynamics of Weyl nodes to be the solid state analogue of particle motion around black holes. In fact similar ideas of simulating relativistic physics in solid state systems have already been exploited before, using, for instance site dependent tight-binding hopping amplitudes [102–104], or ultracold quantum gases [14, 64, 99, 129, 140, 141, 146, 153, 157].

In this part of the thesis, our aim is to study the potential of using in-homogeneously tilted Weyl systems as an electronic lensing devices that mimic the so-called gravitational lensing effect in curved spacetimes [53, 56, 161]. However, one advantage of approaching such relativistic effects from a solid state side is that we may understand certain microscopic effects not directly accessible in actual gravitational systems, such as the question what happens when the wave-packet reaches the event horizon? We thus also provide an analysis using a microscopic tight-binding model, both to confirm the effective continuum theory and to better understand such subtle questions. This part is based on the work [59], where Dr. Hegde, Dr. Haller, Dr. De Beule and I contributed equally to the analytical analysis of both the geodesic equations of motion and the transverse shift, while the numerical calculation and simulation of the lattice model and the were carried out mainly by the coauthor Dr. Haller.

4.2 Tilted Weyl semi-metals

4.2.1 Weyl Semi-metals

Weyl semi-metals are a class of topological materials which has a number of interesting properties. The name reflects the fact these three dimensional materials are gapless, but the conduction and valence bands touch at discrete points, instead of a continuum as in a normal metal (the Fermi surface). Thus the carrier density is much lower than that of the normal metal due to the vanishing density of states at the band crossing points, hence a much lowered conductivity and the name semi-metal. Weyl semi-metals are characterized by a linear dispersion around these band crossing points, known as the Weyl nodes. Weyl semi-metals also furnish an example of topological phase of matter since the Weyl nodes can in fact be viewed as a 3-dimensional monopole in the momentum space. More precisely, each node is a source or sink of Berry curvature charge, where the Berry curvature, discussed also in **Part I** of this thesis, may be viewed as an emergent magnetic field in the momentum space.

Around a Weyl node located at $\boldsymbol{k}_0$ in Brillouin zone, the point where two non-degenerate bands touch, the band dispersions are linear below some cut-off momentum, and the Weyl Hamiltonian provides a low energy effective model for such band structure, which is

$$H_w(\boldsymbol{k}) = \chi\, v_F\, (\boldsymbol{k} - \boldsymbol{k}_0) \cdot \boldsymbol{\sigma}, \tag{4.2.1}$$

where v_F is the Fermi velocity, and $\boldsymbol{\sigma} = (\sigma_x, \sigma_y, \sigma_z)$ is the vector of Pauli matrices. $\chi = \pm 1$ is called the node's chirality, which as we discussed in **Part I** can in fact be seen as the

topological charge (Chern number) associated with the Weyl node. Without loss of generality, we may take $\boldsymbol{k}_0$ to be at the origin, or put another way, we measure energy difference from the respective node. The spectrum of this minimal model is easy to calculate as $E_\pm(\boldsymbol{k}) = \pm v_F|\boldsymbol{k}|$. We have already discussed this simple model, modulo the Fermi velocity, in Section 2.1.3 of this thesis. In particular, we have shown that the curvature associated with the Weyl nodes is computed to be

$$\boldsymbol{\Omega}_\chi = -\chi\frac{1}{2}\frac{\boldsymbol{k}}{|\boldsymbol{k}|^3}. \tag{4.2.2}$$

We also saw in Section 2.1.3 that the chirality χ has the interpretation as a topological charge of a monopole in the momentum space.

The Weyl semi-metal is a remarkable class of materials, one of whose interesting property being simulating a relativistic system. Indeed, the Weyl Hamiltonian proposed by Weyl [162], was thought to describe the relativistic neutrino[119]. In fact the linear dispersion relation is already suggestive of this fact. In special relativity we have the energy momentum relation $E^2 = (mc^2)^2 + (\boldsymbol{p}c)^2$, which for massless particle reduces to $E = \pm c|\boldsymbol{p}|$. We see that this is precisely the dispersion relation we have in Weyl semi-metals, with the analogue of the speed of light c being now the Fermi velocity v_F. Furthermore, in the following we shall explain that, if we modify the Weyl Hamiltonian by adding a spatially varying term, it can in fact simulate the motion of a massless particle near a black hole, thus providing a potential tabletop lab for studying general relativistic effects.

4.2.2 Tilted Weyl systems

The linear dispersion around the Weyl form a cone given by the equation $E_\pm = v_F|\boldsymbol{k}|$. The semi-metallic nature of the system can be rephrased as the Fermi level interacts exactly with the apex of the cone, i.e. the Weyl nodes. However, there are other classes of 3−dimensional materials that also have a linear dispersion, but do not fit exactly this description. More generally, we may add a term to the Weyl Hamiltonian H_W as

$$H_1(\boldsymbol{k}) = (\boldsymbol{u}\cdot\boldsymbol{k})\,\sigma_0 + \chi\, v_F\, \boldsymbol{k}\cdot\boldsymbol{\sigma}, \tag{4.2.3}$$

where the additional term given by $\boldsymbol{u}$ is called a nodal tilt. The eigenvalues can easily be calculated as $E_\pm(\boldsymbol{k}) = \boldsymbol{u}\cdot\boldsymbol{k} \pm v_F\,|\boldsymbol{k}|$, still a linear dispersion. In momentum space, the first term coming from the tilt rotates the Weyl cone, while deforming it at the same time, namely changing the slope of the cone. As $|\boldsymbol{u}| > v_F$, the cone over tilts, and should we fix

the chemical potential, the Fermi level intersects the Weyl cone and form electron and hole pockets. In this case the system is metallic, and we have a type-II Weyl node, whilst below the critical value of the tile, it is a type-I tilted Weyl node.

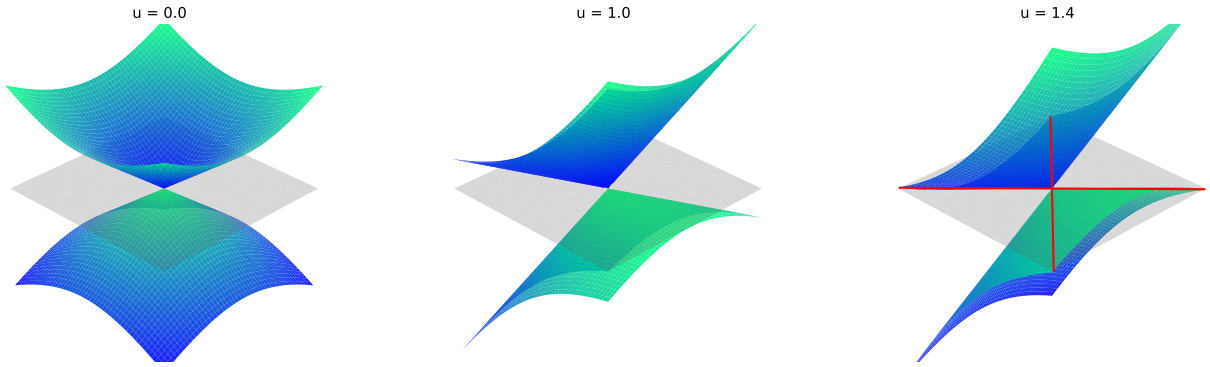

Figure 4.1. Transition from type-I to type-II Weyl semimetals with increasing tilt parameter u, with $v_F = 1$. Red curves show the Fermi level intersections forming electron and hole pockets.

This motivates us to consider a spatially varying tilt profiles, $\boldsymbol{u} \to \boldsymbol{u}(\boldsymbol{r})$, where we have a family of titled Weyl cones that is similar to the light cones in curved space-times, varying from point to point. We shall establish and explore this connection to analogue gravity below. The effective Hamiltonian has explicit spatial dependence now as well $H_1(\boldsymbol{k}) \to H_1(\boldsymbol{r}, \boldsymbol{k})$. With a spatially dependent tilt profile, as we have discussed extensively in **Part I**, position operators act as momentum space covariant derivative, and thus spatial in-homogeneity couples Bloch states with different momentum. Indeed, there we have seen that these spatial dependence would in general give rise to new geometric contributions that modify the semi-classical equations of motion. To isolate the effects due to the spatial geometry, we will assume that tilt profiles have spatial variations that are smooth on the relevant electronic length scales. More specifically, we assume that the tilt profile varies on a scale much larger than the inverse momentum difference between Weyl nodes, and the inverse of the momentum cutoff that was implicitly imposed in taking the linear dispersion in Eq. (4.2.3). In particular, the tilt profile $\boldsymbol{u}(\boldsymbol{r})$ varies on scales much larger than the width of the typical wave-packet formed in, for instance, the transport process, and thus quantum geometric corrections to the semi-classical equations involving the quantum metric can be ignored [87, 91]. We shall discuss the lattice effects in more detail in the later section Section 4.4 on lattice simulation of the continuum theory.

Provided these assumptions, we can quantize the theory by promoting the tilt term to an

Hermitian operator via

$$\boldsymbol{u}\cdot\boldsymbol{k}\to\boldsymbol{u}(\boldsymbol{r})\cdot(-i\boldsymbol{\nabla}_{\boldsymbol{r}})+\frac{1}{2}\left(-i\boldsymbol{\nabla}_{\boldsymbol{r}}\cdot\boldsymbol{u}(\boldsymbol{r})\right), \tag{4.2.4}$$

which provides an effective model for a nodal band structure in a spatially varying tilt texture. The second term in the above is needed to preserve hermiticity [21, 130]. In this part of the thesis, $\nabla_{\boldsymbol{r}}$ will denote the normal vector derivative. The same applies to $\nabla_{\boldsymbol{k}}$. It is clear that the only modification to the dispersion is changing $\boldsymbol{u}\to\boldsymbol{u}(\boldsymbol{r})$, namely $E_{\pm}(\boldsymbol{k},\boldsymbol{r})=\boldsymbol{u}(\boldsymbol{r})\cdot\boldsymbol{k}\pm v_F|\boldsymbol{k}|$. Note, however, that the tilt term in the Hamiltonian is proportional to the identity matrix and therefore the eigenstates remain unchanged compared to the untilted Weyl nodes. As a result, the Berry curvature remains the same, and there are no real-space Berry curvature contributions that emerge from a band system in inhomogeneous texture (see for instance [165]).

4.2.3 Gravitational analogue

As we discussed earlier, the linear dispersion of Weyl nodes resembles that of a massless relativistic particle. More remarkably, it has been suggested that an inhomogeneously tilted Weyl system may form a potential solid state platform to simulate the particle motion around curved spacetimes near black holes [21, 56, 63, 70, 80, 93, 104, 130, 154, 155, 161, 169]. For definiteness let us restrict to a given chirality. From a kinematic point of view, the gravitational analogy can then be understood as follows. We will use the mostly plus metric sign convention of $(-+++)$, and the four-momentum vector reads $k_\mu=(-E/v_F,\boldsymbol{k})$ (equivalently $k^\mu=(v_FE,\boldsymbol{k})$). Note v_F here takes the role of speed of light as in actual relativistic system. The quasi-particle dispersion near a tilted Weyl node $E_\pm=\boldsymbol{u}(\boldsymbol{r})\cdot\boldsymbol{k}\pm v_F|k|$ can then be re-written as that of a particle in a curved spacetime as

$$g^{\mu\nu}k_\mu k_\nu=0, \tag{4.2.5}$$

via introducing an effective metric $g^{\mu\nu}$. Explicitly the inverse metric reads

$$g_{\mu\nu}=\begin{pmatrix}-1+|\boldsymbol{u}|^2/v_F^2 & -u_x/v_F & -u_y/v_F & -u_z/v_F\\ -u_x/v_F & 1 & 0 & 0\\ -u_y/v_F & 0 & 1 & 0\\ -u_z/v_F & 0 & 0 & 1\end{pmatrix}, \tag{4.2.6}$$

or in more compact tensor notation, the metric and inverse metric read

$$g_{\mu\nu} = \begin{pmatrix} -1 + |\mathbf{u}|^2/v_F^2 & -u_j/v_F \\ -u_i/v_F & \delta_{ij} \end{pmatrix}, \quad g^{\mu\nu} = \begin{pmatrix} -1 & -u^j/v_F \\ -u^i/v_F & \delta^{ij} - u^i u^j/v_F^2 \end{pmatrix}. \tag{4.2.7}$$

This in fact is nothing but the famous Schwarzschild metric that describes a black hole written in Painlevé-Gullstrand coordinates $(t, \boldsymbol{r})$ [21, 56, 63, 70, 80, 93, 104, 130, 154, 155, 161, 169]. In fact, the line element of the metric Eq. (4.2.7) reads

$$ds^2 = g_{\mu\nu} dx^\mu dx^\nu = -\left(1 - \frac{|\boldsymbol{u}(\boldsymbol{r})|^2}{v_F^2}\right) v_F^2 dt^2 - 2\boldsymbol{u}(\boldsymbol{r}) \cdot d\boldsymbol{r} dt + d\boldsymbol{r}^2. \tag{4.2.8}$$

and upon making the change of variable

$$\tau = t + \int \frac{\boldsymbol{u}}{1 - |\boldsymbol{u}|^2/v_F^2} \cdot d\boldsymbol{r}.$$

the metric Eq. (4.2.7) is then transformed to

$$ds^2 = -(1 - |\boldsymbol{u}|^2) d\tau^2 + \frac{dr^2}{1 - |\boldsymbol{u}|^2} + r^2(d\theta^2 + \sin^2\theta d\phi^2), \tag{4.2.9}$$

which is precisely the Schwarzschild metric, with v_F playing the role of c. The gravitational physics related to the metric is not the focus of the thesis, and thus we will not go into details but provide only a brief description of the Painlevé-Gullstrand metric. Note that the analogue Schwarzschild metric Eq. (4.2.9) has a singularity when $|\boldsymbol{u}| = v_F$. For the actual Schwarzschild spacetime, $\boldsymbol{u}(\boldsymbol{r}) = -v_F\sqrt{r_s/r}\hat{\boldsymbol{r}}$, where the singularity thus occurs at $r = r_s$, known as the horizon radius, and the singularity implies the Schwarzschild metric describes a spherically symmetric black hole. On the other hand, we can re-write the Painlevé-Gullstrand metric Eq. (4.2.6) as

$$ds^2 = -v_F^2 dt^2 + (d\boldsymbol{r} - \boldsymbol{u}(\boldsymbol{r}) dt)^2, \tag{4.2.10}$$

where the tilt $\boldsymbol{u}(\boldsymbol{r})$ has an interpretation as a local free-fall velocity field under the gravity of the black hole [120], and the Painlevé-Gullstrand metric represents what a free-falling observer experiences. In particular, when $\boldsymbol{u}$ vanishes such as at the spatial infinity from the black hole, the metric reduces to that of flat Minkowski metric.

The gravitational analogue may also be discussed from a dynamics point of view. Specifically, we may show that semiclassical trajectories of wave-packets in in-homogeneously tilted Weyl

nodes can be mapped to the geodesics of the curved spacetime the corresponding to the emergent metric (see Section B.1).

4.3 Cylindrical tilt and lensing

With the connection to the particle motion in curved space-time discussed above, let us now consider wave packets in the in-homogeneously tilted Weyl nodes. We consider excitations above the Weyl node, and thus the wave-packets are constructed from states associated with the $E_+(\boldsymbol{r},\boldsymbol{k})$-band with dispersion $E_+(\boldsymbol{k},\boldsymbol{r}) = \boldsymbol{u}(\boldsymbol{r})\cdot\boldsymbol{k} + v_F\,|\boldsymbol{k}|$. We assume the wave-packet has a well-defined center of mass position $\boldsymbol{r}$ and momentum $\boldsymbol{k}$, and in the absence of external perturbing electromagnetic fields, the semiclassical equations of motion read

$$\begin{aligned}\dot{\boldsymbol{r}} &= \boldsymbol{\nabla}_{\boldsymbol{k}} E_+(\boldsymbol{r},\boldsymbol{k}) + \dot{\boldsymbol{k}}\times\boldsymbol{\Omega}(\boldsymbol{k}) = \boldsymbol{u}(\boldsymbol{r}) + v_F\hat{\boldsymbol{k}} + \dot{\boldsymbol{k}}\times\boldsymbol{\Omega}(\boldsymbol{k}),\\ \dot{\boldsymbol{k}} &= -\boldsymbol{\nabla}_{\boldsymbol{r}} E_+(\boldsymbol{r},\boldsymbol{k}) = -\boldsymbol{\nabla}_{\boldsymbol{r}}(\boldsymbol{u}(\boldsymbol{r})\cdot\boldsymbol{k}),\end{aligned} \tag{4.3.1}$$

where recall the Berry curvature is $\boldsymbol{\Omega}(\boldsymbol{k}) = \chi\,\boldsymbol{k}/(2\,k^3)$ and $k = |\boldsymbol{k}|$.

The Schwarzschild metric describes a static spherical black hole, which thus requires a rotationally symmetric tilt profile to form an exact mapping. However, such a highly symmetric tilt is not easily found or engineered in a three-dimensional solid state systems. On the other hand, a tilt profile with a slightly reduced, axial symmetry could in principle result from straining a Weyl semi-metal, and thus provides a more realistic possibility. One possibility of inducing such such a cylindrical tilt by applying mechanical strain has been discussed previously, where a microscopic displacement field $\boldsymbol{h}(\boldsymbol{r})$ might induce nodal tilts $u_i \propto (\partial_i h_j)\,k_{0j}$ around a certain axis, where $2\boldsymbol{k}_0$ is the separation between Weyl nodes [9]. Therefore, in the following of the thesis, we shall consider axially symmetric tilt profiles, i.e., a cylindrical tilting field $\boldsymbol{u}(\boldsymbol{r}) = u(\rho)\hat{\boldsymbol{\rho}}$, where $\hat{\boldsymbol{\rho}}$ is the unit vector along the radial direction of the cylinder, and ρ is the radius in cylindrical coordinates (ρ,ϕ,z).

In the cylindrical coordinates, the semiclassical equations read

$$\dot{\boldsymbol{r}} = \boldsymbol{u}(\rho) + v_F\,\hat{\boldsymbol{k}} + \dot{\boldsymbol{k}}\times\boldsymbol{\Omega}, \tag{4.3.2}$$

$$\dot{\boldsymbol{k}} = -\frac{\partial u}{\partial\rho}\,(\boldsymbol{k}\cdot\hat{\boldsymbol{\rho}})\,\hat{\boldsymbol{\rho}} - \frac{uL_z}{\rho^2}\,\hat{\boldsymbol{\phi}}, \tag{4.3.3}$$

where $\boldsymbol{L} = \boldsymbol{r}\times\boldsymbol{k}$ is the orbital angular momentum, and explicitly $L_z = \rho\,\boldsymbol{k}\cdot\hat{\boldsymbol{\phi}} \equiv \rho k_\phi$. We recognize two contributions in the semi-classical equations of motion of wave-packets, where

the first and second terms in Eq. (4.3.3) are the group velocity $\boldsymbol{\nabla}_{\boldsymbol{k}} E_+(\boldsymbol{r},\boldsymbol{k})$ given by the Weyl dispersion relation, and is tilt dependent. The third term is a geometric contribution to the wave-packet dynamics, the anomalous velocity, whose sign is given by the chirality χ. The two equations are coupled through the anomalous velocity term, and upon substituting the second equation into the first, we obtain

$$\dot{\boldsymbol{r}} = \boldsymbol{u}(\rho) + v_F\,\hat{\boldsymbol{k}} - \frac{\chi}{2k^3}\left[\frac{\boldsymbol{k}\cdot\hat{\boldsymbol{\rho}}}{\rho}\left(\frac{\partial u}{\partial\rho} - \frac{u}{\rho}\right) L_z\,\hat{\boldsymbol{z}} + k_z\left(\frac{u\,L_z}{\rho^2}\,\hat{\boldsymbol{\rho}} - (\boldsymbol{k}\cdot\hat{\boldsymbol{\rho}})\,\frac{\partial u}{\partial\rho}\,\hat{\boldsymbol{\phi}}\right)\right]. \quad (4.3.4)$$

Our analysis of the electron dynamics would be based on the above equation, and it is helpful to consider the symmetry and associated conservation laws associated with the semiclassical equations of motion. First of all, our tilt profile is static, and the tilted Weyl Hamiltonian is time-independent, hence we have the conservation of energy $\dot{E}_\pm(\boldsymbol{r},\boldsymbol{k}) = 0$, which is consistent with the fact that the effective metric describes an analogue Schwarzschild black hole that is static. Second, the tilt profile is axially symmetric, namely that is is invariant under rotation around the z-axis, and thus the angular momentum along the axial direction is conserved: $\dot{J}_z = 0$, where $\boldsymbol{J} = \boldsymbol{L} + \boldsymbol{s}$ is the total angular momentum that is the sum of orbital and spin angular momentum, the helicity $\boldsymbol{s} = \chi\hat{\boldsymbol{k}}/2$, where here $\hat{\boldsymbol{k}} = \frac{\boldsymbol{k}}{|\boldsymbol{k}|}$. Let us add some remarks to the spin angular momentum. For the Weyl Hamiltonian, the spin operator that generates a spinor rotation is given by the Pauli matrices $\frac{1}{2}\boldsymbol{\sigma}$ does not directly give an observable intrinsic spin. That would require a rest frame to be properly defined, for otherwise it is mixed with the orbital part, while a massless particle has no rest frame just as photons. The actual analogue of a spin angular momentum is the projection of the spin operator along the direction of motion, namely the helicity, and $\boldsymbol{s}$ is the expectation value of it evaluated at a state with definite momentum $\boldsymbol{k}$, which we take from the E_+-band. Finally, we note that the cylindrically symmetric system also has translation invariance along the z-direction, which implies the momentum conservation $\dot{k}_z = 0$. Furthermore, the equations of motion are invariant under the discrete transformation where $u \to -u$, $\boldsymbol{k} \to -\boldsymbol{k}$ and $t \to -t$.

4.3.1 Trajectory analysis

In the above, the form of the tilt is assumed to be axially symmetric, but otherwise general. To be more definite, we shall now specialize to the class of axially symmetric tilt profiles $\boldsymbol{u}(\rho) = u(\rho)\,\hat{\boldsymbol{\rho}}$ of the form of the form $u(\rho) = -v_F\,(\rho_t/\rho)^\alpha$. We set the tilt center to be at the origin, and ρ_t is the radius at which at which $u(\rho = \rho_t) = -v_F$. Recalling the form of the Schwarzschild metric, we see this is the event horizon radius from the center of the analogue black hole. For the Weyl node, this sets the point at which the tilted Weyl node

transitions from type I to a type II, while the parameter α that determines how fast the tilt vanishes sets how rapid the gravitational attraction decays outside the analogue event horizon [21, 130, 154, 155]. On the one hand, this form of tilt profile is an obvious generalization of the analogue Schwarzschild black hole metric with $\alpha = 1/2$; on the other hand, it may represent the dominant part of a more general form of tilt profile in an asymptotic expansion near the tilt center.

Our aim is to analyze the motion of an incoming electron wave-packet, which we take to be injected perpendicularly to the cylindrical axis, i.e., with initial $k_z = 0$. This implies the helicity, namely the spin angular momentum also vanishes, $s_z = 0$ and by the conservation of linear momentum, $\dot{k}_z = \dot{s}_z = 0$, namely that they will remain zero. Furthermore, this in fact implies that in this case the orbital and spin angular momentum are conserved separately, for we also have $\dot{J}_z = 0$ and thus $\dot{L}_z = 0$. In the dynamics of classical particles, the fact that k_z remains zero and angular momentum is conserved implies the motion is restricted to the xy-plane, and for analyzing the trajectory in this scenario we only need to consider the ρ and ϕ components of the equations of motion Eq. (4.3.1). However, unlike a purely classical particle, there is an additional motion due to the Berry curvature induced anomalous velocity along z direction, which exists even for $k_z = 0$. This will be discussed separately in Section 4.5, and we will neglect it for now, focusing on the planar motion.

In general, we may expect the trajectories of the electron motion to fall into two distinct classes, lensing and capture, corresponding to the scattering and bound orbit scenario repetitively. A lensed trajectory is one in which the electron begins with moving towards the tilt center from afar, approaches this region, and then escapes to infinity, i.e. a scattering motion. In an optical analogy, the lensing due to the in-homogeneous tilt may also be intuitively understood as light refraction due to texture of the propagation medium, and as such, it might be said we study the "tiltronics" using Weyl nodes. In contrast, a captured trajectory is one where the incoming wave-packet falls into the "black hole", and never escapes again. Between the lensed and captured trajectory, there is a critical situation where the incoming electron orbits around the region of strong tilt and neither falls in nor escapes, which is known as the “separatrix”, and is related to the notion of "photon sphere" in black hole physics [120]. These types of trajectories, together with one corresponding to radial escape from the tilt, are demonstrated in Fig. 4.2. The above is clearly a rather classical picture of the electron dynamics, which follows from using the semi-classical equations. We shall give a microscopic quantum mechanical description of the wave-packet propagation using a lattice model in Section 4.4, so that the meaning of "falling" is better understood.

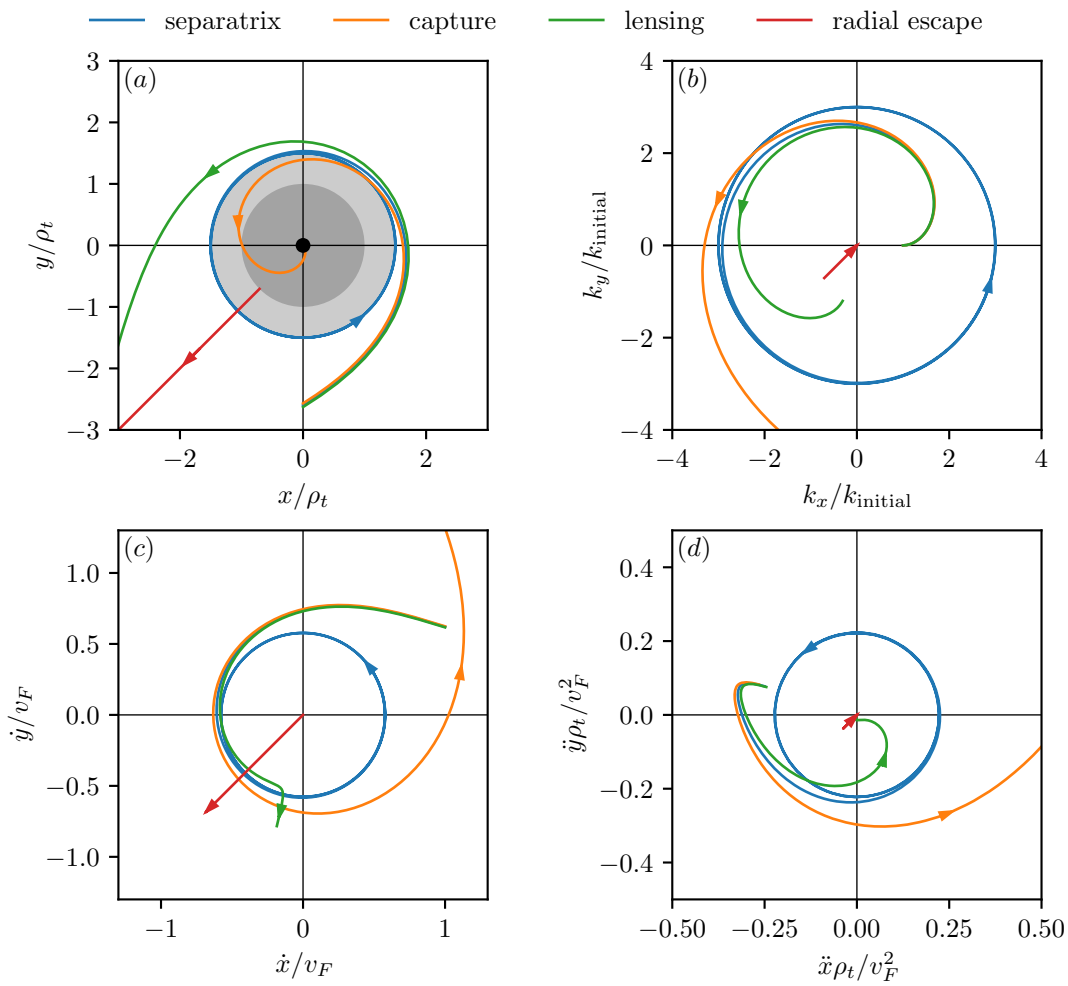

Figure 4.2. Panel (a) and (b) show the trajectories given by the solutions of $\boldsymbol{r}(t)$ and $\boldsymbol{k}(t)$ for the tilt profile $u = -v_F\sqrt{\rho_t/\rho}$ respectively. Differently colored trajectories correspond to lensing, escape, in-falling, and orbiting solutions respectively. The radial escape trajectory starts at a distance $1.0001\rho_t$ from the tilt center, and initial momenta are chosen as $k_x = k_y$, $k_z = 0$. Panels (c) and (d) display the corresponding velocity and acceleration components of each type of trajectories. The arrows indicate the direction of time evolution, with trajectories oriented toward increasing time.

Let us now analyze the lensing and capturing motion in terms of the equations of motion, which we only need the components projected to the (x, y)-plane by symmetry as we discussed above. Thus we focus on the (ρ, ϕ)-components of $\boldsymbol{r}$ and $\boldsymbol{k}$, whose corresponding

equations read

$$\dot{\rho} = u(\rho) + v_F \frac{\boldsymbol{k}\cdot\hat{\boldsymbol{\rho}}}{k}, \tag{4.3.5a}$$

$$\rho\,\dot{\phi} = v_F \frac{\boldsymbol{k}\cdot\hat{\boldsymbol{\phi}}}{k}, \tag{4.3.5b}$$

$$\frac{d(\boldsymbol{k}\cdot\hat{\boldsymbol{\rho}})}{dt} - (\boldsymbol{k}\cdot\hat{\boldsymbol{\phi}})\,\dot{\phi} = -\frac{\partial u}{\partial \rho}(\boldsymbol{k}\cdot\hat{\boldsymbol{\rho}}), \tag{4.3.5c}$$

$$\frac{d(\boldsymbol{k}\cdot\hat{\boldsymbol{\phi}})}{dt} + (\boldsymbol{k}\cdot\hat{\boldsymbol{\rho}})\,\dot{\phi} = -\frac{u(\rho)}{\rho}(\boldsymbol{k}\cdot\hat{\boldsymbol{\phi}}). \tag{4.3.5d}$$

We would like to analyze the motion in terms of the impact parameters, which are the conserved quantities: energy E_+, and angular momentum L_z. For this, note that $L_Z = \rho\boldsymbol{k}\cdot\hat{\boldsymbol{\phi}}$ in cylindrical coordinates, and thus with $k_z = 0$, $k^2 = (\boldsymbol{k}\cdot\hat{\boldsymbol{\rho}})^2 + L_z^2/\rho^2$. Substituting in these identities, and the dispersion relation of the titled Weyl nodes, we may express the radial equation of motion $\dot{\rho}$ as a function of the impact parameters and ρ. Indeed, after some manipulations, we find

$$\dot{\rho}^2 = \frac{1}{k^2}\left[E_+^2 - \varepsilon_{\mathrm{p,eff}}(\rho)\right], \tag{4.3.6}$$

$$\varepsilon_{\mathrm{p,eff}}(\rho) = \frac{L_z^2}{\rho^2}\left(v_F^2 - u(\rho)^2\right). \tag{4.3.7}$$

Here we introduced an effective potential energy $\varepsilon_{\mathrm{p,eff}}(\rho)$, and the radial equation of motion Eq. (4.3.6) resembles the energy equation of a classical free particle, whose total energy is $\varepsilon_{\mathrm{tot,eff}} = E_+^2$ that is the sum of an effective kinetic energy $\varepsilon_{\mathrm{k,eff}} = m_{\mathrm{eff}}\,\dot{\rho}^2/2$ with a mass $m_{\mathrm{eff}} = 2\,k^2$, and an effective potential $\varepsilon_{\mathrm{p,eff}}(\rho)$. This is of course not an exact analogy, because k is a dynamical variable, not being conserved, and thus m_{eff} is not really a parameter of motion. Nevertheless, it is a useful one, which allows us to understand the motion by energetics, namely to classify the types of trajectories according to the behavior of the effective poetical energy, as discussed below.

For a general tilt profile $u(\rho)$, the effective potential $\varepsilon_{\mathrm{p,eff}}(\rho)$ consists of a positive, repulsive part given by v_F that is $\propto 1/\rho^2$, and an attractive part which depends on the specific form of the tilt. Due to the competition between the two parts, the potential energy in general, then, have both minima and maxima. For the tilt profiles $u(\rho) = -v_F\,(\rho_t/\rho)^\alpha$ considered here, we find that $\varepsilon_{\mathrm{p,eff}}(\rho)$ has exactly one maximum for a given value of L_z, see Fig. 4.3. In particular, for $\alpha = 1/2$, which is the closest analogue of a Schwarzschild-like tilt profile $u(\rho) = -v_F\sqrt{\rho_t/\rho}$, we have effective potential consists of a repulsive potential energy $\propto 1/\rho^2$ and an attractive cubic term $\propto 1/\rho^3$, as in the Schwarzschild black hole [33].

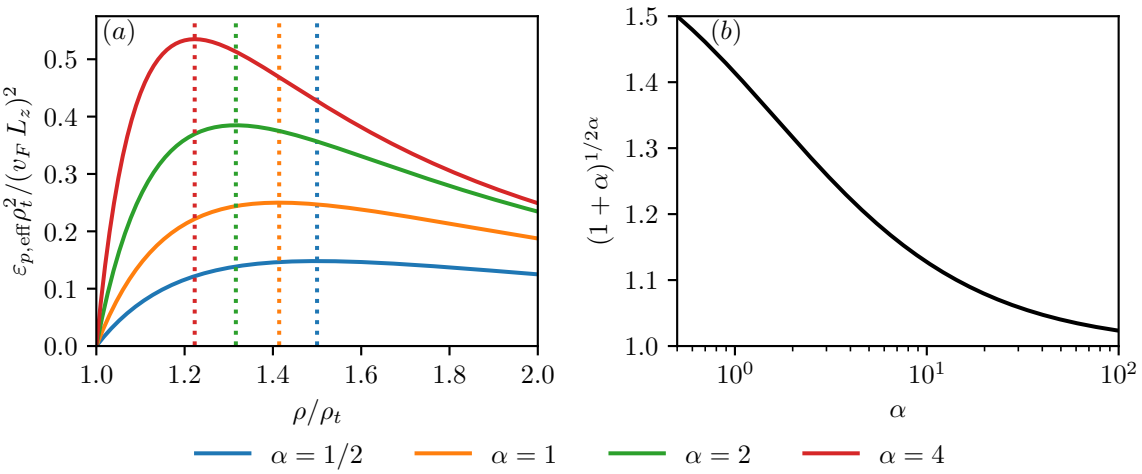

Figure 4.3. In panel (*a*) the effective potential for tilt profiles $u(\rho) = -v_F(\rho_t/\rho)^\alpha$ is plotted for a range of α. The analogue horizon is located at $\rho/\rho_t = 1$, while the maxima of the effective potential locating at $\rho_s = \rho_t(1+\alpha)^{1/2\alpha}$ are indicated by the dashed lines. In panel (*b*) we plotted how the location of the maxima varies with the exponent α.

Finally, we may now analyze quantitatively the types of the particle trajectory discussed earlier using the total energy E_+ and the effective potential $\varepsilon_{\mathrm{p,eff}}$.

1. Lensing: in this case the wave-packet first moves towards the tilt center and then shoots off to infinity. By attraction of the tilt, the trajectory will be deflected and thus possesses a periapsis of the trajectory, the point of closest approach to the tilt center at some ρ_p. It is clear that $\dot\rho = 0$ at the periapsis, and from Eq. (4.3.6), we see it is also the point at which $E_+^2 = \varepsilon_{\mathrm{p,eff}}(\rho_p)$. Solving for ρ_p, we have the implicit equation $E_+\,\rho_p = |L_z|\,\sqrt{v_F^2 - u(\rho_p)^2}$.

2. Capture: in this case the particle simply moves towards the center, and $\dot\rho$ never vanishes within the range of the validity of the theory (i.e. excluding the tilt center). By Eq. (4.3.6), this case happens when $E_+^2 > \varepsilon_{\mathrm{p,eff}}$ throughout the motion, and the effective potential never reaches the maximum.

3. Separatrix: this is a critical case in which the wavepacket approaches the tilt center at first, and then performs an angular motion orbiting around it. In this case, similar to that at the periaspsis of a lensing trajectory, $E_+^2 = \varepsilon_{\mathrm{p,eff}}(\rho_s)$ at the orbiting radius ρ_s. This is an unstable bound state motion, and related to the so-called photon sphere in the black hole physics. There is only one such radius for which such orbiting motion is allowed, and is given by $\rho = \rho_s = \rho_t(1+\alpha)^{1/2\alpha}$ (see Fig. 4.3).

In all of the above discussions, we have in mind a particle that is ejected from somewhere far away from the tilt center, namely the initial radius of the particle is larger than ρ_t, the

analogue black hole horizon radius. Let us now consider the case of escape or emission of particles near the tilt. However, should the analogy to black hole physics hold, we expect that no particles can escape from within the horizon. Indeed, for $\rho < \rho_t$, $u(\rho) < -v_F$ with our choice of tilt profiles and clearly $\boldsymbol{k}\cdot\hat{\boldsymbol{\phi}} \leq |\boldsymbol{k}|$, by Eq. (4.3.5a) we therefore conclude $\dot{\rho} < 0$ at radii within the horizon ρ_t; that is particles cannot be emitted from within ρ_t of the tilt center. On the other hand, if the particle is released from outside of the horizon, namely with initial radius $\rho_{\text{initial}} > \rho_t$, then the escape should be possible. For simplicity, let us consider the radial escape case, where $\boldsymbol{k} = k\hat{\boldsymbol{\rho}} > 0$. The momentum being along the radial direction gives a straight outward trajectory, which can be seen from Eq. (4.3.5b), where we obtain $\dot{\phi} = 0$ in this case. To show that it does escape indeed, we note that $u(\rho) > -v_F$, while the term in Eq. (4.3.5a) is simply v_F, hence $\dot{\rho} > 0$. Furthermore, $\ddot{\rho} = u'(\rho)\dot{\rho} > 0$, so it is not dragged back again.

4.3.2 Lensing and deflection angle

Having understood the formation of different trajectory types from an energetic point of view, let us study the two-dimensional motion in the (ρ, ϕ)-plane in more detail. In this section, we compute the lensing angle and the detailed condition of the formation of an orbiting trajectory. For this purpose, by dividing $\dot{\phi}$ and $\dot{\rho}$, we may express the angular coordinate as a function of the radius to obtain the trajectory equation. Using $\boldsymbol{k}\cdot\hat{\boldsymbol{\phi}} = L_z/\rho$, we have that

$$\frac{d\phi}{d\rho} = \frac{\dot{\phi}}{\dot{\rho}} = \pm\frac{v_F\, L_z}{\rho^2\sqrt{E_+^2 - \varepsilon_{\text{p,eff}}(\rho)}}, \tag{4.3.8}$$

where the sign corresponds to whether the particle is approaching or leaving the center of the tilt, i.e., the sign of $\dot{\rho}$.

Using Eq. (4.3.8), we can compute the deflection angle of a lensed trajectory, in a manner analogous to the standard calculations for gravitational lensing by black holes[160], which gives

$$\pi + \varphi = 2\int_{\rho_p}^{\infty} \frac{v_F\, d\rho}{\sqrt{\frac{1}{\rho_p^2}(v_F^2 - u(\rho_p)^2)\rho^4 - \rho^2(v_F^2 - u(\rho)^2)}}, \tag{4.3.9}$$

where φ is the angle of deflection. More details about the derivation and evaluation of the integral is given in Section B.2. The above result shows that the deflection angle is determined by ρ_p, the closest distance of approach. This integral may be numerically evaluated, and in Fig. 4.4, we show that the numerical values of the integral in Eq. (4.3.9) indeed coincide with those obtained from the exact solution of Eq. (4.3.1), with initial

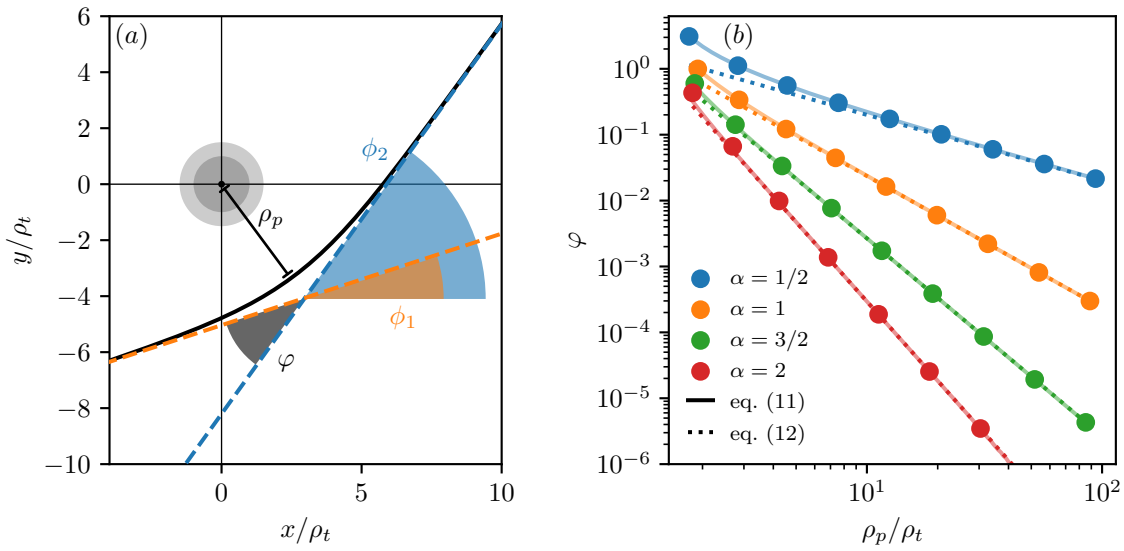

Figure 4.4. In panel (*a*), a typical lensing trajectory is plotted (black line). The deflection angle φ is given by the asymptotic trajectories, drawn as blue and yellow dashed lines, with $\varphi = \phi_2 - \phi_1$. In panel (*b*) we plotted the deflection angles resulting from different periapsides and tilt profiles. Solid and dotted lines represent the results that are calculated using exact numerical integration of Eq. (4.3.9) and the approximate analytic result in Eq. (4.3.10), respectively.

conditions giving the same ρ_p. To gain more insight, let us consider the asymptotic behavior of the lensing angle for trajectories whose periapsides are far from the tilt center such that $\rho_p/\rho_t \gg 1$. In this limit, we may obtain analytically from Eq. (4.3.9) that, again detailed in Section B.2, the deflection angle to leading order in ρ_t/ρ_p is

$$\varphi \approx \frac{u(\rho_p)^2}{v_F^2} \frac{\sqrt{\pi}\,\Gamma\left(\frac{3}{2}+\alpha\right)}{\Gamma\left(1+\alpha\right)}. \tag{4.3.10}$$

For the specific case of a Schwarzschild-like tilt profile with $\alpha = 1/2$, i.e., $u(\rho) = -v_F\sqrt{\rho_t/\rho}$, we have $\varphi \approx 2\,u(\rho_p)^2/v_F^2$.

4.3.3 Capture and Separatrix

Recall our early discussion about the notion of separatrix, which is the boundary dividing the trajectories into the escaping (lensing) and in-falling types. Referring to our Eq. (4.3.6), we know that the former situation occurs for a trajectory having initial conditions such that $E_+^2 > \varepsilon_{\text{p,eff}}^{\max}$ and $\dot{\rho} < 0$ initially, and the semi-classical equations of motion predict the wave-packet to be attracted towards the origin and then escaping away. Conversely, any trajectory with $E_+^2 < \varepsilon_{\text{p,eff}}^{\max}$ are said to be inside the separatrix, since in this case the fate of the incoming wave-packet would spiral inward to the origin. The final part of the process would be a plunge towards the center, and the velocity and acceleration diverge, hence marking a break-down of the equations of motion Eq. (4.3.5). From the gravity perspective, this simply means

we do not know what happens in the black hole. For our solid state system, however, we should be able to observe some physical consequences since the "black hole" in our case is an analogue one after all. We shall discuss such issues using a lattice model in Section 4.4.

Finally, let us discuss the situation where the particle trajectory lies exactly on the separatrix. In this case, we have the precise vanishing of $\dot{\rho}$, or $E_+^2 = \varepsilon_{\mathrm{p,eff}}^{\max}$. The wave-packets would approach the origin of the tilt up to a distance at $\rho_s = \rho_t(1+\alpha)^{1/2\alpha}$, and then remain orbiting at this radius. To show this, note by definition, both the radial velocity $\dot{\rho}$ and the radial acceleration $\ddot{\rho}$ shall vanish, while the radial acceleration is obtained by taking a further derivative of Eq. (4.3.6), the vanishing of which then gives

$$\ddot{\rho}|_{\rho=\rho_s} = -\frac{1}{k^2}\left(\frac{1}{2}\frac{\partial \varepsilon_{\mathrm{p,eff}}}{\partial \rho} + \dot{\rho}\,\dot{k}\,k\right)_{\rho=\rho_s} = 0. \tag{4.3.11}$$

Since $\dot{\rho} = 0$, we see that the condition reduces to that $\varepsilon_{\mathrm{p,eff}}(\rho)$ has a maximum $\frac{\partial \varepsilon_{\mathrm{p,eff}}}{\partial \rho} = 0$ at $\rho = \rho_s$, whose solution is easily solved to be $\rho_s = \rho_t(1+\alpha)^{1/2\alpha}$ using the dispersion relation. However, the effective potential has a local maximum at ρ_s, so $\partial^2 \varepsilon_{\mathrm{p,eff}}/\partial \rho^2$ is negative at $\rho = \rho_S$, and therefore the orbit is an unstable one. That is any small change to the impact parameters will cause the wave-packet to either plunge into the tilt center, or simply shoots off again.

Earlier we have remarked that the case of a spherically symmetric tilt profile with $\alpha = 1/2$, i.e., replacing $u(\rho)\hat{\boldsymbol{\rho}} \to u(r)\hat{\boldsymbol{r}} = -v_F\sqrt{r_H/r}\,\hat{\boldsymbol{r}}$, corresponds to the Schwarzschild spacetime. The semi-classical equations of motion, neglecting anomalous velocity terms, describe the propagation of a massless particle around a Schwarzschild black hole with an event horizon at r_H. In this context, the family of all orbiting trajectories fall on a sphere, and the separatrix is known as the photon sphere [33, 120, 160]. The existence of photon spheres is an important property of black holes, and it is an active topic of investigation to this day, due to both its importance in gravitational wave detection measurements[30], as well as theoretical studies of black holes[38, 57, 123]. In fact, the photon sphere is what is captured in the recent black hole images taken by the Event Horizon Telescope [7], making it one of the few directly observed aspects of black holes, which is also taken as evidence of the existence of black holes at all instead of other more regular types of massive astrological object. In our discussion of Weyl semimetals with inhomogeneous nodal tilts, we may then identify the separatrix between lensed and captured trajectories as the analogue of photon sphere in black holes, and since the tilt profiles that we considered are axially symmetric, the separatrix has

the shape of a cylinder instead of a sphere, therefore we may dub it the "photon cylinder".

4.4 Lattice simulations

In the former section Section 4.3 we have already seen that the semiclassical equations have a limited range of applicability, where we saw that it is unclear what happens to the wave-packet after plunging into the center of the tilt. Such questions arise from using the semi-classical equations,and in this section we shall check the validity of results obtained from such effective continuum description by a microscopic computations, and, in particular, understand the fate of wave-packets crossing the separatrix. It has for example been discussed in refs. [21, 130] that in order to obtain the correct description of transport in in-homogeneously tilted Weyl nodes, one needs to include in the calculation additional large momentum states. We shall use an effective two-dimensional lattice model from which the tilted Weyl Hamiltonian follows as an approximation. Note that this is possible since we have already seen that if we neglect the possible transverse deflections from Berry curvature, the electron dynamics is effectively two-dimensional by the axial symmetry. We will first re-do the semi-classical analysis using the lattice mode to check the consistency of the lattice and continuum model, and then a full quantum mechanical simulation.

4.4.1 Effective lattice model

We start with writing down a minimal model for a tilted Weyl semimetal with two Weyl nodes. In second quantization formalism, such a low-energy continuum Hamiltonian is provided by $\hat{H} = \sum_{\boldsymbol{k}} \hat{c}^{\dagger}_{\boldsymbol{k}} H(\boldsymbol{k}) \hat{c}_{\boldsymbol{k}}$, where we have a two-component spinor $\hat{c}_{\boldsymbol{k}} = (\hat{c}_{\uparrow,\boldsymbol{k}}, \hat{c}_{\downarrow,\boldsymbol{k}})^T$, and a Hamiltonian matrix,

$$H_2(\boldsymbol{k}) = [u_x k_x + u_y k_y + u_z(k_z + k_0)]\,\sigma_0 + v_F k_x \sigma_x + v_F k_y \sigma_y + \frac{1}{2m^*}(k^2 - k_0^2)\sigma_z. \quad (4.4.1)$$

Here $k_0 > 0$ is the separation between the two Weyl nodes, one located at $\boldsymbol{k} = (0, 0, -k_0)$ and zero energy, the other at $\boldsymbol{k} = (0, 0, k_0)$ at energy $2u_z k_0$. The first term term proportional to σ_0 gives a nodal tilt, and the last term proportional to $1/2m^*$ induces the separation between the nodes, and at the same time gives a quadratic modification to the linear dispersion relation along the z direction.

Now we shall construct a lattice model on a square lattice with lattice constant a that shall give the tilted Weyl node dispersion in the continuum limit. To focus on, say, the first Weyl node, we fix $k_z = -k_0$ while letting k_x and k_y vary. There is no loss of generality for doing this because k_z is conserved by translational invariance along the z direction for an axially symmetric tilt profile. It is not hard to see that a two-dimensional square lattice model which

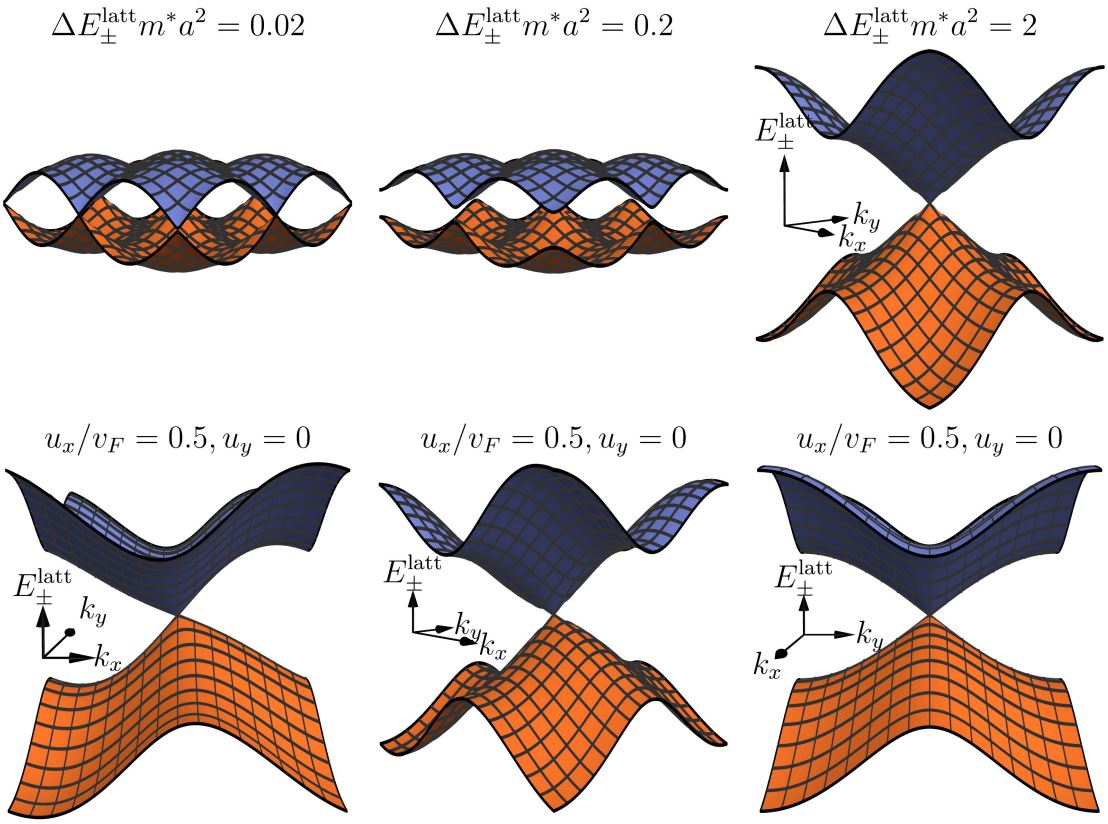

Figure 4.5. Lattice dispersion relations around the Weyl node with zero energy, restricted the first Brillouin zone. Figures in the top row are those with un-tilted Weyl nodes, and we see the degenerates modes at the edges of the Brillouin zone are gapped by $\Delta E_{\pm}^{\text{latt}}$. In the bottom row, the figures show that the Weyl cones are tilted by u_x and u_y, with the gap fixed to be $\Delta E_{\pm}^{\text{latt}} m^* a^2 = 2$.

reduces to the low energy Hamiltonian Eq. (4.4.1) when $k_x, k_y \ll 1/a$ is $\hat{H} = \sum_{\boldsymbol{k}} \hat{c}_{\boldsymbol{k}}^\dagger H(\boldsymbol{k}) \hat{c}_{\boldsymbol{k}}$, with

$$H_{\text{latt}}(\boldsymbol{k}) = a^{-1} \left[(u_x \sin(k_x a) + u_y \sin(k_y a))\sigma_0 + v_F \sin(k_x a)\sigma_x + v_F \sin(k_y a)\sigma_y \right] + \frac{1}{m^* a^2} \left[2 - \cos(k_x a) - \cos(k_y a) \right] \sigma_z. \tag{4.4.2}$$

At the boundary of the Brillouin zone, additional gapless modes are formed (top left of Fig. 4.5), which are then gapped by the m^* terms in the Hamiltonain, with gap size $\Delta E_{\pm}^{\text{latt}} = 4(m^* a^2)^{-1}$ and $8(m^* a^2)^{-1}$. In Fig. 4.5, we show how these degeneracies at the boundary of the Brillouin zone are lifted by $\Delta E_{\pm}^{\text{latt}}$, and the tilting of the Weyl cones centered at $k_x = k_y = 0$ through u_x and u_y.

The above model gives a uniformly titled Weyl Hamiltonian, and to induce inhomogeneity, we shall first Fourier transform the Bloch Hamiltonian in Eq. (4.4.2) to real space in the

(x, y)-plane. Using $\hat{c}_{\boldsymbol{r}} = \frac{1}{N}\sum_{\boldsymbol{r}} \mathrm{e}^{-\mathrm{i}\boldsymbol{k}\cdot\boldsymbol{r}}\hat{c}_{\boldsymbol{k}}$, where $\boldsymbol{r}$ are the lattice sites, we have

$$\begin{aligned}\widehat{H}_{\text{latt}} = \frac{1}{a}\sum_{i\in\{x,y\}}\sum_{\boldsymbol{r}'-\boldsymbol{r}=\hat{\boldsymbol{i}}}\left(\hat{c}^{\dagger}_{\boldsymbol{r}}\left[\mathrm{i}u_i\sigma_0/2 + \mathrm{i}v_F\sigma_i/2 - \frac{1}{2m^*a}\sigma_z\right]\hat{c}_{\boldsymbol{r}'} + h.c.\right) \\ + \frac{2}{m^*a^2}\sum_{\boldsymbol{r}}\hat{c}^{\dagger}_{\boldsymbol{r}}\sigma_z\hat{c}_{\boldsymbol{r}}\ . \end{aligned} \tag{4.4.3}$$

We make the tilt spatially varying by promoting the constant tilt to be site dependent $u_i \to u_i(\boldsymbol{r}-\boldsymbol{r}_0)$, where $\boldsymbol{r}_0$ is the location of the tilt center. To avoid singularity that might arise, we regularize the tilt by taking the average between two lattice nodes, so that the lattice model we shall use is

$$\begin{aligned}\widehat{H}_{\text{latt}} = \frac{1}{a}\sum_{i\in\{x,y\}}\sum_{\boldsymbol{r}'-\boldsymbol{r}=\hat{\boldsymbol{i}}}\hat{c}^{\dagger}_{\boldsymbol{r}}\left[\mathrm{i}u_i\left(\frac{\boldsymbol{r}+\boldsymbol{r}'}{2}-\boldsymbol{r}_0\right)\sigma_0/2 + \mathrm{i}v_F\sigma_i/2 - \frac{1}{2m^*a}\sigma_z\right]\hat{c}_{\boldsymbol{r}'} + h.c. \\ + \frac{2}{m^*a^2}\sum_{\boldsymbol{r}}\hat{c}^{\dagger}_{\boldsymbol{r}}\sigma_z\hat{c}_{\boldsymbol{r}}\ . \end{aligned} \tag{4.4.4}$$

Writing the above Hamiltonian as $\widehat{H}_{\text{latt}} = \sum_{\boldsymbol{r},\boldsymbol{r}'}\hat{c}^{\dagger}_{\boldsymbol{r}}H_{\boldsymbol{r},\boldsymbol{r}'}\hat{c}_{\boldsymbol{r}'}$ defies the real-space Hamiltonian matrix $H_{\boldsymbol{r},\boldsymbol{r}'}$, i.e., a non-constant hopping amplitude.

Let us take $m^*av_F = 1$, and diagonalizing the lattice model Eq. (4.4.4) the dispersion is obtained to be

$$E^{\text{latt}}_{\pm} = \sum_i \frac{u_i(\rho,\phi)}{a}\sin(k_ia) \pm \varepsilon^{\text{latt}}(\boldsymbol{k}), \tag{4.4.5}$$

$$\varepsilon^{\text{latt}}(\boldsymbol{k}) = \frac{v_F}{a}\sqrt{6 - 4\cos(k_ya) + 2\cos(k_xa)(\cos(k_ya)-2)}, \tag{4.4.6}$$

where $u_x = u(\rho)\cos\phi$ and $u_y = u(\rho)\sin\phi$, and the first in Eq. (4.4.5) is the tilt term, while $\varepsilon^{\text{latt}}(\boldsymbol{k})$ is the dispersion of the lattice Weyl node given by Eq. (4.4.4).

We first study the wave-packet dynamics using the microscopic lattice model by numerically integrating the coupled equations of motion Eq. (4.3.1) using the lattice dispersion instead, and compare it with the results obtained from the continuum dispersion relation that was used previously. To begin with, note that the dispersion we used in Section 4.3 is obtained from linearizing the lattice dispersion, which is valid only near the nodal point. Thus we expect deviations of the results obtained from the lattice model as compared to that of the linearized continuum model, due to the finite curvature of the Weyl cone. In fact, note that the lattice dispersion Eq. (4.4.6) is not precisely axially symmetric around the z-axis. However, the symmetry does hold approximately. To see this, Taylor expand $\varepsilon^{\text{latt}}(\boldsymbol{k})$ about

an arbitrary momentum $\boldsymbol{\kappa}$

$$\varepsilon^{\text{latt}}(\boldsymbol{k}) = \boldsymbol{v}_{\text{eff}}(\boldsymbol{\kappa}) \cdot (\boldsymbol{k} - \boldsymbol{\kappa}) + \varepsilon^{\text{latt}}(\boldsymbol{\kappa}) + \mathcal{O}\left((\boldsymbol{k} - \boldsymbol{\kappa})^2\right), \tag{4.4.7}$$

where the group velocity at $\boldsymbol{\kappa}$ is

$$\boldsymbol{v}_{\text{eff}}(\boldsymbol{\kappa}) = \frac{v_F^2}{a\varepsilon^{\text{latt}}(\boldsymbol{\kappa})} \left[\sin(\kappa_x a)(2 - \cos(\kappa_y a))\hat{\boldsymbol{e}}_x + \sin(\kappa_y a)(2 - \cos(\kappa_x a))\hat{\boldsymbol{e}}_y\right]. \tag{4.4.8}$$

As far as dynamics is concerned, the constant $\varepsilon^{\text{latt}}(\boldsymbol{\kappa})$ is just an energy shift, and does not contribute to the equations of motion. Therefore we may safely neglect it. We see that to the linear order, the lattice dispersion is indeed invariant under a rotation in the xy plane. Zero in on the Weyl node, we expand $\boldsymbol{v}_{\text{eff}}(\boldsymbol{\kappa})$ near $\boldsymbol{\kappa} = 0$. After some algebra, it can be obtained that $\boldsymbol{v}_{\text{eff}} \approx v_F\hat{\boldsymbol{k}}$, up to third order in $\boldsymbol{\kappa}$, and therefore $\boldsymbol{v}_{\text{eff}} = v_F\hat{\boldsymbol{k}}$ near $\varepsilon^{\text{latt}} = 0$. The lattice dispersion near this point then reads $\epsilon^{\text{latt}}(\boldsymbol{k}) \approx v_F\hat{\boldsymbol{k}} \cdot \boldsymbol{k} = v_F|\boldsymbol{k}|$, precisely the linear dispersion we sought after.

Now we are in a position to discuss the fate of the horizon in the lattice model. The horizon may be defined as the points at which the group velocity vanishes: $\boldsymbol{v}_g(\boldsymbol{r}_t, \boldsymbol{k}) = \partial E/\partial \boldsymbol{k} = 0$. Indeed, in our earlier continuum model of a Weyl node with tilt profile $\boldsymbol{u}(\boldsymbol{r}) = u(\rho)\hat{\boldsymbol{\rho}}$, where $u(\rho) = -v_F(\rho/\rho_t)^\alpha$, we have $\boldsymbol{v}_g(\boldsymbol{r}_t, \boldsymbol{k}) = \partial E/\partial \boldsymbol{k} = \boldsymbol{u}(\boldsymbol{r}_t) + v_F\hat{\boldsymbol{k}} = 0$, and the group velocity vanishes at $\rho = \rho_t$, $\hat{\boldsymbol{\rho}} = \hat{\boldsymbol{k}}$. The fact the ρ_t is indeed an analogue of horizon is discussed in Section 4.3, where we showed that particles cannot escape from $\rho < \rho_t$ using the semi-classical equations of motion. For the lattice model Eq. (4.4.5), however, unless we retain the linearizing approximation above, the equation $\boldsymbol{v}_g(\boldsymbol{r}_t, \boldsymbol{k}) = \boldsymbol{u}(\boldsymbol{r}_t) + \boldsymbol{v}_{\text{eff}}(\boldsymbol{k}) = 0$ has momentum-dependent solutions $\boldsymbol{r}_t(\boldsymbol{k})$. For a given $\boldsymbol{k}$, the analysis in Section 4.3 shall still follow, that is, there is no outward trajectory for such a particle from within $|\boldsymbol{r}_t(\boldsymbol{k})|$. This means that the analogue of the horizon is no longer a single surface with some fixed radius ρ_t, but a family of momentum dependent constraints on the trajectories for particles. That is, the horizon is washed out on the microscopic scale. Nevertheless, in Section 4.4.3, where we compare the trajectories computed from semi-classical equations of motion and microscopic simulations, we shall see that the first approach is still valid up to the length scales ρ_t. As for the "photon cylinder", the separatrix between lensing and capture trajectories, since it is an unstable orbit it should be of no surprise that trajectories obtained using the lattice model will not exactly reproduce such an orbiting motion.

In Fig. 4.6 for comparison we presented the trajectories calculated from using the lattice

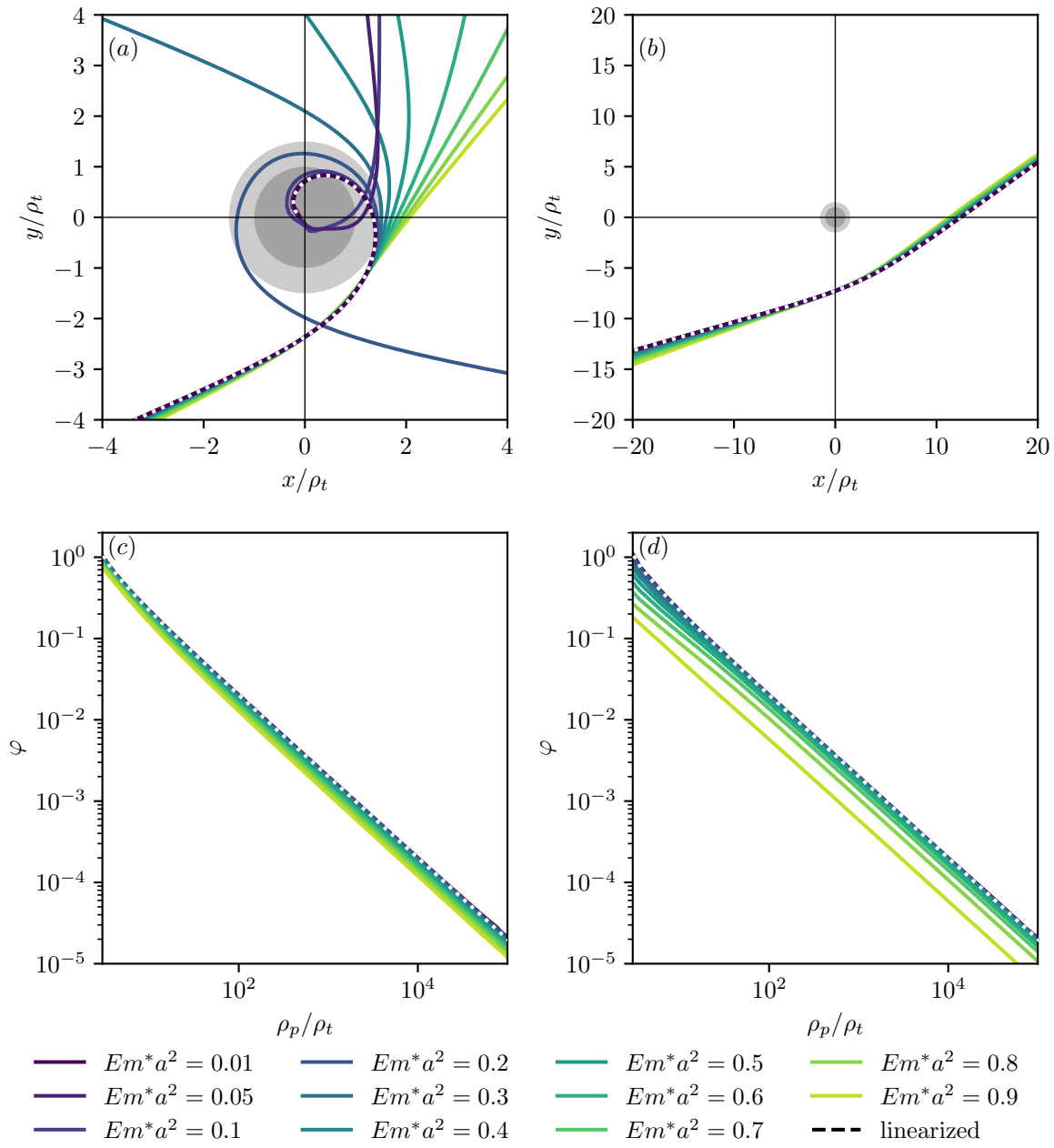

Figure 4.6. In panel (*a*) and (*b*) semi-classical trajectories obtained by using the continuum (dashed line) and lattice (solid lines) model are plotted for $\alpha = 1/2$ with different impact parameters. Initial coordinates are chosen at $x = 0$, and initial momenta $k_y = 0$. For the trajectory from the continuum model, we sued the impact parameters $k_y = 0$ and $k_x\rho_t = 2$. The larger gray sphere represents the photon cylinder, while the inner sphere represents the event horizon. Panel (*a*) shows that the would-be capture trajectories in the continuum model are in fact slingshot motion when the lattice dispersion is used. Panel (*b*) displays the lensed trajectories with various energies, which shows that there are only small deviations in the lattice model from those in the continuum model . In (*c*) and (*d*), we plotted the lensing angle with initial conditions $k_x = -k_y$, and $k_y = 0$ respectively. It is clear that the asymptotic scaling behavior of the deflection angle (see Eq. (4.3.10)) holds.

model together with those from the continuum model with a Schwarzschild-like tilt. Most importantly, we see from panel (*a*) of Fig. 4.6 that the would-be capture trajectory of the

continuum Weyl node model (depicted as the dashed line) does not really just terminate at the origin. Rather, it shoots off again similar to the lensed trajectories. This is physically acceptable for otherwise the particle conservation is violated; after all, we are dealing with solid sate systems and not actual black holes. At small energies (with $\hbar = 1$), $Em^*a^2 \lesssim 0.01$, the trajectories obtained using the linearized dispersion agree with those found using the lattice dispersion Eq. (4.4.6). In contrast, the solution to the capture trajectory for $Em^*a^2 = 0.01$ using the continuum model has a divergence near the origin, and thus we have to terminate the trajectory.

In panel (b) of Fig. 4.6 we platted a series of lensing trajectories obtained using the lattice dispersion, as well as the dashed line using the continuum model. The initial conditions are chosen so that they have the same energies as in panel (a) (the initial positions are different though of course). It can be seen from the plot that the lattice and continuum trajectories match very well, and thus we may conclude for lensing trajectories that stay relatively far way from the tilt center, the continuum tilted Weyl model provides a very good approximation. Furthermore, in panels (c)-(d), we present deflection angles calculated for trajectories associated with the same energy scales but different periapsides ρ_p. Thus in the lattice model we still have the same scaling behavior of the deflection angle $\varphi \propto (u(\rho_p)/v_F)^2$ that we found in the continuum model (see Eq. (4.3.10)).

In conclusion, we find that the semiclassical equations of motion obtained using the low-energy model Eq. (4.4.2) agree rather well with those using the lattice Hamiltonian Eq. (4.4.5). We also discovered that the capture trajectory that falls inside the tilt center, beyond which the continuum theory fails to be applicable, becomes slingshot trajectories demonstrating no such singularities if the regularized lattice model is used. Furthermore, the asymptotic scaling behavior of the deflection angle exists and matches in both cases. Thus from the lattice perspective, the capture motion may be viewed as a special case of the lensed trajectory in which it winds around with a deflection angle $\varphi > \pi/2$. And this is the trace that the photon cylinder leaves in the lattice model, where the separatrix is such that, below it we have the slingshot trajectories.

4.4.2 The microscopic setup

In the above we studied the semi-classical equations of motion using the lattice Hamiltonian, and showed that the results agree with those obtained from the continuum Weyl model. Now we perform a quantum mechanical analysis using the lattice dispersion in Eq. (4.4.4), where we simulate the propagation of an injected particle on the two dimensional lattice using the

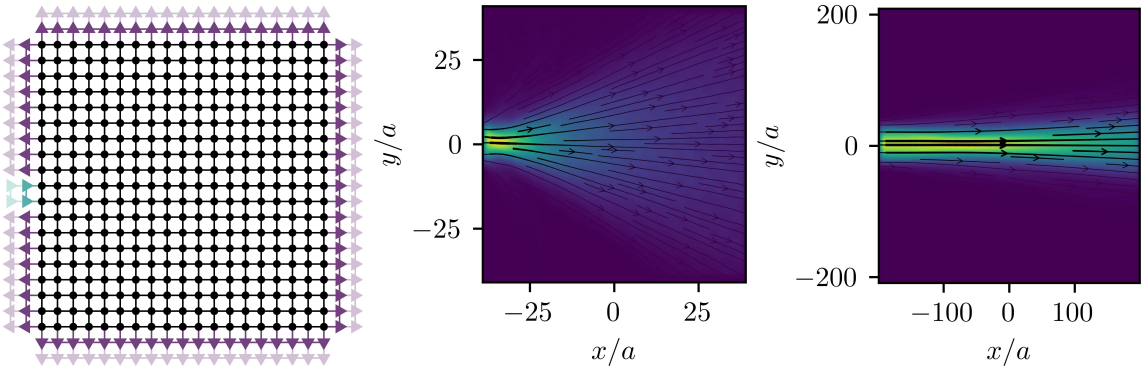

Figure 4.7. The left-most panel depicts the Kwant setup with the system size $L_x = L_y = 19$. The bulk lattice sites are represented by black dots, where electron hoppings are depicted by black lines. The purple and green triangles the semi-infinite leads, explained in the matin text. We inject particles from the blue lead, which may leak out in the purple lead regions. The panels on the right display the charge density (color gradient) calculated with different system sizes using the for un-tilted Weyl dispersions. Both uses energy $Em^*a^2 = 0.8$ and initial momentum $k_x a = 0.832$. The directed lines present the charge current vector field. We see that the wave-packet is more focused with a larger system size.

Kwant library [55]. Let us first describe the Kwant set-up. We use a rectangular lattice consisting of (L_x, L_y) sites that are coupled to six semi-infinite leads. The bulk would have the tilted lattice dispersion Eq. (4.4.4), while the leads have a vanishing tilt profile. One of the leads, the one along the $-\hat{\boldsymbol{e}}_x$ axis where the wave-packets would be injected from, is chosen to be narrow compared to the diameter of the scattering region ($\approx 0.1L_y$). The injected wave-packet corresponds to an incoming particle in the semi-classical picture, and is constructed to have a well-defined average position initially and subsequently spread along the $\hat{\boldsymbol{e}}_y$-direction. The injected particles then move across the bulk and escape from the other leads on the other side, which fully cover the remaining edge sites.

Reflections from the lattice boundary might cause unwanted interference. However, these are suppressed if the horizon radius ρ_t of the tilt profile, which sets the length scale of strong tilt region, is small. More specifically if the tilt profile is such that $\rho_t \ll L_m a$, where $L_m a$ is the minimum distance between the tilt center and the boundary site at which the injected wave leaks out. To simulate the semi-classical regime, we need the horizon radius tilt to be much larger than the lattice spacing $\rho_t \gg a$. Let N_l be the number of bulk lattice sites connected to lead l, then each one of the semi-infinite leads has $2N_l$ bands, which are the transverse projections of the lattice dispersion Fig. 4.5. Since we assume no tilt terms in the leads, the dispersion relations of the leads can be obtained from each other by swapping $k_x \leftrightarrow k_y$ appropriately. We depicted schematically the wave-packets with two different systems sizes in Fig. 4.7. The smaller one with $L_x = L_y = 19$ shows that the wave-packet will

spread out as it travels across the sample bulk. On the other hand, with the same energy, the wave-packet appears to be much more focused in the larger system with over 400 sites depicted on the right in Fig. 4.7. Thus to have wave-packets that have sharply peaked center of mass position, which we need in order to apply the semi-classical equations of motion, a larger system size shall be used.

The finite system size presents a limitation since the wave-packet will never reach its asymptotic deflection angle, which requires a very large number of sites. To resolve the difficulty, instead of computing the deflection angle, we directly calculate the local charge density and compare it with the trajectories computed from the semi-classical equations of motion. Let $|\psi\rangle$ be a scattering state, whose wavefunction is $\psi_{\boldsymbol{r}} = \langle \boldsymbol{r}|\psi\rangle$, then the charge density operator is simply

$$n_{\boldsymbol{r}} = \psi^{\dagger}_{\boldsymbol{r}}\psi_{\boldsymbol{r}}. \tag{4.4.9}$$

4.4.3 Numerical results

We now compute the local charge density for different scattering states and compare them with those obtained from solving the semi-classical equations of motion using the lattice model, Eq. (4.4.6). The initial momenta for the semiclassical equations of motions are the same as those for the injecting lead modes, and the edge sites of the injecting lead give the initial position of the semi-classical wave-packet. This ensures that we use the same set of initial conditions to make a meaningful comparison. As we discussed earlier in this section, the horizon in the lattice model is slightly different from that in the continuum model. Although both are defined as points at which the group velocity vanishes, they are not located at a surface with fixed radius but rather have a momentum dependence. That is, states with different momenta actually experience different horizon radii. However, this should not give a drastic effect, and to continue, we still fix the horizon radius to be at where $u(\rho_t) = -v_F$ at energy $E = 0$ in the lattice computations.

The charge density is computed for a Schwarzschild-like tilt ($\alpha = 1/2$) at a high energy ($Em^*a^2 = 0.8$), and the results of the Kwant simulation is displayed in Figure 4.8. Recall that the photon cylinder has a radius $\rho_s = 3\rho_t/2$, where ρ_t is the analogue event horizon radius. They are depicted as the semi-transparent disks in Figure 4.8. Seven of the semi-classical trajectories are displayed, which are depicted by the directed solid lines. We see that, generally the semi-classical trajectories agree quite well with the quantum mechanical

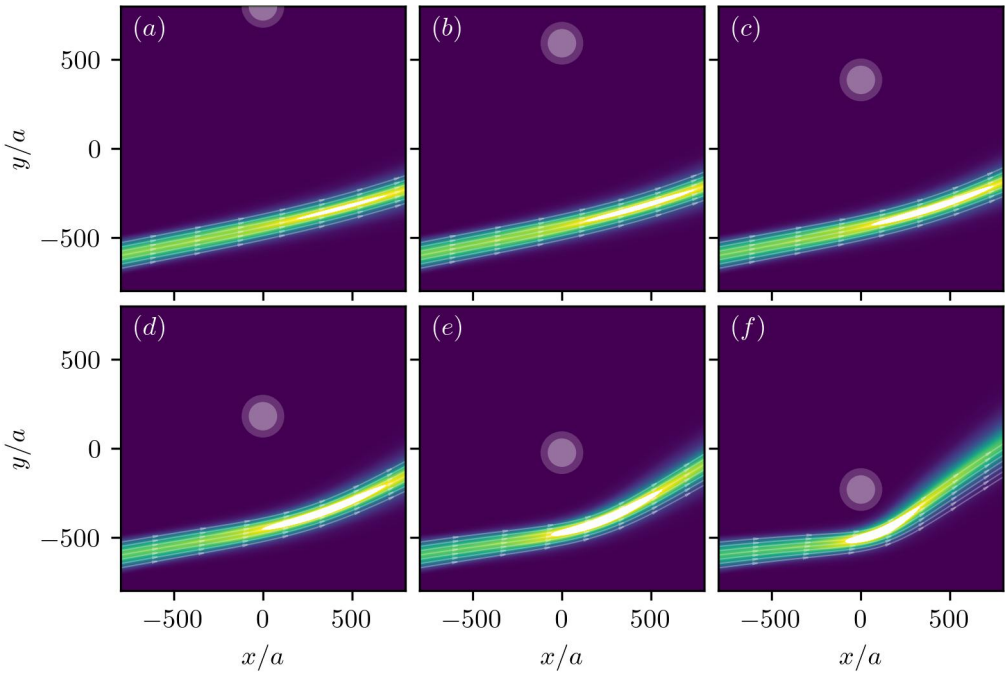

Figure 4.8. Lensing trajectories for different initial conditions, with $\alpha = 1/2$. The disk with radius ρ_t and $\rho_s = 3\,\rho_t/2$ represent the photon cylinder and analogue horizon respectively. The energy of all trajectories is fixed to $Em^*a^2 = 0.8$, with initial momenta are $k_y = 0$ and $k_x a = 0.823$. The semiclassical trajectories obtained from integrating the equations of motion are indicated by directed arrows, while the trajectories obtained from calculating the local density is indicated as color gradient. They agree rather well when the injected wave travels far from the tilt center ((*a*)- (*d*)). From (*e*) and (*f*) we see that when the wave packet gets closer to the tilt center there are some deviations, where the semi-classical trajectories are seen to be deflected more.

ones. In particular, the agreement is better the further away the wave-packet is from the tilt center, namely when the periapsides ρ_p are much larger than ρ_s. Closer to the separatrix at ρ_s, we find that there are some deviations from each other, where the semi-classical results predict a stronger lensing effect, and larger deflection angles.

We saw from the previous section that the would-be capture trajectories become slingshots using the lattice model. In the quantum mechanical calculation, however, more drastic effects are seen when the particles travel inside the horizon, where the wave-packets seem to experience some violent scatterings and separate. To investigate this phenomenon, we would like to zoom in around the tilt center. With a fixed system size, this means we need a larger horizon radius ρ_t. However, this introduces more unwanted boundary reflections around the system-lead interface since the tilt would still be present there. For this reason, we switch to a tilt profile with $\alpha = 1$ instead, which has a faster decay rate than the Schwarzschild-like tilt, and larger horizon radius may be used.

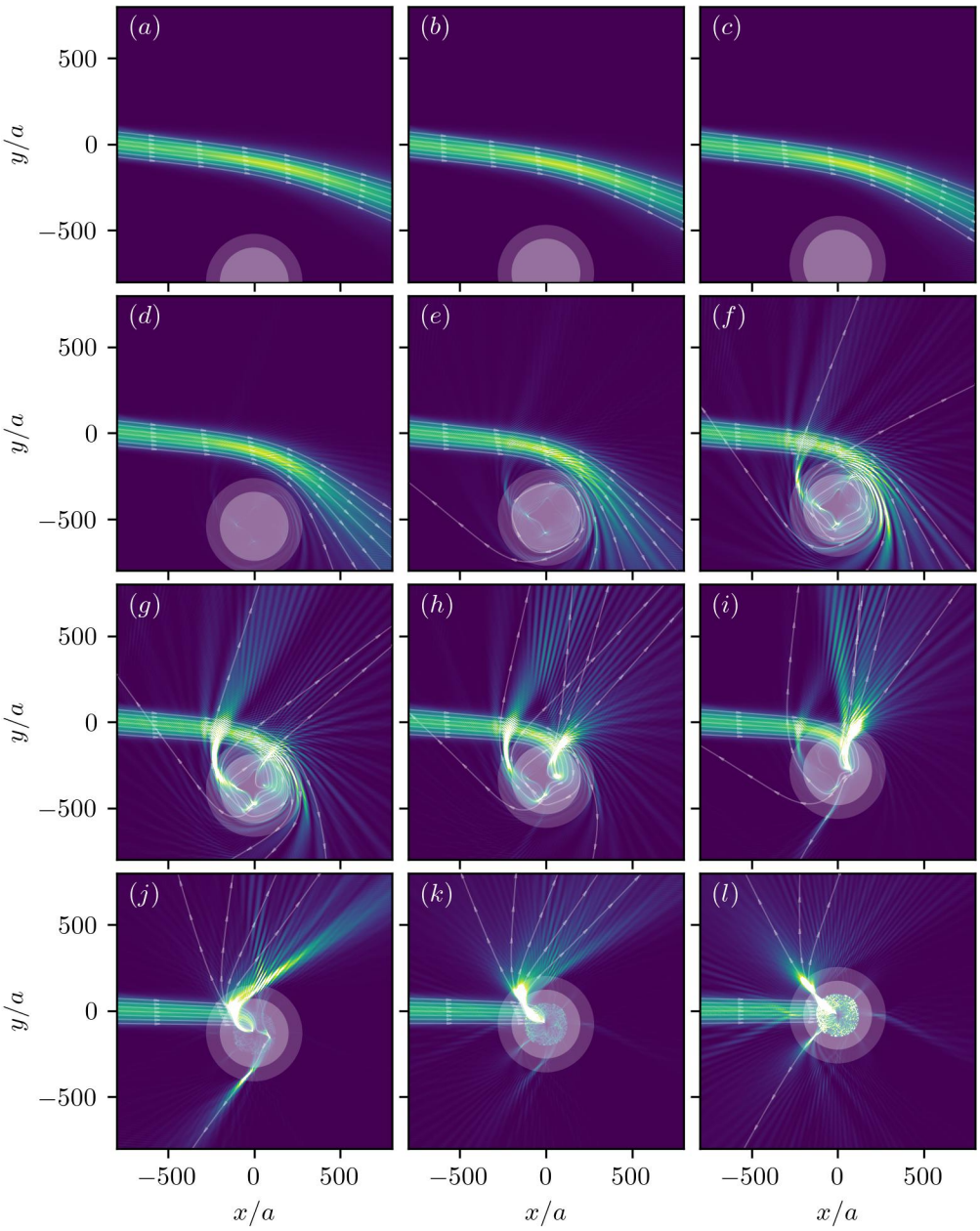

Figure 4.9. Trajectories with different initial conditions are plotted for the tilt profile with $\alpha = 1$, with energy fixed to $Em^*a^2 = 0.4$, and initial momenta $k_y = 0$, $k_x a = 0.403$. The plotting style is same as those in Fig. 4.8. In (e) to (f) we see that the microscopic simulations show some significant differences from the cases where the wave-packets travels away from the center. Not only the outgoing wave-packets deviates significantly from the semi-classical ones, they do not even stay coherent, but splits into beams. Moreover, in (k) and (l) we see that there are aa large number of scatterings that happen within a smaller disk, inside the horizon.

The results of the simulation are presented in Fig. 4.9, where we use a lower energy $Em^*a^2 = 0.4$. Overall, qualitatively the same types of trajectories are observed. From panels (a), (b) and (c) we see that the same lensed trajectories when the wave-packets are staying far away from the tilt center are obtained. In panels (d) to (i), we see when moving near the tilt center, where we should have slingshot motion in semi-classical approach, we

find however that the injected wave-packets do no stay focused, but rather split into various jets upon leaving the tilt center, and deviates significantly from the semi-classical predictions. When multiple jets cross each other, some interference patterns are observed. In panels (j) to (l), we display the simulation of trajectories that pass the tilt center. Here for some of the semi-classical wave-packets the numerical evaluation suffer from instability, and we have to terminate around the tilt center escape from the analogue black hole (where the velocity exceeds $100\, v_F$). This seems to suggest that not all of the semi-classical trajectories escape from within the horizon ρ_t. For instance in panel (K), only 5 out of the 7 semiclassical trajectories escape However, the dominant jets free from this instability still follow the semi-classical trajectories. More interestingly, we see some violent scatterings confined within a circular domain of size $\approx 0.8\rho_t$ near the tilt center. At the moment of the completion of this thesis, we do not know explanation of these phenomena that we observe in the quantum mechanical calculation, which we think is an interesting question that is worthy of further investigation.

In conclusion, the quantum mechanical simulations of the lattice model confirm that overall the semiclassical equations of motion do indeed provide a valid description of the particle motion, as long as it is moving far away from the tilt center. This includes the slingshot motion that we obtained using the lattice dispersion in the semi-classical approach. However, when near the center of the analogue black hole, where the tilt strength is large the semi-classical picture seems to break down, where the wave-packet does not stay focused but split, and some scattering pattern confined within a certain region near the tilt center is observed.

4.5 Berry curvature and transverse shift

In Section 4.3, we analyzed semi-classical equations of motion of tilted Weyl nodes. As we discussed there, due to the axial symmetry of the tilt profiles, $\dot{z}$ decouples from the other coordinates for particles with initial momentum $k_z = 0$, and the motion is planar. However, the semi-classical equations of motion Eq. (4.3.1) also includes the anomalous velocity term due to Berry curvature, and this actually causes a movement along the z direction. In this section we show analyze the transverse shift caused by the anomalous velocity. To isolate this effect, we still assume $k_z = 0$, so that the initial $\dot{z} = 0$ when the particle is injected from far from the tilt center.

With $k_z = 0$, and a cylindrical tilt profile, the z component of the equation of motion

Eq. (4.3.2) has only contribution from the anomalous velocity term due to the finite Berry curvature of Weyl semi-metals, i.e., the term $\dot{\boldsymbol{k}} \times \boldsymbol{\Omega}$. Note that the direction of this term depends on the chirality χ of the Weyl nodes, which is the topological charge it carries, and thus has no classical analogue. This anomalous velocity term leads to a variety of different phenomena in Weyl semi-metals, depending on the physical origin of the force $\dot{\boldsymbol{k}}$. For instance, it is used to explain the chirality-dependent Hall conductance in Weyl materials [49, 65, 73], and the Imbert-Federov shift [74] or chiral impurity scattering [75]. Similarly in tilted Weyl semi-metals it is known to cause a chiral Hall response [88, 98], and different refraction ratio in potential barrier tunneling [167]. In non-equilibrium transport, the transverse motion this Berry curvature term induces 'anomalous currents', which leads to the chiral magnetic and chiral vortical effects in Weyl systems and have been investigated in connection to the so-called chiral anomaly that originated from high-energy physics [13, 35, 36, 89, 127, 135, 139, 166]. Our discussion of the transverse shift concerns its effect in the case of tilted Weyl nodes. By our mapping of a tilted Weyl node to curved spacetime, this hints at a similar effect to massless particles traveling around a black hole. In fact, such an effect for photons has indeed been studied in the gravitational context, where it is known as the gravitational spin Hall effect [54, 61, 110].

Since the force $\dot{\boldsymbol{k}}$ has only $\hat{\boldsymbol{\rho}}$ and $\hat{\boldsymbol{\phi}}$ components, the anomalous velocity only has z-component, which explicitly reads

$$\dot{z} = -\frac{\chi}{2k^3}\left(\frac{\partial u}{\partial \rho} - \frac{u}{\rho}\right)(\boldsymbol{k}\cdot\hat{\boldsymbol{\rho}})\,\frac{L_z}{\rho}. \tag{4.5.1}$$

For the lensed trajectories, as shown in Fig. 4.10, the wavepacket moves in the z-direction, while the motion on the xy-plane is un-altered as before. Similar to the deflection angle, this transverse shift can be calculated using the equations of motion, which gives

$$\frac{dz}{d\rho} = \frac{\dot{z}}{\dot{\rho}} = -\frac{\chi}{2\,k^3}\frac{\frac{\boldsymbol{k}\cdot\hat{\boldsymbol{\rho}}}{\rho}\left(\frac{\partial u}{\partial \rho} - \frac{u}{\rho}\right)L_z}{u + v_F\,\frac{\boldsymbol{k}\cdot\hat{\boldsymbol{\rho}}}{k}}. \tag{4.5.2}$$

Analytically expressions can be obtained for lensed trajectories that stay far away from the tilt center ($\rho_p/\rho_t \gg 1$), which is found to be

$$\Delta z \approx -\frac{\chi}{L_z}\,\rho_p\,\frac{u(\rho_p)^2}{v_F^2}\,\frac{\sqrt{\pi}\,\Gamma\left(\alpha+\frac{1}{2}\right)}{2\,\Gamma(\alpha)}. \tag{4.5.3}$$

We leave the details of the derivation and calculation of the above results to the appendix (see Section B.3).

This term has a remarkable consequence for the trajectory on the photon sphere. Although the anomalous velocity does not affect the motion projected to the xy-plane, and the location of separatrix itself receives no change when the Berry curvature is taken into account. However, due to this transverse shift, depending on chirality, the wavepacket will spiral upward or downward along the z direction while staying at a fixed radius. This is depicted in Fig. 4.14.

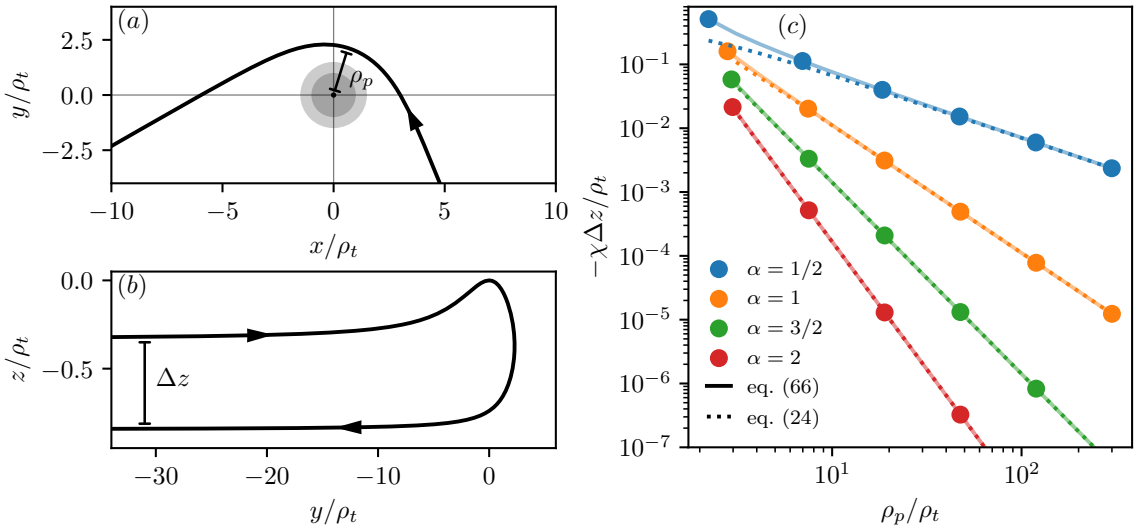

Figure 4.10. In panels (a) and (b), we plotted a typical lensed trajectory that is projected onto the the xy and yz planes respectively. Here we use $\alpha = 1/2$, $\rho_p/\rho_t = 2.23$. The transverse shift is calculated to be $\Delta z = -0.512$. In (c), we plotted the transverse shifts $-\Delta z$ calculated by numerically integrating the semiclassical equations of motion (dots), and the shift formula Eq. (B.3.6) (solid lines). The dotted lines are the results obtained from using the asymptotic formula Eq. (4.5.3) (dotted line) for different α (different colors). It is clear that for $\rho > \rho_t$, where the wave-packets stay far away from the tilt center, the asymptotic approximation is very accurate. All results are for the chirality $\chi = +1$.

4.5.1 Spin precession

Note that the anomalous velocity depends on the chirality χ, and in the early parts of the thesis, we know that in the solid state context, it is in fact a momentum space topological charge associated with the Berry curvature monopole. Therefore it is not surprising that the anomalous velocity is related to the topological spin-transport of massless particles [23, 24, 142–144]. Furthermore, the semiclassical equations of motion coincide with those

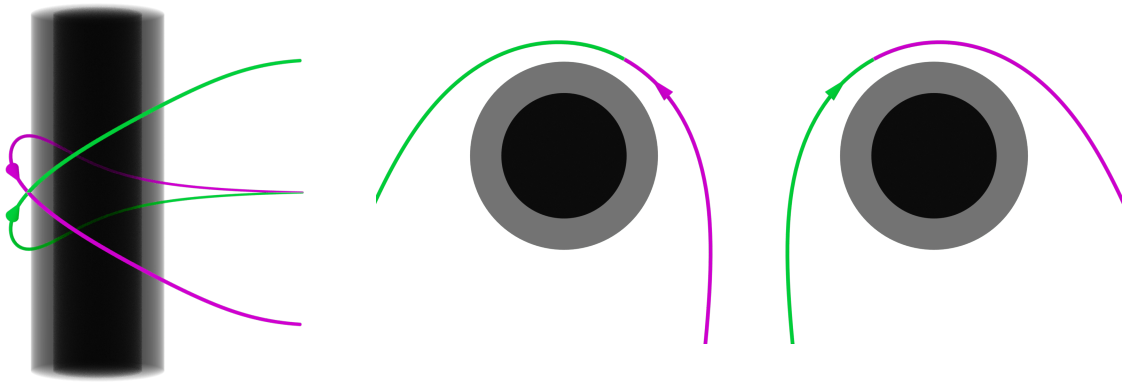

Figure 4.11. Lensing trajectories for different chiralities. The black and gray cylinder represent the analog horizon and photon cylinder respectively. The projected trajectories show that the planar motion is not affected by the anomalous velocity.

of a massless spinning particle, i.e a Weyl fermion [41, 42], and thus it is of interest to study the spin dynamics in more detail.

Recall the proper notion of the spin angular momentum of the Weyl particle is its helicity, which when evaluated to a state with definite momentum is $\boldsymbol{s} = \chi/2\hat{\boldsymbol{k}}$, and its dynamics is then given by

$$\frac{d\boldsymbol{s}}{dt} = \frac{\chi}{2}\frac{(\boldsymbol{k}\times\dot{\boldsymbol{k}})}{k^3}\times\boldsymbol{k} = \boldsymbol{\omega}_{\text{sp}}\times\boldsymbol{s}, \tag{4.5.4}$$

where we have introduced a frequency $\boldsymbol{\omega}_{\text{sp}} = (\boldsymbol{k}\times\dot{\boldsymbol{k}})/k^2$. This is a spin precession. Explicitly for our axially symmetric tilt, assuming again $k_z = 0$, we have

$$\boldsymbol{\omega}_{\text{sp}} = \frac{(\boldsymbol{k}\cdot\hat{\boldsymbol{\rho}})}{\rho\, k^2}\left(\frac{\partial u}{\partial\rho} - \frac{u}{\rho}\right) L_z\,\hat{\boldsymbol{z}}. \tag{4.5.5}$$

Using the explicit form of the Berry curvature of the Weyl Hamiltonian, this precession is directly related to the anomalous velocity $\dot{\boldsymbol{r}}_A$ as

$$\dot{\boldsymbol{r}}_A = \dot{\boldsymbol{k}}\times\boldsymbol{\Omega} = -\frac{\chi}{2\,k}\,\boldsymbol{\omega}_{\text{sp}}, \tag{4.5.6}$$

from which we see that the transverse shift from the anomalous velocity may be intuitively understood as a spin spinning effect, a sort of "Magnus effect" as in a banana kick in football.

In our case, $\dot{\boldsymbol{k}}$ originates from the analogue gravitation attraction due to the the tilt profile, and in turn, this spin dynamics also induces dynamics in the orbital angular momentum, since we require the conservation of the total angular momentum. The dynamics of position, mo-

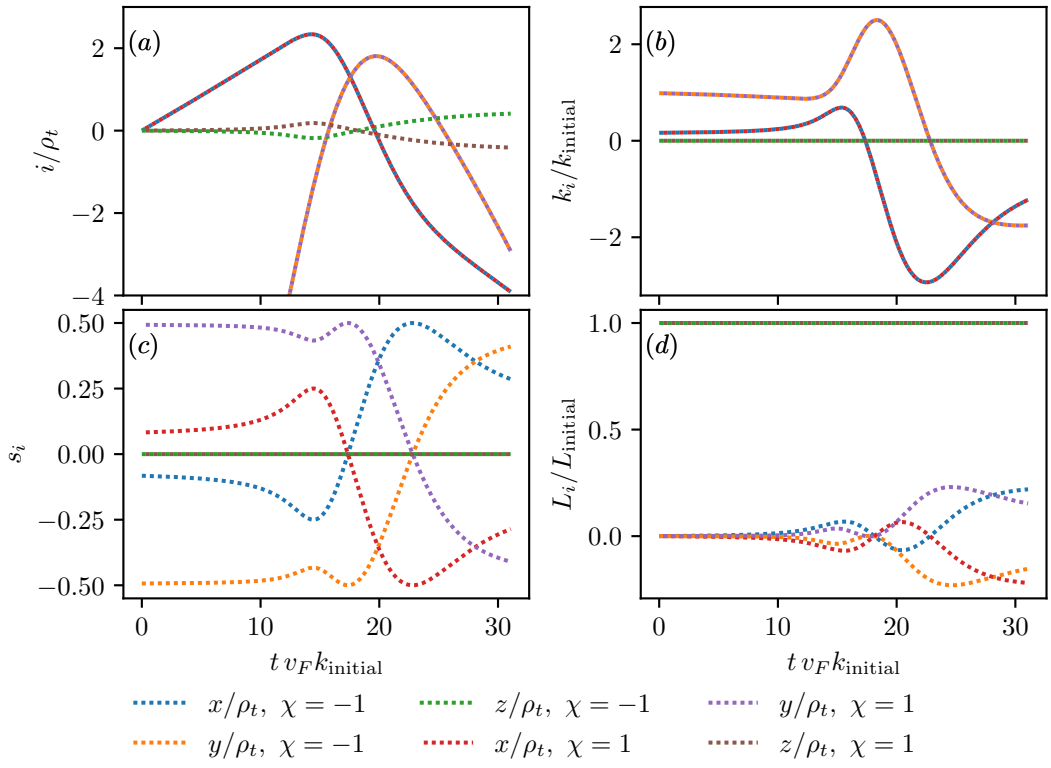

Figure 4.12. In panels (*a*) and (*b*), evolution of the *x*- and *y*-components of the position and momenta are plotted. As expected, they are independent of the chirality. On the other hand, plotted in panels (*c*) and (*d*), the *z*-coordinate and the *x*- and *y*-components of spin and orbital angular momentum do depend on the chirality, which have opposite evolution as shown in the plots. In panel (*d*) we see that the orbital angular momentum is increased.

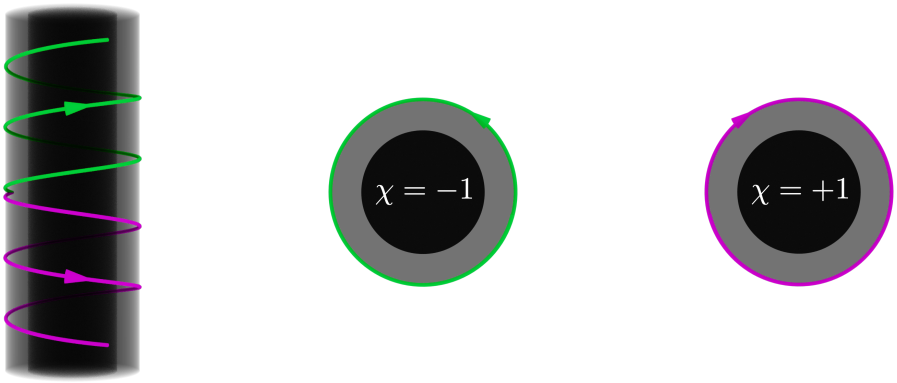

Figure 4.13. The trajectories on the photon cylinder for the Schwarzschild-like tilt. The dark inner cylinder represents the analogue horizon.

mentum, spin and orbital angular momentum are shown in Fig. 4.12 and Fig. 4.14 for the lensed and photon cylinder trajectory, respectively. Back in Section 4.3, we already remarked that with $k_z = 0$, by axial symmetry the *z*-component of the spin and orbital angular momentum s_z and L_z are actually conserved separately, and thus we only need to consider the dynamics in the *x*- and *y*-components of spin and angular moment.

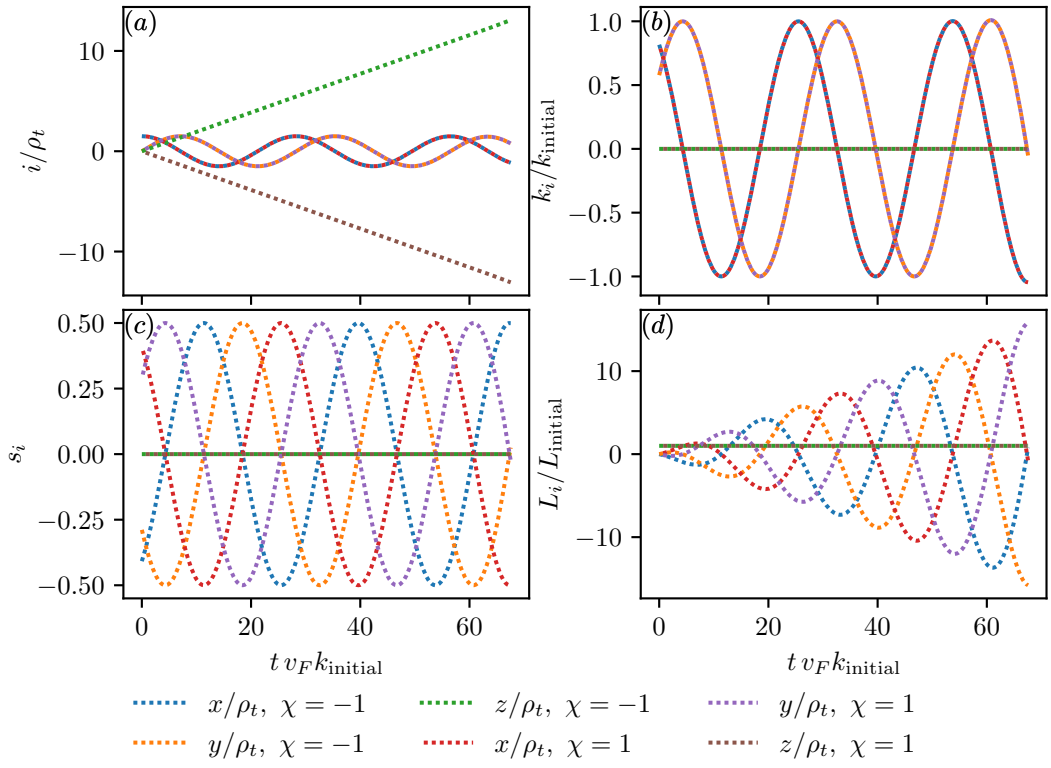

Figure 4.14. In panels (a) and (b), the dynamics of the $x-$ and y-components of the coordinates and momentum are shown, which confirms the assertion that the planar motion is independent of the chirality. They oscillate around the $\hat{z}$ axis during the winding motion along the photon cylinder. On the other hand, panels (c) and (d) show that the z-coordinate and the planar components of the spin and orbital angular momenta are chirality dependent. The spin precession undergoes an oscillatory motion (panel (c)), while the angular momentum grows in magnitude in addtion (panel (d)).

From Fig. 4.12 we see that the shift occurs around the periapsis of the lensed trajectory, accompanied by a rapid change of the non-conserved components of momentum, and angular momentum. After leaving the tilt center, the transverse shift approaches the asymptotic values calculated in Eq. (4.5.3), where the comparison to the exact numerical results are shown in Fig. 4.10. The spin dynamics ceases when the electron no longer feels the tilt, and we see from plots in panels (c) and (d) that part of the x- and y-components of the spin angular momentum is transferred to orbital angular momentum, and the particle leaves the tilt region with a higher orbital angular as can be seen from the plots. Plots in panels (b) and (c) clear show an oscillatory pattern associated with the spin precession. Here as well, we see that magnitude of the orbital angular momentum grows, shown in (d).

We have also plotted the orbiting trajectories on the photon cylinder in Fig. 4.14. The trajectories corresponding to the two chiralities craw along the cylinder in opposite directions along the z-axis, due to the different sign of the anomalous velocity term.

Since the Weyl nodes have an apparent connection to Weyl fermions, which are relativistic particles with spin, we may also discuss the anomalous velocity and spin precession in the context of relativistic quantum mechanics. The characteristic quantum numbers of a Weyl fermion can be identified as momentum and spin [40, 113], and indeed such an anomalous velocity term has been obtained in a quantum mechanical approach and shown to be related to the spin dynamics [143]. More generally, the implications of the Lorentz invariance of the Weyl Hamiltonian on the semi-classical dynamics have been extensively studied, see for instance [8, 35, 41–43, 142–144]. In the tilted Weyl nodes, the anomalous velocity and spin dynamics can be further understood using the notion of local Lorentz boosts. Intuitively we know that the tilted Weyl cones form the analogue of moving light cones in curved space-times, while the latter may be obtained from Lorentz boosts that vary from point to point [160]. Similarly, the tilted Weyl Hamiltonian may be obtained from an un-tilted one using a Lorentz transformation [126, 148, 168]. We may then obtain the evolution of the spin angular momentum for a particle moving in a spatially varying tilt profile from performing a sequence of non-collinear Lorentz boosts at each point. This is the physics of Thomas precession, and thus we see the Berry curvature induced spin precession may be understood in this way as well [143]. This gives another example where the tilted Weyl nodes are an ideal playground for studying relativistic effects in solid state systems.

4.6 Summary

In this chapter we have studied the dynamics of electrons around tilted Weyl nodes, specifically in the context of mapping its trajectory to that of the geodesics of a particle moving around an analogue black hole. We considered an inhomogeneous tilt profile that is cylindrically symmetric, and studied the dynamics in three different approaches : (i) an effective continuum description where the electron trajectory is taken to be the geodesic equations corresponding to the effective metric given by the titled Weyl Hamiltonian; (ii) the semi-classical equations of motion using the dispersion relations given by a microscopic lattice model, and (iii) a numeric computation using quantum-mechanical scattering states in the lattice model.

We found that the geodesic equations of the effective metric given by our axially symmetric tilt profile also has an analogue "photon cylinder" as in actual Schwarzschild black hole, i.e., an unstable orbit which separates captured trajectories from scattering trajectories corresponding to gravitational lensing. The semi-classical equations of motion of the continuum model encounter difficulties when the particles plunge into the tilt center, where the trajectories have to be terminated by hand. However, the semi-classical equations of motion remain a valid approximation if we use the lattice dispersion instead of the simple Weyl Hamiltonian. There we found that the in-falling trajectories using the continuum model become slingshot motion, where the particles escape again, instead of being captured. Moreover, we compared the trajectories obtained using the semi-classical equations of motion with those from a quantum-mechanical calculation. We found that as long as the wave-packets travel at a distance from the horizon, the two approaches agree rather well. In particular, the deflection angle of the electron lensing possesses an asymptotic scaling behavior in both approaches. More interestingly, we found that when getting even closer to the tilt center, there appears a region inside which violent scatterings occur. This is some phenomenon inside the "even horizon" and is worthy of further investigation. Beyond the geodesic equation of motion, the Berry curvature provides an additional anomalous velocity contribution to the semi-classical equation of motion. We have also shown that while this term does not affect the in-plane component of the trajectories, it induces a transverse shift instead, with the direction given by the chirality of the Weyl cone, or equivalently its topological charge.

Appendix for Part II

B.1 Geodesic equation

In this appendix we shall demonstrate explicitly the mapping of a tilted Weyl node with spatially inhomogeneous tilt to relativistic Weyl fermions in curved spacetimes [21, 56, 63, 70, 80, 93, 104, 130, 154, 155, 161, 169]. This mapping can be done at the level of the Hamiltonian, where we write it by introducing the tetrad (also known as vielbeins), which is defined as a set of fields that satisfy $g_{\mu\nu}(\boldsymbol{r}) = e^a_\mu e^b_\nu \eta_{ab}$, with η_{ab} being the flat spacetime Minkowski metric[21, 154, 155, 161]. Roughly speaking the tetrads represent a local Lorentz frame, using which we may define a set of local Pauli matrices and spinor covariant derivatives which couple the Weyl fermion to gravity. For our purposes, however, it is sufficient to take a simpler approach, where we shall show that the dispersion relation of a tilted Weyl node coincides with that of a particle in a curved spacetime with a metric $g_{\mu\nu}$, the Painlevé-Gullstrand form of Schwarzschild metric. It is also known as the acoustic metric[120, 156]. Here and in the following, the metric signature is $(-+++)$, and the four vector is denoted by $x^\mu = (ct, \boldsymbol{x})$ (c is the speed of light).

Explicitly, by a change of coordinates which we already mentioned in the main text, the famous Schwarzschild black hole metric may be re-written as

$$ds^2 = g_{\mu\nu}dx^\mu dx^\nu = -\left(1 - \frac{u(\boldsymbol{r})^2}{c^2}\right)c^2dt^2 - 2\boldsymbol{u}(\boldsymbol{r})\cdot d\boldsymbol{r}dt + d\boldsymbol{r}^2, \tag{B.1.1}$$

which is known as the Painlevé-Gullstrand metric . The field $\boldsymbol{u}(\boldsymbol{r})$, which corresponds to the inhomogeneous tilt of the Weyl node can be interpreted as the local free-fall velocity field under the gravity of a black hole[120]. We may write the metric tensor $g_{\mu\nu}$ in a matrix form, which reads

$$g = \frac{1}{c}\begin{pmatrix} u(\boldsymbol{r})^2/c - c & -u_x(\boldsymbol{r}) & -u_y(\boldsymbol{r}) & -u_z(\boldsymbol{r}) \\ -u_x(\boldsymbol{r}) & c & 0 & 0 \\ -u_y(\boldsymbol{r}) & 0 & c & 0 \\ -u_z(\boldsymbol{r}) & 0 & 0 & c \end{pmatrix}, \tag{B.1.2}$$

where the components of the matrix g is $(g)_{\mu\nu}g_{\mu\nu}$ (and not the inverse metric $g^{\mu\nu}$). For a massless particles moving in this spacetime, the energy momentum relation is given by $g^{\mu\nu}k_\mu k_\nu = 0$, where $k_\mu = (-E/c, \boldsymbol{k})$ is the momentum four-vector, which reads explicitly

$$0 = g^{\mu\nu}k_\mu k_\nu = k^2 - \frac{(E - \boldsymbol{u}(\boldsymbol{r})\cdot\boldsymbol{k})^2}{c^2}. \tag{B.1.3}$$

Solving for the energy, we find that the solutions are precisely the dispersion relation of a tilted Weyl cone

$$E_{\pm} = \boldsymbol{u}(\boldsymbol{r}) \cdot \boldsymbol{k} \pm c|\boldsymbol{k}|. \tag{B.1.4}$$

This then establishes the Weyl cone associated with the tilted Weyl nodal point can be mapped to the local light-cone structure at each point in a curved spacetime [154]. For the Schwarzschild spacetime, the velocity field $\boldsymbol{u}(\boldsymbol{r})$ reads explicitly $\boldsymbol{u}(\boldsymbol{r}) = -c\sqrt{r_H/r}\,\hat{\boldsymbol{r}}$ in spherical coordinates, where $\hat{\boldsymbol{r}}$ is the unit vector, $r_H = GM/c^2$ is the radius of the event horizon, G denotes the universal gravitational constant and M corresponds to the mass of a black hole. In electronic systems, the analogy is readily established by replacing the speed of light by the Fermi velocity v_F, and the black hole radius is a parameter r_t given by the tilt profile, $r_H \to r_t$, which marks the boundary between a type I and an overtilted type II region.

In the main text, in contrast to the spherical Schwarzschild blakc hole, we considered tilt profiles with axial symmetry. However, as far as the motion projected onto the plane perpendicular to the axis, the motion described by the geodesic equation is identical to that given by the semi-classical equations of tilted Weyl node, if the Berry curvature term is neglected. Specifically, we shall demonstrate the equivalence between Hamilton's equations given by the dispersion relation coincides with the geodesic equation, which is the equation of motion for a particle moving under gravity. The key lies in the fact that in the Hamiltonian approach to study a general relativistic particle, the appropriate Hamiltonian to be used is [33]

$$\mathcal{H}(\{x^{\alpha}(\tau)\}, \{k_{\beta}(\tau)\}) = \frac{1}{2} g^{\mu\nu}(\{x^{\alpha}(\tau)\}) k_{\mu}(\tau) k_{\nu}(\tau), \tag{B.1.5}$$

where $\{x^{\mu}(\tau)\}$ and $\{k_{\mu}(\tau)\}$ are the canonical coordinates and momenta, and τ is an affine parameter, which in general is not the time coordinate. We shall justify the relativistic Hamiltonian by first deriving the geodesic equation from it, and then establish the mapping by showing that it also gives the equations of the tilted Weyl node. We have that the Hamilton's equations read

$$\frac{dx^{\mu}}{d\tau} = \frac{\partial \mathcal{H}}{\partial k_{\mu}} = g^{\mu\nu} k_{\nu}, \tag{B.1.6}$$

$$\frac{dk_{\mu}}{d\tau} = -\frac{\partial \mathcal{H}}{\partial x^{\mu}} = -\frac{1}{2}(\partial_{\mu} g^{\nu\sigma}) k_{\nu} k_{\sigma}, \tag{B.1.7}$$

where $\partial_\mu g^{\nu\sigma} = \frac{\partial g^{\nu\sigma}}{\partial x^\mu}$. By multiplying both sides of the first equation with the metric tensor, and using $g_{\mu\nu}g^{\nu\alpha} = \delta^\alpha_\mu$, we obtain the relation

$$k_\mu = g_{\mu\nu}\frac{dx^\nu}{d\tau}, \tag{B.1.8}$$

namely, the four-momenta is just the four-velocity. Taking a further derivative of the first equation with respect to τ, we have

$$\frac{d^2x^\mu}{d\tau^2} = g^{\mu\nu}\frac{dk_\nu}{d\tau} + (\partial_\lambda g^{\mu\nu})\frac{dx^\lambda}{d\tau}k_\nu = g^{\mu\nu}\frac{dk_\nu}{d\tau} + (\partial_\lambda g^{\mu\nu})\frac{dx^\lambda}{d\tau}g_{\nu\sigma}\frac{dx^\sigma}{d\tau}.$$

Substituting in Eq. (B.1.7), we get

$$\frac{d^2x^\mu}{d\tau^2} = -\frac{1}{2}g^{\mu\nu}(\partial_\nu g^{\sigma\lambda})k_\sigma k_\lambda + (\partial_\lambda g^{\mu\nu})g_{\nu\sigma}\frac{dx^\lambda}{d\tau}\frac{dx^\sigma}{d\tau}. \tag{B.1.9}$$

We eliminate k_σ by using Eq. (B.1.8) and arrive at

$$\frac{d^2x^\mu}{d\tau^2} = -\frac{1}{2}g^{\mu\nu}(\partial_\nu g^{\sigma\lambda})g_{\sigma\alpha}g_{\lambda\beta}\frac{dx^\alpha}{d\tau}\frac{dx^\beta}{d\tau} + (\partial_\lambda g^{\mu\nu})g_{\nu\sigma}\frac{dx^\lambda}{d\tau}\frac{dx^\sigma}{d\tau}. \tag{B.1.10}$$

From $g_{\mu\nu}g^{\nu\sigma} = \delta^\sigma_\mu$ follows $\partial_\sigma g^{\mu\nu} = -g^{\mu\alpha}(\partial_\sigma g_{\alpha\beta})g^{\beta\nu}$, which leads to

$$\begin{aligned}
\frac{d^2x^\mu}{d\tau^2} &= \frac{1}{2}g^{\mu\nu}g^{\sigma\gamma}g_{\sigma\alpha}(\partial_\nu g_{\gamma\kappa})g^{\kappa\lambda}g_{\lambda\beta}\frac{dx^\alpha}{d\tau}\frac{dx^\beta}{d\tau} - g^{\mu\alpha}(\partial_\lambda g_{\alpha\beta})g^{\beta\nu}g_{\nu\sigma}\frac{dx^\lambda}{d\tau}\frac{dx^\sigma}{d\tau} && \text{(B.1.11a)}\\
&= \frac{1}{2}g^{\mu\nu}(\partial_\nu g_{\alpha\beta})\frac{dx^\alpha}{d\tau}\frac{dx^\beta}{d\tau} - g^{\mu\alpha}(\partial_\lambda g_{\alpha\sigma})\frac{dx^\lambda}{d\tau}\frac{dx^\sigma}{d\tau} && \text{(B.1.11b)}\\
&= \frac{1}{2}g^{\mu\nu}\Big((\partial_\nu g_{\alpha\beta}) - 2(\partial_\alpha g_{\nu\beta})\Big)\frac{dx^\alpha}{d\tau}\frac{dx^\beta}{d\tau} && \text{(B.1.11c)}\\
&= \frac{1}{2}g^{\mu\nu}\Big((\partial_\nu g_{\alpha\beta}) - (\partial_\alpha g_{\nu\beta}) - (\partial_\beta g_{\nu\alpha})\Big)\frac{dx^\alpha}{d\tau}\frac{dx^\beta}{d\tau} && \text{(B.1.11d)}\\
&= -\Gamma^\mu_{\alpha\beta}\frac{dx^\alpha}{d\tau}\frac{dx^\beta}{d\tau}, && \text{(B.1.11e)}
\end{aligned}$$

where $\Gamma^\mu_{\alpha\beta} = g^{\mu\nu}(\partial_\alpha g_{\nu\beta} + \partial_\beta g_{\nu\alpha} - \partial_\nu g_{\alpha\beta})/2$ are the Christoffel symbols. This is precisely the geodesic equation [33, 160]. Acceleration in general relativity is defined in terms of the covariant derivative ∇_α as

$$a^\mu(\tau) = \frac{dx^\alpha}{d\tau}\nabla_\alpha\frac{dx^\mu}{d\tau} \equiv \frac{dx^\alpha}{d\tau}\left(\partial_\alpha\frac{dx^\mu}{d\tau} + \Gamma^\mu_{\alpha\beta}\frac{dx^\beta}{d\tau}\right). \tag{B.1.12}$$

And we see that the geodesics, i.e. trajectories $x^\alpha(\tau)$ are solutions to the geodesic equation satisfy

$$a^\mu(\tau) = \frac{d^2x^\mu}{d\tau^2} + \Gamma^\mu_{\alpha\beta}\frac{dx^\alpha}{d\tau}\frac{dx^\beta}{d\tau} = 0. \tag{B.1.13}$$

That is geodesics are exactly those curves with with a vanishing acceleration $a^\mu(\tau) = 0$, which is just the weak form of general equivalence [160].

Having shown the Hamiltonian Eq. (B.1.5) does indeed give the geodesic equation, we shall now also show that the Hamilton equations can be re-written as the semiclassical equations of motion of the tilted Weyl node. For this we need to change the parameterization of the dynamical variables from τ to t.

In fact, besides Hamilton's equations, for Eq. (B.1.5) to describe the general dynamics of a massless relativistic particle with the correct energy-momentum relation, one has to impose as an on-shell constraint that $\mathcal{H}\left(\{x^i\},\{k_i\}\right) = 0$, where x^μ and k^μ are solutions to Hamilton's equations [33]. Recall the definition of the four-momentum $k_\mu = (-E/c, \boldsymbol{k})$, and we may write out the relativistic Hamiltonian explicitly as

$$\mathcal{H}\left(E,\{x^i\},\{k_i\}\right) = \frac{E^2}{2c^2}g^{00} - \frac{E}{c}g^{0i}k_i + \frac{1}{2}g^{ij}k_ik_j. \tag{B.1.14}$$

In the main text it is remarked that there are two solutions of energy $E(\{x^i\},\{k_i\})$ which satisfy this equation, and are exactly the tilted dispersion relation of the tilted Weyl node. Upon taking the derivative of $\mathcal{H}\left(\{x^i\},\{k_i\}\right) = 0$ with respect to k_i, and noting that the Hamilton's equation of the 0-component of x^μ reads

$$\frac{dt}{d\tau} = \frac{1}{c}\frac{dx^0}{d\tau} = \frac{1}{c}\frac{\partial\mathcal{H}}{\partial k_0} = -\frac{\partial\mathcal{H}}{\partial E}, \tag{B.1.15}$$

we have

$$0 = \frac{\partial\mathcal{H}}{\partial E}\frac{\partial E}{\partial k_i} + \frac{\partial\mathcal{H}}{\partial k_i} = -\frac{dt}{d\tau}\frac{\partial E}{\partial k_i} + \frac{\partial\mathcal{H}}{\partial k_i}. \tag{B.1.16}$$

Or, using Eq. (B.1.6),

$$\frac{dx^i}{d\tau} = \frac{\partial E}{\partial k_i}\frac{dt}{d\tau}. \tag{B.1.17}$$

From this we immediately obtain the semiclassical equations of motion

$$\frac{dx^i}{dt} = \frac{dx^i}{d\tau}\left(\frac{dt}{d\tau}\right)^{-1} = \frac{\partial E}{\partial k_i}. \tag{B.1.18}$$

Similarly, we may obtain the semi-classical equation for the momentum by taking the partial derivative of Eq. (B.1.14) with respect to x^i, where we get

$$0 = -\frac{\partial E}{\partial k_i}\frac{dt}{d\tau} + \frac{\partial \mathcal{H}}{\partial x^i}. \tag{B.1.19}$$

Again using the Hamilton's equation, we obtain for the momenta

$$\frac{dk_i}{dt} = \frac{dk_i}{d\tau}\left(\frac{dt}{d\tau}\right)^{-1} = -\frac{\partial E}{\partial x^i}. \tag{B.1.20}$$

This then completes the mapping between the Weyl node to the particle in curved space-times.

B.2 Deflection angle

In this appendix, we shall discuss the calculation of the deflection. For this, we shall derive the so-called trajectory equation, which expresses the angular coordinate ϕ as function of r.

First, let us check a claim that we made in the main text, where we stated that the in-plane dynamics ($\theta = \pi/2$) in the Schwarzschild spacetime with $\boldsymbol{u}(\boldsymbol{r}) = u(r)\hat{\boldsymbol{r}}$ is the same as that of the axially symmetric case. To show this, we first transform the metric to spherical coordinates. This can be effected by acting on the metric matrix with the Jacobian matrix of the coordinate transformation $(x, y, z) \to (r\sin(\theta)\cos(\phi), r\sin(\theta)\sin(\phi), r\cos(\theta))$. We have

$$J^T g J = \begin{pmatrix} u(r)^2/c^2 - 1 & -u(r)/c & 0 & 0 \\ -u(r)/c & 1 & 0 & 0 \\ 0 & 0 & r^2 & 0 \\ 0 & 0 & 0 & r^2\sin^2(\theta) \end{pmatrix}, \tag{B.2.1}$$

which defines the transformed metric $g'_{\mu\nu} \equiv (J^T g J)_{\mu\nu}$. Using the transformed inverse metric, the relativistic energy-momentum relation reads

$$\mathcal{H} = \frac{1}{2}\left(k_1^2 + \frac{k_2^2}{r^2} + \frac{k_3^2}{r^2\sin(\theta)^2} - \frac{(E - k_1 u(r))^2}{c^2}\right), \tag{B.2.2}$$

where the k_i's are the momenta in the transformed coordinates, and not the Euclidean ones. These are of course related to the spherical coordinates components of $\boldsymbol{k}$: k_r, k_θ and k_ϕ. Let us again solve for E that satisfies $\mathcal{H} = 0$, which gives

$$E_\pm = k_1 u(r) \pm c\sqrt{k_1^2 + \left(k_2^2 + k_3^2\csc^2(\theta)\right)/r^2}. \tag{B.2.3}$$

For this to agree with Eq. (B.1.4), we then need to identify $k_1 = k_r$ and $k_2^2 + k_3^2\csc(\theta) = r^2(k_\theta^2 + k_\phi^2)$, where $k_r = \boldsymbol{k}\cdot\hat{\boldsymbol{r}}$, $k_\theta = \boldsymbol{k}\cdot\hat{\boldsymbol{\theta}}$, $k_\phi = \boldsymbol{k}\cdot\hat{\boldsymbol{\phi}}$. We also used that by definition, $k_x^2 + k_y^2 + k_z^2 = k_r^2 + k_\theta^2 + k_\phi^2$, and $\boldsymbol{u}(\boldsymbol{r})\cdot\boldsymbol{k} = u(r)k_r$. We may restrict the motion onto the xy-plane, by imposing the constraint $\boldsymbol{L} = L_z\hat{\boldsymbol{z}} = rk_\phi\hat{\boldsymbol{z}}$, namely the angular momentum points perpendicularly to the plane of motion. This then implies the momentum also lies on the xy-plane. Note a planar motion also implies that $d\theta/d\tau = k_2/r^2 = 0$, and thus k_2 as well as k_θ vanish. By our discussion above, this leads to that the angular momentum is $k_3 = L_z$, and is a conserved quantity. With these considerations, the equations of motion of

the ϕ, r coordinates read

$$\frac{d\phi}{d\tau} = \frac{k_3}{r^2}, \tag{B.2.4}$$

$$\frac{dr}{d\tau} = k_r\left(1 - \frac{u(r)^2}{c^2}\right) + E\frac{u(r)}{c^2} = \pm\frac{1}{c}\sqrt{E^2 - \frac{k_3^2}{r^2}\Big(c^2 - u(r)^2\Big)}. \tag{B.2.5}$$

Transforming to real time by multiplying both sides of the above equations by the factor $(dt/d\tau)^{-1} = (\partial\mathcal{H}/\partial E)^{-1} = \pm c/\sqrt{k_r^2 + L_z^2/r^2}$, we recover the plane semi-classical equations of motion Eq. (4.3.6), except for different tilt profiles u are being used.

We may now immediately obtain the trajectory equation by dividing the two equations using quotient rule of total derivative, which gives

$$\frac{d\phi}{dr} = \pm\frac{c\,L_z}{r^2\sqrt{E^2 - \varepsilon_{\mathrm{p,eff}}(r)}}. \tag{B.2.6}$$

This is Eq. (4.3.8) in the main text, with the mere differences being the replacement $c \to v_F$ and $r \to \rho$.

Finally re-arranging the differentials, we may then calculate the deflection angle by (we now use the notations as in the main text)

$$\int d\phi = \pm\int \frac{v_F\,L_z\,d\rho}{\rho^2\sqrt{E_+^2 - \varepsilon_{\mathrm{p,eff}}(\rho)}}. \tag{B.2.7}$$

We need to determine the signs. Recall the periapsis is the point of closest approach to the center of the tilt profile on the trajectory. Let it be at $\rho = \rho_p$, and denote the tilt at the periapsis as $u_p^2 = u(\rho_p)^2 = v_F^2(\rho_t/\rho_p)^{2\alpha}$. When the particle is approaching from far away up to the periapsis, the angular component measured from the tilt center decreases due to attraction, and thus we shall the $-$ sign. Conversely, when it shoots off leaving the periapsis, we shall take the $+$ sign.

The periapsis is completely determined by the impact parameters L_z and E_+, since by definition we have

$$\left.\frac{d\rho}{d\phi}\right|_{\rho=\rho_p} = 0, \tag{B.2.8}$$

which implies that

$$0 = \left(\frac{d\rho}{d\phi}\right)^2\Big|_{\rho=\rho_p} = \left(\frac{E_+}{L_z}\right)^2 \rho_p^4 - \rho_p^2(v_F^2 - u_p^2), \tag{B.2.9}$$

and thus

$$\left(\frac{E_+}{L_z}\right)^2 = \frac{1}{\rho_p^2}(v_F^2 - u_p^2). \tag{B.2.10}$$

Substitute this into Eq. (B.2.6) and thus eliminating E and L_z, the deflection angle is then given by

$$\begin{aligned}\pi + \varphi &= \int_{\phi_1}^{\phi_1+\pi+\varphi} d\phi = \left(-\int_{\infty}^{\rho_p} + \int_{\rho_p}^{\infty}\right) \frac{v_F}{\sqrt{\frac{1}{\rho_p^2}(v_F^2 - u_p^2)\rho^4 - \rho^2(v_F^2 - u(\rho)^2)}} d\rho \\ &= 2\int_{\rho_p}^{\infty} \frac{v_F}{\sqrt{\frac{1}{\rho_p^2}(v_F^2 - u_p^2)\rho^4 - \rho^2(v_F^2 - u(\rho)^2)}} d\rho,\end{aligned} \tag{B.2.11}$$

where $\varphi = \phi_1 - \phi_2$ is the deflection angle as shown in Fig. 4.4. This Eq. (4.3.9) in our main text. This integral can be numerically evaluated, but lacks an analytical expression. However, for $\rho_t/\rho_p \ll 1$, we may perform an asymptotic expansion in ρ_t/ρ_p. To leading order, we find

$$\pi + \varphi \approx 2\int_{\rho_p}^{\infty} d\rho \left(\frac{\rho_p}{\rho\sqrt{\rho^2 - \rho_p^2}} + \frac{\rho_p\left(u_p^2\rho^2 - u^2\rho_p^2\right)}{v_F^2\,\rho\left(\rho^2 - \rho_p^2\right)^{3/2}}\right) \tag{B.2.12}$$

$$= \pi + 2\int_{\rho_p}^{\infty} d\rho \frac{\rho_p\left(u_p^2\rho^2 - u^2\rho_p^2\right)}{v_F^2\,\rho\left(\rho^2 - \rho_p^2\right)^{3/2}} \tag{B.2.13}$$

The second term may be evaluated by changing the integration variable to the dimensionless $s = \rho/\rho_p$, and from the integral table we obtain a final expression for the lensing angle in terms of the gamma function

$$\varphi \approx \frac{u_p^2}{v_F^2}\int_1^{\infty} ds \frac{s^2 - s^{-2\alpha}}{s\,(s^2-1)^{3/2}} = \frac{u_p^2}{v_F^2}\frac{\sqrt{\pi}\,\Gamma\left(\frac{3}{2}+\alpha\right)}{\Gamma\left(1+\alpha\right)}. \tag{B.2.14}$$

B.3 Transverse shift

In this appendix, we shall give the details for calculating the transverse shift Δz. As in the main text, without loss generality we set $k_z = 0$. Similar to the calculation of deflection angle, we divide the equations of motion Eq. (4.3.4) and Eq. (4.3.5a), and use quotient to obtain

$$\frac{dz}{d\rho} = \frac{\dot{z}}{\dot{\rho}} = -\frac{\chi}{2\,k^3}\frac{\frac{\boldsymbol{k}\cdot\hat{\boldsymbol{\rho}}}{\rho}\left(\frac{\partial u}{\partial \rho} - \frac{u}{\rho}\right) L_z}{u + v_F\,\frac{\boldsymbol{k}\cdot\hat{\boldsymbol{\rho}}}{k}}. \tag{B.3.1}$$

We eliminate $\boldsymbol{k}\cdot\hat{\boldsymbol{\rho}}$ and k in favor of the conserved impact parameters E_+ and L_z by using

$$E_+ = u\,\boldsymbol{k}\cdot\hat{\boldsymbol{\rho}} + v_F\,k, \tag{B.3.2}$$

$$k^2 = (\boldsymbol{k}\cdot\hat{\boldsymbol{\rho}})^2 + L_z^2/\rho^2. \tag{B.3.3}$$

There are two solution, which we shall label as $(\boldsymbol{k}\cdot\hat{\boldsymbol{\rho}}, k) \to (k_\rho^{(\sigma)}, k^{(\sigma)})$ with $\sigma = \pm 1$. These

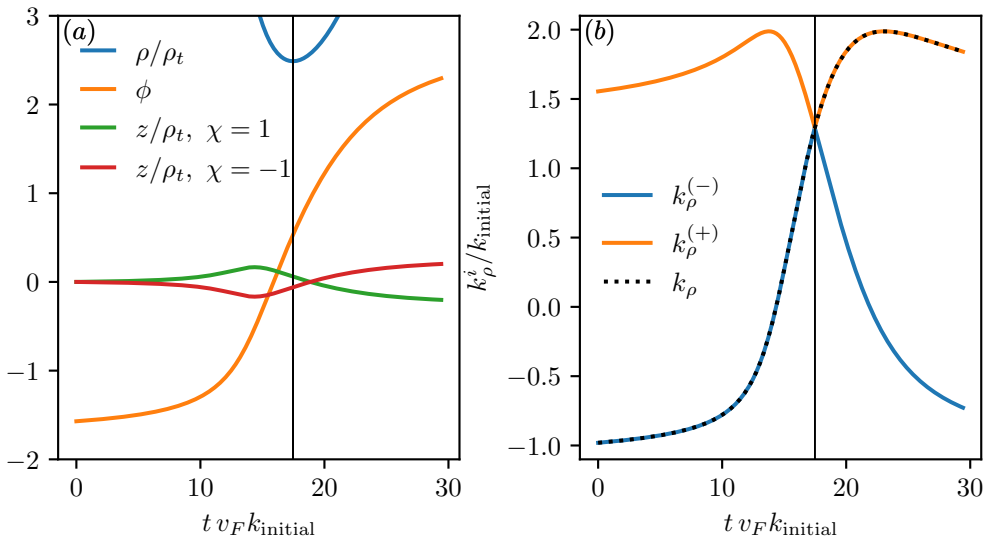

Figure B.15. Coordinates of an arbitrary lensing trajectory. Spatial coordinates are plotted in panel (a), while panel (b) displays the two roots $k_\rho^{(\sigma)}$, together with k_ρ of the trajectory. At the periapsis (marked by a black line), k_ρ switches between the two branches.

solutions read

$$k_\rho^{(\sigma)} = \frac{E_+\,u - \sigma\,\frac{\sqrt{L_z^2\,u^2\,v_F^2 - L_z^2\,v_F^4 + E_+^2\,v_F^2\,\rho^2}}{\rho}}{u^2 - v_F^2}, \tag{B.3.4}$$

$$k^{(\sigma)} = \sqrt{\left(k_\rho^{(\sigma)}\right)^2 + \frac{L_z^2}{\rho^2}}. \tag{B.3.5}$$

The two signs of σ determine which one of the solution we shall take in evaluating the shift angle. While approaching the periapsis ρ_p, we shall use the one with $\sigma = +1$, and when escaping, $\sigma = -1$. see also Fig. B.15. Substituting this in Eq. (B.3.1), we then have the integral expression of the transverse shift

$$\begin{aligned}\Delta z &= -\int_{\infty}^{\rho_p} d\rho\, \frac{\chi}{2\,(k^{(-)})^3}\, \frac{\frac{k_\rho^{(-)}}{\rho}\left(\frac{\partial u}{\partial \rho} - \frac{u}{\rho}\right) L_z}{u + v_F\, \frac{k_\rho^{(-)}}{k^{(-)}}} - \int_{\rho_p}^{\infty} d\rho\, \frac{\chi}{2\,(k^{(+)})^3}\, \frac{\frac{k_\rho^{(+)}}{\rho}\left(\frac{\partial u}{\partial \rho} - \frac{u}{\rho}\right) L_z}{u + v_F\, \frac{k_\rho^{(+)}}{k^{(+)}}} \\ &= \int_{\rho_p}^{\infty} d\rho \left(\frac{\chi}{2\,(k^{(-)})^3}\, \frac{\frac{k_\rho^{(-)}}{\rho}\left(\frac{\partial u}{\partial \rho} - \frac{u}{\rho}\right) L_z}{u + v_F\, \frac{k_\rho^{(-)}}{k^{(-)}}} - \frac{\chi}{2\,(k^{(+)})^3}\, \frac{\frac{k_\rho^{(+)}}{\rho}\left(\frac{\partial u}{\partial \rho} - \frac{u}{\rho}\right) L_z}{u + v_F\, \frac{k_\rho^{(+)}}{k^{(+)}}} \right). \end{aligned} \tag{B.3.6}$$

Again these integrals admit no analytic solutions. Howver, for lensed trajectories that stay far from the tilt center, i.e., trajectories for which $\rho_t/\rho \ll 1$, which implies $u, u_p \ll v_F$, we may obtain an analytic expression by expanding the integrand in ρ_t/ρ. To leading order, the integral can then be approximated as

$$\Delta z \approx \chi \int_{\rho_p}^{\infty} d\rho\, \frac{u^2\,(1+\alpha)\,\rho_p^2\,(\rho^2 - 2\,\rho_p^2)}{L_z\, v_F^2\, \rho^3\, \sqrt{\rho^2 - \rho_p^2}}. \tag{B.3.7}$$

Changing the integration variable to dimensionless $s = \rho/\rho_p$, we have the asymptotic value of the shift angle as

$$\begin{aligned}\Delta z &\approx \chi\, \frac{(1+\alpha)}{L_z}\, \rho_p \left(\frac{\rho_t}{\rho_p}\right)^{2\alpha} \int_1^{\infty} ds\, \frac{s^{-3-2\alpha}\,(s^2-2)}{\sqrt{s^2-1}} \\ &= -\chi\, \frac{(1+\alpha)}{L_z}\, \rho_p \left(\frac{\rho_t}{\rho_p}\right)^{2\alpha} \frac{\sqrt{\pi}\,\alpha}{2}\, \frac{\Gamma\left(\alpha + \frac{1}{2}\right)}{\Gamma(2+\alpha)} \\ &= -\chi \frac{u_p^2}{v_F^2}\, \frac{\rho_p}{L_z}\, \frac{\sqrt{\pi}\,\Gamma\left(\alpha + \frac{1}{2}\right)}{2\,\Gamma(\alpha)}, \end{aligned} \tag{B.3.8}$$

valid for $\rho_t/\rho_p \ll 1$.

Chapter 5
Conclusion

In the two parts of this thesis, we have explored role of geometry in the semi-classical equations of motion of electrons in crystalline solids. They are directed at two aspects: the momentum space quantum geometric contributions to effective electron dynamics, and the remarkable analog gravitational lensing phenomena in tilted Weyl semi-metals.

In Part I, we developed a systematic operator algebra formalism to study the quantum geometric contributions to the semi-classical equations of motion when an inhomogeneous external electromagnetic field is applied. We demonstrated how band projection plays a fundamental role in the emergence of such corrections, since it substantially modifies the commutation relations and is the origin of such geometric terms. This observation highlights the fact that such corrections to the semi-classical equations of motion as the familiar Berry curvature induced anomalous velocity are fundamentally multi-band effects. Given the generality of our approach, this may prove to be useful in the study of quantum geometry in other physical systems as well, and not just electronic systems. Furthermore, let us also mention that the momentum generating operator $\hat{M}_{\mathcal{B}}(\boldsymbol{a}) = \left(\mathrm{e}^{-\mathrm{i}\boldsymbol{a}\cdot\hat{\boldsymbol{r}}}\right)_{\mathcal{B}}$ may be viewed as the Fourier components of the density operator $\delta(\boldsymbol{r}-\hat{\boldsymbol{r}})$, if we take $\boldsymbol{a}$ to be a crystal momentum and not just a parameter to be differentiated with. It is recently realized that [159], if their commutators close to form an algebra, namely $[\hat{M}_{\mathcal{B}}(\boldsymbol{a}), \hat{M}_{\mathcal{B}}(\boldsymbol{b})] = f(\boldsymbol{a}, \boldsymbol{b}; \boldsymbol{c})\hat{M}_{\mathcal{B}}(\boldsymbol{c})$, then the resultant algebra is necessarily of the so-called Girvin-MacDonald-Platzman(GMP) form [50, 51]. The GMP algebra was first found in the fractional quantum Hall effect (FQHE), where the projection is onto the lowest Landau level. It was argued that the density operators forming a GMP algebra is a key signature of fractional Chern insulators [115, 117], systems which have the FQHE in a topological band without magnetic field. It is then possible that the operator formalism and operator form of quantum geometric quantities introduced in this thesis may be of use in understanding the band structure of such novel phases of matter.

In Part II, we transitioned from momentum space geometry to real-space phenomena by examining electron dynamics in in-homogeneously tilted Weyl semi-metals. Here we explored a remarkable analogy between the semiclassical trajectories of electrons near Weyl nodes and gravitational lensing effect of massless particles moving in curved space-times. Using both a low-energy effective continuum description and microscopic lattice model, we studied various aspects of the lensing effects, including the scaling behavior of deflection angles, particle capture by the "photon cylinder", and transverse shifts due to the Berry curvature. These findings bridge concepts from condensed matter physics and general relativity, paving a way to the study of relativistic physics using topological semi-metals. In outlook, we envision that such spatially-varying tilt profiles in Weyl semi-metals may be can be experimentally realized using a magnetization texture or locally applied strain, which might lead to a field of "tiltronics". That is by engineering different tilt profiles in topological semi-metals, we may be able to produce devices that have a manipulatable electronic transport behavior. In fact note how the separatrix has a similar role of a high- pass filter in electronics [67]. This then also leads to the question of how such spatially-varying tilt profiles can be realized in the lab. We have already mentioned the possibility of applying strain. Another, probably more easily engineered, option is to use a magnetization texture [93]. Regardless of its origin, the presence of such spatial in-homogeneity requires one to consider the effect of impurity and disorder that may affect the bulk electron transport. On top of that, it is also natural to ask whether the geometric contributions to electron dynamics in in-homogeneous external fields studied in **Part I** of the thesis would also show up. We shall leave all such questions for future research.

[1] E.N. Adams and E.I. Blount. Energy bands in the presence of an external force field—ii. *J. Phys. Chem. Solids*, 10(4):286–303, August 1959.

[2] Stephen L. Adler. Axial-Vector Vertex in Spinor Electrodynamics. *Phys. Rev.*, 177:2426–2438, Jan 1969.

[3] Junyeong Ahn, Guang-Yu Guo, and Naoto Nagaosa. Low-frequency divergence and quantum geometry of the bulk photovoltaic effect in topological semimetals. *Phys. Rev. X*, 10:041041, Nov 2020.

[4] Junyeong Ahn, Guang-Yu Guo, Naoto Nagaosa, and Ashvin Vishwanath. Riemannian geometry of resonant optical responses. *Nat. Phys.*, 18, 03 2022.

[5] Junyeong Ahn and Naoto Nagaosa. Theory of optical responses in clean multi-band superconductors. *Nat. Comm.*, 12, 2020.

[6] Vivek Aji. Adler-Bell-Jackiw anomaly in Weyl semimetals: Application to pyrochlore iridates. *Phys. Rev. B*, 85:241101, Jun 2012.

[7] Kazunori Akiyama et al. First M87 Event Horizon Telescope Results. I. The Shadow of the Supermassive Black Hole. *Astrophys. J. Lett.*, 875:L1, 2019.

[8] Krzysztof Andrzejewski, Agnieszka Kijanka-Dec, Piotr Kosinski, and Pawel Maslanka. Chiral fermions, massless particles and Poincare covariance. *Physics Letters B*, 746:417–423, 2015.

[9] Vicente Arjona and María A. H. Vozmediano. Rotational strain in Weyl semimetals: A continuum approach. *Phys. Rev. B*, 97:201404, May 2018.

[10] N. P. Armitage, E. J. Mele, and Ashvin Vishwanath. Weyl and Dirac semimetals in three-dimensional solids. *Rev. Mod. Phys.*, 90:015001, Jan 2018.

[11] N. W. Ashcroft and N. D. Mermin. *Solid State Physics*. Holt-Saunders, 1976.

[12] Alexander Avdoshkin and Fedor K. Popov. Extrinsic geometry of quantum states. *Phys. Rev. B*, 107:245136, Jun 2023.

[13] Gök çe Başar, Dmitri E. Kharzeev, and Ho-Ung Yee. Triangle anomaly in weyl semimetals. *Phys. Rev. B*, 89:035142, Jan 2014.

[14] Carlos Barceló, Stefano Liberati, and Matt Visser. Analogue gravity. *Living Reviews in Relativity*, 8, dec 2005.

[15] Jan Behrends, Sthitadhi Roy, Michael H. Kolodrubetz, Jens H. Bardarson, and Adolfo G. Grushin. Landau levels, Bardeen polynomials, and Fermi arcs in Weyl semimetals: Lattice-based approach to the chiral anomaly. *Phys. Rev. B*, 99:140201, Apr 2019.

[16] J. S. Bell and R. Jackiw. A PCAC puzzle: $\pi^0 \to \gamma\gamma$ in the σ-model. *Il Nuovo Cimento A*, 60:47, 1970.

[17] Ingemar Bengtsson and Karol Zyczkowski. *Geometry of Quantum States*. Cambridge University Press, May 2006.

[18] Baptiste Bermond, Maxim Chernodub, Adolfo G. Grushin, and David Carpentier. Anomalous Luttinger equivalence between temperature and curved spacetime: From black hole's atmosphere to thermal quenches. 2022.

[19] B. Andrei Bernevig and Taylor L. Hughes. 2013.

[20] Michael V. Berry. Quantal phase factors accompanying adiabatic changes. *Proc. Roy. Soc. Lond. A*, 392:45–57, 1984.

[21] Christophe De Beule, Solofo Groenendijk, Tobias Meng, and Thomas L. Schmidt. Artificial event horizons in Weyl semimetal heterostructures and their non-equilibrium signatures. *SciPost Phys.*, 11:095, 2021.

[22] Raffaello Bianco and Raffaele Resta. Orbital magnetization as a local property. *Phys. Rev. Lett.*, 110:087202, Feb 2013.

[23] K. Yu Bliokh. Topological spin transport of a relativistic electron. *Europhysics Letters (EPL)*, 72:7–13, oct 2005.

[24] K.Yu. Bliokh and Yu.P. Bliokh. Topological spin transport of photons: the optical Magnus effect and Berry phase. *Physics Letters A*, 333:181–186, dec 2004.

[25] Felix Bloch. Über die quantenmechanik der elektronen in kristallgittern. *Zeitschrift für Physik*, 52:555–600, 1929.

[26] Eugene I. Blount. Formalisms of band theory. *J. Phys. C: Solid State Physics*, 13:305–373, 1962.

[27] Barry Bradlyn and Mikel Iraola. Lecture notes on berry phases and topology. *SciPost Phys. Lect. Notes*, page 51, 2022.

[28] Jan Carl Budich and Björn Trauzettel. From the adiabatic theorem of quantum mechanics to topological states of matter. *physica status solidi (RRL) – Rapid Research Letters*, 7(1–2):109–129, January 2013.

[29] A A Burkov. Chiral anomaly and transport in weyl metals. *J. Phys.: Cond. Mat.*, 27(11):113201, February 2015.

[30] Vitor Cardoso, Edgardo Franzin, and Paolo Pani. Is the Gravitational-Wave Ringdown a Probe of the Event Horizon? *Phys. Rev. Lett.*, 116:171101, Apr 2016.

[31] Angelo Carollo, Davide Valenti, and Bernardo Spagnolo. Geometry of quantum phase transitions. *Physics Reports*, 838:1–72, January 2020.

[32] A. H. Castro Neto, F. Guinea, N. M. R. Peres, K. S. Novoselov, and A. K. Geim. The electronic properties of graphene. *Rev. Mod. Phys.*, 81:109–162, Jan 2009.

[33] S. Chandrasekhar. *The mathematical theory of black holes*. Clarendon Press/Oxford University Press (International Series of Monographs on Physics. Volume 69), 1983.

[34] Ming-Che Chang and Qian Niu. Berry phase, hyperorbits, and the hofstadter spectrum. *Phys. Rev. Lett.*, 75:1348–1351, Aug 1995.

[35] Jing-Yuan Chen, Dam T. Son, Mikhail A. Stephanov, Ho-Ung Yee, and Yi Yin. Lorentz Invariance in Chiral Kinetic Theory. *Phys. Rev. Lett.*, 113:182302, Oct 2014.

[36] Maxim N. Chernodub, Alberto Cortijo, Adolfo G. Grushin, Karl Landsteiner, and María A. H. Vozmediano. Condensed matter realization of the axial magnetic effect. *Phys. Rev. B*, 89:081407, Feb 2014.

[37] Martin Claassen, Ching Hua Lee, Ronny Thomale, Xiao-Liang Qi, and Thomas P. Devereaux. Position-momentum duality and fractional quantum hall effect in chern insulators. *Phys. Rev. Lett.*, 114:236802, Jun 2015.

[38] Clarissa-Marie Claudel, K. S. Virbhadra, and G. F. R. Ellis. The geometry of photon surfaces. *Journal of Mathematical Physics*, 42:818, 2001.

[39] Matheus S. M. de Sousa, Antonio L. Cruz, and Wei Chen. Mapping quantum geometry and quantum phase transitions to real space by a fidelity marker. *Phys. Rev. B*, 107:205133, May 2023.

[40] W. G. Dixon. Dynamics of extended bodies in general relativity. I. Momentum and angular momentum. *Proc. Roy. Soc. Lond. A*, 314:499–527, 1970.

[41] C. Duval, M. Elbistan, P.A. Horváthy, and P.-M. Zhang. Wigner–Souriau translations and Lorentz symmetry of chiral fermions. *Physics Letters B*, 742:322–326, 2015.

[42] C. Duval and P. A. Horváthy. Chiral fermions as classical massless spinning particles. *Phys. Rev. D*, 91:045013, Feb 2015.

[43] M. Elbistan and P.A. Horvathy. Anomalous properties of spin-extended chiral fermions. *Physics Letters B*, 749:502–506, 2015.

[44] Zyun Francis Ezawa. *Quantum Hall Effects: Field Theoretical Approach and Related Topics*. WORLD SCIENTIFIC, November 2000.

[45] HERMAN FESHBACH. Unified theory of nuclear reactions. *Reviews of Modern Physics*, 36(4):1076–1078, October 1964.

[46] G. Floquet. Sur les équations différentielles linéaires à coefficients périodiques. *Annales scientifiques de l'École normale supérieure*, 12:47–88, 1883.

[47] Kenji Fukushima, Dmitri E. Kharzeev, and Harmen J. Warringa. Chiral magnetic effect. *Phys. Rev. D*, 78:074033, Oct 2008.

[48] Yang Gao and Di Xiao. Nonreciprocal directional dichroism induced by the quantum metric dipole. *Phys. Rev. Lett.*, 122:227402, Jun 2019.

[49] Suvendu Ghosh, Debabrata Sinha, Snehasish Nandy, and A. Taraphder. Chirality-dependent planar hall effect in inhomogeneous weyl semimetals. *Phys. Rev. B*, 102:121105, Sep 2020.

[50] S. M. Girvin, A. H. MacDonald, and P. M. Platzman. Collective-excitation gap in the fractional quantum hall effect. *Phys. Rev. Lett.*, 54:581–583, Feb 1985.

[51] S. M. Girvin, A. H. MacDonald, and P. M. Platzman. Magneto-roton theory of collective excitations in the fractional quantum hall effect. *Phys. Rev. B*, 33:2481–2494, Feb 1986.

[52] Johannes Gooth, Anna C. Niemann, Tobias Meng, Adolfo G. Grushin, Karl Landsteiner, Bernd Gotsmann, Fabian Menges, Marcus Schmidt, Chandra Shekhar, Vicky Süß, Ruben Hühne, Bernd Rellinghaus, Claudia Felser, Binghai Yan, and Kornelius Nielsch. Experimental signatures of the mixed axial–gravitational anomaly in the Weyl semimetal NbP. *Nature*, 547:324–327, 2017.

[53] E. V. Gorbar, V. A. Miransky, I. A. Shovkovy, and P. O. Sukhachov. Pseudomagnetic lens as a valley and chirality splitter in dirac and weyl materials. *Phys. Rev. B*, 95:241114, Jun 2017.

[54] Pierre Gosselin, Alain Bérard, and Hervé Mohrbach. Spin hall effect of photons in a static gravitational field. *Phys. Rev. D*, 75:084035, Apr 2007.

[55] Christoph W Groth, Michael Wimmer, Anton R Akhmerov, and Xavier Waintal. Kwant: a software package for quantum transport. *New Journal of Physics*, 16:063065, June 2014.

[56] Shan Guan, Zhi-Ming Yu, Ying Liu, Gui-Bin Liu, Liang Dong, Yunhao Lu, Yugui Yao, and Shengyuan A. Yang. Artificial gravity field, astrophysical analogues, and topological phase transitions in strained topological semimetals. *npj Quantum Materials*, 2, may 2017.

[57] Shahar Hadar, Daniel Kapec, Alexandru Lupsasca, and Andrew Strominger. Holography of the Photon Ring. 2022.

[58] F. D. M. Haldane. Berry curvature on the fermi surface: Anomalous hall effect as a topological fermi-liquid property. *Phys. Rev. Lett.*, 93(20):206602, November 2004.

[59] Andreas Haller, Suraj Hegde, Chen Xu, Christophe De Beule, Thomas L. Schmidt, and Tobias Meng. Black hole mirages: Electron lensing and Berry curvature effects in inhomogeneously tilted Weyl semimetals. *SciPost Phys.*, 14:119, 2023.

[60] Andreas Haller, Suraj Hegde, Chen Xu, Christophe De Beule, Thomas L. Schmidt, and Tobias Meng. Black hole mirages: Electron lensing and Berry curvature effects in inhomogeneously tilted Weyl semimetals. *SciPost Phys.*, 14:119, 2023.

[61] Abraham I. Harte and Marius A. Oancea. Spin Hall effects and the localization of massless spinning particles. *Phys. Rev. D*, 105:104061, May 2022.

[62] M. Z. Hasan and C. L. Kane. Colloquium: Topological insulators. *Rev. Mod. Phys.*, 82:3045–3067, Nov 2010.

[63] Koji Hashimoto and Yoshinori Matsuo. Escape from black hole analogs in materials: Type-II Weyl semimetals and generic edge states. *Phys. Rev. B*, 102:195128, Nov 2020.

[64] Suraj S. Hegde, Varsha Subramanyan, Barry Bradlyn, and Smitha Vishveshwara. Quasinormal Modes and the Hawking-Unruh Effect in Quantum Hall Systems: Lessons from Black Hole Phenomena. *Phys. Rev. Lett.*, 123:156802, Oct 2019.

[65] Shiva Heidari and Reza Asgari. Chiral Hall effect in strained Weyl semimetals. *Phys. Rev. B*, 101:165309, Apr 2020.

[66] Balázs Hetényi and Péter Lévay. Fluctuations, uncertainty relations, and the geometry of quantum state manifolds. *Phys. Rev. A*, 108:032218, Sep 2023.

[67] Paul Horowitz and Winfield Hill. *The Art of Electronics*. Cambridge University Press, USA, 3rd edition, 2015.

[68] Pavan Hosur and Xiaoliang Qi. Recent developments in transport phenomena in weyl semimetals. *Comptes Rendus Physique*, 14(9–10):857–870, November 2013.

[69] Hsiu-Chuan Hsu, Jhih-Shih You, Junyeong Ahn, and Guang-Yu Guo. Nonlinear photoconductivities and quantum geometry of chiral multifold fermions. *Phys. Rev. B*, 107:155434, Apr 2023.

[70] Huaqing Huang, Kyung-Hwan Jin, and Feng Liu. Black-hole horizon in the Dirac semimetal $Zn_2In_2S_5$. *Phys. Rev. B*, 98:121110, Sep 2018.

[71] P. Huhtala and G. E. Volovik. Fermionic microstates within the Painlevé-Gullstrand black hole. *J. Exp. Theor. Phys.*, 94:853, 2002.

[72] Kukka-Emilia Huhtinen, Jonah Herzog-Arbeitman, Aaron Chew, Bogdan A. Bernevig, and Päivi Törmä. Revisiting flat band superconductivity: Dependence on minimal quantum metric and band touchings. *Phys. Rev. B*, 106:014518, Jul 2022.

[73] Bingyan Jiang, Lujunyu Wang, Ran Bi, Juewen Fan, Jiaji Zhao, Dapeng Yu, Zhilin Li, and Xiaosong Wu. Chirality-Dependent Hall Effect and Antisymmetric Magnetoresistance in a Magnetic Weyl Semimetal. *Phys. Rev. Lett.*, 126:236601, Jun 2021.

[74] Qing-Dong Jiang, Hua Jiang, Haiwen Liu, Qing-Feng Sun, and X. C. Xie. Topological Imbert-Fedorov Shift in Weyl Semimetals. *Phys. Rev. Lett.*, 115:156602, Oct 2015.

[75] Qing-Dong Jiang, Hua Jiang, Haiwen Liu, Qing-Feng Sun, and X. C. Xie. Chiral wave-packet scattering in Weyl semimetals. *Phys. Rev. B*, 93:195165, May 2016.

[76] Aleksi Julku, Sebastiano Peotta, Tuomas I. Vanhala, Dong-Hee Kim, and Päivi Törmä. Geometric origin of superfluidity in the lieb-lattice flat band. *Phys. Rev. Lett.*, 117:045303, Jul 2016.

[77] Robert Karplus and J. M. Luttinger. Hall effect in ferromagnetics. *Phys. Rev.*, 95:1154–1160, Sep 1954.

[78] Tosio Kato. On the adiabatic theorem of quantum mechanics. *J. Phys. Soc. Japan*, 5(6):435–439, 1950.

[79] M. I. Katsnelson, K. S. Novoselov, and A. K. Geim. Chiral tunnelling and the Klein paradox in graphene. *Nature Physics*, 2:620, 2006.

[80] Yaron Kedem, Emil J. Bergholtz, and Frank Wilczek. Black and white holes at material junctions. *Phys. Rev. Research*, 2:043285, Nov 2020.

[81] Charles Kittel and Donald F. Holcomb. Introduction to solid state physics. *American Journal of Physics*, 35(6):547–548, June 1967.

[82] Andy Knoll, Carsten Timm, and Tobias Meng. Negative longitudinal magnetoconductance at weak fields in Weyl semimetals. *Phys. Rev. B*, 101:201402, May 2020.

[83] Shoshichi Kobayashi and Katsumi Nomizu. *Foundations of differential geometry, 2 volume set*. Wiley Classics Library. Wiley-Blackwell, Hoboken, NJ, May 2009.

[84] W. Kohn and J. M. Luttinger. Quantum theory of electrical transport phenomena. *Phys. Rev.*, 108:590–611, Nov 1957.

[85] Viktor Könye, Corentin Morice, Dmitry Chernyavsky, Ali G. Moghaddam, Jeroen van den Brink, and Jasper van Wezel. Horizon physics of quasi-one-dimensional tilted Weyl cones on a lattice. 2022.

[86] Vladyslav Kozii, Alexander Avdoshkin, Shudan Zhong, and Joel E. Moore. Intrinsic anomalous hall conductivity in a nonuniform electric field. *Phys. Rev. Lett.*, 126:156602, Apr 2021.

[87] Vladyslav Kozii, Alexander Avdoshkin, Shudan Zhong, and Joel E. Moore. Intrinsic Anomalous Hall Conductivity in a Nonuniform Electric Field. *Phys. Rev. Lett.*, 126:156602, Apr 2021.

[88] Anirban Kundu, Zhuo Bin Siu, Hyunsoo Yang, and Mansoor B A Jalil. Magnetotransport of Weyl semimetals with tilted Dirac cones. *New Journal of Physics*, 22:083081, aug 2020.

[89] Karl Landsteiner. Anomalous transport of weyl fermions in weyl semimetals. *Phys. Rev. B*, 89:075124, Feb 2014.

[90] Matthew F. Lapa and Taylor L. Hughes. Semiclassical wave packet dynamics in nonuniform electric fields. *Phys. Rev. B*, 99:121111, Mar 2019.

[91] Matthew F. Lapa and Taylor L. Hughes. Semiclassical wave packet dynamics in nonuniform electric fields. *Phys. Rev. B*, 99:121111, Mar 2019.

[92] Qiang Li, Dmitri E. Kharzeev, Cheng Zhang, Yuan Huang, I. Pletikosić, A. V. Fedorov, R. D. Zhong, J. A. Schneeloch, G. D. Gu, and T. Valla. Chiral magnetic effect in zrte5. *Nat. Phys.*, 12(6):550–554, February 2016.

[93] Long Liang and Teemu Ojanen. Curved spacetime theory of inhomogeneous Weyl materials. *Phys. Rev. Research*, 1:032006, Oct 2019.

[94] Long Liang, Tuomas I. Vanhala, Sebastiano Peotta, Topi Siro, Ari Harju, and Päivi Törmä. Band geometry, berry curvature, and superfluid weight. *Phys. Rev. B*, 95:024515, Jan 2017.

[95] Sihang Liang, Jingjing Lin, Satya Kushwaha, Jie Xing, Ni Ni, R. J. Cava, and N. P. Ong. Experimental tests of the chiral anomaly magnetoresistance in the dirac-weyl semimetals na_3Bi and gdptbi. *Phys. Rev. X*, 8:031002, Jul 2018.

[96] Ze Liu, Zhi-Fan Zhang, Zhen-Gang Zhu, and Gang Su. Effect of disorder on berry curvature and quantum metric in two-band gapped graphene. *Phys. Rev. B*, 110:245419, Dec 2024.

[97] J. M. Luttinger. Theory of the hall effect in ferromagnetic substances. *Phys. Rev.*, 112:739–751, Nov 1958.

[98] Da Ma, Hua Jiang, Haiwen Liu, and X. C. Xie. Planar Hall effect in tilted Weyl semimetals. *Phys. Rev. B*, 99:115121, Mar 2019.

[99] Ken K. W. Ma and Kun Yang. Simple analog of the black-hole information paradox in quantum Hall interfaces. *Phys. Rev. B*, 105:045306, Jan 2022.

[100] Émile Mathieu. Mémoire sur le mouvement vibratoire d'une membrane de forme elliptique. *Journal de Mathématiques Pures et Appliquées*, 13:137–203, 1868.

[101] Bruno Mera and Tomoki Ozawa. Kähler geometry and chern insulators: Relations between topology and the quantum metric. *Phys. Rev. B*, 104:045104, Jul 2021.

[102] Lotte Mertens, Ali G. Moghaddam, Dmitry Chernyavsky, Corentin Morice, Jeroen van den Brink, and Jasper van Wezel. Thermalization by a synthetic horizon. 2022.

[103] Corentin Morice, Dmitry Chernyavsky, Jasper van Wezel, Jeroen van den Brink, and Ali G. Moghaddam. Quantum dynamics in 1D lattice models with synthetic horizons. 2021.

[104] Corentin Morice, Ali G. Moghaddam, Dmitry Chernyavsky, Jasper van Wezel, and Jeroen van den Brink. Synthetic gravitational horizons in low-dimensional quantum matter. *Phys. Rev. Research*, 3:L022022, Jun 2021.

[105] Naoto Nagaosa, Jairo Sinova, Shigeki Onoda, A. H. MacDonald, and N. P. Ong. Anomalous hall effect. *Rev. Mod. Phys.*, 82:1539–1592, May 2010.

[106] Mikio Nakahara. *Geometry, Topology and Physics*. CRC Press, October 2018.

[107] H. B. Nielsen and Masao Ninomiya. The Adler-Bell-Jackiw anomaly and Weyl fermions in a crystal. *Physics Letters B*, 130:389, 1983.

[108] W. Nolting and W.D. Brewer. *Fundamentals of Many-body Physics*. Springer International Publishing, 2018.

[109] Nozières, P. and Lewiner, C. A simple theory of the anomalous hall effect in semiconductors. *J. Phys. France*, 34(10):901–915, 1973.

[110] Marius A. Oancea, Jérémie Joudioux, I. Y. Dodin, D. E. Ruiz, Claudio F. Paganini, and Lars Andersson. Gravitational spin Hall effect of light. *Phys. Rev. D*, 102:024075, Jul 2020.

[111] J. Orenstein and Joel E. Moore. Berry phase mechanism for optical gyrotropy in stripe-ordered cuprates. *Phys. Rev. B*, 87:165110, Apr 2013.

[112] Tomoki Ozawa and Bruno Mera. Relations between topology and the quantum metric for chern insulators. *Phys. Rev. B*, 104:045103, Jul 2021.

[113] A. Papapetrou. Spinning test-particles in general relativity. I. *Proc. Roy. Soc. Lond. A*, 209:248, 1951.

[114] S. A. Parameswaran, R. Roy, and S. L. Sondhi. Fractional chern insulators and the W_∞ algebra. *Phys. Rev. B*, 85:241308, Jun 2012.

[115] S. A. Parameswaran, R. Roy, and S. L. Sondhi. Fractional chern insulators and the W_∞ algebra. *Phys. Rev. B*, 85:241308, Jun 2012.

[116] Siddharth A. Parameswaran, Rahul Roy, and Shivaji L. Sondhi. Fractional quantum hall physics in topological flat bands. *Comptes Rendus Physique*, 14(9–10):816–839, June 2013.

[117] Siddharth A. Parameswaran, Rahul Roy, and Shivaji L. Sondhi. Fractional quantum hall physics in topological flat bands. *Comptes Rendus. Physique*, 14(9–10):816–839, June 2013.

[118] Daniel E. Parker, Takahiro Morimoto, Joseph Orenstein, and Joel E. Moore. Diagrammatic approach to nonlinear optical response with application to weyl semimetals. *Phys. Rev. B*, 99:045121, Jan 2019.

[119] Michael E. Peskin. *An Introduction To Quantum Field Theory*. CRC Press, May 2018.

[120] Eric Poisson. *A Relativist's Toolkit: The Mathematics of Black-Hole Mechanics*. Cambridge University Press, 2004.

[121] J. P. Provost and G. Vallee. Riemannian structure on manifolds of quantum states. *Comm. Math. Phys.*, 76(3):289–301, September 1980.

[122] Xiao-Liang Qi and Shou-Cheng Zhang. Topological insulators and superconductors. *Rev. Mod. Phys.*, 83:1057–1110, Oct 2011.

[123] Bernard Raffaelli. Hidden conformal symmetry on the black hole photon sphere. *Journal of High Energy Physics*, 2022, mar 2022.

[124] R. Resta. The insulating state of matter: a geometrical theory. *Eur. Phys. J. B*, 79(2):121–137, jan 2011.

[125] Jorge Martínez Romeral, Aron W. Cummings, and Stephan Roche. Scaling of the integrated quantum metric in disordered topological phases. *Phys. Rev. B*, 111:134201, Apr 2025.

[126] Saber Rostamzadeh, Inanc Adagideli, and Mark Oliver Goerbig. Large enhancement of conductivity in Weyl semimetals with tilted cones: Pseudorelativity and linear response. *Phys. Rev. B*, 100:075438, Aug 2019.

[127] Saber Rostamzadeh, Sevval Tasdemir, Mustafa Sarisaman, S. A. Jafari, and Mark-Oliver Goerbig. Tilt induced vortical response and mixed anomaly in inhomogeneous weyl matter. 2022.

[128] Rahul Roy. Band geometry of fractional topological insulators. *Phys. Rev. B*, 90:165139, Oct 2014.

[129] Sthitadhi Roy, Michael Kolodrubetz, Nathan Goldman, and Adolfo G Grushin. Tunable axial gauge fields in engineered weyl semimetals: semiclassical analysis and optical lattice implementations. *2D Materials*, 5(2):024001, jan 2018.

[130] Daniel Sabsovich, Paul Wunderlich, Victor Fleurov, Dmitry I. Pikulin, Roni Ilan, and Tobias Meng. Hawking fragmentation and Hawking attenuation in Weyl semimetals. *Phys. Rev. Research*, 4:013055, Jan 2022.

[131] J. J. Sakurai and Jim Napolitano. *Modern Quantum Mechanics*. Cambridge University Press, September 2020.

[132] Akihiko Sekine and Kentaro Nomura. Axion electrodynamics in topological materials. *J. Appl. Phys.*, 129(14), April 2021.

[133] Shun-Qing Shen. *Topological Insulators: Dirac Equation in Condensed Matters*. Springer Berlin Heidelberg, 2012.

[134] Ryuichi Shindou and Ken-Ichiro Imura. Noncommutative geometry and non-abelian berry phase in the wave-packet dynamics of bloch electrons. *Nucl. Phys. B*, 720(3):399–435, 2005.

[135] Atsuo Shitade, Kazuya Mameda, and Tomoya Hayata. Chiral vortical effect in relativistic and nonrelativistic systems. *Phys. Rev. B*, 102:205201, Nov 2020.

[136] Steven H Simon. *The Oxford solid state basics*. Oxford Univ. Press, Oxford, UK, 2013.

[137] D. T. Son and B. Z. Spivak. Chiral anomaly and classical negative magnetoresistance of weyl metals. *Phys. Rev. B*, 88:104412, Sep 2013.

[138] D. T. Son and B. Z. Spivak. Chiral anomaly and classical negative magnetoresistance of Weyl metals. *Phys. Rev. B*, 88:104412, Sep 2013.

[139] M. A. Stephanov and Y. Yin. Chiral kinetic theory. *Phys. Rev. Lett.*, 109:162001, Oct 2012.

[140] Michael Stone. Gravitational anomalies and thermal Hall effect in topological insulators. *Phys. Rev. B*, 85:184503, May 2012.

[141] Michael Stone. An analogue of Hawking radiation in the quantum Hall effect. *Classical and Quantum Gravity*, 30:085003, mar 2013.

[142] Michael Stone. Berry phase and anomalous velocity of Weyl fermions and Maxwell photons. *International Journal of Modern Physics B*, 30:1550249, Jan 2016.

[143] Michael Stone, Vatsal Dwivedi, and Tianci Zhou. Berry phase, Lorentz covariance, and anomalous velocity for Dirac and Weyl particles. *Physical Review D*, 91, Jan 2015.

[144] Michael Stone, Vatsal Dwivedi, and Tianci Zhou. Wigner Translations and the Observer Dependence of the Position of Massless Spinning Particles. *Phys. Rev. Lett.*, 114:210402, May 2015.

[145] Michael Stone and JiYoung Kim. Mixed anomalies: Chiral vortical effect and the Sommerfeld expansion. *Phys. Rev. D*, 98:025012, Jul 2018.

[146] Varsha Subramanyan, Suraj S. Hegde, Smitha Vishveshwara, and Barry Bradlyn. Physics of the Inverted Harmonic Oscillator: From the lowest Landau level to event horizons. *Annals of Physics*, 435:168470, dec 2021.

[147] Ganesh Sundaram and Qian Niu. Wave-packet dynamics in slowly perturbed crystals: Gradient corrections and berry-phase effects. *Phys. Rev. B*, 59:14915–14925, Jun 1999.

[148] Serguei Tchoumakov, Marcello Civelli, and Mark O. Goerbig. Magnetic-Field-Induced Relativistic Properties in Type-I and Type-II Weyl Semimetals. *Phys. Rev. Lett.*, 117:086402, Aug 2016.

[149] D. J. Thouless, M. Kohmoto, M. P. Nightingale, and M. den Nijs. Quantized hall conductance in a two-dimensional periodic potential. *Phys. Rev. Lett.*, 49:405–408, Aug 1982.

[150] P. Törmä, S. Peotta, and B. A. Bernevig. Superfluidity and Quantum Geometry in Twisted Multilayer Systems. *Nat. Rev. Phys.*, 4:528, 2022.

[151] Päivi Törmä. Essay: Where can quantum geometry lead us? *Phys. Rev. Lett.*, 131:240001, Dec 2023.

[152] Matisse Wei-Yuan Tu, Ci Li, and Wang Yao. Theory of wave-packet transport under narrow gaps and spatial textures: Nonadiabaticity and semiclassicality. *Phys. Rev. B*, 102:045423, Jul 2020.

[153] William Unruh and Ralf Schützhold. *Quantum analogues: from phase transitions to black holes and cosmology*, volume 718. Springer, 2007.

[154] G. E. Volovik. Black hole and Hawking radiation by type-II Weyl fermions. *JETP Letters*, 104:645–648, Nov 2016.

[155] G. E. Volovik and K. Zhang. Lifshitz Transitions, Type-II Dirac and Weyl Fermions, Event Horizon and All That. *Journal of Low Temperature Physics*, 189:276–299, Dec 2017.

[156] G.E. Volovik and M.A. Zubkov. Emergent Weyl spinors in multi-fermion systems. *Nuclear Physics B*, 881:514–538, 2014.

[157] Grigory E. Volovik. *The Universe in a Helium Droplet*. Oxford University Press, 02 2009.

[158] Dung Vu, Wenjuan Zhang, Cüneyt Şahin, Michael E Flatté, Nandini Trivedi, and Joseph P Heremans. Thermal chiral anomaly in the magnetic-field-induced ideal Weyl phase of $Bi_{1-x}Sb_x$. *Nature Materials*, 20:1525–1531, 2021.

[159] Ziwei Wang and Steven H. Simon. Closed band-projected density algebra must be girvin-macdonald-platzman. *Phys. Rev. Lett.*, 134:136502, Mar 2025.

[160] Steven Weinberg. *Gravitation and cosmology principles and applications of the general theory of relativity*. Wiley, New York, 1976.

[161] Alex Weststrom and Teemu Ojanen. Designer Curved-Space Geometry for Relativistic Fermions in Weyl Metamaterials. *Physical Review X*, 7, oct 2017.

[162] Hermann Weyl. Gravitation and the electron. *Proceedings of the National Academy of Sciences*, 15(4):323–334, April 1929.

[163] E. T. Whittaker and G. N. Watson. *A Course of Modern Analysis*. Cambridge University Press, September 1996.

[164] Di Xiao, Ming-Che Chang, and Qian Niu. Berry phase effects on electronic properties. *Rev. Mod. Phys.*, 82:1959–2007, Jul 2010.

[165] Di Xiao, Ming-Che Chang, and Qian Niu. Berry phase effects on electronic properties. *Rev. Mod. Phys.*, 82:1959–2007, Jul 2010.

[166] Naoki Yamamoto. Photonic chiral vortical effect. *Phys. Rev. D*, 96:051902, Sep 2017.

[167] Can Yesilyurt, Zhuo Bin Siu, Seng Ghee Tan, Gengchiau Liang, Shengyuan A. Yang, and Mansoor B. A. Jalil. Electrically tunable valley polarization in Weyl semimetals with tilted energy dispersion. *Sci. Rep.*, 9:4480, 2019.

[168] Zhi-Ming Yu, Yugui Yao, and Shengyuan A. Yang. Predicted Unusual Magnetoresponse in Type-II Weyl Semimetals. *Phys. Rev. Lett.*, 117:077202, Aug 2016.

[169] Mikhail Zubkov. Analogies between the Black Hole Interior and the Type II Weyl Semimetals. *Universe*, 4:135, nov 2018.